The Design of Active Sites
for Selective Catalytic Conversion of Carbon Dioxide

Soichi Kikkawa

2020

Preface

Since the discovery of fire, human progress has depended on converting chemical resources to thermal energies to extend the time for activities, establish colonies in cold regions, and develop advanced tools by casting and pottering. The technological establishment of the heat engine for converting thermal energy into mechanical work allowed for mass production and transportation through the consumption of fossil fuels, such as coal, oil, and natural gas, in exchange for CO_2 emission as one of the final oxidized products. In the present day, total worldwide energy consumption approached 15 TW, with more than 80% derived from fossil fuels. The world's population has risen dramatically since the Industrial Revolution owing to advancements in childbirth, healthcare, and the extension of the average life span. As reported in World Population Prospects: The 2019 Revision, this upward trend in population size is expected to continue. As countries develop technologically and economically, more chemical resources will be consumed and more CO_2 gases will be emitted. The amount of CO_2 in the atmosphere has continued to increase throughout the last century and reached 405 ppm in 2017 according to the World Meteorological Organization. The Fifth Assessment Report (AR5) of the Intergovernmental Panel on Climate Change (IPCC) stated that, since the Industrial Revolution, human beings are certainly the primary cause of the current state of global warming, although a direct relationship to the emission of greenhouse gases, such as CO_2, has been debated. The Special Report on Global Warming of 1.5 ℃ (SR1.5) stated that we must reduce our CO_2 emissions by 45% from 2010 levels by 2030 and reach "net zero" emission by 2050 if we are to prevent a global catastrophe. We are facing a man-made disaster on a global scale, and it is imperative that we harness our scientific knowledge to reduce CO_2 emissions.

This thesis focuses on the catalytic reduction of CO_2 using heterogeneous catalysts and photocatalysts as promising technologies for recycling CO_2 into useful feedstocks. In particular, the design of active sites for the selective conversion of CO_2 was studied. Studies were performed on Ni-based isolated Pt alloy catalysts for the selective methanation of CO_2. *In situ* and time-resolved infrared spectroscopy and kinetic studies unveiled the crucial role of the isolated Pt atoms within the Ni-based catalyst in efficient and selective CH_4 formation. In addition, the effect of metal-support

interactions between Pt and the γ-Al_2O_3 support on product selectivity during CO_2 hydrogenation was investigated. *In situ* spectroscopy, including infrared spectroscopy and X-ray absorption spectroscopy, and their combined *operando* spectroscopy revealed the role of the interaction between Pt catalysts and the Al_2O_3 support in controlling selectivity. The photocatalytic conversion of CO_2 over Ga_2O_3-based photocatalysts with Ag co-catalyst using H_2O as an electron donor was also investigated. Evaluations of photoabsorption properties, electron donor oxidation, and reduction of CO2 provided insights for the development of photocatalysts that effectively and selectively convert CO_2.

The studies presented in this thesis were conducted at the Department of Molecular Engineering, Graduate School of Engineering, Kyoto University from 2014 to 2019 under the supervision of Professor Tsunehiro Tanaka. The author expresses his sincere gratitude to Professor Tsunehiro Tanaka for his guidance, philosophical suggestions, and continual encouragement throughout this work. The author would also like to acknowledge Professor Kentaro Teramura for his patient direction, valuable suggestions, constructive discussions and advice, and constant encouragement. Grateful thanks are extended to Professor Saburo Hosokawa for his practical advice, stimulating discussions, and useful comments. The author deeply thanks Dr. Hiroyuki Asakura for his useful suggestions, fruitful discussions, and steady encouragement. Cordial thanks are given to Professor Tetsuya Shishido at Tokyo Metropolitan University for his helpful advice and kind encouragement. The author expresses thanks to Professor Hisao Yoshida at Kyoto University, Professor Tomoko Yoshida at Osaka City University, Professor Takashi Yamamoto at Tokushima University, Professor Ryu Abe at Kyoto University, Professor Seiji Yamazoe at Tokyo Metropolitan University, Professor Junya Ohyama at Kumamoto University, Dr. Hiroki Miura at Tokyo Metropolitan University, and Dr. Atsuhiro Tanaka at Kindai University for their valuable advice and heartwarming encouragement. The author is also grateful to the senior members in his laboratory, Dr. Akira Yamamoto, Dr. Zheng Wang, Dr. Shoji Iguchi, Dr. Zeai Huang, Dr. Kosuke Beppu, Dr. Rui Pang, and Mr. Kazuki Tamai for their experimental advice, instructive suggestions, and discussions concerning this study, as well as for their continual encouragement throughout this work. The author is grateful to the staff of SPring-8 in Hyogo prefecture, particularly Mr. Kazuo Kato, for assistance with XAFS measurements.

The author feels a deep debt of gratitude to Mr. Yuto Nakatani for his help with the photoelectrochemical investigation of Yb-modified Ga_2O_3 photocatalysts (Chapter 6) and Mr. Kazutaka Hori and Mr. Masaatsu Ishida, who aided in the study of the electrocatalytic conversion of CO_2 using an Ag cathode (Chapter 7) for their collaboration, diligent work, and instructive discussion regarding these studies. The author also thanks his peers, Mr. Takuya Shibano, Mr. Yosuke Terao, Mr. Yudai Hasegawa, Mr. Hironobu Hayashi, Mr. Raizo Maeda, and Mr. Kazuya Matsuki, for their friendship and cheerful messages. Thanks are extended to Secretary Ms. Mami Nishio and Ms. Yuko Yoshitake for their kind assistance in official affairs. The author is also grateful to all the members of Professor Tsunehiro Tanaka's laboratory.

Last, but not least, the author sincerely thanks his family members for their understanding and encouragement. Special thanks are given to the friends who have supported a fruitful life in Kyoto.

Soichi Kikkawa

Kyoto

January 2020

CONTENTS

General Introduction

Catalytic Reduction of CO_2

Reducing the concentration of carbon dioxide (CO_2) in the atmosphere is essential for ensuring our continued existence.[1] This necessitates a concerted effort to both prevent further pollution and implement strategies for actively decreasing the levels already present. There are currently three routes for minimizing total CO_2 emission.[2-4] The first, and most direct, option involves decreasing CO_2 production through the use of alternative energy sources. For example, simply replacing carbon-rich energy carriers, such as coal, with less carbon-rich fossil fuels, such as oil or natural gas, would reduce CO_2 emissions. Alternatively, using non-fossil fuel energy sources, such as hydrogen or renewable energies like wind and solar power, would eliminate CO_2 emission; however, this would require major transformations to existing energy-supplying infrastructures. The second route involves the use of CO_2 as a feedstock for the production of chemicals and energy sources. The downstream use of CO_2-derived chemicals and energy would result in carbon neutrality, i.e. net zero CO_2 emission. The third possibility involves storing CO_2 in the natural environment. This is achieved either *via* natural sinking processes, such as forestation, or artificial sequestration through direct injection into geological formations and oceans. While this last option, carbon capture and storage (CCS), is relatively well established, the recycling of CO_2 as a feedstock, carbon capture and utilization (CCU), presents a more viable alternative. CCU provides an economic advantage over simply storing CO_2 and mitigates the risk of CO_2 leakage associated with CCS-based techniques.[2, 5]

To implement CCU strategies, a thorough understanding of CO_2 chemistry is essential. CO_2 is a linear, nonpolar molecule containing two polar, high energy (750 kJ mol^{-1}) C=O bonds.[6, 7] Chemical fixation of CO_2 therefore requires a high input of energy to overcome its activation barrier. In addition, CO_2 can be converted into a variety of compounds, making it is essential to control reaction selectivity to ensure the generation of the desired product. Therefore, developing catalysts for the selective and efficient conversion of CO_2 into chemical feedstocks requires the careful design of active sites that considers the mechanism of CO_2 transformation.

Catalytic Hydrogenation of CO_2: The catalytic hydrogenation of CO_2 affords various products, such as methane (CH_4), carbon monoxide (CO), formic acid (HCOOH), formaldehyde (HCHO), methanol (CH_3OH), dimethyl ether (CH_3OCH_3), and hydrocarbons. Due to recent advancements in the production of green hydrogen, the hydrogenation of CO_2 to produce chemical feedstocks has gained attention.[8, 9] H_2 was traditionally produced from fossil fuels by coal gasification and steam reforming of CH_4; in recent years, alternative processes for sustainable H_2 production have been developed using renewable energies, such as solar and wind.[8, 10-12] Although the costs of sustainable H_2 production *via* electrolysis and photovoltaic electrolysis remain higher than those using fossil fuels, catalytic and industrial developments are expected to lower the price of H_2 production.

In Europe, particularly in Germany, a "power-to-gas process" employs surplus electric power to hydrogenate CO_2 into CH_4, which is then injected into the existing gas distribution grid or gas storages.[13, 14] Unlike a traditional syngas-to-methanol process, the catalytic conversion of CO_2 into CH_3OH has also been investigated as a CO_2 recycling strategy and has been successfully demonstrated both in the laboratory and in pilot-scale plants.[8, 15-18] The demand for CH_3OH and other liquid fuels, such as HCOOH and CH_3OCH_3, as raw materials and for use in internal combustion engines is expected to increase in the future.[8, 19, 20] Combining CO production with the Fischer–Tropsch synthesis over a bifunctional catalyst surface has been used for the hydrogenation of CO_2 into C_{2+} hydrocarbons, although this system suffers from poor product selectivity.[21] Both homogeneous and heterogeneous catalysts have been applied to these CO_2 hydrogenation systems.[4] Although homogeneous catalysts display superior activity and selectivity, heterogeneous catalysts are preferable in terms of stability, separation, handling, and reuse. In addition, heterogeneous catalysts simplify reactor design, which results in decreased costs for industrial applications. Therefore, improving product selectivity and efficiency are important areas to address when developing heterogeneous catalysts for CO_2 hydrogenation.

Electrocatalytic and Photocatalytic Conversion of CO_2: A potential strategy for simultaneously suppressing global CO_2 emissions and storing renewable energies involves the electrochemical reduction of CO_2. This process has been investigated in both aqueous and organic

solvents, with the former being preferable in terms of environmental load. Unfortunately, the aqueous system suffers from competition for electron consumption between CO_2 reduction and H_2 production arising from hydronium ion (H_3O^+) reduction. Due to the high energy input required to activate the C=O bond of CO_2 molecules, the standard reduction potentials of CO_2 (eqs. 1–3, vs. normal hydrogen electrode (NHE) at pH = 7) are relatively high compared to that of the hydronium ion (eq. 4, vs. NHE at pH = 7): [22]

$$CO_2+2H^++2e^- \longrightarrow HCOOH \qquad E^{\circ\prime} = -0.61\ \text{V} \qquad (1)$$

$$CO_2+2H^++2e^- \longrightarrow CO+H_2O \qquad E^{\circ\prime} = -0.52\ \text{V} \qquad (2)$$

$$CO_2+8H^++8e^- \longrightarrow CH_4+2H_2O \qquad E^{\circ\prime} = -0.24\ \text{V} \qquad (3)$$

$$2H^++2e^- \longrightarrow H_2 \qquad E^{\circ\prime} = -0.41\ \text{V} \qquad (4)$$

To establish an efficient and economically favorable system for the electrochemical reduction of CO_2, it is essential to design the electrode surface for selective CO_2 reduction at a low energy input. In the late 1900s, Hori *et al*. investigated a range of metal cathodes for use in CO_2 reduction in aqueous solution and classified the metals into four groups based on the product: CO formation (Au, Ag, Zn, Pd, and Ga), $HCOO^-$ formation (Pb, Hg, In, Sn, Cd, and Tl), hydrocarbon formation (Cu), and H_2 formation (Ni, Fe, Pt, and Ti).[23, 24] The development of novel electrocatalysts, such as bimetal, metal oxide-derived, and carbon-based materials, decreased the required potential for CO_2 reduction and improved the selectivity toward the CO_2-derived products by suppressing competing H_2 production.[25, 26]

Since the discovery of photoelectrochemical water splitting using a TiO_2 photoanode equipped with Pt counter electrode by Honda and Fujishima, the photocatalytic reduction of CO_2 using homogeneous and heterogeneous photocatalysts has been widely investigated in parallel with water splitting.[27-33] The stability, reusability, and handling of heterogeneous metal oxide photocatalysts have been extensively evaluated, however, selectively remains a challenge in this system.[32, 33] Upon absorption of photons by the metal oxide photocatalyst, band-gap excitation generates photoexcited electron-hole pairs. To ensure that the electrons are primarily used for the reduction of CO_2, metal particles are typically loaded as electrochemical-reduction sites and/or the oxide surface is modified with CO_2-adsorbable materials. In contrast, homogeneous metal complex molecular catalysts can achieve high selectivity for the photocatalytic reduction of CO_2 because their

ligands can form intermediate species with CO_2; however, strong reducing reagents, such as triethanolamine, are essential for driving the reaction forward while preventing self-degradation of the molecular catalyst.[34]

Catalytic Hydrogenation of CO_2 to CH_4

"CO_2 methanation" or the "Sabatier process" is a classical reaction for the catalytic hydrogenation of CO_2 to CH_4. This system was primarily used for the generation of substitute natural gas and hydrogen purification through the removal of CO_2 impurities prior to the synthesis of ammonia.[35, 36] CO_2 methanation can also be used to provide drinking water and fuels for the International Space Station and could be used to recycle CO_2 from expired breath and H_2 from water electrolysis to aid in the colonization of Mars.[37, 38] At ambient pressure, exothermic CO_2 methanation ($CO_2 + 4H_2 \rightarrow CH_4 + 2H_2O$, $\Delta_r H°_{298\,K} = -164.7$ kJ mol^{-1}) and endothermic reverse water gas shift reactions (RWGS) ($CO_2 + H_2 \rightarrow CO + H_2O$, $\Delta_r H°_{298\,K} = 41.1$ kJ mol^{-1}) compete with each other. While Fischer–Tropsch synthesis predominantly yields the desired long-chain hydrocarbons from syngas, the unfavorable formation of considerable amounts of CH_4 through CO_2 methanation is problematic.[39] A greater fundamental understanding of the mechanism of CO_2 methanation is therefore needed to control the selectivity of these processes.

Supported Metal Catalysts for Methanation of CO_2: Numerous studies on the hydrogenation of CO_2 over single-crystalline metal surfaces or simple supported metal catalysts have documented the selectivity of CO_2 methanation or RWGS reactions based on the active metal species.[40-47] Ni catalysts have been the most widely investigated for industrial use owing to their low cost and availability. The support materials play a significant role in particle dispersion, active phase morphology, and adsorption and catalytic properties. Early studies used metal oxide support materials with large surface areas, such as silica (SiO_2) and alumina (Al_2O_3).[41-43, 45, 46] To improve the activity of Ni-based catalysts for CO_2 methanation, the metal supports were modified with either oxygen defect sites through the use of ceria (CeO_2) and zirconia (ZrO_2) supports or basic sites through modification with alkaline earth elements.[48-51] Unfortunately, Ni catalysts require high reaction temperatures (573–773 K) owing to a low H_2 dissociation activity. In this regard, Ru

catalysts are superior, but their high cost limits their use. To minimize the quantity of supported Ru catalysts used, extensive optimization of particle size, support materials, and reaction mechanisms have been performed.[52-55] To reduce the formation of undesired CH_4 during the Fischer–Tropsch synthesis of long-chain hydrocarbons, the effects of feed-gas composition and pressure over Co- and Fe-based catalysts have been investigated.[56-58] Recent studies using supported Rh and Pd catalysts, which favor CH_4 formation, described the effect of particle size on the reaction and proposed potential mechanisms.[59-64] The choice of support materials has been reported to alter product selectivity, even with the same active metal species. For example, the supported Pt catalyst, which tends to favor CO production, was found to produce CH_4 when CeO_2 was used as the metal support.[65] Additionally, some support materials have been shown to produce atomically dispersed metal species, referred to as single-site catalysts, which allowed for the generation of CO over Ir-, Rh-, Ni-, and Ru-based catalysts, despite typically favoring CH_4 formation.[66-70] To control the electronic and geometric states of active metal species, the introduction of the second metal species (alloy catalysts) has been investigated.

***Mechanism of CH_4 Formation over Supported Metal Catalysts*:** The mechanism of the classical catalytic methanation of CO_2 has been reinterpreted as analytical techniques have progressed. Early mechanisms were primarily based on kinetic analyses.[71] Spectroscopy has shed more light on the reaction mechanism.[72, 73] Various surface analysis techniques, such as infrared spectroscopy, have been used to investigate surface adsorbed species on single-crystal substrates or supported metal catalysts and have provided clues to unveil the ambiguous reaction mechanism.[43, 44, 47, 74] Recent developments in *in situ* observation techniques, including X-ray and infrared spectroscopy, and their combination in *operando* studies[75] provide a greater understanding of the behavior of intermediate species on active metal sites.[36, 50-52, 59, 60, 64, 76-79] Investigations on the effect of metal particle size and support materials on the reaction path have deepened the understanding of the methanation mechanism over supported Ni catalysts.[36, 43, 44, 50, 51, 74, 78-87] The proposed mechanisms of methanation over Ni catalysts are classified into three main groups:[36, 51] (i) CO_2 is dissociated into CO and O species over the Ni surface, leading to hydrogenation to CH_4,[43, 44, 80] (ii) formate species are directly hydrogenated to CH_4,[50, 86] and (iii) formate species are hydrogenated to

CH_4 *via* CO intermediates.[74, 81-85, 87] Pan *et al.* reported that the formation of CH_4 proceeds *via* bidentate formate species on a γ-Al_2O_3 support.[78] Fujita *et al.* found that CH_4 was produced from adsorbed carbon species on a Ni surface *via* bridged CO species. Kai *et al.* proposed that the hydrogenation of surface carbon species determines the overall rate of formation of CH_4.[82] Thus, the effective hydrogenation of the intermediate species by dissociated H species is key to improving CH_4 formation over Ni-based catalysts. In contrast, noble metal catalysts, such as Ru and Rh, have been proposed to act via the co-adsorption of CO and H species onto the metal active sites.[52, 59] It is assumed that the dissociated H species aid in the dissociation of the C–O bond by donating electron density into the metal surface which in turn back donates electron density to the C–O bond, thereby weakening the C–O bond energy.[52, 88]

Strategy to Design Active Sites for the Selective Hydrogenation of CO_2

Single-Atom Alloy Catalysts for Selective Methanation of CO_2: As mentioned above, the key to improving CH_4 formation on Ni catalysts at low temperatures is by promoting hydrogenation of the intermediate species by the dissociated H species over the metal sites. However, high reaction temperatures are generally required owing to the low H_2 dissociation activities of the Ni catalyst. Thus, the addition of noble metal species, such as Rh, Pd, and Pt, into the Ni catalyst is expected to promote hydrogenation by increasing the dissociation of H_2; however, this has the potential to lead to unfavorable reactions, such as CO formation.[79, 89, 90] For example, Pt catalysts, which allow for the dissociation of H_2 at low temperatures, are primarily effective for RWGS reactions.[4] The successive hydrogenation of CO is therefore a more useful strategy for highly selective methanation at low temperatures.

Recently, Sykes and Flytzani-Stephanopoulos reported the development of single-atom alloy catalysts (SAACs). SAACs are generally prepared by doping a relatively inert metal matrix with a limited amount of a more catalytically active atom; e.g., Pt atoms on a Cu matrix.[91-93] The atomically dispersed atoms on the surface of the metal matrix are expected to display distinct geometric and electronic properties due to alloying effects. A prime example of this system involves Pt and Ni, with the electron density of dispersed Pt atoms tuned by electron donation from the atoms of a Ni matrix.[92, 94] The CO methanation activity of this system can be understood through the electronic

interactions occurring between the support and the active metal species.[95, 96] Electron donation from the metal to the 2π anti-bonding orbital of the adsorbed CO species weakens the C−O bond and promotes the hydrogenation of CO to CH_4. Therefore, CO that is strongly adsorbed onto an electron-rich Pt species through overlap of the 2π orbital of the CO and the *d* orbital of the metal is expected to exhibit high desorption durability and a low activation barrier for C−O bond dissociation.[88, 97] In addition, the geometric character of the isolated Pt atoms surrounded by Ni atoms is expected to promote hydrogenation of the adsorbed CO species on Pt atoms by H species attached to the surrounding Ni atoms.

Tuning Selectivity by Metal-Supported Interaction (MSI) During Hydrogenation of CO_2: In many catalytic systems, the interaction between the metal particles and the support surface (metal-support interaction (MSI)) imparts the metal species with unique electronic and geometric characteristics as well as enhanced activities.[98-102] The MSI effect must therefore be taken into account when designing catalysts for the hydrogenation of CO_2, as the type of support material highly influences catalytic activity and reaction selectivity.[65-70, 103-106] For example, Rh catalysts have been successfully applied to the hydrogenation of CO_2 to CH_4. However, Matsubu *et al.* showed that a catalyst composed of atomically dispersed Rh species supported on TiO_2 inhibited the formation of CH_4.[66] Furthermore, Ma *et al.* reported that dispersed Ir species supported on CeO_2 resulted in the selective formation of CO.[68] This contrasts with the high selectivity towards CH_4 formation when the catalyst was prepared with high Ir loading. This finding suggested that the electronic states of the Ir species were influenced by coordination to the surface oxygen atoms of the CeO_2 support, which resulted in low adsorption of CO for use in hydrogenation.

Pt catalysts are known to be effective for RWGS reactions, where a high selectivity for CO production is essential.[76, 77, 104] The MSI between Pt and Al_2O_3 has been investigated and generally results in high dispersion and unique morphology of the Pt particles compared to catalysts prepared using non-MSI materials, such as SiO_2.[98-101, 107-112] Koningsberger *et al.* investigated morphology changes of Pt/γ-Al_2O_3 catalysts during high temperature reduction with H_2.[107] The metal-support interface, consisting of interactions between Pt and tetra- and octa-coordinated Al^{3+} sites, was found to undergo drastic changes at high temperatures, with the Pt particle rearranging from a

three-dimensional structure composed of 11 Pt atoms to a raft-like structure resembling Pt(100). Kwak *et al*. have suggested that the penta-coordinated Al^{3+} sites on the (100) facets of the γ-Al_2O_3 surface anchored atomically dispersed Pt species at low Pt loading, whereas two-dimensional Pt rafts formed at high loading.[99, 109] Thus, understanding the effect of MSI between Pt particles and the γ-Al_2O_3 surface can guide the development of catalytically active sites in supported Pt catalysts to ensure the effective and selective formation of CO *via* RWGS reactions.

Strategy for the Development of Efficient Photocatalytic CO_2 Conversion

While heterogeneous metal oxide photocatalysts are relatively easy to use, it is difficult to tune their selectivity for distinct CO_2-derived products as compared to homogeneous metal complex molecular catalysts. In addition, the photoexcitation of electrons in the valence band of metal oxides, generally from an O 2*p* orbital to the orbitals constituting the conduction band, requires a greater energy input than needed to cross the band gap of typical *n*-type semiconductor photocatalysts (**Figure 1**).[30]

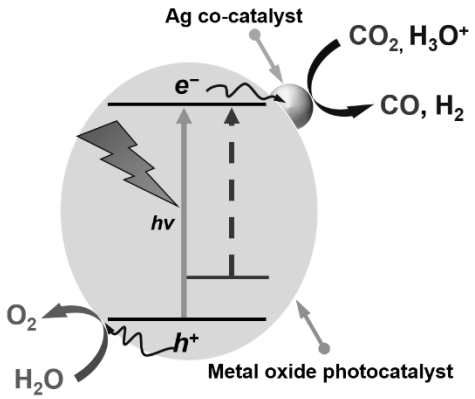

Figure 1 Photocatalytic conversion of CO_2 using H_2O as an electron donor over an oxide photocatalyst and Ag co-catalyst. The $\boldsymbol{e}^-$ and $\boldsymbol{h}^+$ represent the photoexcited electrons and holes, respectively.

It is necessary to have a fundamental understanding of how different wavelengths affect the activity of photocatalysts to ensure that they can effectively reduce CO_2. Unfortunately, this can be complicated as the system is controlled by three interconnected steps: photoabsorption, oxidation of the electron donor by holes, and reduction of CO_2 by photoexcited electrons. Upon photoabsorption,

photoexcited electrons and holes are generated in the catalyst and transfer to the photocatalyst surface to induce reduction and oxidation, respectively. To design photocatalysts for the reduction of CO_2 in an aqueous solution, the potential energy of the photoexcited electrons needs to exceed the potential energy for the two-electron reduction of CO_2 (i.e., $E^{\circ}(CO_2/CO) = -0.61$ V vs. NHE at pH = 7).[22] The reduction of CO_2 to CO is further complicated by competition with the lower reduction potential of H_3O^+ (i.e., $E^{\circ}(H^+/H_2) = -0.41$ V vs. NHE at pH = 7).[113] To utilize H_2O as an electron donor, photogenerated holes must induce the oxidation of H_2O (i.e., $E^{\circ}(O_2/H_2O) = 0.82$ V vs. NHE at pH = 7), which necessitates that the positive holes have higher electropositive potential than the redox couple. By focusing on each element of the reaction, it is possible to understand how the individual steps influence the entire process, which can provide insights for developing efficient photocatalysts for selective CO_2 reduction.

Tuning photoabsorption via band engineering: The photoabsorption capacity of photocatalysts can be manipulated by tuning the band structure. Wide bandgap metal oxide photocatalysts, such as Ga_2O_3 and Ta_2O_5, which produce photogenerated electrons with high potential energy, can induce both the two-electron reduction of CO_2 and the oxidation of H_2O.[114, 115] However, UV light irradiation (λ <300 nm) is required for the photoexcitation of these photocatalysts. To utilize the light across a wide range of wavelengths, the band energy must be tuned through the introduction of midgap states, which can be achieved by doping the catalyst with other elements.

Photoelectrochemical evaluation of oxidation activity over the photocatalyst surface: The oxidation activity at the surface of the photocatalyst can be estimated by evaluating the anodic response following light irradiation when the reduction occurs sufficiently fast. In metal oxide photocatalyst systems, the effect of surface properties on the oxidation activity by positive holes during photocatalysis cannot be investigated apart from the reduction by electrons. Photoelectrochemical investigations enable the evaluation of the net oxidative ability of the positive holes over *n*-type semiconductor photocatalysts owing to the rapid consumption of electrons at a Pt counter electrode. These studies can provide insights into the importance of oxidation during the photocatalytic conversion of CO_2.

Electrochemical evaluation of the CO_2 reduction activity over Ag species: Effective CO_2 reduction sites in a catalyst can be investigated using electrochemical systems with Ag-based cathodes. The external applied potential to the Ag cathodes corresponds to the potential energy of photogenerated electrons occupying the conduction band near the surface of a metal oxide photocatalyst. It is widely accepted that Ag species are active sites for the reduction of CO_2 to CO during the photocatalytic conversion of CO_2 over metal oxide photocatalysts with an Ag co-catalyst.[113, 116-118] However, during the photocatalytic reaction, the elution of the Ag species is considered to occur upon oxidation of Ag metal by positives holes, making it unclear which Ag species is active during the reaction. This complicates photocatalytic design since the size, morphology, valence, and surface configuration of the Ag particles are expected to affect selectivity during CO_2 reduction. The electrochemical reduction of CO_2 using Ag cathodes is expected to reveal these features, which could aid in the design of photocatalysts using Ag particles as co-catalysts for the conversion of CO_2.

Thesis Outline

This thesis focuses on the design of active sites for the selective reduction of CO_2 and consists of three parts divided into seven chapters.

Part I describes the preparation of a Ni-based single-Pt atom alloy catalyst for the efficient and selective methanation of CO_2. The addition of minute quantities of Pt into a γ-Al_2O_3-supported Ni catalyst afforded a relatively high rate of CH_4 formation while maintaining excellent selectivity for CH_4 evolution, despite the bias of the Pt catalyst for the formation of CO. The isolated Pt atoms exhibited a unique *d*-electronic state upon alloying with the Ni atoms at the surface of the Ni matrix. Kinetic studies revealed that the high H_2 dissociation ability of the Pt species improved the hydrogenation of carbon intermediates on the metal surface. *In-situ* and transient infrared studies suggested that the unique geometrical configuration, rather than electronic states, of the isolated Pt atoms, induced CH_4 formation by bridging CO species between the isolated Pt and neighboring Ni atoms.

Part II presents a mechanism for the reductive formation of Pt particles on a γ-Al_2O_3 support and investigates how the active sites form otherwise disfavored CH_4 during CO_2 hydrogenation.

In-situ time-resolved X-ray absorption spectroscopy revealed that the reduction of γ-Al_2O_3-supported PtO_x particles by H_2 resulted in two-dimensional Pt particles with a low coordination number. Combining X-ray absorption spectroscopy with infrared spectroscopy revealed that Pt atoms at the interface between Pt particles and the γ-Al_2O_3 surface were capable of co-adsorbing H and CO species, leading to the methanation of the adsorbed CO species.

Part III illustrates three routes for improving the photocatalytic activity and modulating the selectivity of Ga_2O_3 photocatalysts loaded with Ag co-catalyst for the conversion of CO_2. First, the doping of Rh species into Ga_2O_3 induced midgap states and improved the CO formation under photoirradiation using light with wavelengths >300 nm. Second, photoelectrochemical measurements revealed that the surface modification of Ga_2O_3 with Yb species improved oxidation activity. Finally, pretreating the Ag cathode with O_3 resulted in active Ag particles for the selective electrochemical reduction of CO_2 to CO while suppressing the competitive formation of H_2.

References

1 R. K. Pachauri, M. R. Allen, V. R. Barros, J. Broome, W. Cramer, R. Christ, J. A. Church, L. Clarke, Q. Dahe and P. Dasgupta, *Climate Change 2014: Synthesis Report. Contribution of Working Groups I, II and III to the Fifth Assessment Report of the Intergovernmental Panel on Climate Change*, IPCC, 2014.

2 H. Yang, Z. Xu, M. Fan, R. Gupta, R. B. Slimane, A. E. Bland and I. Wright, *J. Environ. Sci.*, 2008, **20**, 14-27.

3 M. Mikkelsen, M. Jørgensen and F. C. Krebs, *Energy Environ. Sci.*, 2010, **3**, 43–81.

4 W. Wang, S. Wang, X. Ma and J. Gong, *Chem. Soc. Rev.*, 2011, **40**, 3703–3727.

5 R. M. Cuéllar-Franca and A. Azapagic, *J. CO2 Util.*, 2015, **9**, 82–102.

6 S. N. Habisreutinger, L. Schmidt-Mende and J. K. Stolarczyk, *Angew. Chem. Int. Ed. Engl.*, 2013, **52**, 7372–7408.

7 J. Mao, K. Li and T. Peng, *Catal. Sci. Technol.*, 2013, **3**, 2481–2498.

8 A. Alvarez, A. Bansode, A. Urakawa, A. V. Bavykina, T. A. Wezendonk, M. Makkee, J. Gascon and F. Kapteijn, *Chem. Rev.*, 2017, **117**, 9804–9838.

9 G. Centi, E. A. Quadrelli and S. Perathoner, *Energy Environ. Sci.*, 2013, **6**, 1711–1731.

10 J. D. Holladay, J. Hu, D. L. King and Y. Wang, *Catal. Today*, 2009, **139**, 244–260.

11 C. Acar and I. Dincer, *Int. J. Hydrogen Energy*, 2014, **39**, 1–12.

12 M. Wang, Z. Wang, X. Gong and Z. Guo, *Renew. Sust. Energ. Rev.*, 2014, **29**, 573–588.

13 M. Götz, J. Lefebvre, F. Mörs, A. McDaniel Koch, F. Graf, S. Bajohr, R. Reimert and T. Kolb, *Renew. Energy*, 2016, **85**, 1371–1390.

14 A. Varone and M. Ferrari, *Renew. Sust. Energ. Rev.*, 2015, **45**, 207–218.

15 H. Arakawa, M. Aresta, J. N. Armor, M. A. Barteau, E. J. Beckman, A. T. Bell, J. E. Bercaw, C. Creutz, E. Dinjus and D. A. Dixon, *Chem. Rev.*, 2001, **101**, 953–996.

16 I. Ganesh, *Renew. Sust. Energ. Rev.*, 2014, **31**, 221–257.

17 V. P. Haribal, X. Wang, R. Dudek, C. Paulus, B. Turk, R. Gupta and F. Li, *Adv. Energy Mater.*, 2019, **9**, 1901963–1901972.

18 S. Kar, A. Goeppert and G. K. S. Prakash, *Acc. Chem. Res.*, 2019, **52**, 2892–2903.

19 G. A. Olah, *Angew. Chem. Int. Ed. Engl.*, 2005, **44**, 2636–2639.

20 G. A. Olah, A. Goeppert and G. S. Prakash, *J. Org. Chem.*, 2008, **74**, 487–498.

21 W. Zhou, K. Cheng, J. Kang, C. Zhou, V. Subramanian, Q. Zhang and Y. Wang, *Chem. Soc. Rev.*, 2019, **48**, 3193–3228.

22 A. J. Bard, R. Parsons and J. Jordan, *Standard Potentials in Aqueous Solution*, Marcel Dekker, New York and Basel, 1985.

23 Y. Hori, K. Kikuchi and S. Suzuki, *Chem. Lett.*, 1985, **14**, 1695–1698.

24 Y. Hori, H. Wakebe, T. Tsukamoto and O. Koga, *Electrochim. Acta*, 1994, **39**, 1833–1839.

25 B. Kumar, J. P. Brian, V. Atla, S. Kumari, K. A. Bertram, R. T. White and J. M. Spurgeon, *Catal. Today*, 2016, **270**, 19–30.

26 L. Rößner and M. Armbrüster, *ACS Catal.*, 2019, **9**, 2018–2062.

27 A. Fujishima and K. Honda, *Nature*, 1972, **238**, 37–38.

28 M. Halmann, *Nature*, 1978, **275**, 115–116.

29 T. Inoue, A. Fujishima, S. Konishi and K. Honda, *Nature*, 1979, **277**, 637–638.

30 A. Kudo and Y. Miseki, *Chem. Soc. Rev.*, 2009, **38**, 253–278.

31 E. V. Kondratenko, G. Mul, J. Baltrusaitis, G. O. Larrazábal and J. Pérez-Ramírez, *Energy Environ. Sci.*, 2013, **6**, 3112–3135.

32 S. Navalon, A. Dhakshinamoorthy, M. Alvaro and H. Garcia, *ChemSusChem*, 2013, **6**, 562–577.

33 J. L. White, M. F. Baruch, J. E. Pander Iii, Y. Hu, I. C. Fortmeyer, J. E. Park, T. Zhang, K. Liao, J. Gu, Y. Yan, *et al.*, *Chem. Rev.*, 2015, **115**, 12888–12935.

34 H. Takeda and O. Ishitani, *Coord. Chem. Rev.*, 2010, **254**, 346–354.

35 G. Garbarino, P. Riani, L. Magistri and G. Busca, *Int. J. Hydrogen Energy*, 2014, **39**, 11557–11565.

36 K. Jalama, *Catal. Rev.*, 2017, **59**, 95–164.

37 K. P. Brooks, J. Hu, H. Zhu and R. J. Kee, *Chem. Eng. Soc.*, 2007, **62**, 1161–1170.

38 W. Wei and G. Jinlong, *Front. Chem. Sci. Eng.*, 2010, **5**, 2–10.

39 C. G. Okoye-Chine, M. Moyo, X. Liu and D. Hildebrandt, *Fuel Process. Technol.*, 2019, **192**, 105–129.

40 B. Sexton and G. Somorjai, *J. Catal.*, 1977, **46**, 167–189.

41 F. Solymosi and A. Erdőhelyi, *J. Mol. Catal.*, 1980, **8**, 471–474.

42 G. D. Weatherbee and C. H. Bartholomew, *J. Catal.*, 1981, **68**, 67–76.

43 G. D. Weatherbee and C. H. Bartholomew, *J. Catal.*, 1982, **77**, 460–472.

44 D. Peebles, D. Goodman and J. White, *J. Phys. Chem.*, 1983, **87**, 4378–4387.

45 C. K. Vance and C. H. Bartholomew, *Appl. Catal.*, 1983, **7**, 169–177.

46 G. D. Weatherbee and C. H. Bartholomew, *J. Catal.*, 1984, **87**, 352–362.

47 F. Solymosi, *J. Mol. Catal.*, 1991, **65**, 337–358.

48 R. Razzaq, H. Zhu, L. Jiang, U. Muhammad, C. Li and S. Zhang, *Ind. Eng. Chem. Res.*, 2013, **52**, 2247–2256.

49 M. Aziz, A. Jalil, S. Triwahyono, R. Mukti, Y. Taufiq-Yap and M. Sazegar, *Appl. Catal. B: Environ.*, 2014, **147**, 359–368.

50 M. A. A. Aziz, A. A. Jalil, S. Triwahyono and S. M. Sidik, *Appl. Catal. A*, 2014, **486**, 115–122.

51 M. A. A. Aziz, A. A. Jalil, S. Triwahyono and A. Ahmad, *Green Chem.*, 2015, **17**, 2647–2663.

52 S. Eckle, H. G. Anfang and R. J. Behm, *J. Phys. Chem. C*, 2011, **115**, 1361–1367.

53 S. Sharma, Z. Hu, P. Zhang, E. W. McFarland and H. Metiu, *J. Catal.*, 2011, **278**, 297–309.

54 S. Tada, R. Kikuchi, K. Urasaki and S. Satokawa, *Appl. Catal. A*, 2011, **404**, 149–154.

55 J. H. Kwak, L. Kovarik and J. Szanyi, *ACS Catal.*, 2013, **3**, 2449–2455.

56 T. Riedel, M. Claeys, H. Schulz, G. Schaub, S.-S. Nam, K.-W. Jun, M.-J. Choi, G. Kishan and K.-W. Lee, *Appl. Catal. A*, 1999, **186**, 201–213.

57 Y. Zhang, G. Jacobs, D. E. Sparks, M. E. Dry and B. H. Davis, *Catal. Today*, 2002, **71**, 411–418.

58 R. W. Dorner, D. R. Hardy, F. W. Williams, B. H. Davis and H. D. Willauer, *Energy Fuels*, 2009, **23**, 4190–4195.

59 A. Karelovic and P. Ruiz, *Appl. Catal. B: Environ.*, 2012, **113-114**, 237–249.

60 A. Karelovic and P. Ruiz, *ACS Catal.*, 2013, **3**, 2799–2812.

61 J. H. Kwak, L. Kovarik and J. Szanyi, *ACS Catal.*, 2013, **3**, 2094–2100.

62 J. Szanyi and J. H. Kwak, *Phys. Chem. Chem. Phys.*, 2014, **16**, 15117–15125.

63 J. Szanyi and J. H. Kwak, *Phys. Chem. Chem. Phys.*, 2014, **16**, 15126–15138.

64 X. Wang, H. Shi, J. H. Kwak and J. Szanyi, *ACS Catal.*, 2015, **5**, 6337–6349.

65 Y. Wang, H. Arandiyan, J. Scott, K.-F. Aguey-Zinsou and R. Amal, *ACS Appl. Energy Mater.*, 2018, **1**, 6781–6789.

66 J. C. Matsubu, V. N. Yang and P. Christopher, *J. Am. Chem. Soc.*, 2015, **137**, 3076–3084.

67 F. Wang, S. He, H. Chen, B. Wang, L. Zheng, M. Wei, D. G. Evans and X. Duan, *J. Am. Chem. Soc.*, 2016, **138**, 6298–6305.

68 S. Li, Y. Xu, Y. Chen, W. Li, L. Lin, M. Li, Y. Deng, X. Wang, B. Ge, C. Yang, *et al.*, *Angew. Chem. Int. Ed. Engl.*, 2017, **56**, 10761–10765.

69 Y. Guo, S. Mei, K. Yuan, D.-J. Wang, H.-C. Liu, C.-H. Yan and Y.-W. Zhang, *ACS Catal.*, 2018, **8**, 6203–6215.

70 M. M. Millet, G. Algara-Siller, S. Wrabetz, A. Mazheika, F. Girgsdies, D. Teschner, F. Seitz, A. Tarasov, S. V. Levchenko, R. Schlogl, *et al.*, *J. Am. Chem. Soc.*, 2019, **141**, 2451–2461.

71 V. M. Vlasenko and G. Yuzefovich, *Russ. Chem. Rev.*, 1969, **38**, 728.

72 G. Ertl, *Catal. Rev. Sci. Eng.*, 1980, **21**, 201–223.

73 G. Ertl, *Angew. Chem. Int. Ed. Engl.*, 2008, **47**, 3524–3535.

74 S. Fujita, M. Nakamura, T. Doi and N. Takezawa, *Appl. Catal. A*, 1993, **104**, 87–100.

75 A. Urakawa, *Curr. Opin. Chem. Eng.*, 2016, **12**, 31–36.

76 D. Ferri, T. Bürgi and A. Baiker, *Phys. Chem. Chem. Phys.*, 2002, **4**, 2667–2672.

77 A. Goguet, F. C. Meunier, D. Tibiletti, J. P. Breen and R. Burch, *J. Phys. Chem. B*, 2004, **108**, 20240–20246.

78 Q. Pan, J. Peng, T. Sun, S. Wang and S. Wang, *Catal. Commun.*, 2014, **45**, 74–78.

79 I. Sreedhar, Y. Varun, S. A. Singh, A. Venugopal and B. M. Reddy, *Catal. Sci. Technol.*, 2019, **9**, 4478–4504.

80 J. L. Falconer and A. E. Zağli, *J. Catal.*, 1980, **62**, 280–285.

81 S. Fujita, H. Terunuma, H. Kobayashi and N. Takezawa, *React. Kinet. Catal. Lett.*, 1987, **33**, 179–184.

82 T. Kai, T. Takahashi and S. Furusaki, *CJChE*, 1988, **66**, 343–347.

83 S. Fujita, H. Terunuma, M. Nakamura and N. Takezawa, *Ind. Eng. Chem. Res.*, 1991, **30**,

1146–1151.

84 A. Lapidus, N. Gaidai, N. Nekrasov, L. Tishkova, Y. A. Agafonov and T. Myshenkova, *Pet. Chem.*, 2007, **47**, 75–82.

85 E. Vesselli, M. Rizzi, L. De Rogatis, X. Ding, A. Baraldi, G. Comelli, L. Savio, L. Vattuone, M. Rocca and P. Fornasiero, *J. Phys. Chem. Lett.*, 2009, **1**, 402–406.

86 P. A. U. Aldana, F. Ocampo, K. Kobl, B. Louis, F. Thibault-Starzyk, M. Daturi, P. Bazin, S. Thomas and A. C. Roger, *Catal. Today*, 2013, **215**, 201–207.

87 A. Westermann, B. Azambre, M. C. Bacariza, I. Graça, M. F. Ribeiro, J. M. Lopes and C. Henriques, *Appl. Catal. B: Environ.*, 2015, **174-175**, 120–125.

88 G. Blyholder, *J. Phys. Chem.*, 1964, **68**, 2772–2777.

89 D. Liu, Y. Li, M. Kottwitz, B. Yan, S. Yao, A. Gamalski, D. Grolimund, O. V. Safonova, M. Nachtegaal, J. G. Chen, *et al.*, *ACS Catal.*, 2018, **8**, 4120–4131.

90 M. Mihet and M. D. Lazar, *Catal. Today*, 2018, **306**, 294–299.

91 F. R. Lucci, T. J. Lawton, A. Pronschinske and E. C. H. Sykes, *J. Phys. Chem. C*, 2014, **118**, 3015–3022.

92 F. R. Lucci, J. Liu, M. D. Marcinkowski, M. Yang, L. F. Allard, M. Flytzani-Stephanopoulos and E. C. Sykes, *Nat. Commun.*, 2015, **6**, 8550–8557.

93 G. Giannakakis, M. Flytzani-Stephanopoulos and E. C. H. Sykes, *Acc. Chem. Res.*, 2018, **52**, 237–247.

94 J. R. Kitchin, J. K. Norskov, M. A. Barteau and J. G. Chen, *J. Chem. Phys.*, 2004, **120**, 10240–10246.

95 F. Solymosi, I. Tombacz and M. Kocsis, *J. Catal.*, 1982, **75**, 78–93.

96 S. Takenaka, T. Shimizu and K. Otsuka, *Int. J. Hydrogen Energy*, 2004, **29**, 1065–1073.

97 J. A. Rodriguez and D. W. Goodman, *J. Phys. Chem.*, 1991, **95**, 4196–4206.

98 D. Kubička, N. Kumar, T. Venäläinen, H. Karhu, I. Kubičková, H. Österholm and D. Y. Murzin, *J. Phys. Chem. B*, 2006, **110**, 4937–4946.

99 J. H. Kwak, J. Hu, D. Mei, C.-W. Yi, D. H. Kim, C. H. Peden, L. F. Allard and J. Szanyi, *Science*, 2009, **325**, 1670–1673.

100 Y. Zhai, D. Pierre, R. Si, W. Deng, P. Ferrin, A. U. Nilekar, G. Peng, J. A. Herron, D. C. Bell

and H. Saltsburg, *Science*, 2010, **329**, 1633–1636.

101 M. Ahmadi, H. Mistry and B. Roldan Cuenya, *J. Phys. Chem. Lett.*, 2016, **7**, 3519–3533.

102 K. Murata, Y. Mahara, J. Ohyama, Y. Yamamoto, S. Arai and A. Satsuma, *Angew. Chem. Int. Ed. Engl.*, 2017, **56**, 15993–15997.

103 M. D. Porosoff and J. G. Chen, *J. Catal.*, 2013, **301**, 30–37.

104 S. Kattel, B. Yan, J. G. Chen and P. Liu, *J. Catal.*, 2016, **343**, 115–126.

105 S. Kattel, B. Yan, Y. Yang, J. G. Chen and P. Liu, *J. Am. Chem. Soc.*, 2016, **138**, 12440–12450.

106 S. Kattel, P. Liu and J. G. Chen, *J. Am. Chem. Soc.*, 2017, **139**, 9739–9754.

107 M. Vaarkamp, J. T. Miller, F. S. Modica and D. C. Koningsberger, *J. Catal.*, 1996, **163**, 294–305.

108 A. Borgna, T. Garetto, C. Apesteguıa, F. Le Normand and B. Moraweck, *J. Catal.*, 1999, **186**, 433–441.

109 D. Mei, J. H. Kwak, J. Hu, S. J. Cho, J. Szanyi, L. F. Allard and C. H. Peden, *J. Phys. Chem. Lett.*, 2010, **1**, 2688–2691.

110 J. Matos, L. K. Ono, F. Behafarid, J. R. Croy, S. Mostafa, A. T. DeLaRiva, A. K. Datye, A. I. Frenkel and B. Roldan Cuenya, *Phys. Chem. Chem. Phys.*, 2012, **14**, 11457–11467.

111 C. Dessal, T. Len, F. Morfin, J.-L. Rousset, M. Aouine, P. Afanasiev and L. Piccolo, *ACS Catal.*, 2019, **9**, 5752–5759.

112 C. Dessal, A. Sangnier, C. Chizallet, C. Dujardin, F. Morfin, J.-L. Rousset, M. Aouine, M. Bugnet, P. Afanasiev and L. Piccolo, *Nanoscale*, 2019, **11**, 6897–6904.

113 K. Teramura and T. Tanaka, *Phys. Chem. Chem. Phys.*, 2018, **20**, 8423–8431.

114 S. Iguchi, Y. Hasegawa, K. Teramura, S. Kidera, S. Kikkawa, S. Hosokawa, H. Asakura and T. Tanaka, *Sustain. Energ. Fuels*, 2017, **1**, 1740–1747.

115 S. Iguchi, S. Kikkawa, K. Teramura, S. Hosokawa and T. Tanaka, *Phys. Chem. Chem. Phys.*, 2016, **18**, 13811–13819.

116 Z. Wang, K. Teramura, Z. Huang, S. Hosokawa, Y. Sakata and T. Tanaka, *Catal. Sci. Technol.*, 2016, **6**, 1025–1032.

117 H. Nakanishi, K. Iizuka, T. Takayama, A. Iwase and A. Kudo, *ChemSusChem*, 2017, **10**,

112–118.

118 Z. Huang, K. Teramura, H. Asakura, S. Hosokawa and T. Tanaka, *Curr. Opin. Chem. Eng.*, 2018, **20**, 114–121.

Part I

Selective Hydrogenation of CO_2 Toward CH_4 over Isolated Pt Atoms in Ni–Pt Alloy

Chapter 1

Isolated Platinum Atoms in Ni/γ-Al_2O_3 for Selective Hydrogenation of CO_2 Toward CH_4

Abstract

We introduce a catalyst composed of isolated Pt atoms surrounded by Ni atoms in a Ni−Pt alloy (*iso*-Pt), which was prepared on aluminum oxide (Al_2O_3) obtained by a simple impregnation method with typical hydrogen-reduction pretreatment. This catalyst exhibited a relatively high CH_4-formation rate while maintaining excellent selectivity for CH_4 evolution, when compared to bulk Ni atoms (*bulk*-Ni), although bulk Pt atoms (*bulk*-Pt) produced CO rather than CH_4. Kinetics studies revealed that one of the two roles of the *iso*-Pt species in the Ni−Pt alloy is to provide H_2-dissociation sites at low temperature, resulting in high CO_2-methanation activity. FT-IR spectroscopy clarified the second role of the *iso*-Pt species; tuning of the *d*-electronic state by alloying to surrounding Ni atoms leads to CO molecules that are strongly anchored to the *iso*-Pt atoms, which weakens the C−O bond of the CO species attached to the Pt atoms and improves the abilities of the surrounding Ni atoms to promote further methanation with hydrogen.

Introduction

Alloy catalysts are well known to exhibit unique catalytic behavior that is different from that of their monometallic counterparts, as a result of the "ligand effect" and the "ensemble effect"; however the reaction mechanisms of alloy catalysts have not been fully elucidated yet.[1-3] In particular, isolated atoms surrounded by atoms of another element in the alloy, which are referred to as "single atom alloys (SAAs)", have received significant attention.[4-6] Although incipient reports of single crystal SAA substrates have appeared in the surface science field,[7-10] more practical nanoparticle catalysts have been reported in recent years.[11-16] The electronic interactions and geometric-positional relationships between single element "guest" atoms and the surrounding atoms of the "host" element are expected to induce unique catalytic behavior for the following four reasons. i) Isolated atoms are active sites. Shishido *et al*. reported highly-selective hydrosilylations of *α*,*β*-unsaturated ketones and highly-efficient cycloadditions of alkynes using a Pd−Au alloy catalyst, which was due to the geometric character of the active Pd atoms surrounded by Au atoms.[17, 18] ii) The electronic states of active isolated atoms induce high activity. Sykes *et al.* reported that the negative electronic state of monomeric Pd on a Au(111) substrate catalyzed the dissociative adsorption of H_2 at lower temperatures than *bulk*-Pd.[10] iii) Both isolated atoms and their surroundings play cooperative roles. Kobayashi *et al.* reported that mono-atomically dispersed Rh atoms on Co atoms played supportive roles that maintained an active Co^0 state for efficient methane oxidation.[15] iv) Electronic interactions between isolated atoms and the surrounding atoms induce high activity. Sykes *et al.* reported the selective hydrogenation of butadiene to butene over an isolated Pt-atom-containing Pt−Cu alloy. Although, in this case, single Pt atoms actively dissociated H_2, Cu atoms also acted as butadiene adsorption sites.[6, 12, 19] Nagaoka *et al.* reported that a catalyst composed of isolated Pt in a Pt−Co alloy showed activity for exhaust purification due to the activation of NO_x and the oxidizations of CO and hydrocarbons by the electron-rich Pt atoms and the metallic Co atoms, respectively.[16] Clearly, designing catalysts that combine isolated atoms with the surrounding atoms is a useful approach to achieving highly selective and efficient reactions.

The catalytic hydrogenation of carbon dioxide (CO_2) affords various products, such as methane (CH_4), carbon monoxide (CO), formic acid (HCOOH), formaldehyde (HCHO), methanol

(CH_3OH), and hydrocarbons. Controlling selectivity for these products over supported alloy catalysts has attracted significant interest from the perspective of designing effective alloy catalysts based on the tuning of their electronic and geometric properties.[20-23] Among transition metals, Ni is known to exhibit catalytic activity for the formation of CH_4 at ambient pressure *via* the "CO_2 methanation" reaction, although Ni catalysts require high reaction temperatures (723–823 K) compared to those of Ru catalysts due to their low H_2-dissociation activities.[24-26] Under CO_2-hydrogenation conditions, the exothermic CO_2 methanation ($CO_2 + 4H_2 \rightarrow CH_4 + 2H_2O$, $\Delta_r H^\circ_{298\ K} = -164.7$ kJ mol^{-1}) and the endothermic reverse water gas shift reaction (rWGS) ($CO_2 + H_2 \rightarrow CO + H_2O$, $\Delta_r H^\circ_{298\ K} = 41.1$ kJ mol^{-1}) compete with each other; hence, low reaction temperatures favor CH_4 formation. Generally speaking, the dissociation of H_2 over Pt atoms proceeds at low temperatures. Unfortunately, while Pt catalysts are effective for the rWGS reaction, they are not good catalysts for the methanation of CO_2.[24] Since the methanation of CO is also an exothermic reaction ($CO + 3H_2 \rightarrow CH_4 + H_2O$, $\Delta_r H^\circ_{298\ K} = -205.9$ kJ mol^{-1}), the successive hydrogenation of CO by dissociated hydrogen is a useful strategy for highly selective methanation at low temperature. The CO methanation activity is explained by electronic interactions between the supports and the active metal species;[27, 28] in other words, electron donation from the metal to the 2π anti-bonding orbital of the adsorbed CO species weakens the C−O bond and promotes the hydrogenation of CO toward CH_4. Therefore, CO that is strongly adsorbed on an electron-rich Pt species due to overlap between the 2π orbital of the CO and the *d* orbital of the metal is expected to exhibit high desorption durability and a low activation barrier for C−O bond dissociation.[29, 30] Nørskov *et al.* mentioned that the presence of a 3*d* transition metal on Pt(111) facilitated the donation of electrons from the 3*d* metal to the 5*d*-band of Pt.[31] In addition, a structure composed of isolated Pt species surrounded by Ni atoms is expected to induce the rapid hydrogenation of Pt-adsorbed CO by spillover hydrogens on Ni. With this in mind, in this study we designed a catalyst composed of isolated Pt atoms in a Ni−Pt alloy for the selective low-temperature methanation of CO_2. Isolated Pt atoms in the Ni−Pt alloy were produced by a simple impregnation method on aluminum oxide (Al_2O_3) pretreated by reduction with hydrogen. X-ray absorption spectroscopy (XAS) and Fourier-transform infrared (FT-IR) spectroscopy with CO as a probe were used to identify the negative electronic state and the isolated geometric structure of the Pt species in the Ni/Al_2O_3 catalyst. Kinetics studies and FT-IR spectroscopy suggested that isolated negative Pt species play bifunctional roles as

H_2-dissociation sites and CO-adsorption sites for the efficient and selective formation of CH_4. To the best of our knowledge, this is the first report on the design of active sites composed of isolated Pt atoms surrounded by Ni atoms, and that demonstrates the specific roles of isolated Pt atoms during the hydrogenation of CO_2.

Experimental

Ni−Pt alloys were prepared on γ-Al_2O_3 powder (Catalysis Society of Japan, JRC-ALO-7) by an impregnation method using $Ni(NO_3)_2$ and $Pt(NH_3)_2(NO_2)_2$ as precursors. The amount of loaded Ni + Pt was fixed at 1.0 mmol g_{cat}^{-1} with Ni:Pt molar ratios of 100:0, 99:1, 95:5, 75:25, 50:50, 25:75, and 0:100. After impregnation, the catalysts were calcined at 773 K for 5 h, and then grained and sieved to 25–50 mesh. For catalytic activity experiments and characterization, the catalysts were reduced at 1173 K for 1 h under 5% H_2 at a flow rate of 50 mL min^{-1}; this reduction temperature was sufficiently high to reduce Ni-based oxides to Ni metal (**Figure 1**).

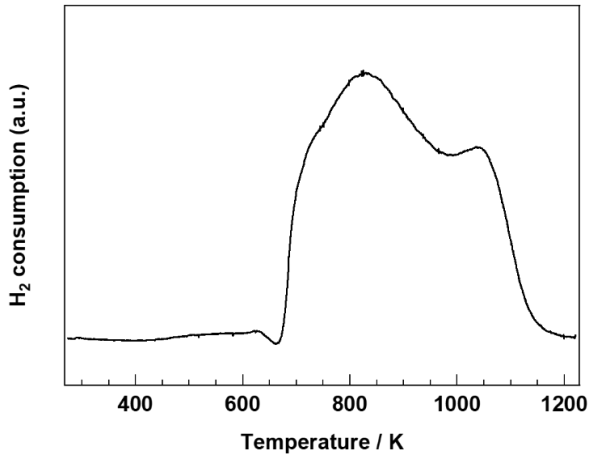

Figure 1. Temperature programmed reduction profile of H_2 (H_2-TPR) of Ni/Al_2O_3, which was performed by using TPR apparatus (BELCAT-B, BEL Japan Inc., Japan) equipped with cryostat (BELCAT-B system with CATcryo, MicrotracBEL Corp.). 2% H_2/Ar (30 mL min^{-1}) was passed through a reaction tube containing the 50 mg of catalyst under atmospheric pressure. The reactor was heated from 273 K to 1223 K with an electronic furnace at 5 K min^{-1}, and the amount of H_2 consumed was monitored with a TC detector contained in BELCAT-B system. The consumed amount of H_2 was equivalent to the theoretical amount of H_2 calculated by following reaction equation: $NiO \rightarrow Ni^0$. All the reduction peaks were located at less than 1173 K, indicating that Ni^{2+} species on Al_2O_3 were reduced to Ni metals during reduction pretreatment.

CO_2 was hydrogenated over 100 mg of catalyst in a fixed-bed flow reactor at ambient pressure. K-type thermocouples in contact with the central part of the catalyst bed were used to measure and control the temperature. Each catalyst was exposed to 50 mL min^{-1} flow of a mixed gas containing 10% CO_2 and 40% H_2 with He as the balance and 0.5% N_2 as the internal standard during catalytic activity testing at elevated temperatures 473–973 K. Apparent reaction orders were determined from the reaction results under a mixture of H_2 and CO_2; the proportions of these gases varied between 10 and 40% at a constant pressure of the other substrate gas at a temperature of 523 K. The CO and CH_4 products were analyzed by gas chromatography (GC) using two GC-8A chromatographs (Shimadzu Corp.) equipped with a thermal conductivity detector (TCD) and a flame ionization detector (FID) using a Molecular Sieve 5A column (Shimadzu Corp.) and He as the carrier gas. All transfer lines were maintained at 373 K to avoid water condensation. Magnesium perchloride was placed downstream of the reaction bed as the desiccant.

The proportion of carbon atoms at the inlet of the reactor to that at the outlet of the reactor was better than 3%. Using the composition of the reactor outlet, the yields of CH_4 (Y_{CH4}) and CO (Y_{CO}) were calculated using the following formula:

$$Y_{CH4} \text{ or } Y_{CO}\ (\%) = 100 \times (F_{CH4,out} \text{ or } F_{CO,out}) / (F_{CO2,in}) \quad (1)$$

where, F_i is the molar ratio of component i contained in the inlet or outlet of the reactor.

The reduced catalysts were subjected to X-ray diffractometry (XRD, Multiflex, Rigaku) with Cu Kα radiation at an accelerator voltage of 40 kV over the 10-90° 2θ range in steps of 0.01°. Transmission electronic microscopy (TEM) images were acquired on a JEOL JEM-2100F microscope at an accelerator voltage of 200 kV. Samples were prepared as follows: Ni−Pt/Al_2O_3 dispersed in 2-propanol was dipped onto a carbon-coated copper grid and dried at room temperature. The X-ray absorption fine structure (XAFS) spectra at the Ni K-edge and Pt L_3-edge were acquired on the BL01B1 beamline of the SPring-8 facility. The XAFS spectra were recorded in transmittance mode at room temperature using Si(111) double-crystal monochromators for the Ni K-edge and Pt L_3-edge measurements, respectively. The samples were reduced at 1173 K under 5% H_2/He, after which the sample pellets were reduced at 873 K in a glass tube purged with H_2. The pellets were packed with an A-500HS oxygen absorber (I.S.O. Inc., Japan) prior to XAFS spectroscopy. The A-500HS absorber was still pink following the XAFS experiments, suggesting that sample oxidation had been prevented.

The data were reduced using a typical procedure in the Athena and Artemis version 0.9.18 software included in the Demeter package.[32] Fourier transforms of the Ni K- and Pt L_3-edge EXAFS oscillations were curve fitted using the FEFF6L code. FT-IR spectra of the adsorbed CO species were acquired on an infrared spectrometer equipped with a mercury cadmium telluride (MCT) detector (FTIR-4200, Jasco). The IR cell was connected to a vacuum line and a 25-mg pellet of pre-reduced Ni−Pt/Al_2O_3 was fixed in a sample-holder cup. FT-IR spectra were collected *in vacuo* at 303 K following H_2 pretreatment at 873 K for 1 h, and then acquired at 303 K following introduction of 0.08 Torr of CO.

Results and discussion

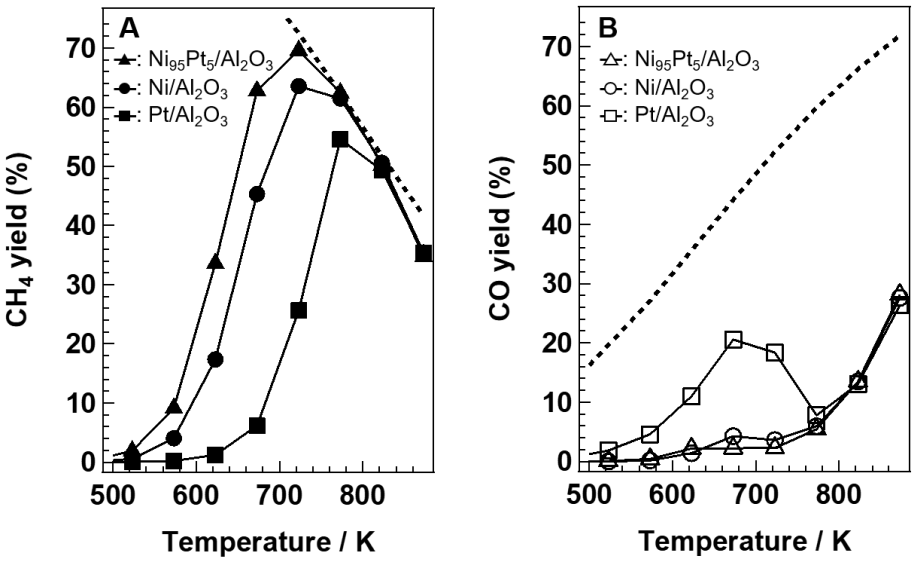

Figure 2. Yields of **(A)** CH_4 and **(B)** CO following hydrogenation of CO_2 over Ni−Pt/Al_2O_3. Closed and open circles, Ni/Al_2O_3; triangles, $Ni_{95}Pt_5$/Al_2O_3; squares, Pt/Al_2O_3. The dashed lines show equilibrium conversions for each reaction; m_{cat} = 100 mg, 10% CO_2, and 40% H_2 in He (total flow rate = 50 mL min^{-1}).

Figure 2(A) and **(B)** shows the yields of CH_4 and CO as functions of temperature during CO_2 hydrogenation, respectively. In **Figure 2(A)**, the Ni/Al_2O_3 catalyst mainly exhibited CH_4-formation activity below 723 K with a low yield of CO. While the CH_4-formation activity over Ni/Al_2O_3 increased with increasing reaction temperature, it decreased when the temperature exceeded 773 K due to the establishment of an equilibrium (dashed line). Although the activity was sufficiently low to achieve conversion equilibrium, the yield of CO over Ni/Al_2O_3 increased with increasing reaction

temperature (**Figure 2(B)**). On the other hand, CO was generated as the main product over Pt/Al_2O_3. Although the yield of CO increased with increasing reaction temperature below 723 K, significant yields of CH_4 were also generated at higher than 673 K. Ni−Pt/Al_2O_3 containing 5 mol% Pt (hereafter, $Ni_{95}Pt_5/Al_2O_3$) exhibited higher yields of CH_4 than Ni/Al_2O_3 below 673 K. Although *bulk*-Pt species are known to act as active sites for CO formation, the yield of CO over $Ni_{95}Pt_5/Al_2O_3$ was as low as that formed over Ni/Al_2O_3. In other words, very small amounts of Pt species within the $Ni_{95}Pt_5/Al_2O_3$ catalyst improved its activity toward CO_2 methanation while suppressing CO formation, suggesting that the Pt species in $Ni_{95}Pt_5/Al_2O_3$ possess unique catalytic properties.

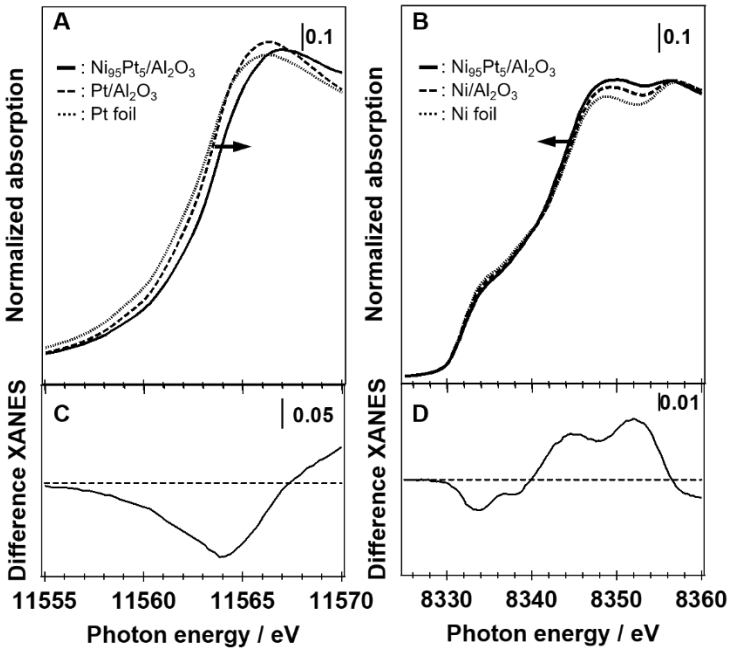

Figure 3. (A) Pt L_3-edge XANES spectra of Pt/Al_2O_3 (dashed line), $Ni_{95}Pt_5/Al_2O_3$ (solid line), and Pt foil (dotted line) **(B)** Ni K-edge XANES spectra of Ni/Al_2O_3 (dashed line), $Ni_{95}Pt_5/Al_2O_3$ (solid line), and Ni foil (dotted line). **(C)** Difference between the Pt L_3-edge XANES spectrum of $Ni_{95}Pt_5/Al_2O_3$ and that of Pt/Al_2O_3. **(D)** Difference between the Ni K-edge XANES spectrum of $Ni_{95}Pt_5/Al_2O_3$ and that of Ni/Al_2O_3. The spectra of pre-reduced samples were acquired in a degassing sealer packed with A-500HS oxygen absorber.

Figures 3(A) and **(B)** show Pt L_3- and Ni K-edge X-ray absorption near edge structure (XANES) spectra of Ni−Pt/Al_2O_3, respectively. In **Figure 3(A)**, the absorption edge of the Pt L_3-edge XANES spectrum of $Ni_{95}Pt_5/Al_2O_3$ alloy is obviously shifted to higher energy than those of Pt/Al_2O_3 and the reference Pt foil, which is also shown in the difference Pt L_3-edge XANES spectrum of $Ni_{95}Pt_5/Al_2O_3$ against Pt/Al_2O_3 (**Figure 3(C)**). Nørskov *et al.* mentioned that the neighboring 3*d*

transition metal atoms broaden and lower the energy of the Pt *d*-band with broadening of the empty 5*d* orbital.[31] We consider that this broadening in the empty Pt $5d_{3/2}$ orbital by alloying with Ni resulted in the negative shift in the energy of the absorption edges of the Pt L_3-edge XANES spectra.[33] In **Figure 3(B)**, The main absorption peak in the Ni K-edge XANES spectrum of Ni/Al_2O_3 exhibits metallic features that are attributed to transitions from the 1*s* to the unoccupied 4*s* and 4*p* orbitals, and the weak shoulder peak at around 8334 eV is attributed to the quadrupole-allowed electronic transition to the 3*d* orbital.[34-37] The Ni K-edge XANES spectrum exhibits an increase in intensity of the white line absorption peak and a decrease in the shoulder peak upon addition of the Pt species when compared to that of Ni/Al_2O_3, which is clearly shown in the difference Ni K-edge XANES spectrum of $Ni_{95}Pt_5/Al_2O_3$ against Ni/Al_2O_3 (**Figure 3(D)**). The increase in the white line absorption is suggestive of a lowering of the electron density of the 4*s* and 4*p* orbitals due to electron transfer from the Ni atoms to their neighboring Pt atoms. In addition, the breaking of the symmetric coordination of the Ni atoms due to the neighboring Pt atoms led to the hybridization of the 4*s* and 4*p* orbitals with the 3*d* orbital of Ni. The decrease in the intensity of the shoulder peak upon addition of Pt is also suggestive of an increase in the density of state of the 3*d* orbital due to hybridization with the 4*s* and 4*p* orbitals. These features were also observed in previous XANES studies of Ni−Pt alloy single crystals by Moraweck *et al.*,[35] and strongly evidences the electron transfer from Ni atoms to Pt atoms in the Ni−Pt alloy catalyst. This electronic interaction between Pt and Ni is expected to affect the adsorption properties of intermediate species such as CO.[30, 38]

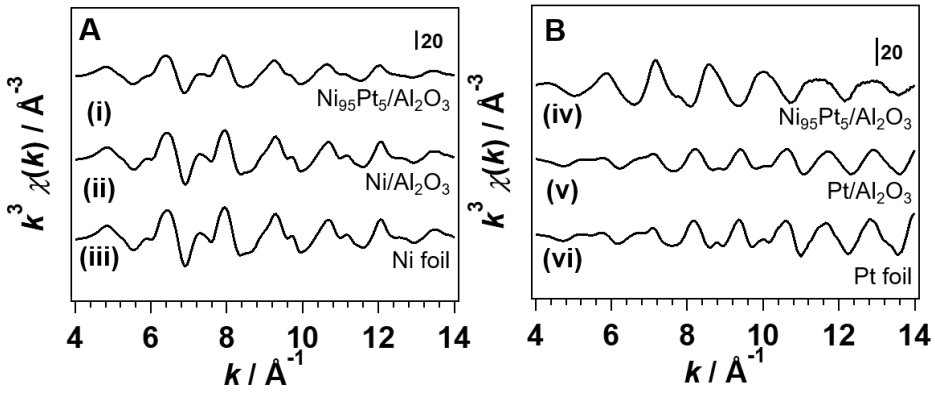

Figure 4. (A) Ni K-edge EXAFS oscillations of (i) $Ni_{95}Pt_5/Al_2O_3$, (ii) Ni/Al_2O_3, and (iii) Ni foil. **(B)** Pt L_3-edge EXAFS oscillations of (iv) $Ni_{95}Pt_5/Al_2O_3$, (v) Pt/Al_2O_3, and (vi) Pt/Al_2O_3.

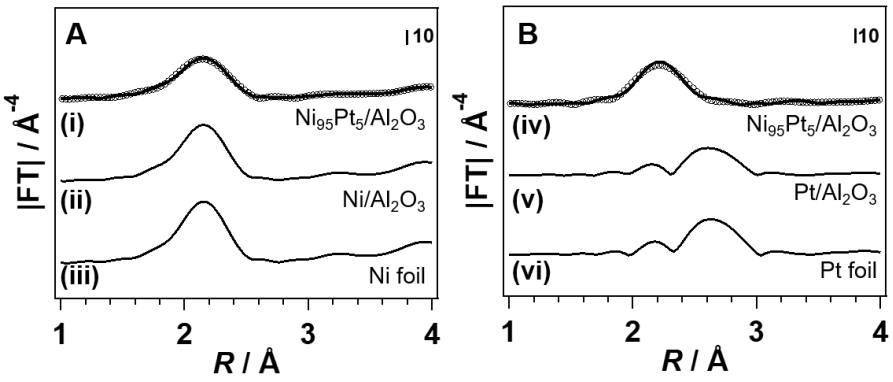

Figure 5. (A) Fourier transforms of the Ni K-edge EXAFS of (i) $Ni_{95}Pt_5/Al_2O_3$, (ii) Ni/Al_2O_3, and (iii) Ni foil. **(B)** Fourier transforms of the Pt L_3-edge EXAFS of (iv) $Ni_{95}Pt_5/Al_2O_3$, (v) Pt/Al_2O_3, and (vi) Pt/Al_2O_3. The blank circles correspond to the fitting curve, the parameters and results of which are listed in **Table 1**. The Ni K-edge ($1.4<\boldsymbol{R}<2.6$) first coordination shell was fitted with the Ni–Ni and Ni–Pt scattering paths of the structure model using the FEFF6L code. The Pt L_3-edge ($1.4<\boldsymbol{R}<2.8$) first coordination shell was fitted with the Pt–Ni and Pt–Pt scattering paths in the same manner.

Figure 4(A) and **(B)** shows the Ni K- and Pt L_3-edge extended X-ray absorption fine structure (EXAFS) oscillations of $Ni_{95}Pt_5/Al_2O_3$ and the reference samples. The Ni K-edge EXAFS oscillation of $Ni_{95}Pt_5/Al_2O_3$ is similar in periodicity to that of Ni/Al_2O_3, suggesting the Ni species in $Ni_{95}Pt_5/Al_2O_3$ are located in similar surroundings to those in Ni/Al_2O_3. On the other hand, the Pt L_3-edge EXAFS oscillations of $Ni_{95}Pt_5/Al_2O_3$ are quite different to those of Pt/Al_2O_3. In addition, the shapes of the Ni K-edge EXAFS and inverted-Pt L_3-edge EXAFS oscillations of $Ni_{95}Pt_5/Al_2O_3$ resemble each other, which indicates that the Pt atoms are in similarly coordinating surroundings to the Ni atoms following formation of the solid-solution-type Ni−Pt alloy. Both the Ni K- and Pt L_3-edge EXAFS oscillations were Fourier transformed in the 3.0–14 Å region, as shown in **Figure 5(A)** and **(B)**, respectively. The Fourier transforms of the Ni K- and Pt L_3-edges of $Ni_{95}Pt_5/Al_2O_3$ were well fitted with Ni−Ni and Ni−Pt (Pt−Ni) fcc-structured scattering shells in the Ni−Pt alloy by considering alloying-promoted lattice extensions determined from the XRD pattern of $Ni_{95}Pt_5/Al_2O_3$ (blank circles); the fitting parameters used are summarized in **Table 1** and the real parts of the Fourier transforms with the fit are shown in **Figure 6**. The contribution of the scattering paths of the Ni and Pt atoms were determined from the Ni K-edge EXAFS oscillation of $Ni_{95}Pt_5/Al_2O_3$, which also suggested that the Ni and Pt species are not segregated, but are homogenized in the Ni−Pt alloy. In addition, the total number of

coordinations to Ni atoms decreased with the addition of Pt, which is consistent with the formation of smaller Ni−Pt alloy particles than those of Ni/Al_2O_3, as observed in the TEM images of pre-reduced $Ni-Pt/Al_2O_3$ (**Figure 7**). In contrast, the Pt L_3-edge EXAFS oscillations reveal that the Pt atoms in $Ni_{95}Pt_5/Al_2O_3$ are fully coordinated by Ni atoms, with no scattering contributions from Pt−Pt bonds observed, suggesting that the Pt atoms are surrounded only by Ni atoms and exist in the bulk of the particles rather than on their surfaces. In addition, the bond distances between the Pt atoms and the first coordinated Ni atoms in $Ni_{95}Pt_5/Al_2O_3$ are quite different from the Pt−Pt distances in Pt/Al_2O_3, while the bond distances between the Ni atoms and the first coordinated Ni atoms in $Ni_{95}Pt_5/Al_2O_3$ are the same as the Ni−Ni distances in Ni/Al_2O_3. The bond distances between the Ni atoms and the first coordinated Pt atoms determined from the Ni K-edge EXAFS spectrum are similar to those between the Pt atoms and the first coordinated Ni atoms determined from the Pt L_3-edge EXAFS spectrum, suggesting that the Ni and Pt atoms are homogeneously mixed.

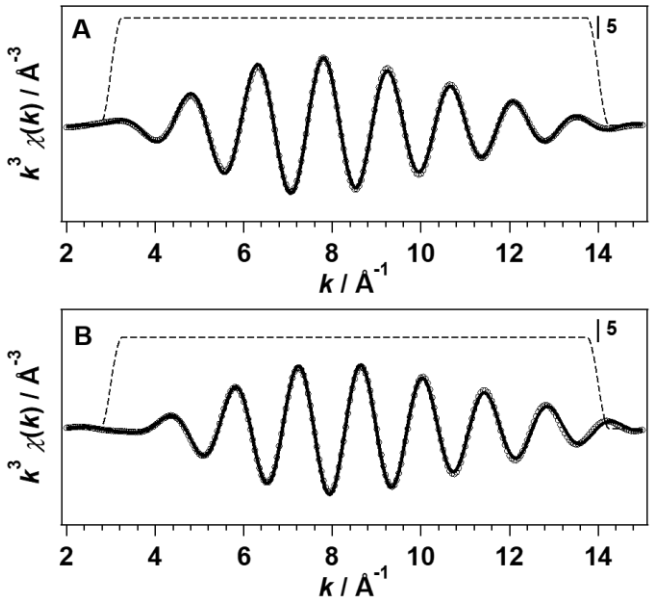

Figure 6. Real part of the backward Fourier transformed EXAFS oscillations of **(a)** Ni K- and **(b)** Pt L_3-edge of $Ni_{95}Pt_5/Al_2O_3$. Circles and dashed lines are the fits and the window functions, respectively.

Table 1. Ni K- and Pt L_3-edge EXAFS curve fitting results for the Ni−Pt/Al_2O_3 catalysts.

Sample	edge	Scatter	C. N.	C.N. Sum.	*r* / 10^{-1} nm	Δ*E* / eV	R-factor
Ni foil	Ni K	Ni	12 (fixed)	-	2.48 (0.01)	−4.1 (0.2)	0.001
Ni/Al_2O_3	Ni K	Ni	10.8 (0.1)	-	2.48 (0.01)	−4.3 (0.4)	0.001
$Ni_{95}Pt_5/Al_2O_3$	Ni K	Ni	7.7 (0.3)	9.1	2.48 (0.01)	−5.4 (1.3)	0.002
		Pt	1.4 (0.5)		2.57 (0.02)		
	Pt L_3	Ni	11.5 (0.3)	11.5	2.54 (0.01)	6.8 (0.8)	0.003
		Pt	-		-		
Pt/Al_2O_3	Pt L_3	Pt	10.3 (0.3)	-	2.75 (0.01)	6.7 (1.1)	0.006
Pt foil	Pt L_3	Pt	12 (fixed)	-	2.76 (0.01)	7.2 (0.1)	0.002

C.N.: Coordination number; Δ*E*: energy shift of the absorption edge; *r*: bond distance. The σ^2 (Debye−Waller factor) values for the Ni−Ni, Ni−Pt, and Pt−Pt shells were fixed at 0.006, 0.006, and 0.005, respectively. S_0^2 values of 0.852 and 0.689 were determined by fitting Ni and Pt foil, respectively. Numbers in parentheses represent uncertainties. The reliability factor (R-factor) is defined as:

$$\text{R-factor} = \Sigma[k^3 \chi_{obs}(k) - k^3 \chi_{cal}(k)]^2 / \Sigma[k^3 \chi_{obs}(k)]^2$$

where, χ_{obs} and χ_{cal} correspond to the observed and calculated data, respectively.

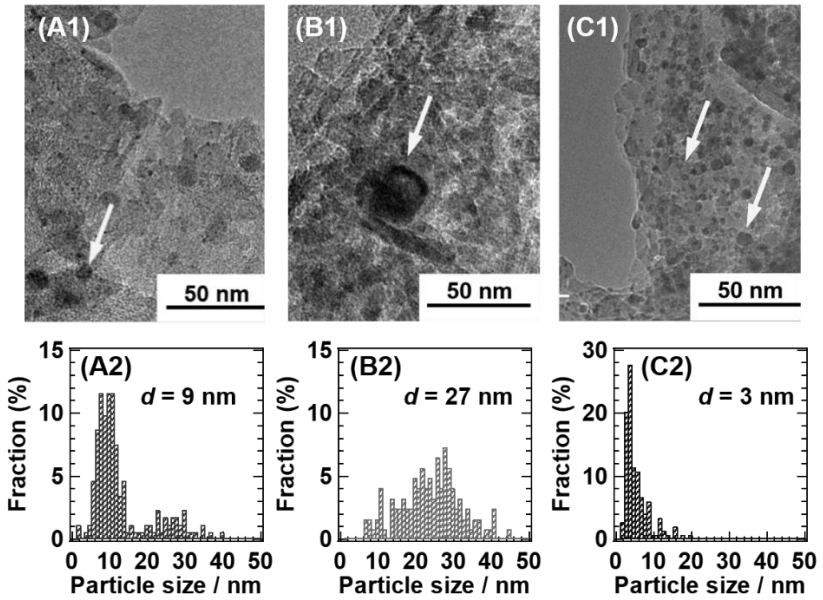

Figure 7. TEM images and size distribution of $Ni_{95}Pt_5/Al_2O_3$ (**(A1)** and **(A2)**), Ni/Al_2O_3 (**(B1)** and **(B2)**), and Pt/Al_2O_3 (**(C1)** and **(C2)**), respectively. The images of previously reduced samples were measured at a magnification of 10^5.

These EXAFS analyses of $Ni_{95}Pt_5/Al_2O_3$ clearly indicate that isolated Pt species surrounded by Ni atoms were formed in the bulk of the solid solution of Al_2O_3-supported Ni−Pt alloy particles. Hence, $Ni_{95}Pt_5/Al_2O_3$ is referred as the "*iso*-Pt catalyst" hereafter. As a result of the ligand effect induced by alloying with surrounding Ni atoms, the state density of the Pt 5*d* orbital of *iso*-Pt was reduced; these atoms are defined as $Pt^{\delta-}$ species. Simultaneously, the state density of the Ni 3*d* orbital ($Ni^{\delta+}$) increased due to electronic interactions with the Pt atoms.

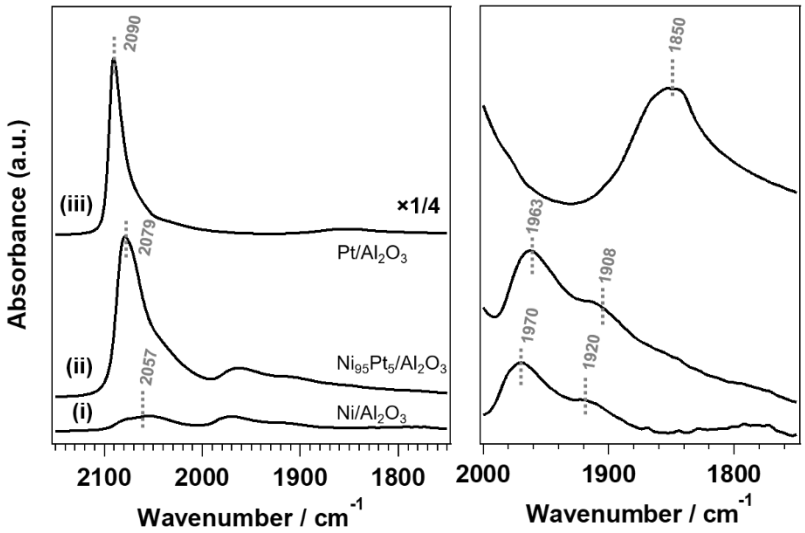

Figure 8. IR difference spectra of Ni−Pt/Al_2O_3 at 303 K under 0.08 Torr of CO. From bottom to top: the spectra of (i) Ni/Al_2O_3, (ii) $Ni_{95}Pt_5/Al_2O_3$, and (iii) Pt/Al_2O_3. Pellets of pre-reduced samples (25 mg) were exposed to H_2 at 873 K for 1 h prior to CO adsorption.

Negatively shifted Pt species ($Pt^{\delta-}$ species) were observed on the surface of the *iso*-Pt catalyst by FT-IR spectroscopy using CO as a probe, which is used to clarify the electronic state of the *d*-electrons of metal species by observing the shift in the *v*(CO) stretching mode resulting from orbital interactions between the *d*-electrons of the metal species and the 2π anti-bonding orbital of CO.[29, 39] **Figure 8** displays FT-IR difference spectra of Ni−Pt/Al_2O_3 under 0.08 Torr of CO at 303 K against those acquired *in vacuo* at 303 K. Weak bands are observed at 2057, 1970, and 1920 cm^{-1} in the FT-IR spectrum of Ni/Al_2O_3 (i), which are assigned to the *v*(CO) stretching mode of on-top CO, and two types of end-on bridged CO species (which are referred to as weakly and strongly adsorbed bridged CO species due to different Ni sites) on metallic Ni particles, respectively.[40, 41] Pt/Al_2O_3 shows a strong on-top CO band at 2090 cm^{-1} and a weak band corresponding to bridged CO species at 1850 cm^{-1} (iii).[42] A strong band was observed at 2079 cm^{-1} in the spectrum of $Ni_{95}Pt_5/Al_2O_3$ (*iso*-Pt) (ii), which

lies between those of on-top CO on Ni/Al_2O_3 and Pt/Al_2O_3. This strong band is assigned to the ν(CO) stretching mode of on-top CO species on metallic Pt because of its similar desorption properties to that observed for Pt/Al_2O_3. The shift to lower frequency of the ν(CO) stretching mode is ascribable to strong overlap between the 5*d*-orbital of Pt and the 2π anti-bonding orbital of CO, suggestive of the presence of $Pt^{\delta-}$ species on the surface of the *iso*-Pt catalyst.[29, 30] The band position of the ν(CO) stretching mode shifts due to the coverage of adsorbed CO species. Especially, dipole-dipole interactions have less impact on *iso*-Pt atoms than on pure Pt surface because the surrounding Ni atoms afford geometrical distances between each CO species. However, the electronegativity of *iso*-Pt atoms could be obtained from both Pt L_3-edge XANES spectra and FT-IR spectra. Although the EXAFS spectra (**Table 1**) indicate that *iso*-Pt species are fully coordinated by other atoms, we conclude that some Pt atoms were drawn from the subsurface to the surface of the alloy due to the strong affinity of Pt for CO. As Sachtler reported, the surface of a Au−Pt or Ag−Pd alloy becomes enriched with the element that forms the stronger bond to CO.[43, 44] Since Pt has a larger heat of adsorption for CO than Ni,[45] the surface of the Ni−Pt alloy is reconstructed (rearranged) in the presence of CO. Bridged CO species were also observed on $Ni_{95}Pt_5/Al_2O_3$, which exhibited FT-IR peaks at 1963 and 1908 cm^{-1} that are assigned to bridged CO species that are weakly and strongly adsorbed to Ni−Ni or Ni−Pt. A negligible absorption peak for bridged CO species on Pt (1850 cm^{-1}) appeared in the spectra of $Ni_{95}Pt_5/Al_2O_3$, which suggests a lack of Pt−Pt sites on this catalyst. These results also indicate that isolated Pt atoms were formed among Ni atoms on the surface of the $Ni_{95}Pt_5$ alloy.

Table 2. Results for the formation of CH_4 and CO during CO_2 hydrogenation over Ni−Pt/Al_2O_3. The total amount of the metal species was fixed at 1 mmol g_{cat}^{-1}. m_{cat} = 100 mg, 10 % CO_2, and 40 % H_2 in He (total flow rate = 50 mL min^{-1}). The reaction temperature was 523 K.

Entry	Catalyst	Ni (wt%)	Pt (wt%)	Formation rates (μmol mol_{metal}^{-1} s^{-1})		Selectivity toward CH_4 (%)
				CH_4	CO	
1	Ni/Al_2O_3	5.9	0	214.3	4.2	98.1
2	$Ni_{99}Pt_1/Al_2O_3$	5.8	0.2	341.1	9.9	97.2
3	$Ni_{95}Pt_5/Al_2O_3$	5.6	1.0	715.2	24.1	96.7
4	$Ni_{75}Pt_{25}/Al_2O_3$	4.4	4.9	205.4	220.2	48.2
5	$Ni_{50}Pt_{50}/Al_2O_3$	2.9	9.8	45.2	489.7	8.5
6	$Ni_{25}Pt_{75}/Al_2O_3$	1.5	14.6	11.2	623.4	1.8
7	Pt/Al_2O_3	0	19.5	13.9	686.3	2.0

The catalytic activities of a series of Ni−Pt/Al_2O_3 catalysts toward CO_2 hydrogenation at 523 K are summarized in **Table 2**. Ni/Al_2O_3 and Pt/Al_2O_3 exhibited high selectivity toward CH_4 (98%) and CO (98%), respectively. $Ni_{99}Pt_1/Al_2O_3$ and $Ni_{95}Pt_5/Al_2O_3$ exhibited higher rates of CH_4 formation than Ni/Al_2O_3. Notably, the rate of CH_4 formation over $Ni_{95}Pt_5/Al_2O_3$ containing the *iso*-Pt species (715 μmol mol_{metal}^{-1} s^{-1}) was more than three-times higher than that observed over Ni/Al_2O_3 (214 μmol mol_{metal}^{-1} s^{-1}), while maintaining high selectivity (97%), despite *bulk*-Pt species mainly producing CO. Even though the metal surface area increased by alloying with Pt, the net activity for CH_4 formation over the $Ni_{95}Pt_5/Al_2O_3$ catalyst was obviously high when compared to that of Ni (**Table 3**). The turnover frequency (TOF) for CH_4 formation at 523 K over $Ni_{95}Pt_5/Al_2O_3$ (15.2 $mmol_{CH4}$ $mol_{surf\_atoms}^{-1}$ s^{-1}), which was normalized by the number of surface-metal atoms determined by H_2 pulse titration, was two times higher than that over Ni/Al_2O_3 (7.24 $mmol_{CH4}$ $mol_{surf\_atoms}^{-1}$ s^{-1}). This improvement in the CH_4-formation activity over the *iso*-Pt catalyst was more pronounced at low temperature; hence the specific catalytic properties of *iso*-Pt atoms, such as H_2-dissociation, are more marked at low temperature. Therefore, we conclude that the *iso*-Pt species play specific roles that improve net activity in addition to the high surface areas of its metal particles. In addition, the *iso*-Pt catalyst exhibited excellent stability in its CH_4 formation activity, maintaining high selectivity even after 30 h of reaction at 673 K (**Figure 9**).

Table 3. Estimated turn over frequency (TOF) of CH_4 formation over Ni/Al_2O_3 and $Ni_{95}Pt_5/Al_2O_3$ at reaction temperatures of 473 K and 523 K.

Catalyst ($1mmol\ g_{cat}^{-1}$, 0.1 g)	R_{CH4}[a] / $\mu mol_{CH4}\ mol_{metal}^{-1}\ s^{-1}$		Surface atom[b] / $\mu mol\ g_{cat}^{-1}$	TOF_{CH4}[a] / $mmol_{CH4}\ mol_{surf\ atoms}^{-1}\ s^{-1}$	
	at 473 K	at 523 K		at 473 K	at 523 K
Ni/Al_2O_3	15.9	214.3	29.6	0.537	7.24
$Ni_{95}Pt_5/Al_2O_3$	96.0	715.2	46.9	2.05	15.2

[a] Formation rate of CH_4 per metal atoms (R_{CH4}) and TOF of CH_4 formation per surface-metal atoms (TOF_{CH4}) were calculated as shown in the following manners,

$$R_{CH4}\ (\text{mol mol}_{metal}^{-1}\ \text{s}^{-1}) = TF\ (\text{mol s}^{-1}) \times F_{CH4} / N_{metal}\ (\text{mol}_{metal})$$

$$TOF_{CH4}\ (\text{mol mol}_{metal}^{-1}\ \text{s}^{-1}) = TF\ (\text{mol s}^{-1}) \times F_{CH4} / (N_{surf}\ (\text{mol g}_{cat}^{-1}) \times 0.1\ (\text{g}))$$

where, TF, F_{CH4}, N_{metal}, and N_{surf} were the total flow of outlet of reactor expressed in mol per sec, the molar ratio of CH_4 contained in outlet of reactor, the expected contained amount of metals in the catalyst, and the estimated molar of metal atoms located at the surface of metal particles per 1.0 g of catalyst, respectively.

[b] The amount of surface-metal atoms was estimated by using adsorption amount of H_2 from pulse titration at 173 K with assuming that the chemisorption stoichiometry is H:M (M = Ni or Pt) = 1. H_2 pulse titration (H_2-pulse) were performed by flow-type chemical adsorption measuring apparatus (BELCAT-B, BEL Japan Inc., Japan) equipped with cryostat (BELCAT-B system with CATcryo, MicrotracBEL Corp.). After pre-reduction treatment with 5% H_2/Ar (30 mL min^{-1}) at 1173 K for 1h, H_2 was injected through a reaction tube containing the 50 mg of catalyst under flowing of Ar as carrier gas at 173 K. The amount of H_2 consumed was monitored with a TC detector contained in BELCAT-B system.

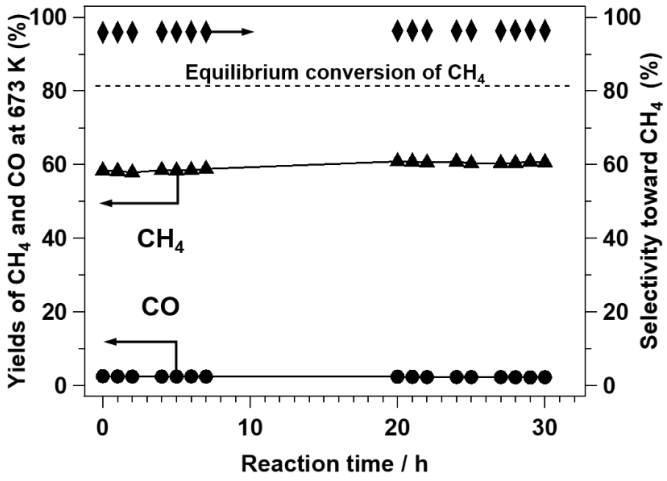

Figure 9. Time course of the yield of products (CH_4: triangles, CO: circles in left axis) over $Ni_{95}Pt_5/Al_2O_3$ at 673 K. The selectivity toward CH_4 was shown in right axis. The dashed lines show equilibrium conversions for CH_4 production at this reaction temperature; m_{cat} = 100 mg, 10% CO_2 and 40% H_2 in He (total flow rate = 50 mL min^{-1}).

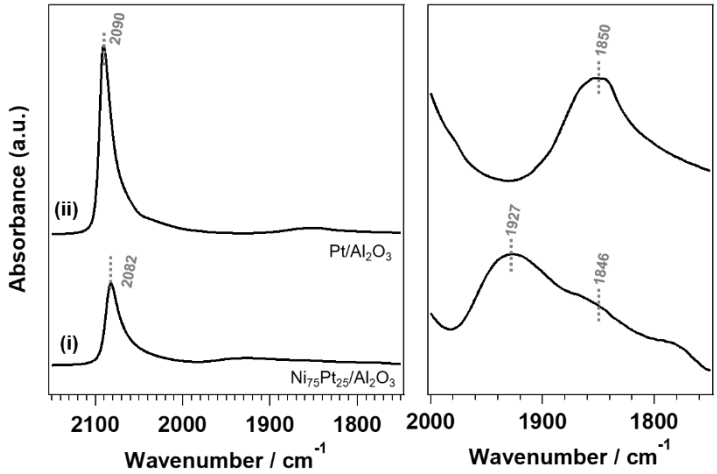

Figure 10. difference IR spectra of (i) Ni/Al_2O_3 and (ii) $Ni_{75}Pt_{25}/Al_2O_3$ at 303 K under 0.08 Torr of CO. The pellet of previously reduced samples (25 mg) were exposed by H_2 at 873 K for 1 h prior to CO adsorption.

Although $Ni_{75}Pt_{25}/Al_2O_3$ showed almost the same CH_4-formation rate as Ni/Al_2O_3, much more CO was evolved, resulting in low selectivity toward CH_4 (50%). Bridged CO species at Pt−Pt sites were observed at 1846 cm^{-1} by FT-IR spectroscopy using CO as a probe, which indicates the presence of Pt−Pt sites on the surface of $Ni_{75}Pt_{25}/Al_2O_3$ (**Figure 10**). EXAFS oscillations also suggest the existence of a Pt−Pt shell in $Ni_{75}Pt_{25}/Al_2O_3$ in addition to the presence of a Pt−Ni scattering path (**Figure 11(A)**). The broader Fourier transform of the Ni K-edge EXAFS for $Ni_{75}Pt_{25}/Al_2O_3$ compared to that of Ni/Al_2O_3 indicates the existence of both Ni−Ni and Ni−Pt scattering paths in the homogeneous Ni−Pt alloy with an expanded lattice (**Figure 11(B)**). The neighboring Pt−Pt sites dispersed on $Ni_{75}Pt_{25}/Al_2O_3$ induce CO production rather than CH_4 formation during the hydrogenation of CO_2.

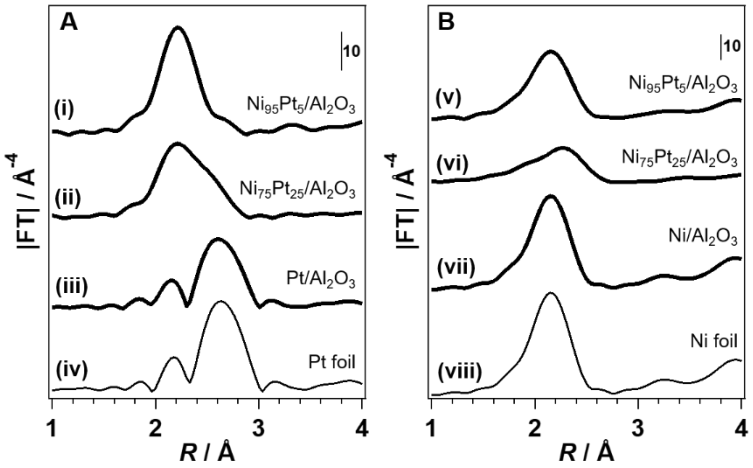

Figure 11. (A) Radial distribution function of Pt L_3-edge EXAFS oscillation of (i) $Ni_{95}Pt_5/Al_2O_3$, (ii) $Ni_{75}Pt_{25}/Al_2O_3$, (iii) Pt/Al_2O_3 and (iv) Pt foil. **(B)** Radial distribution function of Ni K-edge EXAFS oscillation of (v) $Ni_{95}Pt_5/Al_2O_3$, (vi) $Ni_{75}Pt_{25}/Al_2O_3$, (vii) Ni/Al_2O_3 and (viii) Ni foil. The previously reduced samples were measured in a degassing sealer packed with oxygen absorber A-500HS.

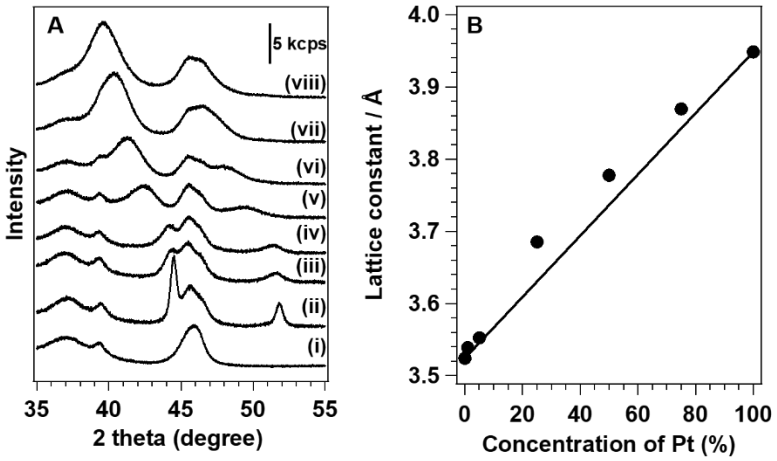

Figure 12. (A) XRD patterns of previously reduced Ni−Pt/Al_2O_3 catalysts. (i) bare-Al_2O_3, (ii) Ni/Al_2O_3, (iii) $Ni_{99}Pt_1/Al_2O_3$, (iv) $Ni_{95}Pt_5/Al_2O_3$, (v) $Ni_{75}Pt_{25}/Al_2O_3$, (vi) $Ni_{50}Pt_{50}/Al_2O_3$, (vii) $Ni_{25}Pt_{75}/Al_2O_3$, and (viii) Pt/Al_2O_3. **(B)** Relationship between Amount of Pt species to the change of lattice constant estimated from plane of (111) facet of fcc structure. Solid line shows theoretic Vegard's law estimated from the lattice constant of *bulk*-Ni and *bulk*-Pt.

The CO-formation rate was observed to increase as the Pt concentration was increased from 25 to 100 mol%. Although Liu *et al.* recently reported that a Pt-rich Ni−Pt alloy on the SBA-15 support exhibited higher activity for CO formation than Pt on SBA-15 during CO_2 hydrogenation,[22] such an increase in CO formation by alloying was not observed in our system. The XRD patterns of a series of Ni−Pt/Al_2O_3 catalysts suggest the formation of homogenous-mixed alloys of Ni and Pt in any Pt/Ni

proportion (**Figure 12**), so the differences in the selectivity toward CH_4 or CO are likely to be dominated by their Pt/Ni surface ratios. These reaction results clearly indicate that *iso*-Pt species within the Ni species prefer to selectively form CH_4, while neighboring Pt−Pt sites induce the desorption of CO as the product.

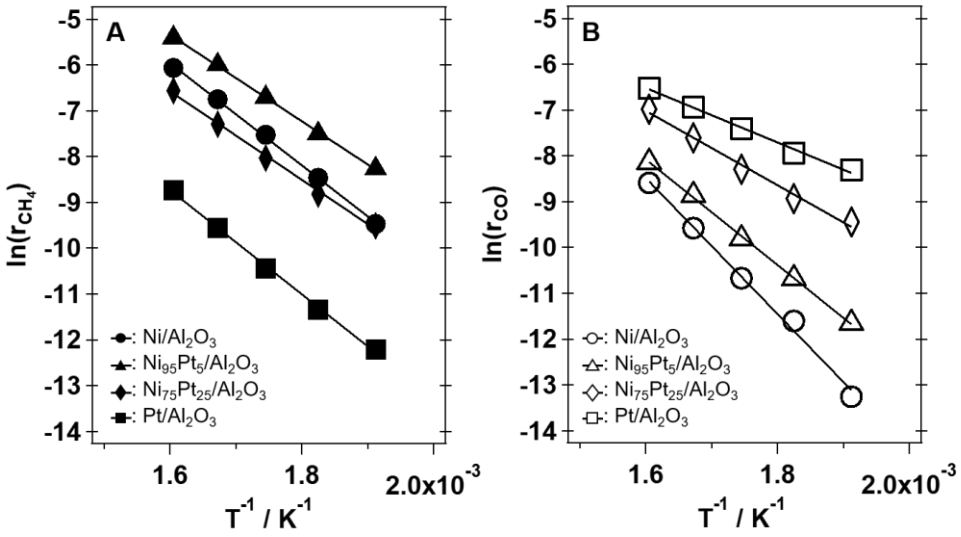

Figure 13. Rates of formation of **(A)** CH_4 and **(B)** CO during CO_2 hydrogenation over Ni−Pt/Al_2O_3 as functions of reaction temperature. Closed and open circles, Ni/Al_2O_3; triangles, $Ni_{95}Pt_5/Al_2O_3$; rhombuses, $Ni_{75}Pt_{25}/Al_2O_3$; squares, Pt/Al_2O_3. The total amount of metal species was fixed at 1 mmol g_{cat}^{-1}. m_{cat} = 100 mg, 10% CO_2, and 40% H_2 in He (total flow rate = 50 mL min^{-1}). The reaction products were analyzed by gas chromatography in 25 K intervals in the 523–623 K range.

Table 4. Apparent activation energies for the formation of CH_4 (E_{a_CH4}) and CO (E_{a_CO}) over Ni−Pt/Al_2O_3. Values were determined from the reaction results shown in **Figure 13**.

Entry	Catalyst	Apparent activation energy / kJ mol^{-1}	
		E_{a_CH4}	E_{a_CO}
1	Ni/Al_2O_3	92	115
2	$Ni_{95}Pt_5/Al_2O_3$	78	96
3	$Ni_{75}Pt_{25}/Al_2O_3$	80	67
4	Pt/Al_2O_3	94	50

The kinetics studies revealed that isolated Pt species in the Ni catalyst decrease the apparent activation energy for the formation of CH_4 (**Figure 13** and **Table 4**); the apparent activation energy

(E_{a_CH4}) over Ni/Al_2O_3, in the 523–623 K range, was determined to be 92 kJ mol^{-1}, which is consistent with previously reported values over Ni-based catalysts.[46, 47] Hence, CH_4 is formed via bridged CO and/or formate species, as reported.[25] In contrast, the addition of 5 mol% Pt addition resulted in a low E_{a_CH4} value of 78 kJ mol^{-1}, which suggests that methanation over the *iso*-Pt catalyst operates through a mechanism with a different rate-determining step (RDS) and a lower activation energy.

The E_{a_CH4} over $Ni_{75}Pt_{25}/Al_2O_3$, which showed activity for the evolution of both of CH_4 and CO, was almost the same as that observed over $Ni_{95}Pt_5/Al_2O_3$. In the case of Pt/Al_2O_3, which generated CO highly selectively, the apparent activation energy for the formation of CO (E_{a_CO}) was found to be 50 kJ mol^{-1}, whereas $Ni_{75}Pt_{25}/Al_2O_3$ (67 kJ mol^{-1}) and $Ni_{95}Pt_5/Al_2O_3$ (96 kJ mol^{-1}) exhibited high E_{a_CO} values due to inhibition of the CO-generating pathway by the competitive production of CH_4. These results indicate that the *iso*-Pt catalyst operates through a unique mechanism that selectively methanates CO_2 compared to that of the *bulk*-Ni catalyst.

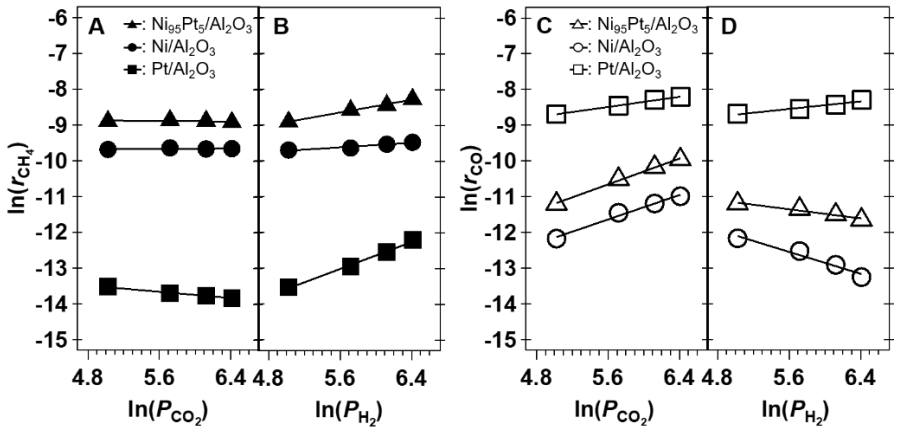

Figure 14. Rates of CH_4 formation over Ni−Pt/Al_2O_3 in **(A)** 10–40% CO_2 at a constant P_{H2} of 40% and in **(B)** 10–40% H_2 at a constant P_{CO2} of 10%. The rate of CO formation in **(C)** 10–40% CO_2 at a constant P_{H2} of 40% and in **(D)** 10–40% H_2 at a constant P_{CO2} of 10%. Closed and open circles, Ni/Al_2O_3; triangles, $Ni_{95}Pt_5/Al_2O_3$; and squares, Pt/Al_2O_3. The total amount of the metal species was fixed at 1 mmol g_{cat}^{-1}. m_{cat} = 100 mg and the total flow rate of the mixed gas (CO_2 + H_2 in He) was 50 mL min^{-1}. The products were analyzed by gas chromatography at a reaction temperature of 523 K.

Figure 14 shows the CH_4- and CO-evolution activities under various compositions of CO_2 and H_2. The apparent reaction orders for the formation of CH_4 and CO in CO_2 and H_2 of varying pressure over the *bulk*-Ni catalyst are described by the following equations:

$$r_{CH_4} = k_{Ni\_CH_4} P_{CO_2}^{0.21} P_{H_2}^{0.16} \quad (2)$$

$$r_{CO} = k_{Ni\_CO} P_{CO_2}^{1.06} P_{H_2}^{-0.76} \quad (3)$$

where r and k are reaction rates and reaction rate constants, and P_{CO2} and P_{H2} are the partial pressures of CO_2 and H_2 in the reaction gas, respectively. For the formation of CH_4, both CO_2 and H_2 reaction orders were positive, indicating that the RDS during hydrogenation involves adsorbed CO_2 species or CO species. The first order observed for CO_2 pressure, and the negative order observed for H_2 pressure during CO formation indicate that the formation of CO over the Ni catalyst was competitively inhibited by the dominant formation of CH_4. Over the *bulk*-Pt catalyst, which generated mainly CO, the apparent reaction orders for the formation of CO in terms of both CO_2 and H_2 were positive:

$$r_{CH_4} = k_{Pt\_CH_4} P_{CO_2}^{-0.23} P_{H_2}^{0.94} \quad (4)$$

$$r_{CO} = k_{Pt\_CO} P_{CO_2}^{0.24} P_{H_2}^{0.27} \quad (5)$$

Hydrogenation of adsorbed CO_2 species is the RDS for the formation of CO over *bulk*-Pt. On the other hand, a negative order in CO_2 pressure and a first order in H_2 pressure were observed during CH_4 formation, which indicates that the poor H/CO ratios at the surfaces of the Pt particles result in low selectivity toward CH_4. The reaction orders for the formation of CH_4, in terms of CO_2 and H_2 pressures, were quite different over the *iso*-Pt catalyst compared to those observed over *bulk*-Ni as shown below:

$$r_{CH_4} = k_{Ni_{95}Pt_5\_CH_4} P_{CO_2}^{-0.02} P_{H_2}^{0.45} \quad (6)$$

$$r_{CO} = k_{Ni_{95}Pt_5\_CO} P_{CO_2}^{1.04} P_{H_2}^{-0.32} \quad (7)$$

The *iso*-Pt catalyst showed a slightly negative order in CO_2 pressure and an almost half order in H_2 pressure for CH_4 formation. Compared with the Ni/Al_2O_3 catalyst, the reaction order in CO_2 was clearly low. The reaction order in H_2 over the *iso*-Pt catalyst was significantly higher than that over the Ni catalyst. The significant differences in reaction orders over the *iso*-Pt catalyst from those over the Ni catalyst clearly indicate a change in the methanation reaction kinetics upon addition of *iso*-Pt. Karelovic *et al.* reported that the Pd/Al_2O_3 catalyst exhibited slightly negative order in CO_2 pressure and a positive order in H_2 pressure for CH_4 formation.[20] Their results clearly indicate that the concentration and the strengths of the surface species adsorbed on the active metal species affect the activity and the selectivity for the hydrogenation of CO_2; that is, a negative order in CO_2 pressure for CH_4 formation suggests methanation inhibition by CO_2-derived adsorbed intermediates.[20, 48] If we assume that the mechanism for methanation over the *iso*-Pt catalyst proceeds by the surface reactions

of adsorbed H and adsorbed CO species, the coverage of CO adsorbed species on *iso*-Pt catalyst predominates over H adsorbed species. Although the dissociation of H_2 is more likely to proceed at low temperature due to the presence of surface Pt species, the absence of sufficient Pt species as dissociation sites for H_2 due to inhibition by CO adsorption led to this process being the RDS. Considering these viewpoints, we conclude that the RDS for CH_4 formation over the *iso*-Pt catalyst is either the hydrogenation of adsorbed-CO species on *iso*-Pt atoms or H_2 dissociation on *iso*-Pt atoms. Although CO formation is first order in CO_2 pressure and negative order in H_2 pressure over the *iso*-Pt catalyst, these trends are the same as those observed for the *bulk*-Ni catalyst; a higher reaction order in H_2 pressure than that of *bulk*-Ni indicates that the addition of Pt species results in an increase in the supply of spillover hydrogen.

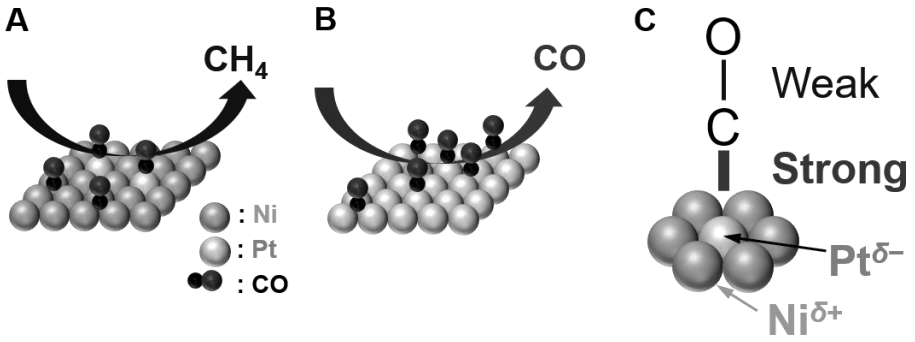

Figure 15. Illustrating the adsorbed CO species on the surfaces of **(A)** the *iso*-Pt catalyst and **(B)** the *bulk*-Pt catalyst. **(C)** A model of adsorbed CO on an isolated $Pt^{\delta-}$ atom surrounded by $Ni^{\delta+}$ atoms.

The addition of very small amounts of Pt resulted in an increase in CH_4-formation activity while maintaining high selectivity toward CH_4. As described above, the high CH_4-formation rate is due to H_2-dissociation activity on Pt species at low temperature. On the other hand, the unique electronic state of the $Pt^{\delta-}$ species induces low CO-evolution activity over *iso*-Pt. The surfaces of the *iso*-Pt and *bulk*-Pt catalysts under CO_2-hydrogenation conditions are shown schematically in **Figure 15(A)** and **(B)**, respectively. CO species adsorbed at $Pt^{\delta-}$ atoms are considered to become hydrogenated to form CH_4, whereas those on *bulk*-Pt are easily desorbed. The observed differences in final products derived from adsorbed CO are due to the electronegativities and geometric surroundings of the *iso*-Pt species. CO molecules adsorbed at $Pt^{\delta-}$ atoms are strongly anchored due to the large orbital overlap between the 5*d* orbital of $Pt^{\delta-}$ and the 2π anti-bonding orbital of CO, resulting in a lower C–O bond energy associated with the stretching mode of the adsorbed CO species on $Pt^{\delta-}$ than that adsorbed at

bulk-Pt, as shown in **Figure 15(C)**. In addition, the surrounding $Ni^{\delta+}$ atoms act as adsorption sites for dissociated hydrogen species that progress the hydrogenation of the C−O bond, weakened by strong back-donation toward the 2π orbital. In contrast, at Pt−Pt sites in the *bulk*-Pt catalyst, the on-top adsorbed and/or bridged CO species desorb as products without further methanation by hydrogen.

In this study, we demonstrated that isolated Pt species in a Ni catalyst play two roles during CO_2 hydrogenation toward CH_4. One involves the high dissociation activity of H_2 at low temperature, which results in high CH_4-formation activity. The other is characteristic of the isolated Pt catalyst: higher adsorption energies are associated with the adsorption sites for CO species than those for Ni species. The negative electronic state of the 5*d* orbital of $Pt^{\delta-}$ weakens the C−O bond of CO species attached to the isolated Pt atoms, leading to further reactions with hydrogen species adsorbed at the surrounding $Ni^{\delta+}$ sites. We conclude that synergism between the "ligand effect" and the "ensemble effect" affords high selectivity for the formation of CH_4.

Conclusions

$Ni_{95}Pt_5/Al_2O_3$ exhibited higher activity for the formation of CH_4 than Ni/Al_2O_3 during CO_2 hydrogenation. In contrast, the CO yield over $Ni_{95}Pt_5/Al_2O_3$ was as low as that over Ni/Al_2O_3, although only CO was generated over bare Pt/Al_2O_3. Isolated Pt atoms (*iso*-Pt) were formed on the surface of the $Ni_{95}Pt_5$ solid-solution-alloy through electronic interactions between $Pt^{\delta-}$ atoms and surrounding $Ni^{\delta+}$ atoms. $Ni_{95}Pt_5/Al_2O_3$ showed a lower apparent activation energy for the formation of CH_4 (E_{a_CH4}) than Ni/Al_2O_3. The reaction orders for CH_4 formation indicated that *iso*-$Pt^{\delta-}$ species in $Ni_{95}Pt_5/Al_2O_3$ catalyze methanation through a mechanism involving a different rate-determining step (RDS) to that of the Ni catalyst. We conclude that *iso*-$Pt^{\delta-}$ species play two roles, namely as H_2-dissociation sites and as adsorption sites for CO. Adsorbed CO species are strongly anchored due to the electronic state of the $Pt^{\delta-}$ species, with the surrounding Ni atoms acting as adsorption sites for dissociated hydrogen, leading to the hydrogenation of CO and the formation of CH_4.

References

1 O. Alexeev and B. Gates, *Ind. Eng. Chem. Res.*, 2003, **42**, 1571–1587.

2 J. G. Chen, C. A. Menning and M. B. Zellner, *Surf. Sci. Rep.*, 2008, **63**, 201–254.

3 Z. Wei, J. Sun, Y. Li, A. K. Datye and Y. Wang, *Chem. Soc. Rev.*, 2012, **41**, 7994–8008.

4 X.-F. Yang, A. Wang, B. Qiao, J. Li, J. Liu and T. Zhang, *Acc. Chem. Res.*, 2013, **46**, 1740–1748.

5 B. Han, R. Lang, B. Qiao, A. Wang and T. Zhang, *Chin. J. Catal.*, 2017, **38**, 1498–1507.

6 G. Giannakakis, M. Flytzani-Stephanopoulos and E. C. H. Sykes, *Acc. Chem. Res.*, 2018, **52**, 237–247.

7 G. Kyriakou, M. B. Boucher, A. D. Jewell, E. A. Lewis, T. J. Lawton, A. E. Baber, H. L. Tierney, M. Flytzani-Stephanopoulos and E. C. H. Sykes, *Science*, 2012, **335**, 1209–1212.

8 M. B. Boucher, M. D. Marcinkowski, M. L. Liriano, C. J. Murphy, E. A. Lewis, A. D. Jewell, M. F. Mattera, G. Kyriakou, M. Flytzani-Stephanopoulos and E. C. H. Sykes, *ACS nano*, 2013, **7**, 6181–6187.

9 J. Liu, F. R. Lucci, M. Yang, S. Lee, M. D. Marcinkowski, A. J. Therrien, C. T. Williams, E. C. Sykes and M. Flytzani-Stephanopoulos, *J. Am. Chem. Soc.*, 2016, **138**, 6396–6399.

10 F. R. Lucci, M. T. Darby, M. F. Mattera, C. J. Ivimey, A. J. Therrien, A. Michaelides, M. Stamatakis and E. C. Sykes, *J. Phys. Chem. Lett.*, 2016, **7**, 480–485.

11 M. B. Boucher, B. Zugic, G. Cladaras, J. Kammert, M. D. Marcinkowski, T. J. Lawton, E. C. Sykes and M. Flytzani-Stephanopoulos, *Phys. Chem. Chem. Phys.*, 2013, **15**, 12187–12196.

12 F. R. Lucci, J. Liu, M. D. Marcinkowski, M. Yang, L. F. Allard, M. Flytzani-Stephanopoulos and E. C. Sykes, *Nat. Commun.*, 2015, **6**, 8550–8557.

13 J. Shan, F. R. Lucci, J. Liu, M. El-Soda, M. D. Marcinkowski, L. F. Allard, E. C. H. Sykes and M. Flytzani-Stephanopoulos, *Surf. Sci.*, 2016, **650**, 121–129.

14 R. Long, Y. Li, Y. Liu, S. Chen, X. Zheng, C. Gao, C. He, N. Chen, Z. Qi, L. Song*, et al.*, *J. Am. Chem. Soc.*, 2017, **139**, 4486–4492.

15 Y. Hou, S. Nagamatsu, K. Asakura, A. Fukuoka and H. Kobayashi, *Commun. Chem.*, 2018, **41**, 1–7.

16 K. Sato, A. Ito, H. Tomonaga, H. Kanematsu, Y. Wada, H. Asakura, S. Hosokawa, T. Tanaka, T. Toriyama, T. Yamamoto*, et al.*, *ChemPlusChem*, 2018, **84**, 1–11.

17 H. Miura, K. Endo, R. Ogawa and T. Shishido, *ACS Catal.*, 2017, **7**, 1543–1553.

18 H. Miura, Y. Tanaka, K. Nakahara, Y. Hachiya, K. Endo and T. Shishido, *Angew. Chem. Int. Ed. Engl.*, 2018, **57**, 6136–6140.

19 F. R. Lucci, T. J. Lawton, A. Pronschinske and E. C. H. Sykes, *J. Phys. Chem. C*, 2014, **118**, 3015–3022.

20 A. Karelovic and P. Ruiz, *ACS Catal.*, 2013, **3**, 2799–2812.

21 F. Studt, I. Sharafutdinov, F. Abild-Pedersen, C. F. Elkjaer, J. S. Hummelshoj, S. Dahl, I. Chorkendorff and J. K. Norskov, *Nat. Chem.*, 2014, **6**, 320–324.

22 D. Liu, Y. Li, M. Kottwitz, B. Yan, S. Yao, A. Gamalski, D. Grolimund, O. V. Safonova, M. Nachtegaal, J. G. Chen*, et al.*, *ACS Catal.*, 2018, **8**, 4120–4131.

23 J. L. Snider, V. Streibel, M. A. Hubert, T. S. Choksi, E. Valle, D. C. Upham, J. Schumann, M. S. Duyar, A. Gallo, F. Abild-Pedersen*, et al.*, *ACS Catal.*, 2019, **9**, 3399–3412.

24 W. Wang, S. Wang, X. Ma and J. Gong, *Chem. Soc. Rev.*, 2011, **40**, 3703–3727.

25 K. Jalama, *Catal. Rev.*, 2017, **59**, 95–164.

26 S. Kattel, P. Liu and J. G. Chen, *J. Am. Chem. Soc.*, 2017, **139**, 9739–9754.

27 F. Solymosi, I. Tombacz and M. Kocsis, *J. Catal.*, 1982, **75**, 78–93.

28 S. Takenaka, T. Shimizu and K. Otsuka, *Int. J. Hydrogen Energy*, 2004, **29**, 1065–1073.

29 G. Blyholder, *J. Phys. Chem.*, 1964, **68**, 2772–2777.

30 J. A. Rodriguez and D. W. Goodman, *J. Phys. Chem.*, 1991, **95**, 4196–4206.

31 J. R. Kitchin, J. K. Norskov, M. A. Barteau and J. G. Chen, *J. Chem. Phys.*, 2004, **120**, 10240–10246.

32 B. Ravel and M. Newville, *J. Synchrotron Radiat.*, 2005, **12**, 537–541.

33 D. E. Ramaker, B. L. Mojet, M. T. G. Oostenbrink, J. T. Miller and D. C. Koningsberger, *Phys. Chem. Chem. Phys.*, 1999, **1**, 2293–2302.

34 L. A. Grunes, *Phys. Rev. B*, 1983, **27**, 2111–2131.

35 B. Moraweck, A. Renouprez, E. Hlil and R. Baudoing-Savois, *J. Phys. Chem.*, 1993, **97**, 4288–4292.

36 P. Lu, T. Teranishi, K. Asakura, M. Miyake and N. Toshima, *J. Phys. Chem. B*, 1999, **103**, 9673–9682.

37 T. Yamamoto, *X-Ray Spectrom.*, 2008, **37**, 572–584.

38 J. Bertolini, B. Tardy, M. Abon, J. Billy, P. Delichere and J. Massardier, *Surf. Sci.*, 1983, **135**, 117–127.

39 R. Hoffmann, *Solids and Surfaces: A Chemist's View of Bonding in Extended Structures*, Wiley VCH, Weinhein, New York, 1988.

40 J. Bertolini and B. Tardy, *Surf. Sci.*, 1981, **102**, 131–150.

41 S. Fujita, M. Nakamura, T. Doi and N. Takezawa, *Appl. Catal. A*, 1993, **104**, 87–100.

42 D. Ferri, T. Bürgi and A. Baiker, *Phys. Chem. Chem. Phys.*, 2002, **4**, 2667–2672.

43 W. Sachtler, *J. Vac. Sci. Technol.*, 1972, **9**, 828–829.

44 W. Sachtler and R. Van Santen, *Adv. Catal*, 1977, **26**, 69–119.

45 J. Norsko, *Rep. Prog. Phys.*, 1990, **53**, 1253–1295.

46 T. K. Campbell and J. L. Falconer, *Appl. Catal.*, 1989, **50**, 189–197.

47 A. E. Aksoylu, A. N. Akin, Z. İ. Önsan and D. L. Trimm, *Appl. Catal. A*, 1996, **145**, 185–193.

48 X. Wang, H. Shi, J. H. Kwak and J. Szanyi, *ACS Catal.*, 2015, **5**, 6337–6349.

Chapter 2

Cooperative Alloy Catalyst Composed of the Pt Atoms Isolated by Ni Atoms and Their Neighboring Ni Atoms: In Situ and Transient FT-IR Studies on Selective Hydrogenation of CO_2 Toward CH_4 Evolution

Abstract

We elucidated the cooperative role of active sites composed of Pt atoms isolated by Ni atoms and their neighboring Ni atoms for the efficient and selective hydrogenation of CO_2 toward CH_4. The stepwise methanation dynamics were revealed by in situ observations and transient changes in the infrared spectra during the hydrogenation of CO_2. It was found that the hydrogenation of CO species attached to the isolated Pt atoms proceeded through a bridging CO species between isolated Pt atoms and their neighboring Ni atoms, leading to an excellent selectivity toward CH_4. Kinetic studies revealed that the high H_2 dissociation ability of the Pt species accelerated the hydrogenation of the carbon species over the surface of the Pt–Ni alloy, thereby avoiding the rate limitations of CH_4 formation that are common for Ni catalysts. The bifunctional role of the isolated Pt atoms therefore allowed the efficient formation of CH_4 while maintaining the excellent selectivity of the Ni catalyst toward CH_4, despite Pt catalysts tending to favor CO production

Introduction

A key requirement in the development of efficient and selective heterogeneous catalysts is the design of active sites matched to the desired application, such as selective hydrogenation/oxidation, reforming processes, fine chemical production, and other important reactions.[1-4] Because of such demands, supported alloy catalysts are often employed owing to their variety of electronic states and geometric surroundings imparted by the ligand effect and the ensemble effect, respectively. However, the means by which such alloy catalysts afford their specific activities are poorly understood because of uncertainties regarding their surface structures and electronic structures. Recently, Sykes and Flytzani-Stephanopoulos reported single atom alloy catalysts (SAACs), which are composed of atomically dispersed atoms on another element of a single-crystal substrate.[5-7] The isolated atoms on the surface that are surrounded by atoms of another element are therefore expected to exhibit specific geometric and electronic properties since the benefits of the alloying effect can be maximized. In the case of SAACs, these special activities can be highlighted by the following two points: (i) whether the isolation of active element atoms drives the selective reaction while suppressing the undesirable reaction over the bulk catalyst, or the neighboring of the isolated atoms and their surrounding atoms is essential to the cooperative roles, and (ii) whether the unique electronic structure contributes to the observed activities or is irrelevant. As such, techniques such as infrared spectroscopy and temperature-programmed desorption analysis, in addition to theoretical approaches, can be employed to reveal the role of each component element.[7]

Among the various transition metals, Ni is known to be active in the methanation of CO_2 ($CO_2 + 4H_2 \rightarrow CH_4 + 2H_2O$, $\Delta_r H^\circ_{298\ K} = -164.7$ kJ mol^{-1}), although the methanation mechanism remains a topic of debate over the simple Ni catalyst.[8-23] More specifically, the proposed mechanisms of methanation over the Ni catalyst can be classified into main three groups:[20, 22] (i) CO_2 is dissociated into CO and O species over the Ni surface, leading to subsequent hydrogenation to CH_4,[8-10] (ii) formate species are directly hydrogenated to CH_4,[17, 18] and (iii) formate species are hydrogenated to CH_4 *via* CO intermediates.[11-16, 21] In this context, Pan *et al.* reported that the formation of CH_4 proceeds *via* a bidentate formate species on the γ-Al_2O_3 support.[19] Fujita *et al.* found that CH_4 was produced from adsorbed carbon species *via* bridging CO species adsorbed on the Ni surface. In addition, Kai *et al.*

proposed that the hydrogenation of surface carbon species determines the overall rate of CH_4 formation.[12] In any case, the key to improving the Ni-based catalytic activity toward CH_4 formation at low temperatures is ensuring an efficient hydrogenation of the intermediate species by the H species dissociated over the metal sites. The addition of noble metal species, such as Rh, Pd, and Pt, into the Ni catalyst is therefore expected to promote the dissociation of H_2, although this also has the potential to lead to unfavorable reactions.[23-25]

In **Chapter 1**, we reported that the addition of tiny amounts of Pt species into a Ni/Al_2O_3 catalyst efficiently promoted the methanation of CO_2.[26] Interestingly, the excellent selectivity toward CH_4 over Ni/Al_2O_3 was maintained even after addition of the Pt species, despite Pt catalysts exhibiting activity for the reverse water-gas-shift reaction (rWGS) ($CO_2 + H_2 \rightarrow CO + H_2O$, $\Delta_r H^\circ_{298\ K} = 41.1$ kJ mol^{-1}). The dramatic decrease in the apparent activation energy for CH_4 formation upon the addition of Pt therefore indicates that compared to the simple Ni/Al_2O_3 catalyst, the Ni–Pt alloy possesses unique active sites for CH_4 production. Interestingly, X-ray absorption spectroscopy revealed that the added Pt species were surrounded by Ni atoms in a homogeneously mixed Ni–Pt alloy. These isolated Pt atoms were negatively charged because of electron transfer from the surrounding Ni atoms. In addition, Fourier transform infrared (FT-IR) spectroscopy using a CO probe indicated that the absorption of bridging CO species attached on Pt–Pt sites was negligible, thereby suggesting that the isolated Pt atoms were surrounded by Ni atoms on the surface, and not only in the bulk. These specific electronic and/or geometric characters of the isolated Pt atoms in the Ni–Pt alloy thereby lead to the efficient formation of CH_4 while also suppressing the formation of CO. More specifically, the negatively charged Pt atoms may possess unique CO adsorption and H_2 dissociation properties compared to Ni and Pt atoms alone. In addition, neighboring Pt–Ni sites may contribute to the formation of intermediates, thereby promoting CH_4 formation.

Thus, we herein report the use of infrared spectroscopy and kinetic studies to reveal the role of the isolated Pt atoms in Ni–Pt alloy catalysts to ensure a more efficient and selective hydrogenation of CO_2 toward CH_4. To the best of our knowledge, this is the first report into cooperative alloy sites composed of isolated Pt atoms and neighboring Ni atoms, and so would be expected to contribute to the development of novel catalysts for the selective hydrogenation of CO_2.

Experimental

The Ni–Pt alloy catalyst containing isolated Pt atoms, i.e., the *iso*-Pt alloy catalyst, was prepared on γ-Al_2O_3 powder (Catalysis Society of Japan, JRC-ALO-7) by an impregnation method using $Ni(NO_3)_2$ and $Pt(NH_3)_2(NO_2)_2$ as precursors at a Pt/(Ni+Pt) ratio of 5 mol%.[26] The amount of loaded Ni+Pt was fixed at 1.0 mmol g_{cat}^{-1}. For reference, Ni loaded on Al_2O_3 (Ni/Al_2O_3) and Pt loaded on Al_2O_3 (Pt/Al_2O_3) were prepared in the same manner. Following impregnation, the catalysts were calcined at 773 K for 5 h, and then reduced at 1173 K for 1 h under 5% H_2 prior to use.

The hydrogenation of CO_2 was carried out over the desired catalyst (100 mg) in a fixed-bed flow reactor at ambient pressure. K-type thermocouples in contact with the central part of the catalyst bed were used to measure and control the temperature. Following H_2 pretreatment, each catalyst was exposed to a 50 mL min^{-1} flow of a mixed gas containing 10% CO_2 and 40% H_2 with He as the balance and 0.5% N_2 as the internal standard, and the catalytic activity was measured at 25 K intervals between 473 and 573 K. Apparent reaction orders were determined from the results obtained under a mixture of H_2 and CO_2; the proportions of these gases were varied between 10 and 40% at a constant pressure of the other substrate gas at 523 K. The CO and CH_4 products were analyzed by gas chromatography (GC) using two GC-8A chromatographs (Shimadzu Corp., Japan) equipped with a thermal conductivity detector (TCD) and a flame ionization detector (FID), along with a 5Å Molecular Sieve column (Shimadzu Corp., Japan) and He as the carrier gas. All transfer lines were maintained at 373 K to avoid water condensation. Magnesium perchloride was placed downstream of the reaction bed as the desiccant.

The proportion of carbon atoms at the inlet of the reactor compared to that at the outlet of the reactor was >3%. The rates of formation of CH_4 or CO per metal atom (R_{CH4} or R_{CO}) in addition to the turnover frequencies for CH_4 or CO formation per surface-metal atom (TOF_{CH4} or TOF_{CO}) were calculated according to the following equations:

$$R_{CH4} \text{ or } R_{CO} \text{ (mol mol}_{metal}^{-1}\text{ s}^{-1}\text{)} = TF \times (F_{CH4} \text{ or } F_{CO}) / (N_{metal} \times 0.1)$$

$$TOF_{CH4} \text{ or } TOF_{CO} \text{ (mol mol}_{metal}^{-1}\text{ s}^{-1}\text{)} = TF \text{ (mol s}^{-1}\text{)} \times (F_{CH4} \text{ or } F_{CO}) / (N_{surf} \times 0.1)$$

where F_i is the molar ratio of component i contained in the inlet or outlet of the reactor, and TF, N_{metal}, and N_{surf} are the total flow of the reactor outlet expressed in mol s^{-1}, the expected contained amount of

metal per 1.0 g of catalyst, and the estimated molar amount of metal atoms located at the metal particle surface per 1.0 g of catalyst, respectively.

IR spectra were collected over Ni–Pt/Al_2O_3 using an infrared spectrometer equipped with an MCT detector (FTIR-4700, Jasco, Japan) through the integration of 128 scans with a resolution of 4 cm^{-1}. Prior to measurement, the samples were reduced at 1173 K under a 5% H_2 atmosphere in a fixed-bed reactor for 1 h. The reduced sample (25 mg) was pressed into a pellet with a diameter of 10 φ, and this pellet was placed into the sample holder cup of the flowing system of a quartz infrared spectroscopy cell for analysis in transmittance mode (Makuhari Rikagaku Garasu Inc., Japan). In the case of Pt/Al_2O_3, a 5 mg pellet was used to avoid saturation of the absorbance owing to its high adsorption of CO. A background IR spectrum was collected under a flow of He at 523 K following H_2 pretreatment at 773 K for 1 h. The total flow of gases was fixed at 50 mL min^{-1}. After recording the background spectra, 1% CO_2 was introduced over 60 min and then 4% H_2 was added to monitor the hydrogenation of the adsorbed CO_2-derived species. After 60 min flow under hydrogenation conditions (i.e., 1% CO_2 and 4% H_2 diluted with He), the flow gas composition was switched to 4% H_2/He or He. Observations of the hydrogenation of the adsorbed CO species were also conducted following H_2 pretreatment at 773 K, and the 1% CO/He flow was switched to a 4% H_2/He flow at 523 K. The gases at the outlet of the IR cell were analyzed by quadrupole mass spectrometry (BELMass, MicrotracBEL Corp., Japan). For desorption of the CO species, the CO/He flow was switched to He for 60 min.

H_2 pulse titration (H_2-pulse) experiments were performed to estimate the dispersion using a flow-type chemical adsorption measuring apparatus (BELCAT-B, BEL Japan Inc., Japan) equipped with a cryostat (BELCAT-B system with CATcryo, MicrotracBEL Corp., Japan). Following pre-reduction treatment with 5% H_2/Ar (30 mL min^{-1}) at 1173 K for 1 h, H_2 was injected through the reaction tube containing the catalyst (50 mg) under a flow of Ar as the carrier gas at 173 K. The amount of H_2 consumed was monitored using a TC detector contained within the BELCAT-B system. The dispersion of metal atoms was estimated using the adsorption amount of H_2 determined from pulse titration experiments at 173 K, assuming that the chemisorption stoichiometry is H:M (M = Ni or Pt) = 1.

Results and discussion

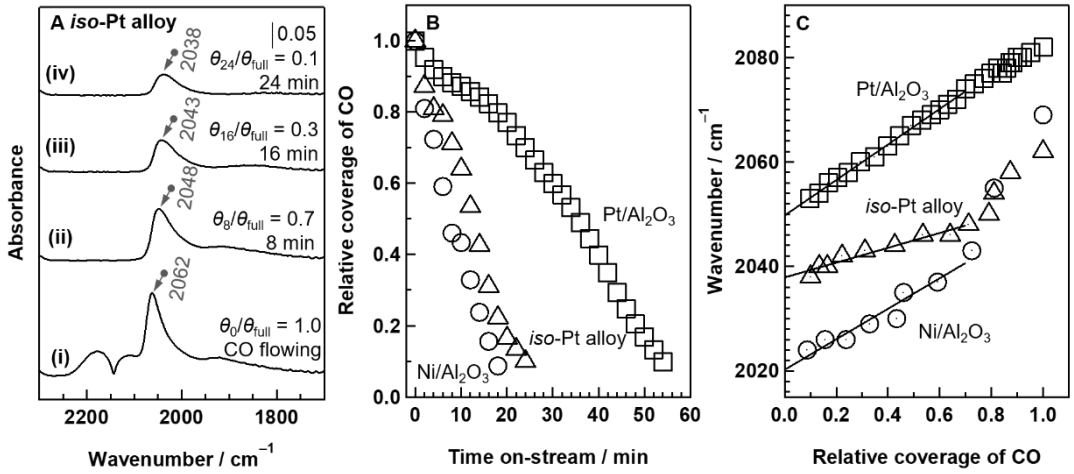

Figure 1. (A) FT-IR spectra recorded at 523 K over the *iso*-Pt alloy catalyst after switching of the gas flow from 5% CO/He to He over 60 min. From bottom to top: (i) 5% CO/He flow over the *iso*-Pt alloy catalyst, and after (ii) 8, (iii) 16, and (iv) 24 min from switching to He. **(B)** The time course of the relative coverage (θ/θ_{full}) of CO species over the *iso*-Pt alloy catalyst (triangles), Ni/Al_2O_3 (circles), and Pt/Al_2O_3 (squares). **(C)** The frequency shifts of the peaks derived from on-top CO species over the *iso*-Pt alloy catalyst (triangles), Ni/Al_2O_3 (circles), and Pt/Al_2O_3 (squares). The cross-section was calculated by integration of the absorption band of the adsorbed CO species between 1700 and 2100 cm^{-1}. The relative coverage (θ) is represented as the cross-section under a He flow divided by that under a CO/He flow.

Figure 1(A) shows the desorption properties of the adsorbed CO species at 523 K over the Ni–Pt alloy (5 mol% Pt) loaded on Al_2O_3 (i.e., the *iso*-Pt alloy catalyst), which indicates the affinity of the adsorbed CO species to the Ni–Pt alloy surface. Under a flow of CO/He (**Figure 1(A-i)**), the *iso*-Pt alloy catalyst gave a strong absorption band corresponding to the on-top CO species (i.e., the CO species adsorbed on a single Pt atom, 2062 cm^{-1}), in addition to weak bands corresponding to bridging CO species. After switching the gas flow to He, desorption took place, resulting a decrease in the peak intensity. The relative coverage (θ/θ_{full}) of CO was calculated against the peak area of the adsorbed CO species at 523 K under a flow of CO as the ratio of the cross-section between 1700 and 2100 cm^{-1} under He divided by that under CO/He. **Figure 1 (parts A-ii**, **A-iii**, and **A-iv)** shows the FT-IR spectra of the adsorbed CO species over the *iso*-Pt alloy catalyst at $\theta_{time}/\theta_{full}$ values of 0.7, 0.3, and 0.1, respectively. As observed, a time of 24 min was required to achieve a θ/θ_{full} value of 0.1 after switching to a He flow, and this was accompanied by a low frequency shift in the absorption band of the on-top

CO species due to weakened dipole-dipole interactions between the adsorbed CO species. **Figure 1(B)** compares the values of θ/θ_{full} as a function of time over the *iso*-Pt alloy catalyst with those over Ni loaded on Al_2O_3 (Ni/Al_2O_3) and Pt loaded on Al_2O_3 (Pt/Al_2O_3), for which the desorption properties are shown in **Figure 2**. As indicated, the θ/θ_{full} values of the $Ni–Pt/Al_2O_3$ catalysts decrease gradually over time. In the case of the Pt/Al_2O_3 catalyst, a θ/θ_{full} value of 0.1 was reached after 54 min, which was significantly slower than the corresponding value for the *iso*-Pt alloy catalyst. Furthermore, the isolated Pt alloy exhibited a higher CO desorption durability than Ni/Al_2O_3, the latter of which gave a θ/θ_{full} value of 0.1 after 18 min. The higher desorption durability of the CO species over the *iso*-Pt alloy catalyst compared to that over Ni/Al_2O_3 therefore suggested that the isolated Pt atoms act as adsorption sites for the CO intermediates during the hydrogenation of CO_2.

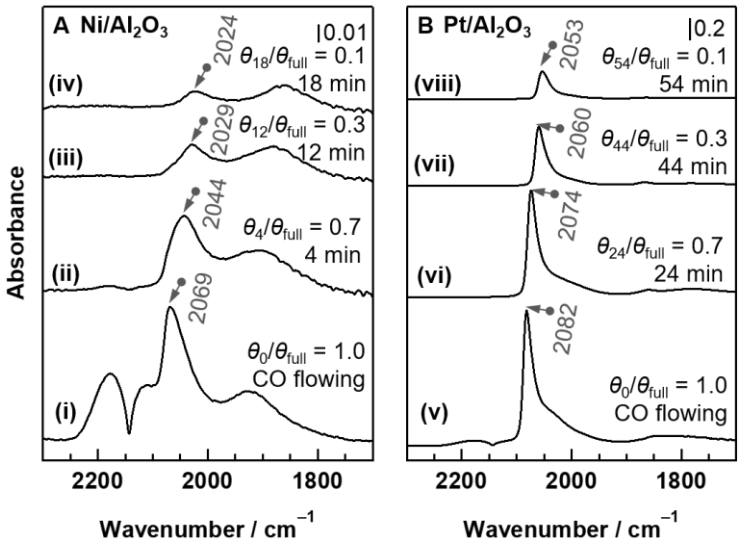

Figure 2. FT-IR spectra recorded at 523 K after switching the gas flow from 5% CO/He to He over 60 min. **(A)** From bottom to top: (i) under 5% CO/He flow over Ni/Al_2O_3, and after (ii) 4, (iii) 12, and (iv) 18 min from switching to He. **(B)** From bottom to top: (v) under 5% CO/He flow over Pt/Al_2O_3, and after (vi) 24, (vii) 44, and (viii) 54 min from switching to He.

Figure 1(C) shows the relationships between the θ/θ_{full} values of CO and the frequency of the C–O stretching mode of the on-top CO species over the $Ni–Pt/Al_2O_3$ catalysts. In the case of the *iso*-Pt alloy catalyst, the peak corresponding to the CO species at 2063 cm^{-1} shifted to 2038 cm^{-1} at a θ/θ_{full} value of 0.1, and below a θ/θ_{full} value of 0.7, the shift exhibited a linear trend, although it should be noted that the shift in the initial stages of the desorption process was not linear owing to the desorption of bridging CO species. In addition, Ni/Al_2O_3 exhibited a peak shift from 2069 to 2024 cm^{-1}, which

was in a similar trend to that observed for the *iso*-Pt alloy catalyst. In the case of the Pt/Al_2O_3 catalyst, the corresponding peak shifted from 2082 to 2054 cm^{-1} at a θ/θ_{full} value of 0.1. As such, the peak shift observed over the *iso*-Pt alloy catalyst due to a decrease in the dipole-dipole interaction was insignificant compared to that observed in the case of Pt/Al_2O_3, thereby suggesting that the adsorbed CO species were distant in their location, and so indicating that the Pt atoms in the Ni–Pt alloy were isolated by surrounding Ni atoms.

The net frequency of the C–O stretching mode of the CO species was then estimated by extrapolation to $\theta/\theta_{full} = 0$. In the case of the *iso*-Pt alloy catalyst, the net frequency was lower than that determined for the Pt/Al_2O_3 catalyst, likely owing to the large backdonation from the isolated Pt atoms. Indeed, these Pt atoms exhibited unique electronic properties, i.e., compared to bulk Pt atoms, they were negatively charged through electronic interactions with the surrounding Ni atoms.[26-28] This electronegativity and large backdonation therefore resulted in a high resistance to desorption for the CO species, and the efficient dissociative hydrogenation of weakened C–O bonds to give CH_4. However, the desorption rates of the CO species (see **Figure 1(B)**) followed the order *iso*-Pt alloy catalyst > Pt/Al_2O_3, and so it was considered that the strong adsorption energy of the CO species did not have any significant effect on the desorption rates of CO attached to the Pt atoms, since the employed reaction temperature was sufficient to promote the desorption of the adsorbed CO species.

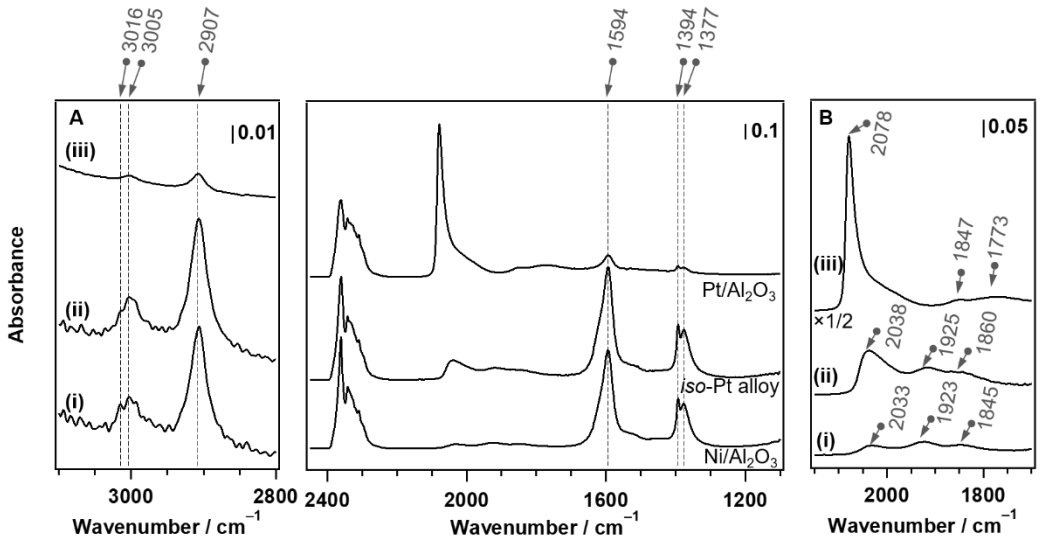

Figure 3. FT-IR spectra of the adsorbed species over the Ni–Pt alloy catalysts during the hydrogenation of CO_2 at 523 K. **(A)** Wide view, and **(B)** expanded view in the region corresponding to the adsorbed CO species over (i) Ni/Al_2O_3, (ii) the *iso*-Pt alloy catalyst, and (iii) Pt/Al_2O_3. The spectra were recorded under flows of 1% CO_2 and 4% H_2 in He for 60 min. The pellets of previously reduced samples (Ni/Al_2O_3 and *iso*-Pt catalyst: 25 mg, Pt/Al_2O_3: 5 mg) were reduced under a 5% flow of H_2 at 773 K for 1 h. The background spectrum was recorded at 523 K under a flow of He.

Figure 3(A) shows the in situ FT-IR spectra recorded during the hydrogenation of CO_2 after 60 min of flowing the reaction mixture gas (i.e., CO_2 and H_2) over Ni/Al_2O_3, the *iso*-Pt alloy catalyst, and Pt/Al_2O_3. The formation of CO species adsorbed on the metal surfaces (peaks at 1700–2100 cm^{-1}) and formate species adsorbed on the supports (peaks at 3005, 2907, 1594, 1394, and 1377 cm^{-1})[29-32] were observed among these catalysts. In addition, for only the *iso*-Pt alloy catalyst and Ni/Al_2O_3, the triple-degenerate stretching vibration mode of the C–H bond of CH_4 appeared at 3016 cm^{-1}. In the expanded spectral region corresponding to the adsorbed CO species (**Figure 3(B)**), Ni/Al_2O_3 shows signals assigned to the on-top CO species (2033 cm^{-1}) and the weakly- and strongly-bonded bridging CO species (1923 and 1845 cm^{-1}), respectively.[14] In addition, the spectra of the *iso*-Pt alloy catalyst also exhibits these three signals, although the peak corresponding to the on-top CO species was more intense than that observed for Ni/Al_2O_3. It should be noted here that the metallic surface areas of the *iso*-Pt alloy catalyst (46.9 μmol g_{cat}^{-1}) and Pt/Al_2O_3 (129.2 μmol g_{cat}^{-1}), estimated by H_2 chemisorption measurements at 173 K, were larger than that of Ni/Al_2O_3 (29.6 μmol g_{cat}^{-1}). Furthermore, the total absorption cross-section of CO species over Ni/Al_2O_3 during the hydrogenation process was significantly smaller than those over the other two catalysts, and so we considered that the absorption

bands could be mainly attributed to the CO species adsorbed on the Pt atoms, since little CO adsorption took place on the Ni surface under the hydrogenation conditions, or any CO species attached to the Ni atoms were rapidly hydrogenated to CH_4. Since the Pt sites were surrounded by Ni atoms, the on-top CO species attached to the Pt atoms (2038 cm^{-1}) and the bridging CO species between the isolated Pt atoms and their neighboring Ni atoms (1925 and 1860 cm^{-1}) were assigned. Moreover, Pt/Al_2O_3 exhibited strong absorption bands corresponding to the on-top CO species (2079 cm^{-1}) and negligible broad absorption bands corresponding to the bridging CO species (from 1773 to 1847 cm^{-1}), indicating that the CO species attached to the Pt atoms mainly exist as on-top CO species.[33-36] In contrast, the CO species present on the isolated Pt atoms adopt bridging structures with neighboring Ni atoms, and therefore play a significant role in the formation of CH_4 over the Pt atoms present in Ni–Pt alloy catalysts.

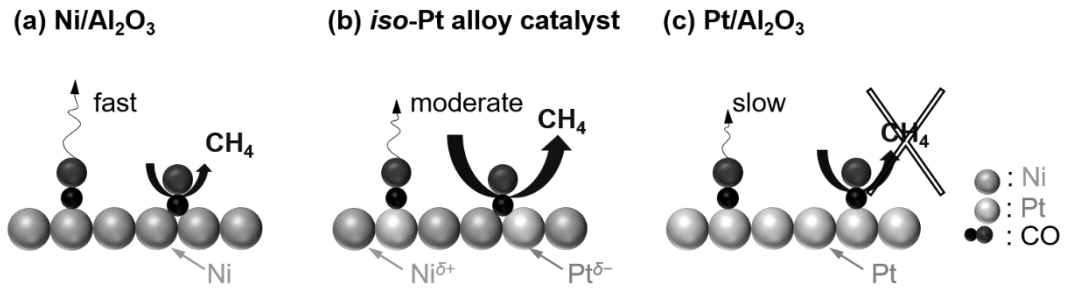

Figure 4. Illustration of the adsorbed species and the reactions taking place over (a) Ni/Al_2O_3, (b) the *iso*-Pt catalyst, and (c) Pt/Al_2O_3 during the hydrogenation of CO_2.

As discussed above and outlined in **Figure 4**, the formation of bridging CO species is essential to the selective evolution of CH_4. In the case of Pt/Al_2O_3, the adsorbed CO species mainly exist as on-top CO species, thereby resulting in a low catalytic activity toward the formation of CH_4 over the Pt catalyst. In contrast, like the neighboring Ni–Ni sites in Ni/Al_2O_3, the isolated Pt atoms and their neighboring Ni atoms in the *iso*-Pt alloy catalyst anchor the CO species in the form of a bridge, leading to a high selectivity toward CH_4. Here, upon the addition of Pt to Ni/Al_2O_3, the desorption rate of CO was suppressed, even at the reaction temperatures employed herein. As such, we could consider two possibilities leading to the high activity observed upon Pt addition, namely a relatively high CO

adsorption capacity by the *iso*-Pt alloy catalyst to enhance the hydrogenation of CO intermediates, or a relatively high H_2 dissociation ability over Pt compared to Ni.

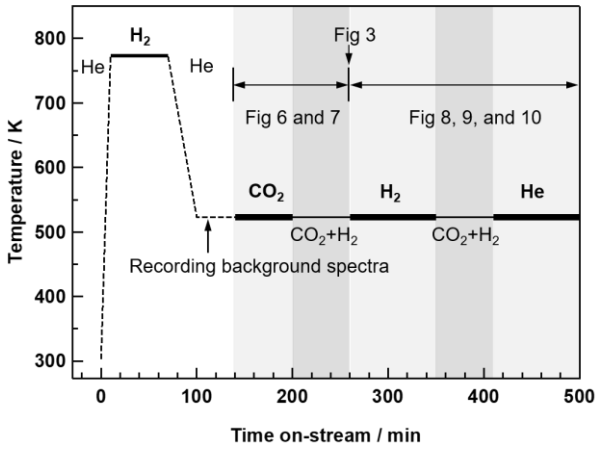

Figure 5. Representation of the reaction temperature and the gas composition employed during the experiment with time-on-stream. Reduction pretreatment was performed at 773 K under 5% H_2/He. A background spectrum was recorded at 523 K under a flow of He. The total gas flow was fixed at 50 mL min^{-1}.

To further discuss the efficient and selective formation of CH_4 using the *iso*-Pt alloy catalyst, the dynamics of the adsorbed species under the perturbative feeding of reaction substrates were observed continuously. Indeed, in situ transient FT-IR spectroscopy is a powerful tool for revealing the reaction pathway and the reaction dynamics of key intermediates for the hydrogenation of CO_2.[14, 37-40] According to the experimental scheme displayed in **Figure 5**, we observed the transient changes of the FT-IR spectra during hydrogenation of the adsorbed CO_2 species, in addition to the further hydrogenation or desorption dynamics of the intermediates during the methanation reaction. Thus, we focus on the effect of Pt addition on the H_2 dissociation process, where the dynamic behavior during the hydrogenation of the adsorbed CO_2 species over the *iso*-Pt alloy catalyst is compared to that over Ni/Al_2O_3 (**Figure 6**). Furthermore, we focus on the dynamics of the key intermediates for the selective evolution of CH_4, where the transient changes in the adsorbed species over the *iso*-Pt alloy catalyst and over Ni/Al_2O_3 are monitored after gas switching from the hydrogenation conditions (CO_2+H_2) to H_2/He or He (**Figure 8** and **9**). We also note that previous studies have suggested that the adsorbed CO species play the role of a poorly reactive spectator rather than as a main intermediate[37] or inhibitor to H_2 dissociation[39, 40] during the hydrogenation of CO_2. Thus, the hydrogenation of the adsorbed CO

species to give CH_4 is also observed upon gas switching from CO/He to H_2/He and the gas products are monitored by quadrupole mass spectrometry (**Figure 11**).

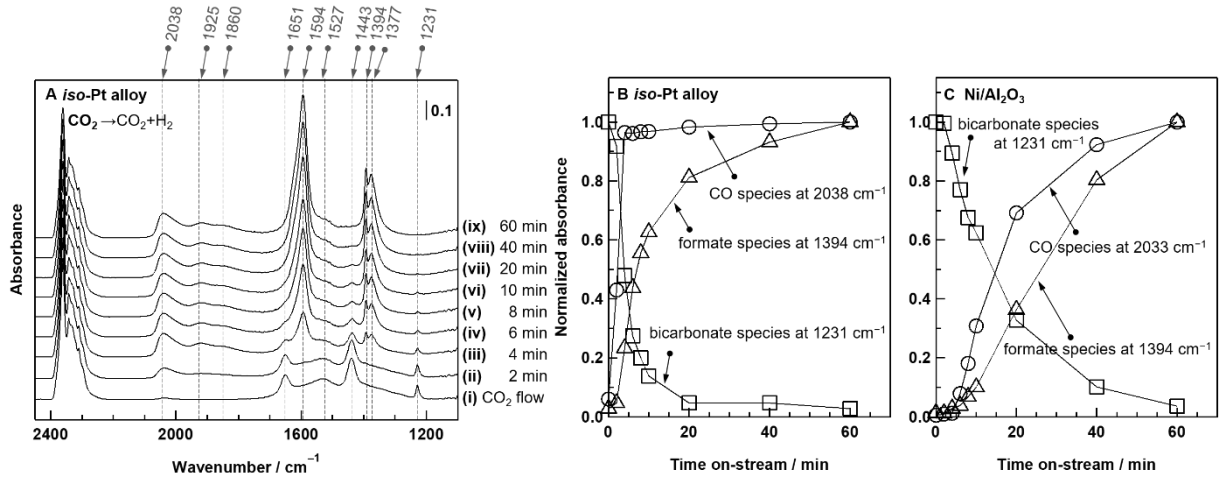

Figure 6. (A) FT-IR spectra recorded during 60 min on-stream at 523 K over the *iso*-Pt alloy catalyst after switching the gas flow from 1% CO_2/He to the hydrogenation conditions (1% CO_2 and 4% H_2 in He). From bottom to top: (i) CO_2 flow, and after the introduction of H_2 at (ii) 2, (iii) 4, (iv) 6, (v) 8, (vi) 10, (vii) 20, (viii) 40, and (ix) 60 min. Variation in absorbance with time-on-stream **(B)** for the *iso*-Pt alloy catalyst, and **(C)** for Ni/Al_2O_3 after switching of the gas flow, normalized by their maximum values. Circles; on-top CO species (*iso*-Pt alloy catalyst; at 2038 cm^{-1}, Ni/Al_2O_3; at 2033 cm^{-1}), squares; formate species at 1394 cm^{-1}, triangles; bicarbonate species at 1231 cm^{-1}.

The dynamic behavior during the hydrogenation of the adsorbed CO_2 species was then monitored to reveal whether the addition of Pt species effectively supplied the dissociated H species to the CO_2 species adsorbed on the support. Thus, **Figure 6(A-i)** shows the various FT-IR spectra recorded over the *iso*-Pt alloy catalyst under a flow of 1% CO_2/He over 60 min. More specifically, bicarbonate (1651, 1443, and 1231 cm^{-1}) and carbonate (1527 cm^{-1}) species, which reacted with the hydroxyl groups present on the Al_2O_3 support, were observed.[29-32] Upon gas switching from CO_2/He to the reaction mixture gas of 1% CO_2 and 4% H_2, the amount of adsorbed CO_2 species decreased, and this was accompanied by the formation of their hydrogenated products. As shown in **Figure 6(A-iii)**), 4 min after H_2 injection, peaks corresponding to the symmetric and asymmetric stretching vibration modes of the bidentate (1594 and 1394 cm^{-1}, respectively) and monodentate (1377 cm^{-1}) formate species appeared,[19, 41, 42] and adsorption bands corresponding to the CO species adsorbed on the metal atoms (2038 1925, and 1860 cm^{-1}) were observed. As the reaction progressed, the quantities of both

formate and CO species increased. In addition, **Figure 6(B)** shows the variation in the representative absorption peak intensities for the on-top CO species, the formate species, and the bicarbonate species over time, where the absorption corresponding to the bicarbonate species at 1231 cm^{-1} rapidly decreased, essentially disappearing ~20 min after H_2 injection. Moreover, signals corresponding to the on-top CO species (2038 cm^{-1}) and the formate species appeared after 2 min, and the CO species reached saturation after 20 min.

In contrast, in the case of Ni/Al_2O_3 (**Figure 6(C)**, for the raw spectra see **Figure 7**), a slow decrease in the adsorption peak attributed to the bicarbonate species was observed, while that corresponding to the on-top CO species at 2033 cm^{-1} gradually increased upon formation of the formate species. These results indicate that hydrogenation of the bicarbonate species over Ni/Al_2O_3 to give the formate species proceeded more slowly than over the *iso*-Pt alloy catalyst, and it also appears that the formate species decomposed into CO and also hydroxyl groups on the Al_2O_3 support These transient changes in the spectra support a previously reported mechanism suggesting that CH_4 is produced *via* bidentate formate species over a γ-Al_2O_3 support.[19]

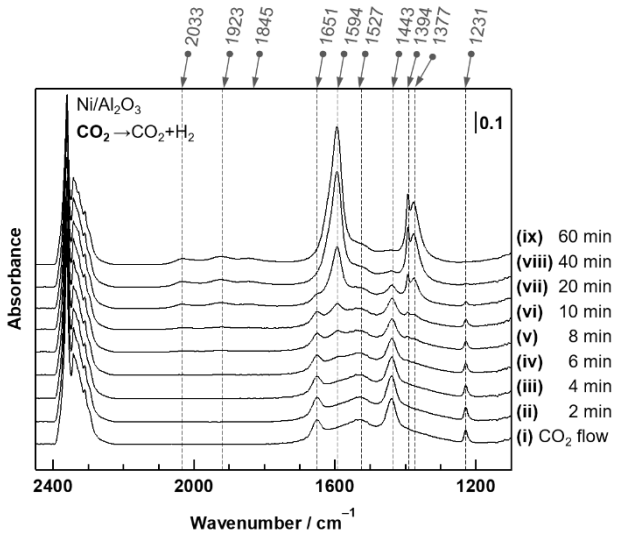

Figure 7. FT-IR spectra recorded during 60 min on-stream at 523 K over the Ni/Al_2O_3 catalyst after switching the gas flow from 1% CO_2/He to the hydrogenation conditions (i.e., 1% CO_2 and 4% H_2 in He). From bottom to top: (i) CO_2 flow, and after the introduction of H_2 at (ii) 2, (iii) 4, (iv) 6, (v) 8, (vi) 10, (vii) 20, (viii) 40, and (ix) 60 min.

Our comparison between the hydrogenation dynamics of the adsorbed CO_2 species over the *iso*-Pt alloy catalyst and Ni/Al_2O_3 revealed that the Pt species effectively supplied the dissociated H

species to the adsorbed CO_2 species on the support, although we should also consider the high dispersion of the alloy particles. Indeed, the addition of Pt atoms appeared to clearly accelerate hydrogenation of the adsorbed CO_2 species due to their high H_2 dissociation ability, although this is not necessarily related to the rate of the overall reaction.

Hydrogenation dynamics of the adsorbed CO species for the selective formation of CH_4: the hydrogenation and/or desorption behavior of the intermediates over the active metal sites, and in particular those of the CO species, were monitored to elucidate additional details relating to the dynamics of the key intermediates over isolated Pt atoms in the Ni–Pt alloy for the selective evolution of CH_4. The transient changes of the adsorbed species during the hydrogenation of CO_2 were monitored as a function of time-on-stream. As indicated in the scheme presented in **Figure 5**, the gas flow composition was switched from hydrogenation conditions (CO_2+H_2/He) to H_2/He or He. We therefore considered that the active sites were maintained through perturbation of the gas feed, since the FT-IR spectra obtained during the hydrogenation of CO_2 were repeatable following the perturbation.

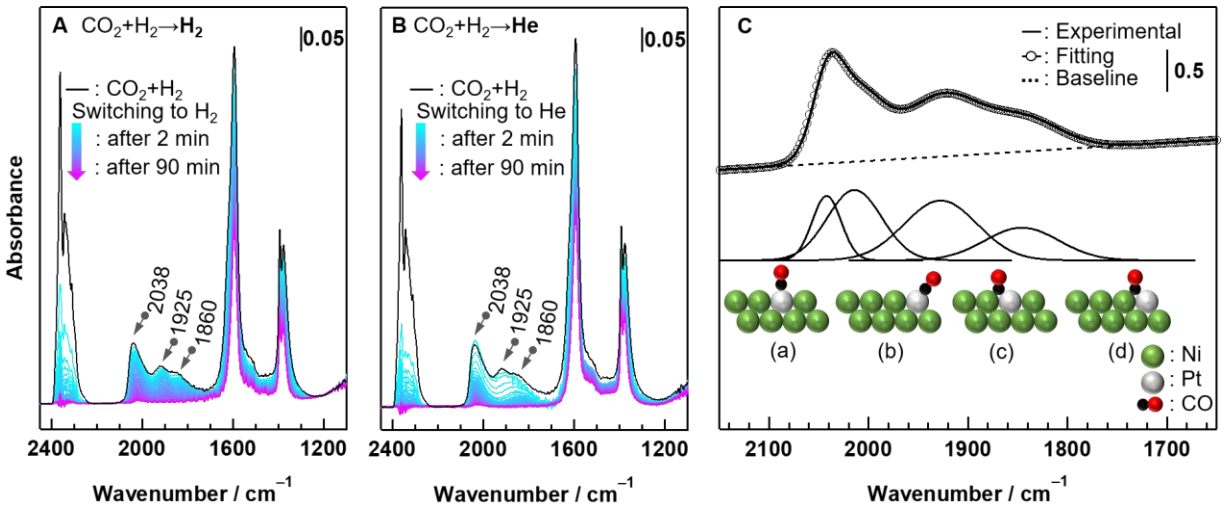

Figure 8. (A) and **(B)** Transient changes in the FT-IR spectra after switching the gas flow from 1% CO_2 and 4% H_2 in He to **(A)** 1% H_2/He and **(B)** He for 90 min over the *iso*-Pt alloy catalyst at 523 K. For clarity, an offset at 2200 cm^{-1} was applied to the spectra. **(C)** Fitting of the FT-IR spectrum of the adsorbed CO species over the *iso*-Pt alloy catalyst during the hydrogenation of CO_2 at 523 K. The solid line, circles, and dashed line correspond to the experimental spectrum, the fitting spectrum, and the baseline, respectively. The four Gaussian curves are attributed to (a) CO_{OHF} species, (b) CO_{OLF} species, (c) CO_{BHF} species, and (d) CO_{BLF} species from high to low frequencies.

Figures 8(A) and **6(B)** display the changes in the FT-IR spectra of the adsorbed CO species over the *iso*-Pt alloy catalyst after switching from hydrogenation conditions to H_2/He and He, respectively. The changes observed under the H_2/He flow were related to the methanation and desorption dynamics of the adsorbed CO species, while those observed under the He flow give information relating only to the desorption dynamics. As expected, the absorption attributed to CO_2 molecules in the gas phase (i.e., from 2200 to 2400 cm^{-1}) gradually decreased after stopping the feed of CO_2. Under a flow of H_2 (**Figure 8(A)**), the three signals, corresponding to the adsorbed CO species, and the formate species gradually decreased in intensity over time. In contrast, under a flow of He (**Figure 8(B)**), the peak at 2038 cm^{-1} initially increased in intensity 2 min after switching the gas flow to He, but then decreased in intensity once again. In addition, interestingly, the peak at 1925 cm^{-1} immediately decreased in intensity compared to the other signals observed, unlike in the case of the H_2/He flow.

We then divided the absorption bands derived from the adsorbed CO species over the *iso*-Pt catalyst under hydrogenation at 523 K into four Gaussian peaks by peak fitting (**Figure 8(C)**). Indeed, the resulting spectrum corelated well with the simulated adsorption bands obtained by the combination of four Gaussian curves. Since the Pt sites were surrounded by Ni atoms, the CO species were assigned as on-top CO species and bridging CO species, as described previously, where the differences in the frequencies between the high and low frequency CO species were attributed to their site configurations. More specifically, during the hydrogenation of CO_2, Ni/Al_2O_3 presented two types of bridging CO species (i.e., at 1923 and 1845 cm^{-1}), along with a weak signal corresponding to CO species at 2023 cm^{-1} (**Figure 3-i**). Fujita *et al.* also reported the formation of two bridging CO species, i.e., at 1910 and 1830 cm^{-1}, where the higher and lower frequencies signals were assigned to weakly- and strongly-adsorbed bridging CO species, respectively. In contrast, uniform bridging CO species have also been observed on the clean surface of Ni(111) single crystals,[43-47] where these species would likely be attached to the geometrically nonuniform surface of Ni, such as the terrace and corner sites. In this case, the Ni atoms at the corner sites would be expected to act as the adsorption sites for CO species, owing to their stronger adsorption energies compared to those of the sufficiently-coordinated Ni atoms located at terrace sites. These corner CO species are therefore expected to exhibit a low frequency C−O stretching mode due to the strong backdonation.[27, 48] Similarly, the isolated Pt atoms located at corner

sites would lower the frequency of the C–O stretching mode compared to those located at terrace sites. Our results therefore indicate that the different frequencies observed for the CO_{HF} (high frequency CO) and CO_{LF} (low frequency CO) species over the *iso*-Pt alloy catalyst could be attributed to the configuration of the isolated Pt atoms in the Ni–Pt alloy particles, such as the terrace and corner sites, as depicted in the inset of **Figure 8(C)**.

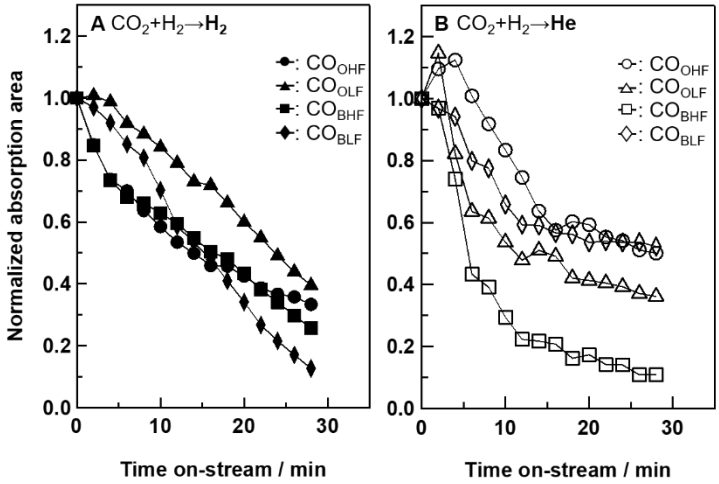

Figure 9. (A) Variation in the normalized absorption areas of the adsorbed CO species on the *iso*-Pt alloy catalyst with time at 523 K after switching the gas to H_2/He for 90 min. Closed circles, CO_{OHF} species; triangles, CO_{OLF} species; squares, CO_{BHF} species; and rhombus, CO_{BLF} species. **(B)** Variation in the normalized absorption areas of the adsorbed CO species on the *iso*-Pt alloy catalyst at 523 K after switching the gas to He for 90 min. Open circles, CO_{OHF} species; triangles, CO_{OLF} species; squares, CO_{BHF} species; and rhombus, CO_{BLF} species.

Figures 9(A) and **9(B)** display the variations in the normalized absorption areas of the transient FT-IR spectra with time after switching the flow gas as outlined in **Figures 8(A)** and **8(B)**, respectively. More specifically, after switching to H_2/He (**Figure 9(A)**), the four peaks gradually decreased in intensity, albeit at slightly different rates. These decreases were attributed to the desorption and hydrogenation of the adsorbed CO species on the *iso*-Pt alloy. In contrast, after switching to a flow of He (**Figure 9(B)**), the peak areas of the on-top CO species at higher frequency (CO_{OHF} species) and at lower frequency (CO_{OLF} species) increased prior to decreasing once again, while the peak area corresponding to the bridged CO species at higher frequency (CO_{BHF} species) rapidly decreased compared to the case of switching to a flow of H_2. These results therefore provide details regarding the desorption dynamics of the bridging CO species, i.e., upon switching to a flow of He gas, hydrogenation of the bridging CO species is slow, and the adsorbed CO species begin to desorb.

We expect that the bridging CO species desorb through on-top CO species owing to the lower adsorption energy for the latter, while the gaseous CO species are maintained by decomposition of the formate species present on the support. Therefore, the number of on-top CO species increased temporally. In contrast, we note that in the presence of H_2, the on-top CO species are hydrogenated through the bridging CO species.

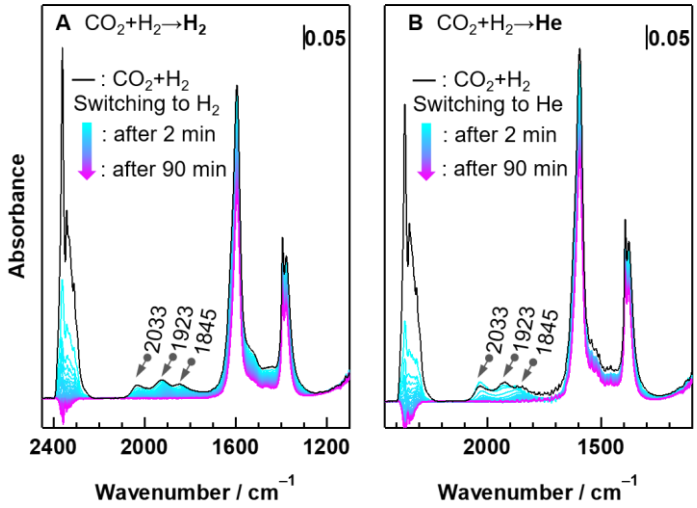

Figure 10. Transient changes in the FT-IR spectra after switching the gas flow from 1% CO_2 and 4% H_2 in He to **(A)** 4% H_2/He, and **(B)** He for 90 min over Ni/Al_2O_3 at 523 K. The pellet of the previously reduced sample was reduced under a 5% H_2 flow at 773 K for 1 h. A background spectrum was taken at 523 K under a flow of He. The total gas flow was fixed at 50 mL min^{-1}.

In the case of Ni/Al_2O_3 (**Figure 10(A)**), the CO species exhibited a similar gradual reduction to that over the *iso*-Pt alloy catalyst after switching to a flow of H_2. Upon desorption under a He flow (**Figure 10(B)**), the peak at 1923 cm^{-1} rapidly decreased in intensity, while a new peak appeared at 2033 cm^{-1} prior to reducing in intensity. Fujita *et al.* reported a similar decreasing trend in the adsorbed CO species over an Ni catalyst to those observed over our *iso*-Pt alloy catalyst and Ni/Al_2O_3, thereby suggesting that CH_4 formation proceeded *via* the bridging CO species.[14]

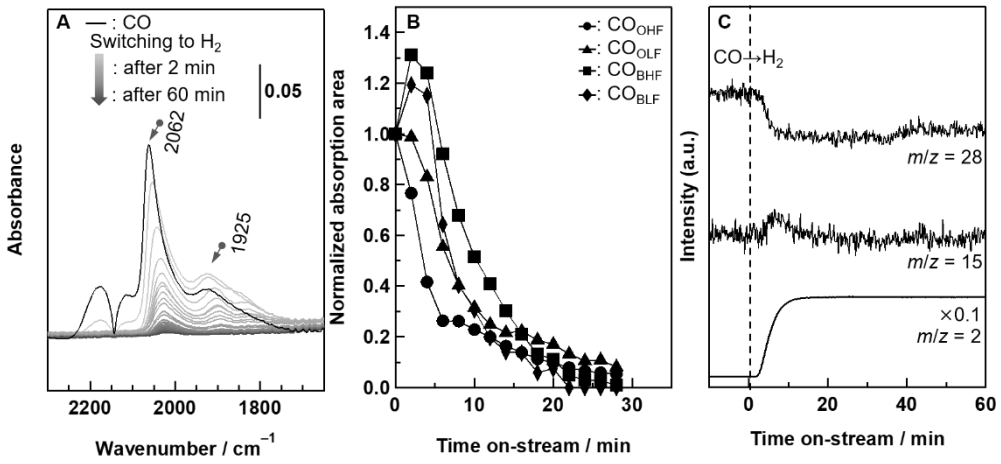

Figure 11. (A) Transient changes in the FT-IR spectra after switching the gas flow from 1% CO/He to 1% H_2/He for 60 min over the *iso*-Pt alloy catalyst at 523 K. **(B)** Variation in the normalized absorption area of the adsorbed CO species on the *iso*-Pt alloy catalyst at 523 K over time. Closed circles, CO_{OHF} species; triangles, CO_{OLF} species; squares, CO_{BHF} species; rhombus, CO_{BLF} species. **(C)** The corresponding MS signals (m/z = 2, 15, and 28) collected at the reactor outlet after switching the gas flow from 1% CO/He to 4% H_2/He.

To confirm the formation of CH_4 *via* the hydrogenation of the adsorbed CO species, the hydrogenation dynamics of the adsorbed CO species were monitored. Thus, **Figure 11(A)** shows the FT-IR spectra for the species obtained over the *iso*-Pt alloy catalyst after switching the gas flow from CO/He to H_2/He. Under a flow of CO/He (black line), the absorption bands of the CO species in the gas phase were observed between 2150 and 2250 cm^{-1}. After switching the gas flow, the CO absorption bands immediately disappeared, indicating that these spectra could be employed to monitor the hydrogenation/desorption dynamics of the adsorbed species. In addition, the absorption band corresponding to the on-top CO species, located at 2062 cm^{-1}, rapidly decreased in intensity, while that of the bridging CO species temporally increased after 2 min of H_2 injection, prior to dropping once again. Peak fitting was then conducted using four Gaussian peaks, and the variation in peak area with time was plotted, as shown in **Figure 11(B)**. It was found that after 2 min of H_2 flow, the peaks corresponding to both bridging CO species increased prior to dropping, thereby indicating that the on-top CO species transformed to bridging CO species in the presence of H_2 and then were either desorbed or hydrogenated. **Figure 11(C)** shows the mass signals recorded over time at the downstream point following switching of the gas flow from CO/He to H_2/He. In addition to an increase in the m/z =2 signal of H_2 and a decrease in the m/z =28 signal of CO, a signal at m/z =15 signal appeared, which

was attributed to a fragment of CH_4. As shown in **Figure 12**, a peak corresponding to the stretching vibration mode of the C–H bond of CH_4 appeared at 3016 cm^{-1} upon the introduction of H_2, although this slowly disappeared over 20 min. These results therefore confirm that CH_4 formation took place *via* the adsorbed CO species over the *iso*-Pt alloy catalyst.

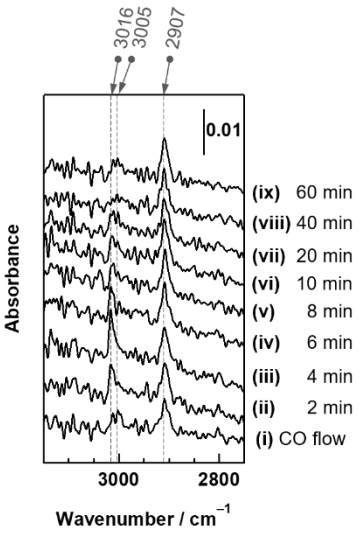

Figure 12. Transient changes in the FT-IR spectra after switching the gas flow from 1% CO/He to **(A)** 4% H_2/He, and **(B)** He for 60 min over the *iso*-Pt alloy catalyst at 523 K. The pellet of the previously reduced sample was reduced under a flow of 5% H_2 at 773 K for 1 h. A background spectrum was taken at 523 K under a flow of He. The total gas flow was fixed at 50 mL min^{-1}.

Overall, the in situ transient FT-IR results revealed the key dynamics of CO intermediates for the selective evolution of CH_4, where the on-top CO species attached to isolated Pt atoms were hydrogenated *via* bridging CO species between isolated Pt atoms and their neighboring Ni atoms in the presence of H_2, leading to an excellent selectivity toward CH_4. Upon desorption, the bridging CO species desorbed through on-top CO species attached to the isolated Pt atoms.

In addition, the methanation mechanism of CO_2 over the *iso*-Pt alloy catalyst and over Ni/Al_2O_3 at 523 K was elucidated. In the case of the *iso*-Pt alloy catalyst, it was found that the bicarbonate and carbonate species were hydrogenated to yield formate species by dissociated H species over the metal sites, thereby leading to decomposition into CO and hydroxyl groups (from **Figure 6**). The CO species adsorbed onto individual metal surfaces prior to transforming into bridging CO species (from **Figure 8** and **9**), which in turn led to hydrogenation by dissociated H species (from **Figure 11**).

This mechanism is similar to that taking place over Ni/Al_2O_3, and so is consistent with the method proposed by Fujita *et al* for a Ni catalyst.[14]

Interestingly, the isolated Pt atoms acted as adsorption sites for the on-top CO species, while the presence of neighboring Ni atoms led to the formation of bridging CO species, similar to those observed at the Ni–Ni sites of Ni/Al_2O_3. Moreover, the addition of Pt atoms appeared to accelerate the hydrogenation of the adsorbed CO_2 species owing to their high H_2 dissociation ability, although this is not necessarily related to the rate of the overall reaction. To reveal the influence of the isolated Pt atoms on efficient CH_4 formation, kinetic studies were performed as follows.

From the in situ transient FT-IR studies described above, the following elementary steps were proposed to take place during the methanation of CO_2 over both the *iso*-Pt alloy catalyst and Ni/Al_2O_3, and these are consistent with the proposed mechanism of hydrogenation of the adsorbed CO species *via* formate intermediates:[11-16, 21]

$$S-OH + CO_2 \underset{k_{-1}}{\overset{k_1}{\rightleftharpoons}} S-OCOOH \quad (1)$$

$$M + 1/2H_2 \underset{k_{-2}}{\overset{k_2}{\rightleftharpoons}} M-H \quad (2)$$

$$S-OCOOH + 2M-H \underset{k_{-3}}{\overset{k_3}{\rightleftharpoons}} S-OCHO + 2M + H_2O \quad (3)$$

$$S-OCHO \underset{k_{-4}}{\overset{k_4}{\rightleftharpoons}} S-OH + CO \quad (4)$$

$$M + CO \underset{k_{-5}}{\overset{k_5}{\rightleftharpoons}} M-CO \quad (5)$$

$$M-CO + M \underset{k_{-6}}{\overset{k_6}{\rightleftharpoons}} M-C + M-O \quad (6)$$

$$M-C + M-H \underset{k_{-7}}{\overset{k_7}{\rightleftharpoons}} M-CH + M \quad (7)$$

$$M-CH + 3M-H \underset{k_{-8}}{\overset{k_8}{\rightleftharpoons}} M-CH_4 + 3M \quad (8)$$

$$M-O+2M-H \underset{k_{-9}}{\overset{k_9}{\rightleftarrows}} M-H_2O+2M \quad (9)$$

$$M-CH_4 \underset{k_{-10}}{\overset{k_{10}}{\rightleftarrows}} M+CH_4 \quad (10)$$

$$M-H_2O \underset{k_{-11}}{\overset{k_{11}}{\rightleftarrows}} M+H_2O \quad (11)$$

where S and M are the adsorption sites over the Al_2O_3 support and the metal atoms, respectively. Thus, initially, CO_2 reacts with the hydroxyl group of the Al_2O_3 support, leading to the formation of a bicarbonate species.[19] Formate species are then formed *via* hydrogenation of the bicarbonate species by dissociated H species provided by the alloy surface, and subsequently, the formate species decompose into CO and hydroxyl groups. Following dissociation of the C–O bonds of these adsorbed CO species, the surface C and O species were hydrogenated to give CH_4 and H_2O, respectively. Kai *et al* reported that the hydrogenation of surface carbon species (eq. (7)) is the rate-determining step of methanation over a Ni catalyst.[12] The rate of CH_4 formation was then expressed in eq. (12) based on the partial pressures of CO_2 (P_{CO2}) and H_2 (P_{H2}), and assuming the rate-limiting step approximation and insignificant partial pressures of the CH_4 and H_2O products.

$$r = \frac{N_{total}\left(k_7 K_1 K_2{}^8 K_3 K_4 K_5 K_6 K_8 K_{10}\right)^{1/5} \dfrac{P_{CO_2}{}^{1/5} P_{H_2}{}^{4/5}}{P_{H_2O}{}^{2/5}}}{1 + K_2 P_{H_2}{}^{1/2} + K_1 K_2{}^2 K_3 K_4 K_5 \dfrac{P_{CO_2} P_{H_2}}{P_{H_2O}} + K_1 K_2{}^4 K_3 K_4 K_5 K_6 K_8 K_{10} \dfrac{P_{CO_2} P_{H_2}{}^2}{P_{H_2O}{}^2}} \quad (12)$$

where N_{total}, k_7, and K_n are the total number of adsorption sites on the metal particles, the rate constant of the forward reaction of eq. (7), and the equilibrium constant for each elementary step, respectively.

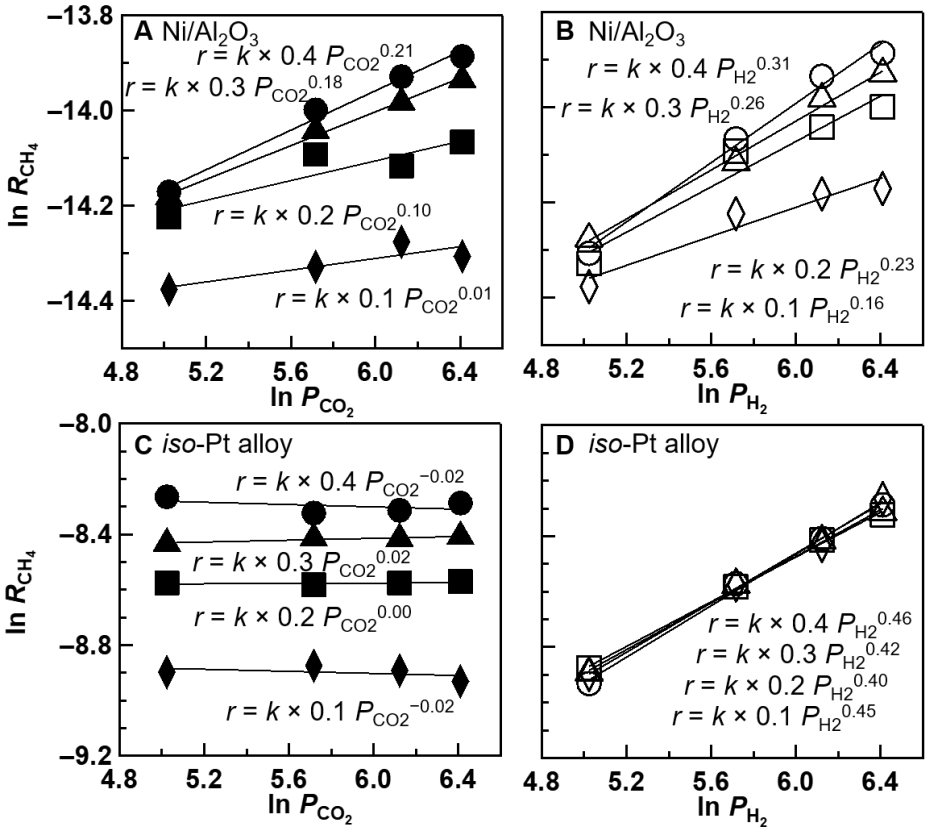

Figure 13. Rates of CH_4 formation under a series of CO_2 and H_2 partial pressures. **(A)** Over Ni/Al_2O_3 with constant P_{H2} (closed circles, 40%; triangles, 30%; squares, 20%; rhombus, 10%). **(B)** Over Ni/Al_2O_3 with constant P_{CO2} (open circles, 40%; triangles, 30%; squares, 20%; rhombus, 10%). **(C)** Over the *iso*-Pt alloy catalyst with constant P_{H2} (closed circles, 40%; triangles, 30%; squares, 20%; rhombus, 10%). **(D)** Over the *iso*-Pt alloy catalyst with constant P_{CO2} (open circles, 40%; triangles, 30%; squares, 20%; rhombus, 10%).

The above eq. (12) was consistent with the results of kinetic studies using a series of P_{CO2} and P_{H2} (**Figures 13(A)** and **13(B)**), where the rate of CH_4 formation over Ni/Al_2O_3 under a series of P_{CO2} values with constant P_{H2} values and that under a series of P_{H2} values with constant P_{CO2} values were examined. The rate equation was expressed based on a power law as $r_{Ni} = k_{Ni}P_{CO2}^{(0.01–0.21)}P_{H2}^{(0.16–0.31)}$. The apparent reaction orders in P_{CO2} varied with the partial pressure of the counter substrate of H_2, and vice versa, being matched with eq. (11). We therefore considered that the rate of methanation over Ni/Al_2O_3 at this temperature was determined by the hydrogenation of the carbon species. In this case, the addition of the Pt species resulted in the acceleration of this step, thereby improving the catalytic activity for the formation of CH_4 and altering the rate-determining step.

Figures 13(C) and **13(D)** show that the rate of CH_4 formation over the *iso*-Pt alloy catalyst exhibited a different trend from that observed over Ni/Al_2O_3 upon varying the gas partial pressures. More specifically, the rate of CH_4 formation showed little dependence on P_{CO2}. In contrast, the rate of CH_4 formation increased at a high P_{H2} with constant P_{CO2}. In addition, the apparent reaction orders at the various substrate partial pressures were maintained under a variety of partial pressures of the counter substrate, thereby giving $r_{isoPt} = k_{isoPt}P_{CO2}^{(-0.02–0.02)}P_{H2}^{(0.40–0.46)}$. These results therefore correspond with the following rate equation, assuming that the rate-determining step is H_2 dissociation:

$$r = \frac{N_{total} k_2 P_{H_2}^{1/2}}{1 + \frac{K_1 K_3 K_4 K_5}{K_a^{1/4}} \frac{P_{CO_2}^{3/4} P_{CH_4}^{1/4}}{P_{H_2O}^{1/2}} + \frac{K_a^{1/2}}{K_7 K_8 K_{10}} \frac{P_{CO_2}^{1/2} P_{CH_4}^{1/2}}{P_{H_2O}} + \frac{K_a^{3/8}}{K_8 K_{10}} \frac{P_{CO_2}^{3/8} P_{CH_4}^{5/8}}{P_{H_2O}^{3/4}} + \frac{K_a^{1/4}}{K_9 K_{11}} \frac{P_{CO_2}^{1/4} P_{H_2O}^{1/2}}{P_{CH_4}^{1/4}}} \quad (13)$$

where k_2 and K_n are the rate constants of the forward reaction of eq. (2) and the equilibrium constant for each elementary step, respectively. The product of the equilibrium constants for the elementary steps is expressed as $K\alpha$. The rate of CH_4 formation over the *iso*-Pt alloy catalyst correlated well with eq. (13), thereby suggesting that H_2 dissociation was the rate-determining step.

We then wished to examine why the rate of CH_4 formation was limited by H_2 dissociation despite the addition of Pt addressing the issue of limited H_2 dissociation over the Ni catalyst. As mentioned previously, the addition of isolated Pt atoms should promote the hydrogenation of surface carbon species due to the increased dissociation of H_2; however, this resulted in the rate-determining step becoming H_2 dissociation due to competition between the bifunctional role of the isolated Pt atoms, which acted as both H_2 dissociation sites (eq. (14)) and CO adsorption sites (eq. (15)):

$$2Pt + H_2 \rightleftarrows 2Pt - H \quad (14)$$

$$Pt + CO \rightleftarrows Pt - CO \quad (15)$$

During the hydrogenation reaction, the isolated Pt sites are mainly covered by CO species, resulting in insufficient H_2 dissociation sites, and thereby leading to eq. (14) (i.e. eq. (2)) becoming the rate-determining step. For the Pd/Al_2O_3 catalyst, it has been suggested that CH_4 formation is inhibited by poisoning of the adsorbed CO intermediates.[39, 40] With these considerations in mind, the efficient

formation of CH_4 over isolated Pt atoms was attributed to a smooth hydrogenation of carbon deposits promoted by the high H_2 dissociation ability of Pt, although insufficient H_2 dissociation sites limited the formation of CH_4.

Overall, our results revealed that the isolated Pt atoms present in the Pt–Ni alloy acted as H_2 dissociation sites at low temperatures. In addition, these isolated Pt atoms acted as highly active CO adsorption sites. As discussed in terms of the spectroscopic observations, intermediate bridging CO species formed between isolated Pt atoms and their neighboring Ni atoms, which in turn led to a high selectivity toward CH_4.

$$Pt-CO+Ni \rightleftarrows Pt-C(=O)-Ni \qquad (16)$$

During the hydrogenation, the C–O bonds of bridged CO species were dissociated, leading to subsequent-hydrogenation toward CH_4 and H_2O. In addition, we assumed that the surrounding Ni atoms acted as adsorption sites for the H species, thereby leading to the successive hydrogenation of the bridging CO species. Upon the desorption, in contrast, the bridged CO species desorbed through the on-top CO species attached onto isolated Pt atoms. This formation of the bridged CO species is key to selective CH_4 formation over *iso*-Pt alloy catalyst. In contrast, the Pt catalyst, having Pt–Pt sites, produced CO as a product owing to the absence of neighboring Ni sites, and a lack of formation of bridging CO species to promote hydrogenation. We therefore concluded that the unique ensemble effect of the isolated Pt atoms in the Ni–Pt alloy catalyst, and not the ligand effect, induced the selective hydrogenation of CO_2 toward CH_4. In addition, the high activity for H_2 dissociation promoted hydrogenation of the surface carbon species, which is the rate-determining step for CH_4 formation over a Ni catalyst, although an insufficient number of H_2 dissociation sites limited the reaction. Our findings therefore indicate that tuning the adsorption energy of isolated Pt sites by controlling the electronic states or through the addition of third element atoms as H_2 dissociation sites that exhibit low degrees of CO poisoning should be effective in promoting the formation of CH_4.

Conclusions

We herein reported our investigation into the role of the isolated Pt atoms in a Ni–Pt alloy catalyst (*iso*-Pt alloy catalyst) for the efficient and selective formation of CH_4 through the use of in situ transient Fourier transform infrared (FT-IR) observations and kinetic studies during the hydrogenation of CO_2. The selective formation of CH_4 over the *iso*-Pt alloy catalyst was initially surprising, due to Pt catalysts tending to exhibit activity toward CO production. However, this interesting result was attributed to the formation of bridging CO intermediates between the isolated Pt atoms and their neighboring Ni atoms, similar to those that form between the Ni–Ni sites of Ni catalysts. In addition, transient changes in the FT-IR spectra indicated that the CO species attached to isolated Pt atoms (i.e., on-top CO species) were hydrogenated toward CH_4 *via* the bridging CO species, and the bridging CO species desorbed through on-top CO species attached onto isolated Pt atoms. A power law equation based on the kinetic studies revealed that the rate-determining step for the Ni catalyst was hydrogenation of the surface carbon species, while upon the addition of the Pt species, the H_2 dissociation step became the rate-determining step. It was found that the ability of Pt to supply dissociated H species to the surface carbon species promoted the hydrogenation reaction; however, the presence of insufficient numbers of H_2 dissociation sites limited the formation of CH_4, since the isolated Pt atoms at the surface were mainly covered by CO species. With these considerations in mind, we could conclude that the enhanced H_2 dissociation ability of the Pt species (compared to Ni) resulted in the efficient formation of CH_4 over the *iso*-Pt alloy catalyst. Moreover, we concluded that the isolated Pt atoms within the Ni catalyst played a bifunctional role, namely as the adsorption sites for on-top CO species (which transformed into CO bridges between Pt and Ni) to afford a high selectivity toward CH_4, and efficient H_2 dissociation sites to promote hydrogenation, thereby addressing the issues related to the rate-determining step of the Ni catalyst.

References

1 F. Besenbacher, I. Chorkendorff, B. Clausen, B. Hammer, A. Molenbroek, J. K. Nørskov and I. Stensgaard, *Science*, 1998, **279**, 1913–1915.

2 M. H. Ab Rahim, M. M. Forde, R. L. Jenkins, C. Hammond, Q. He, N. Dimitratos, J. A. Lopez-Sanchez, A. F. Carley, S. H. Taylor, D. J. Willock*, et al.*, *Angew. Chem. Int. Ed.*, 2013, **52**, 1280–1284.

3 Y. Cao, B. Chen, J. Guerrero-Sánchez, I. Lee, X. Zhou, N. Takeuchi and F. Zaera, *ACS Catal.*, 2019, **9**, 9150–9157.

4 J. L. Snider, V. Streibel, M. A. Hubert, T. S. Choksi, E. Valle, D. C. Upham, J. Schumann, M. S. Duyar, A. Gallo, F. Abild-Pedersen*, et al.*, *ACS Catal.*, 2019, **9**, 3399–3412.

5 F. R. Lucci, T. J. Lawton, A. Pronschinske and E. C. H. Sykes, *J. Phys. Chem. C*, 2014, **118**, 3015–3022.

6 F. R. Lucci, J. Liu, M. D. Marcinkowski, M. Yang, L. F. Allard, M. Flytzani-Stephanopoulos and E. C. Sykes, *Nat. Commun.*, 2015, **6**, 8550–8557.

7 G. Giannakakis, M. Flytzani-Stephanopoulos and E. C. H. Sykes, *Acc. Chem. Res.*, 2018, **52**, 237–247.

8 J. L. Falconer and A. E. Zağli, *J. Catal.*, 1980, **62**, 280–285.

9 G. D. Weatherbee and C. H. Bartholomew, *J. Catal.*, 1982, **77**, 460–472.

10 D. Peebles, D. Goodman and J. White, *J. Phys. Chem.*, 1983, **87**, 4378–4387.

11 S. Fujita, H. Terunuma, H. Kobayashi and N. Takezawa, *React. Kinet. Catal. Lett.*, 1987, **33**, 179–184.

12 T. Kai, T. Takahashi and S. Furusaki, *CJChE*, 1988, **66**, 343–347.

13 S. Fujita, H. Terunuma, M. Nakamura and N. Takezawa, *Ind. Eng. Chem. Res.*, 1991, **30**, 1146–1151.

14 S. Fujita, M. Nakamura, T. Doi and N. Takezawa, *Appl. Catal. A*, 1993, **104**, 87–100.

15 A. Lapidus, N. Gaidai, N. Nekrasov, L. Tishkova, Y. A. Agafonov and T. Myshenkova, *Pet. Chem.*, 2007, **47**, 75–82.

16 E. Vesselli, M. Rizzi, L. De Rogatis, X. Ding, A. Baraldi, G. Comelli, L. Savio, L. Vattuone,

M. Rocca and P. Fornasiero, *J. Phys. Chem. Lett.*, 2009, **1**, 402–406.

17 P. A. U. Aldana, F. Ocampo, K. Kobl, B. Louis, F. Thibault-Starzyk, M. Daturi, P. Bazin, S. Thomas and A. C. Roger, *Catal. Today*, 2013, **215**, 201–207.

18 M. A. A. Aziz, A. A. Jalil, S. Triwahyono and S. M. Sidik, *Appl. Catal. A*, 2014, **486**, 115–122.

19 Q. Pan, J. Peng, T. Sun, S. Wang and S. Wang, *Catal. Commun.*, 2014, **45**, 74–78.

20 M. A. A. Aziz, A. A. Jalil, S. Triwahyono and A. Ahmad, *Green Chem.*, 2015, **17**, 2647–2663.

21 A. Westermann, B. Azambre, M. C. Bacariza, I. Graça, M. F. Ribeiro, J. M. Lopes and C. Henriques, *Appl. Catal. B: Environ.*, 2015, **174-175**, 120–125.

22 K. Jalama, *Catal. Rev.*, 2017, **59**, 95–164.

23 I. Sreedhar, Y. Varun, S. A. Singh, A. Venugopal and B. M. Reddy, *Catal. Sci. Technol.*, 2019, **9**, 4478–4504.

24 D. Liu, Y. Li, M. Kottwitz, B. Yan, S. Yao, A. Gamalski, D. Grolimund, O. V. Safonova, M. Nachtegaal, J. G. Chen*, et al.*, *ACS Catal.*, 2018, **8**, 4120–4131.

25 M. Mihet and M. D. Lazar, *Catal. Today*, 2018, **306**, 294–299.

26 S. Kikkawa, K. Teramura, H. Asakura, S. Hosokawa and T. Tanaka, *J. Phys. Chem. C*, 2019, **123**, 23446–23454.

27 G. Blyholder, *J. Phys. Chem.*, 1964, **68**, 2772–2777.

28 J. R. Kitchin, J. K. Norskov, M. A. Barteau and J. G. Chen, *J. Chem. Phys.*, 2004, **120**, 10240–10246.

29 C. Morterra, A. Zecchina, S. Coluccia and A. Chiorino, *J. Chem. Soc. Faraday Trans.*, 1977, **73**, 1544–1560.

30 N. Favero and C. VittorioáFolonari, *J. Chem. Soc., Faraday Trans.*, 1993, **89**, 135–150.

31 J. Szanyi and J. H. Kwak, *Phys. Chem. Chem. Phys.*, 2014, **16**, 15117–15125.

32 J. Szanyi and J. H. Kwak, *Phys. Chem. Chem. Phys.*, 2014, **16**, 15126–15138.

33 C. Olsen and R. Masel, *Surf. Sci.*, 1988, **201**, 444–460.

34 R. Barth, R. Pitchai, R. L. Anderson and X. E. Verykios, *J. Catal.*, 1989, **116**, 61–70.

35 R. Barth and A. Ramachandran, *J. Catal.*, 1990, **125**, 467–471.

36 D. Ferri, T. Bürgi and A. Baiker, *Phys. Chem. Chem. Phys.*, 2002, **4**, 2667–2672.

37 A. Goguet, F. C. Meunier, D. Tibiletti, J. P. Breen and R. Burch, *J. Phys. Chem. B*, 2004, **108**,

20240–20246.

38 S. Eckle, H. G. Anfang and R. J. Behm, *J. Phys. Chem. C*, 2011, **115**, 1361–1367.

39 A. Karelovic and P. Ruiz, *ACS Catal.*, 2013, **3**, 2799–2812.

40 X. Wang, H. Shi, J. H. Kwak and J. Szanyi, *ACS Catal.*, 2015, **5**, 6337–6349.

41 A. Erdöhelyi, M. Pásztor and F. Solymosi, *J. Catal.*, 1986, **98**, 166–177.

42 A. Haghofer, D. Ferri, K. Föttinger and G. Rupprechter, *ACS Catal.*, 2012, **2**, 2305–2315.

43 W. Erley, H. Wagner and H. Mach, *Surf. Sci.*, 1979, **80**, 612–619.

44 M. Trenary, K. Uram, F. Bozso and J. Yates Jr, *Surf. Sci.*, 1984, **146**, 269–280.

45 S. Tang, M. Lee, Q. Yang, J. Beckerle and S. Ceyer, *J. Chem. Phys.*, 1986, **84**, 1876–1883.

46 L. Surnev, Z. Xu and J. Yates Jr, *Surf. Sci.*, 1988, **201**, 1–13.

47 L. Surnev, Z. Xu and J. Yates Jr, *Surf. Sci.*, 1988, **201**, 14–26.

48 J. A. Rodriguez and D. W. Goodman, *J. Phys. Chem.*, 1991, **95**, 4196–4206.

Part II

Tuning the Selectivity During Hydrogenation of CO_2 over Supported Pt Catalysts

Chapter 3

In Situ Time-Resolved XAS Study on Metal-Support-Interaction-Induced Morphology Change of PtO_2 Nanoparticles Supported on γ-Al_2O_3 *via* Reduction by H_2

Abstract

The metal-support interaction (MSI) between Al_2O_3 and novel metal nanoparticle plays a significant role in the particle morphologies, their electronic states, and their catalytic performances of novel metal catalysts supported on Al_2O_3. It was reported that the reduction treatment of γ-Al_2O_3-supported Pt nanoparticles with H_2 resulted in a morphology change of Pt particles from three-dimensional 11 Pt atoms to a raft-like structure similar to Pt (100) over γ-Al_2O_3; however, the dynamic behavior of the morphology change is still unclear. We therefore focused on the MSI between Pt and/or PtO_x nanoparticles and γ-Al_2O_3 surface by observing the reduction process of PtO_x nanoparticles over γ-Al_2O_3 surface using *in situ* time-resolved X-ray absorption spectroscopy (XAS) technique. The combination of the temperature-programmed reduction profile under H_2 flow (H_2-TPR profile) of PtO_x loaded on γ-Al_2O_3 and *in situ* Pt L_3-edge XAS observation clearly indicated that PtO_x particles were stabilized by the interaction with the γ-Al_2O_3 surface as compared to the reference PtO_2 powder; the relatively stabilized PtO_x species were reduced below 423 K, and the interfacial PtO_x species on γ-Al_2O_3 surface were reduced above 423 K. Furthermore, the time-resolved XAS observation during the *in situ* reduction at 473 K revealed that the three-dimensional morphology of PtO_x particles changed to two-dimensional low-coordinated Pt particles because of the bond dissociation between interfacial PtO_x species and γ-Al_2O_3 surface.

Introduction

Supported noble metal catalysts are one of the most important groups of heterogeneous catalysts for industrial processes and emission purification systems, and are demanded to reduce their usage in terms of element strategy and economic efficiency.[1-3] The redox properties of VIIIB noble metal elements, such as Rh, Pd, Ir, and Pt, are essential driving forces in catalytic cycles, and the combination of active metal species and their supports help to improve their redox capabilities and catalytic performances.[4-7] Strong metal-support interaction (SMSI) refers to the unique interaction between VIIIB noble metals and reducible oxide supports, such as TiO_2, Nb_2O_5, and CeO_2, on reduction treatment with H_2.[8, 9] SMSI modifies metal nanoparticles with reducible supports (e.g., TiO_{2-x}) and/or forms pseudo alloys with reducible supports accompanied by electron donation (e.g. $TiPt_3$), whereas inert support materials, such as SiO_2, are hardly affected.

Among the commonly used support materials for industrial applications, Al_2O_3 is generally classified under non-SMSI support for VIIIB noble metals, whereas the high temperature calcination results in the complex oxide of Al_2O_3 with surface-modified transition-metal elements, such as Fe, Co, Ni, and Zn.[10, 11] However, the metal-support interaction (MSI) between Al_2O_3 and VIIIB noble metal nanoparticles also plays a significant role in the particle morphologies, their electronic states, and the catalytic performances of noble metal catalysts supported on Al_2O_3.[12-21] Mansour et al. found that the Pt particles on interaction with Al_2O_3 showed a large number of unfilled *d* states as compared to those supported on SiO_2.[12] Koningsberger et al. reported that the reduction treatment with H_2 resulted in a morphology change of Pt particles from three-dimensional 11 Pt atoms to a raft-like structure similar to Pt (100) over γ-Al_2O_3, of which the surface consisted of tetra- and octa-coordinated Al^{3+} sites.[13] Moreover, Kwak et al. proposed that penta-coordinated Al^{3+} sites on the (100) facets of the γ-Al_2O_3 surface anchored atomically dispersed Pt species at low loadings of Pt, whereas two-dimensional Pt rafts formed at high loadings.[14, 16] Furthermore, the interaction between the Al^{3+} sites and the other noble metals, such as Pd, was also reported to be strongly related to the crystal phase and surface composition of Al_2O_3.[22] Therefore, understanding the formation mechanism of metal nanoparticles under interaction with their supports is important in order to develop shape-controlling methods and to design catalytic active sites at metal-support interfaces.[17, 18]

To elucidate the effect of MSI on the loading, activation, and sintering process of metal species on the supports, a number of approaches using *in situ* observation techniques have been employed, such as transmission electron microscopy (TEM),[19, 23] scanning tunneling microscopy (STM),[24] Fourier transform infrared (FTIR) spectroscopy,[25] UV-vis diffuse reflectance spectroscopy (DRS),[26] and X-ray absorption spectroscopy (XAS),[15, 27, 28] or a combination of *operando* studies.[20, 29] *In situ* time-resolved XAS is one of the most powerful tools for monitoring the reductive formation of nanoparticles;[17, 30-33] the loading, activation, and sintering process of the metal species on the supports;[30-33] and their working states under reaction conditions,[29, 34-37] revealing the temporal change in the valent and coordination environment of the target elements. For instance, Shishido et al. investigated the formation mechanism of Pt nanoparticles from $Pt(NH_3)_4(NO_3)_2$ precursors over SiO_2 supports in an inert and reductive atmosphere using time-resolved observation of the valent environment of Pt species, Pt–Pt bond formation, and formation products with ramping temperature. They found that surface-stabilized Pt species with oxygen atoms on SiO_2 surface (Si-O-Pt-O-Si) was formed in a He-filled atmosphere, whereas reduction by H_2 formed Pt nanoparticles followed by direct decomposition of $Pt(NH_3)_4(OSi)_2$.[32] The current study focuses on the MSI between Pt and/or PtO_x nanoparticles and Al_2O_3 surface by observing the reduction process of PtO_x nanoparticles over Al_2O_3 surface using *in situ* time-resolved XAS technique. The durability for this reduction process, where the nanoparticles were prepared by annealing of $Pt(NH_3)_2(NO_2)_2$ precursors, was evaluated utilizing a temperature-programmed reduction profile under H_2 flow (H_2-TPR profile) that monitored the valent environment of Pt species. The time-resolved XAS observations of *in situ* reduction afforded us the temporal change in the valent and coordination environment of Pt species, which in turn revealed the dynamic reduction behavior due to the morphology change from three-dimensional PtO_x nanoparticles to two-dimensional low-coordinated Pt metal particles. Thus, this study provides the first observation of dynamic morphology change of Pt nanoparticles under interaction with Al_2O_3, which can help in the development of a methodology to control the morphology of Pt particles.

Experimental

Pt was loaded onto Al_2O_3 (JRC-ALO-7 supplied by the Catalysis Society of Japan; γ-Al_2O_3, S_{BET} = 163.5 $m^2 \cdot g^{-1}$) and SiO_2 (JRC-SIO-13 supplied by the Catalysis Society of Japan; amorphous SiO_2, S_{BET} = 284.7 $m^2 \cdot g^{-1}$) by impregnation with an aqueous solution of $Pt(NH_3)_2(NO_2)_2$ (Furuya metal Co. Ltd., Japan) at 353 K. The impregnated samples were annealed at 673 K for 5 h in air, and 5 wt% Pt (256 μmol· g^{-1}) was used.

Pt L_3-edge XAS spectra were measured using BL01B1[38] beamline in SPring-8 (Japan Synchrotron Radiation Research Institute, Hyogo, Japan; 8 GeV, 100 mA). The X-ray absorption fine structure (XAFS) spectra were collected using a double-crystal Si(111) monochromator. Higher harmonic X-rays were rejected by setting the glancing angle of the Rh-coated mirrors to 3.0 mrad. The incident (I_0) and transmitted (I_1) X-ray flux were measured (17 and 31 cm, respectively) using ionization chambers filled with N_2 (85%) + Ar (15%) and Ar (100%), respectively. The photon energy of the X-ray was calibrated at the inflection point of Pt L_3-edge X-ray absorption near edge structure (XANES) spectra of Pt foil to 11564 eV. Static and *in situ* XAS were carried out with quick scan in transmittance mode. [39] The reference materials of Pt foil (5 μm thick), Pt metal powder (Niraco Co. Ltd., Japan), and PtO_2 powder (Wako Pure Chemical Industries Ltd., Japan) were measured in transmittance mode.

In situ Pt L_3-edge XAS of PtO_x-loaded catalysts under temperature-programmed reduction operation was performed in a modified heating XAS cell (ASPF-20-03, Kyowa Vacuum Co. Ltd., Japan). In a sample holder (7 φ inside diameter), 5 wt% PtO_x loaded on Al_2O_3 (PtO_x/Al_2O_3) and SiO_2 (PtO_x/SiO_2) (27 mg, 25–50 mesh) were pelletized, and 2% H_2/He was passed through the samples for 1 h at 303 K. Then, the cell was heated from 303 K to 773 K with an electronic furnace at 10 $K \cdot min^{-1}$. The amount of consumed H_2 was monitored with a thermal conductivity (TC) detector (GC-8A, Shimadzu Corp., Japan) in the laboratory using the above reaction system with the same XAS cell.

Time-resolved Pt L_3-edge XAS was performed on PtO_x-loaded catalysts during *in situ* reduction in the *in situ* XAS cell at constant temperatures of 323, 373, and 473 K. The samples were heated up to each temperature under 400 $mL \cdot min^{-1}$ of He flow. Then, the flow gas was switched to 500 ppm of H_2/He by a remote-controlled solenoid valve, and simultaneously quick scan XAFS

measurements were recorded. The acquisition time of each spectrum was 87.5 s. The inflection point of the first spectrum was collected after 24 s of H_2 injection.

The data reduction was performed using Athena and Artemis software ver. 0.9.25 included in the Ifeffit 1.2.12 package.[40] The k^3-weighted EXAFS oscillation in the range of 3−12 $Å^{-1}$ was Fourier transformed, and the curve fitting analyses were performed in the range of 1.3−2.5 Å in *R* space. For curve fitting analyses, the backscattering factor and the phase shift of each scattering path were calculated with FEFF6L using the crystal structures of fcc Pt metal (*Fm*−3*m*) and PtO_2 (*Pnnm*). Furthermore, the amplitude reduction factor (S_0^2) was estimated by fitting the reference spectrum of Pt foil in the range of 2.0−3.9 Å in *R* space with the parameters calculated by FEFF. The coordination numbers (*C.N.s*) of reference Pt metal and PtO_2 powder were determined by fitting their spectra, which were measured at room temperature, in the range of 2.0−3.0 and 1.0−2.0 Å, respectively. Assuming that there was no evident change in the *C.N.* below 473 K, the Debye-Waller factors at each temperature were determined by fitting the spectra of reference Pt metal and PtO_2 powder diluted with Al_2O_3 powder by increasing the temperature in the *in situ* XAS cell under 2% H_2/He and 20% O_2/He flow, respectively. For the simultaneous fitting of the Pt−O and Pt−Pt first shells at several temperatures, the value of ΔE was fixed at the same value among the spectra of PtO_2 and Pt metal, respectively. The fitting results for the aforementioned are compiled in **Table 1**.

Table 1. Fitting parameters of reference samples [a].

Sample	Scatter	Sampling temperature / K	Fitting range in *R* space / Å	*C.N.*	*r* / Å	Δ*E* /eV	σ² (10^{-3})	*R*-factor
Pt foil	Pt–Pt	298	2.0–3.9	12 (fixed)	2.77 (0.01)	8.03 (0.55)	4.91 (0.21)	0.001
Pt powder	Pt–Pt	298	2.0–3.0	9.87 (0.39)	2.75 (0.01)	6.98 (0.47)	6.70 (0.20)	0.001
PtO_2 powder	Pt–O	298	1.0–2.0	4.87 (0.6)	2.02 (0.01)	14.21 (1.33)	1.69 (0.73)	0.006
Pt powder	Pt–Pt	298	2.0–3.0	9.87 (fixed)	2.75 (0.01)	6.72 (0.23)	6.73 (0.07)	0.001
		373		9.87 (fixed)	2.75 (0.01)		7.22 (0.06)	
		423		9.87 (fixed)	2.75 (0.01)		7.52 (0.07)	
		473		9.87 (fixed)	2.75 (0.01)		7.74 (0.10)	
PtO_2 powder	Pt–O	298	1.0–2.0	4.87 (fixed)	2.02 (0.01)	14.29 (1.13)	1.46 (0.01)	0.022
		423		4.87 (fixed)	2.02 (0.01)		2.17 (0.01)	
		473		4.87 (fixed)	2.02 (0.01)		2.55 (0.01)	

[a] *C.N.*: coordination number; *r*: bond distance; Δ*E*: energy shift of the absorption edge; σ²: Debye−Waller factor.
The amplitude reduction factor (S_0^2) value of 0.869 was determined by fitting Pt foil. respectively. Numbers in parentheses represent uncertainties for the fits. The reliability factor (*R*-factor) is defined as *R*-factor = $\Sigma[k^3\chi_{obs}(k) - k^3\chi_{cal}(k)]^2 / \Sigma[k^3\chi_{obs}(k)]^2$, where χ_{obs} and χ_{cal} correspond to the observed and calculated data, respectively.

H_2-TPR at a low temperature was carried out in a flow-type reactor with cryostat (BELCAT-B system with CATcryo, MicrotracBEL Corp., Japan). A flow gas of 5% H_2/Ar (30 mL· min^{-1}) was passed through a reaction tube containing 50 mg of the catalyst under atmospheric pressure. For reference, H_2-TPR was performed on PtO_2 powder with comparable molar mass to Pt. After passing 5% H_2/Ar through the samples for 1 h at 173 K, the reactor was heated from 173 to 1223 K using an electronic furnace at 5 K·min^{-1}, and the amount of H_2 consumed was monitored with a TC detector of

BELCAT-B system. CO pulse titration was performed by a flow-type chemical adsorption measuring apparatus (BELCAT-II, MicrotracBEL Corp., Japan). After pre-reduction treatment with 5% H_2/He (30 $mL \cdot min^{-1}$) at 473 or 773 K for 30 min, CO was injected through a reaction tube containing 50 mg of the catalyst with flowing He as carrier gas at 323 K. The amount of CO consumed was monitored with a TC detector of BELCAT-II system. The amount of surface-metal atoms was estimated using the adsorption amount of CO from pulse titration at 323 K, assuming that the chemisorption stoichiometry is CO:Pt = 1. Average particle size was estimated from the adsorption amount of CO with a hemisphere model. Specific surface areas of the support material and as-prepared sample were estimated by the adsorption of N_2 at 173 K using the Brunauer–Emmett–Teller (BET) method (BELSORP-miniII, MicrotracBEL Corp., Japan). TEM images were obtained using JEM-2100F (JEOL Ltd., Japan) at an accelerating voltage of 200 kV.

Results and discussion

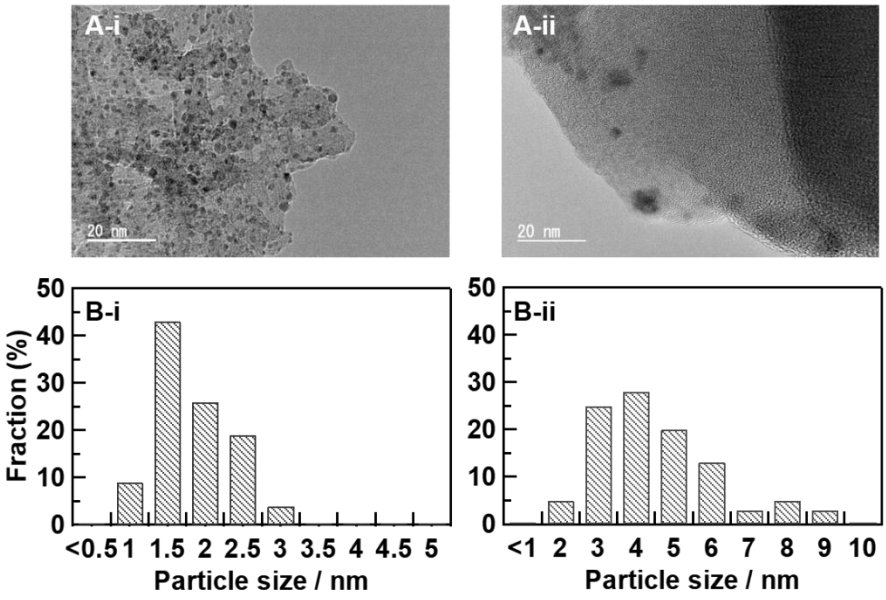

Figure 1. (A) TEM images of (i) PtO_x/Al_2O_3 and (ii) PtO_x/SiO_2. **(B)** particle size distribution of (i) PtO_x/Al_2O_3 and (ii) PtO_x/SiO_2. The images of as-prepared samples were measured at a magnification of 2.5×10^5.

Figure 1(A-i) and **(A-ii)** present the TEM images of PtO_x/Al_2O_3 and PtO_x/SiO_2 catalysts after annealment at 673 K in air, respectively. Highly dispersed particles were observed, of which diameter histograms are shown in **Figure 1(B-i)** and **(B-ii)**. The size distribution of PtO_x nanoparticles in PtO_x/Al_2O_3 was found to be 1.5±0.1 nm, whereas PtO_x/SiO_2 showed larger particles with an average particle size of 3.4±0.3 nm.

Table 2. Dispersions of PtO_x and Pt^0 particles loaded on Al_2O_3 and SiO_2 supports.

Catalyst (5wt% Pt)	S_{BET} [a] / $m^2\ g^{-1}$	Particle size of PtO_x [b] / nm	Reduced at 473 K		Reduced at 773 K	
			Particle size [c] / nm	Dispersion [c] / %	Particle size [c] / nm	Dispersion [c] / %
PtO_x/Al_2O_3	162.2	1.5±0.1	1.6	72	2.1	54
PtO_x/SiO_2	261.2	3.4±0.3	3.1	36	3.4	33

[a] Specific surface area of as-prepared samples was estimated by the adsorption of N_2 at 173 K with using the BET method.
[b] Size distribution of PtO_x particles was obtained from TEM images.
[c] Amount of surface-metal atoms was estimated by using adsorption amount of CO from pulse titration at 323 K.

Although the surface area of PtO_x/Al_2O_3 (S_{BET} = 162.2 $m^2 \cdot g^{-1}$) was smaller than that of PtO_x/SiO_2 (S_{BET} = 261.2 $m^2 \cdot g^{-1}$) (**Table 2**), there was a higher dispersion of PtO_x nanoparticles on Al_2O_3 than on SiO_2, owing to the stabilization caused by the interaction between the metal species and the support surface. To ensure the effect of reduction temperature on dispersion, CO pulse titration was performed on PtO_x-loaded samples following reduction for 30 min at 473 and 773 K. The Pt nanoparticles loaded on Al_2O_3 after reduction at 473 K was similar in size (1.6 nm) to the PtO_x particles of as-prepared PtO_x/Al_2O_3. Assuming a hemi-cuboctahedron model for three-dimensional particles, the dispersion of 72% of Pt nanoparticles was equivalent to a cluster of 37 atoms. Thus, it seems that a negligible aggregation occurred at this reduction temperature. After reduction by H_2 at 773 K, the dispersion decreased to 54%, owing to the aggregation or the morphology change of the Pt particles. **Figure 2** shows the enlarged views of TEM images of Pt particles of as-prepared PtO_x/Al_2O_3 **(A)** and PtO_x/Al_2O_3 reduced at 773 K by H_2/He **(B)**. Although at this resolution there was no evident morphology change, the clear contrast between the dispersed particles and Al_2O_3 support indicated that

the oxygen in PtO_x was removed by H_2 reduction. Pt particles on SiO_2 after reduction at 473 and 773 K showed particle sizes of 3.1 and 3.4 nm, respectively, exhibiting the aggregated particles as compared to those on Al_2O_3 support.

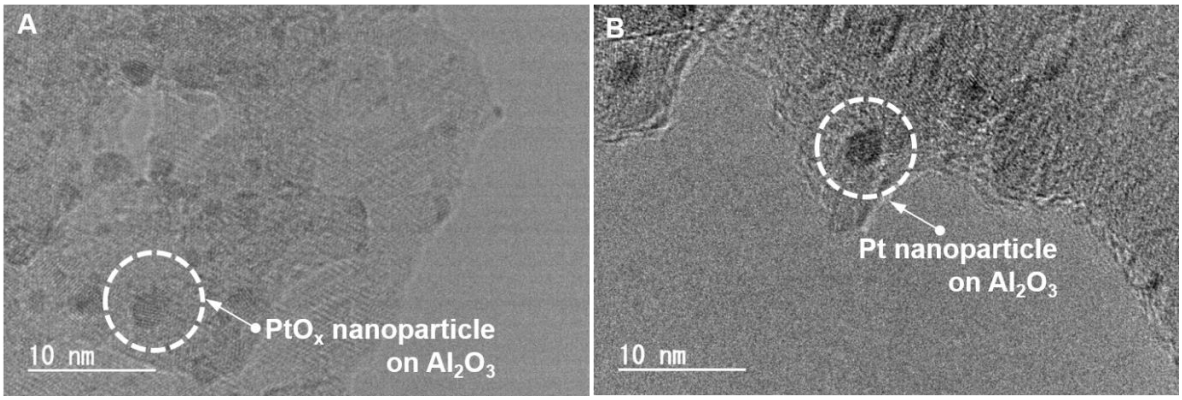

Figure 2. (A) TEM image of as prepared PtO_x/Al_2O_3. **(B)** TEM image of PtO_x/Al_2O_3 reduced at 773 K for 30 min by 5% H_2/He. The images were measured at a magnification of 6.0×10^5.

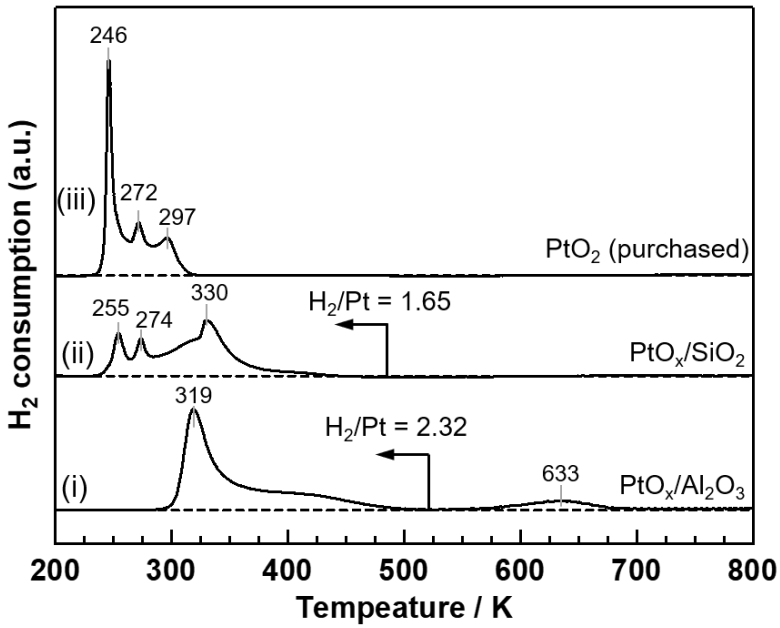

Figure 3. Low-temperature H_2-TPR profiles of (i) PtO_x/Al_2O_3, (ii) PtO_x/SiO_2, and (iii) reference PtO_2 powder. After flow of 5% H_2/Ar through the samples for 1 h at 173 K, the reactor was heated from 173 K to 1223 K with an electronic furnace at 5 K min^{-1}.

The H_2-TPR profile of PtO_x/Al_2O_3 (**Figure 3**) consists of a low-temperature peak at 319 K with broad peak tailing and a short high-temperature peak at 633 K. The low-temperature peak was

assignable to the reduction of PtO_2 particles on Al_2O_3 support, as reported by Huizinga et al.[41] The ratio of the amount of consumed H_2 below 523 K to that of the contained Pt species was 2.32, which was almost equivalent to the H_2 consumption when PtO_2 species on Al_2O_3 was reduced to Pt^0 ($PtO_2+2H_2 \rightarrow Pt+2H_2O$). Thus, we can consider that PtO_2 particles were obtained from the annealing of $Pt(NH_3)_2(NO_2)_2$ on Al_2O_3 at 473 K under air. The high-temperature peak was considered assignable to the reduction of oxygen atoms on Al_2O_3 surface and the following formation of hydroxyl groups or oxygen vacancies.

Conversely, the profile of PtO_x/SiO_2 (**Figure 3(ii)**) had three peaks below 473 K derived from the reduction of PtO_x species. The ratio of the amount of consumed H_2 below 473 K to that of the contained Pt species was 1.65, indicating that a part of the PtO_x species was reduced during the annealing process. The peaks at 255 and 274 K were similar to the profile of reference PtO_2 powder, which had peaks at 246 and 272 K (**Figure 3(iii)**), suggesting that those peaks were derived from the reduction of surface oxygen of PtO_2 particles. The other peak of PtO_x/SiO_2 was located at a temperature (330 K) higher than that of reference PtO_2 (297 K), indicating that the PtO_x species on SiO_2 were stabilized due to the interaction between PtO_x and SiO_2 surface as compared to bulk PtO_2.

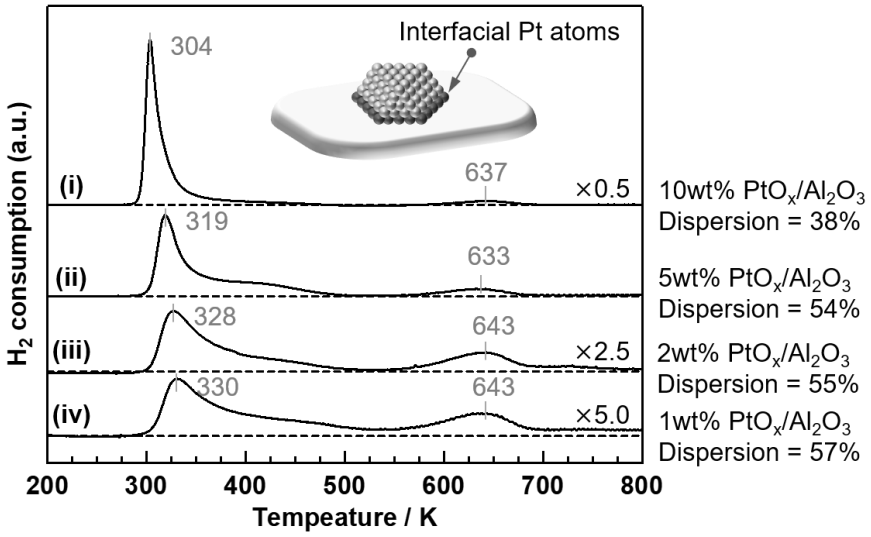

Figure 4. Low-temperature H_2-TPR profiles of (i) 10wt% PtO_x/Al_2O_3, (ii) 5wt% PtO_x/Al_2O_3, (iii) 2wt% PtO_x/Al_2O_3 and (iv) 1wt% PtO_x/Al_2O_3. After flow of 5% H_2/Ar through the samples for 1 h at 173 K, the reactor was heated from 173 K to 1223 K with an electronic furnace at 5 K min^{-1}. The dispersion of Pt particles was estimated by using adsorption amount of CO from pulse titration at 323 K, following to the reduction pretreatment by 5% H_2/He at 773 K for 1 h.

The PtO_x species on Al_2O_3 exhibited H_2 consumption peaks at temperatures higher than 300 K, indicating that the surface of PtO_x particles was also stabilized. This can be because of either the small particle size (diameter *ca.* 1.5 nm) or the interaction with Al_2O_3 surface. We deem that the H_2 consumption for the reduction of surface PtO_x particles supported on Al_2O_3 was included in the main peak at 319 K. Furthermore, the peak tailing of H_2 consumption peak at 319 K for PtO_x/Al_2O_3 was assignable to the reduction of PtO_x species at the PtO_x–Al_2O_3 interface. To prove this interpretation, H_2-TPR profiles of PtO_x/Al_2O_3 samples were obtained at various Pt loadings (**Figure 4**).

1 wt% of Pt-loaded PtO_x/Al_2O_3 with a dispersion of 57% Pt after reduction at 473 K exhibited the main peak at 330 K and a large peak tailing. In contrast, for 10 wt% Pt-loaded PtO_x/Al_2O_3 with large particles at a 38% dispersion, the H_2 consumption profile consisted of a large main peak and negligible peak tailing. For instance, the hemi-cuboctahedron model for Pt nanoparticles with a 50% dispersion comprised 185 Pt atoms with 33% of the Pt atoms at the PtO_x–Al_2O_3 interface, whereas the model with a dispersion of 38% included 24% of interfacial Pt atoms (See **Table 3**). Thus, the peak tailing was assignable to the reduction of PtO_x species at the PtO_x–Al_2O_3 interface, which were reduced at a higher temperature than the other PtO_x species. Thus, the interfacial PtO_x species were stabilized by Al_2O_3 as compared to the other PtO_x species. To observe the reduction behavior of PtO_x particles supported on Al_2O_3 as a function of temperature, XAS was performed during H_2-TPR operation.

Table 3. Structure model of hemi-cuboctahedron particle [a].

Num. of atoms on a side	Num. of contained atoms	Num. of surface atoms	Num. of interfacial atoms	Dispersion (%)	*C.N.*(Pt–Pt)
3	37	27	19	73	5.8
4	92	55	37	60	7.2
5	185	93	61	50	8.0
7	525	199	127	38	9.1
8	792	267	169	34	9.4
9	1137	345	217	30	9.7

[a] The model of supported Pt particle was assumed to be hemi-cuboctahedron structure with n atoms on a side. The number of contained atoms ($A_{total}(n)$), surface atoms ($A_{surface}(n)$), interfacial atoms with support surface ($A_{nterface}(n)$), and bonding between each atoms are expressed in the following equations:

$$A_{total}(n) = 1/3\ n\ (5n^2-3n+1)$$
$$A_{surface}(n) = A_{total}(n)-A_{total}(n-1) = 5n^2-7n+3$$
$$A_{interface}(n) = 3n^2-3n+1$$
$$N_{bonding}(n) = 4(5n^3-12n^3+10n-3)$$

The dispersion of Pt atoms was calculated by the division of $A_{surface}(n)$ by $A_{total}(n)$. The averaged coordination number is the division of $N_{bonding}(n)$ by $A_{total}(n)$.

Figure 5(A) shows the change in Pt L_3-edge XANES spectra of PtO_x/Al_2O_3 during H_2-TPR operation and those of reference Pt foil and PtO_2. The XANES spectrum of as-prepared PtO_x/Al_2O_3 showed a large absorption peak similar to that of PtO_2. After H_2 flow at 303 K, the white line (WL) intensity of XANES spectrum was lower than that of the as-prepared particles. Up to 533 K under H_2 flow, a series of WL intensities decreased with the increase in sample temperature, and above 533 K, the X-ray absorption edge and absorption peak slightly shifted to low energy. The spectrum at 773 K was similar to that of Pt foil. Interestingly, in the inset graph of **Figure 5(A)**, the XANES spectral change between the spectrum of the as-prepared particles and that at 423 K under TPR operation exhibits the isosbestic point, whereas the isosbestic point was not observed above 423 K. Since the isosbestic point of spectral change indicates the simple one-step reaction of A→B, the change above 423 K included more than two changes in the states of Pt species. **Figure 5(B)** shows the WL intensities steady decreasing with increase in the sample temperature, and reaching a minimum intensity of 1.2 at 533 K. **Figure 5(C)** displays the corresponding H_2 consumption profile during H_2-TPR operation performed in our laboratory. A low-temperature peak with peak tailing below 533 K and a negligible

high-temperature peak located at around 700 K were observed. Although a part of PtO_x species was reduced even after H_2 flow at 303 K, the low- and high-temperature peaks were assignable to the reduction of PtO_x species and Al_2O_3 surface as shown in **Figure 3**, respectively. The peak tailing of the low-temperature peak appeared above 423 K, indicating the progress of the second reduction step of PtO_x species. Since the WL intensities decreased only negligibly above 533 K, the H_2 consumption peak at around 700 K was irrelevant to the reduction of PtO_x; the low-energy shift observed in the XANES spectra was likely due to the aggregation or the morphology change. From the results of H_2-TPR of PtO_x/Al_2O_3 over various Pt loadings (**Figure 4**), we assume that there are two kinds of PtO_x species: species at the PtO_x–Al_2O_3 interface and the other species at the surface and bulk except those at the interface. Since the isosbestic point disappeared above 423 K during H_2-TPR operation, the reduction of PtO_x species at the PtO_x–Al_2O_3 interface (A'→B or B') were considered to proceed following the reduction of other PtO_x species (A→B). To reveal the formation dynamics of Pt particles upon the reduction of PtO_x–Al_2O_3 interface, the *in situ* reduction behavior of PtO_x particles over Al_2O_3 at a constant temperature was monitored by time-resolved XAS.

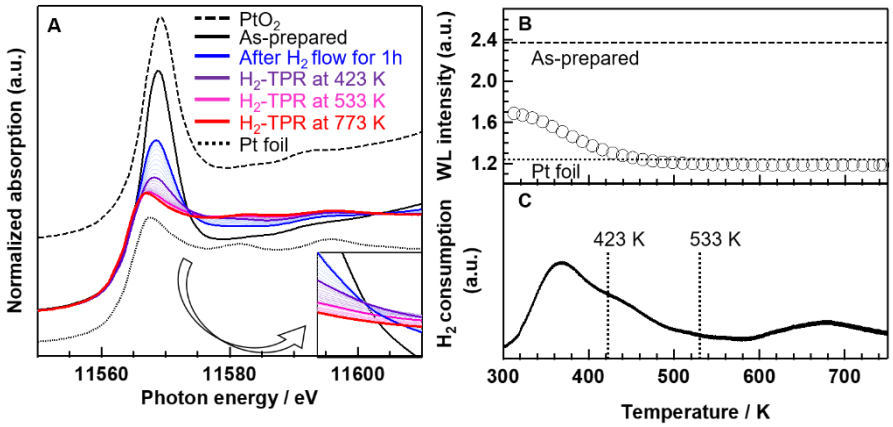

Figure 5. (A) A series of Pt L_3-edge XANES spectra of PtO_x/Al_2O_3 during H_2-TPR operation. Black line; as-prepared PtO_x/Al_2O_3 under He flow at 303 K, blue line; after 1h of 2% H_2/Ar flow at 303 K, purple line; under H_2-TPR at 423 K, pink line; under H_2-TPR at 533 K, red line; under H_2-TPR at 773 K. Dotted line; Pt foil measured at 303 K, Dashed line; PtO_2 powder measured at 303 K. The XAFS cell was heated from 303 K to 773 K with ramping temperature at 10 K min^{-1}. **(B)** The change in WL intensities of Pt L_3-edge XANES spectra of PtO_x/Al_2O_3 during H_2-TPR operation as a function of sample temperature. Dashed line; the WL intensity of Pt L_3-edge XANES spectrum of as-prepared PtO_x/Al_2O_3, Dotted line; the WL intensity of Pt L_3-edge XANES spectrum of Pt foil. **(C)** H_2-TPR profile measured in the laboratory with the same set up with XAFS measurement. The TPR profile was obtained after 1h of 2% H_2/Ar flow at 303 K.

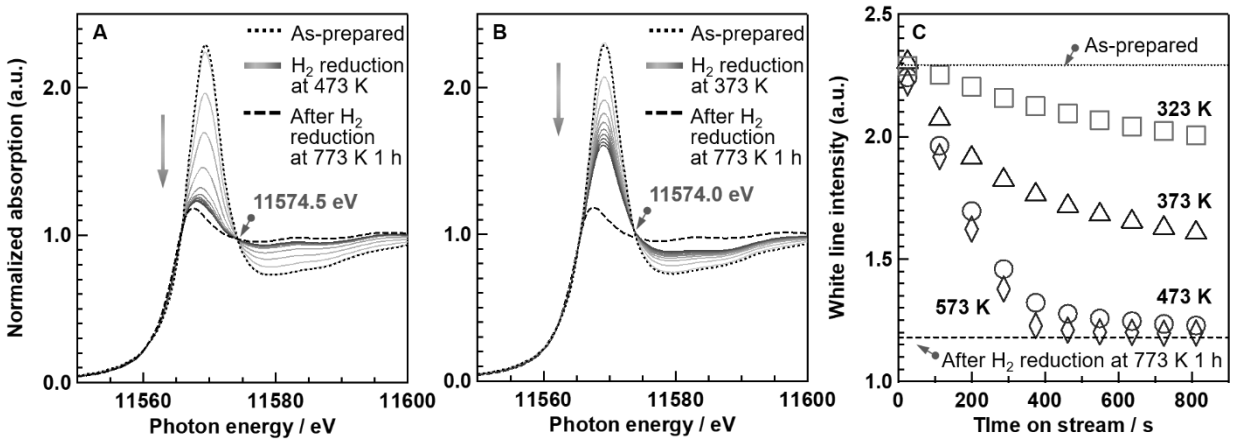

Figure 6. (A) A series of Pt L_3-edge XANES spectra of PtO_x/Al_2O_3 during *in situ* reduction with 500 ppm H_2/He at 473 K for *ca.* 900 s. **(B)** A series of Pt L_3-edge XANES spectra of PtO_x/Al_2O_3 during *in situ* reduction with 500 ppm H_2/He at 373 K for *ca.* 900 s. Dotted line; as-prepared PtO_x/Al_2O_3, dashed line; PtO_x/Al_2O_3 after 500 ppm H_2 reduction at 773 K 1h. The obtained ten spectra were recorded each 87.5 s from H_2 injection. **(C)** The temporal change in the WL intensities of Pt L_3-edge XANES spectra of PtO_x/Al_2O_3 during *in situ* reduction with 500 ppm H_2/He. Circles; reduced at 473 K, triangles; reduced at 373 K, squares; reduced at 323 K, and rhombus; reduced at 573 K. Dotted line; WL intensity of Pt L_3-edge XANES spectrum of as-prepared PtO_x/Al_2O_3, dashed line; WL intensity of Pt L_3-edge XANES spectrum of PtO_x/Al_2O_3 after 500 ppm H_2 reduction at 773 K 1h.

Figure 6(A) and **(B)** show a series of Pt L_3-edge XANES spectra of PtO_x/Al_2O_3 during *in situ* reduction with 500 ppm H_2/He at 473 and 373 K, respectively. After 24 s of H_2 injection at 473 K, the WL intensity of the first plot of XANES spectrum slightly decreased as compared to that of as-prepared particles. The intensities decreased with time, and the spectral change displayed the isosbestic point at 11574.5 eV. After 811.5 s of H_2 injection at 473 K, the WL intensity of the tenth plot of XANES spectrum was higher than that of PtO_x/Al_2O_3 reduced under 500 ppm H_2/He flow at 773 K for 1 h, indicating that the oxidized Pt species slightly remained after reduction at 473 K. For a series of Pt L_3-edge XANES spectra of PtO_x/Al_2O_3 during *in situ* reduction at 373 K, the temporal decrease was slower than that at 473 K, and despite the reduction of both kinds of PtO_x species, the isosbestic point in the temporal change of the spectra indicated the progress of their simultaneous reduction at 473 K.

As shown in **Figure 6(C)**, at 473 K, the WL intensities rapidly decreased and were close to a constant value after 811.5 s, although the intensity was slightly higher than that of reduced PtO_x/Al_2O_3 at 773 K. The temporal change at 573 K immediately reached the same height as that of reduced

PtO_x/Al_2O_3 at 773 K, indicating that almost all Pt species were reduced at 573 K. During the *in situ* reduction at 323 K and 373 K, the interfacial PtO_x species with Al_2O_3 surface, remained the same, so the change in WL intensities exhibited the insufficient decrease. Thus, the interfacial PtO_x species on Al_2O_3 surface remained with the PtO_x particles reduced at 373 K, whereas at 473 K they were completely reduced. The behavior of the decrease in the number of Pt–O bonds and the increase in the number of Pt–Pt bonds was evaluated by the corresponding EXAFS oscillations under the proceeding reduction.

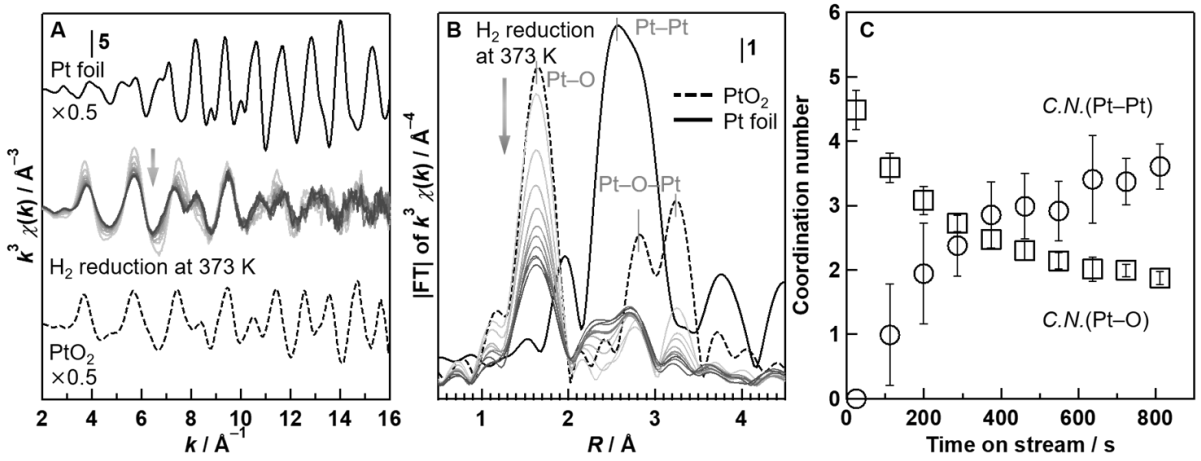

Figure7. (A) A series of Pt L_3-edge EXAFS oscillations of PtO_x/Al_2O_3 during *in situ* reduction with 500 ppm H_2/He at 373 K. Solid line; Pt L_3-edge EXAFS oscillation of Pt foil acquired at room temperature, dashed line; Pt L_3-edge EXAFS oscillation of PtO_2 acquired at room temperature. **(B)** A series of Fourier-transformed Pt L_3-edge EXAFS oscillations of PtO_x/Al_2O_3 during *in situ* reduction with 500 ppm H_2/He at 373 K. Solid line; Fourier-transformed Pt L_3-edge EXAFS oscillation of Pt foil acquired at room temperature, dashed line; Fourier-transformed Pt L_3-edge EXAFS oscillation of PtO_2 acquired at room temperature. **(C)** The temporal change in the *C.N.*(Pt–O)s (squares) and *C.N.*(Pt–Pt)s (circles) of PtO_x/Al_2O_3 during *in situ* reduction with 500 ppm H_2/He at 373 K.

Figure 7(A) and **(B)** illustrate a series of Pt L_3-edge EXAFS oscillations and their Fourier transforms of PtO_x/Al_2O_3 during *in situ* reduction with 500 ppm H_2/He flow at 373 K, respectively. The first plot of EXAFS oscillation after 24 s of H_2 injection displayed a shape identical to that of reference PtO_2 powder. The amplitude intensities decreased with time and were slightly close to that of Pt foil as the reduction proceeded, though the PtO_x species were insufficiently reduced as shown by the change in their XANES spectra. The first plot of Fourier transformed EXAFS oscillation after 24 s of H_2 injection showed peaks at 1.63, 2.79, and 3.25 Å, which were assignable to the contribution of

Pt–O scattering. As the reduction of PtO_x proceeded, the peak at around 2.0–3.0 Å gradually appeared, which was assignable to the first coordination of Pt–Pt scattering, whereas the peak intensities of Pt–O scattering decreased.

Curve fitting analysis was performed in the range of 1.3−2.5 Å in *R* space for deconvolution of the contribution of each scattering of Pt–O and Pt–Pt. The Debye−Waller factors of each scattering of Pt–O and Pt–Pt at a series of sampling temperatures (**Table 1**) were estimated by the fits for the *in situ* measured spectra of purchased Pt metal powder and PtO_2 powder diluted with Al_2O_3 powder. As an example, the fifth plot of Pt L_3-edge Fourier transformed EXAFS oscillation after 374 s of H_2 injection at 373 K was well fitted into the combination of the contribution of the scattering of Pt–O and Pt–Pt shell (**Figure 8**). **Figure 7(C)** displays the temporal changes in the coordination numbers of the first Pt–O and Pt–Pt shell, including the error of fitting. After 24 s of H_2 injection at 373 K, PtO_x/Al_2O_3 comprised only Pt–O bonds with an average *C.N.* of 4.5. With time, the *C.N.*s of Pt–O (*C.N.*(Pt–O)) decreased exponentially. After 811.5 s of H_2 injection at 373 K, the tenth plot of PtO_x/Al_2O_3 included the scattering of coordinated oxygen atoms, which was consistent with the results of XANES spectra, i.e., part of PtO_x species remained at this reduction temperature. Contrarily, as the reduction of Pt–O bond proceeded, the *C.N.*s of Pt–Pt (*C.N.*(Pt–Pt)) exhibited an exponential increase, and after 811.5 s of H_2 injection reached a value of 3.8. It should be noted that this value was the average of the *C.N.*s of the reduced Pt^0 and remaining PtO_2 species. Thus, the net *C.N.*(Pt–Pt) of reduced Pt^0 species was expected to be higher than the observed value. The average C.N. can be calculated by assuming a hemi- cuboctahedron model for three-dimensional particles, e.g., Pt nanoparticles with a dispersion of 73% Pt show an average C.N. of 5.8 (See **Table 3**).

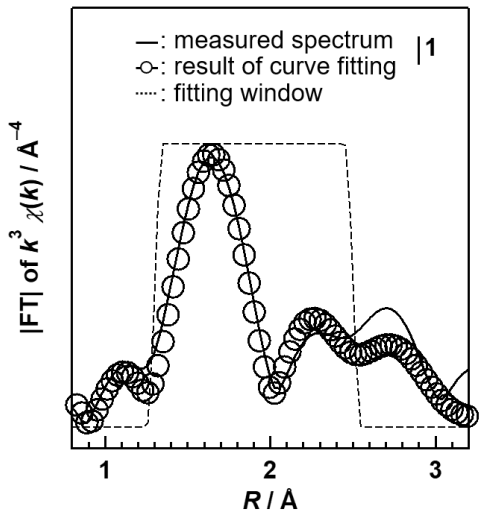

Figure 8. Result of the curve-fitting analysis of Pt L_3-edge EXAFS oscillation of PtO_x/Al_2O_3 after 374 s of H_2 injection at 373 K. Solid line shows measured Fourier-transformed EXAFS spectrum, and circles are the result of curve fitting of the first coordination shell ($1.3< \boldsymbol{R} <2.5$).

PtO_x species on Al_2O_3 were almost completely reduced to Pt^0 metals by the *in situ* reduction at 473 K. **Figure 9(A)** and **(B)** show the EXAFS oscillation and their Fourier transforms during the *in situ* reduction at 473 K, respectively. The oscillations and the peaks of Pt–O scattering clearly displayed a fast decrease as compared to those at 373 K. As shown in **Figure 9(C)**, after H_2 injection the *C.N.*(Pt–O) dramatically and consistently decreased, and after 374 s nearly reached 0. Simultaneously, the *C.N.*(Pt–Pt) increased and reached 4.0 after 374 s of H_2 injection. Despite the complete reduction of PtO_x species to Pt^0 species, the *C.N.*(Pt–Pt) (4.0) was lesser than the average *C.N.* (5.8), which was estimated by assuming a hemi-cuboctahedron model for Pt particles.

Figure 10(A) and **(B)** illustrates the temporal change in *C.N.*(Pt–O) and *C.N.*(Pt–Pt) against the corresponding WL intensities of each Pt L_3-edge XANES spectrum, which is representative of the degree of reduction progress of PtO_x species during *in situ* reduction of PtO_x/Al_2O_3 at 323, 373, and 473 K, respectively. As the reduction proceeded and the WL intensities decreased, the *C.N.*(Pt–O) linearly decreased, suggesting that the electron density of Pt species was enriched accompanied by the dissociation of Pt–O bonds. At the reduction temperatures 323 and 373 K, the *C.N.*(Pt–Pt) linearly increased as the reduction of PtO_x species proceeded. During the *in situ* reduction at 373 K, *C.N.*(Pt–Pt) increased to 3.8, although the WL intensity of the corresponding spectrum indicated that a part of PtO_x species remained. *C.N.*(Pt–Pt) linearly increased for the *in situ* reduction at 473 K as well,

although the inclination of the increase was different from those at 323 and 373 K. Moreover, when PtO_x species were completely reduced to Pt^0 species, *C.N.*(Pt–Pt) was equal to 4.0.

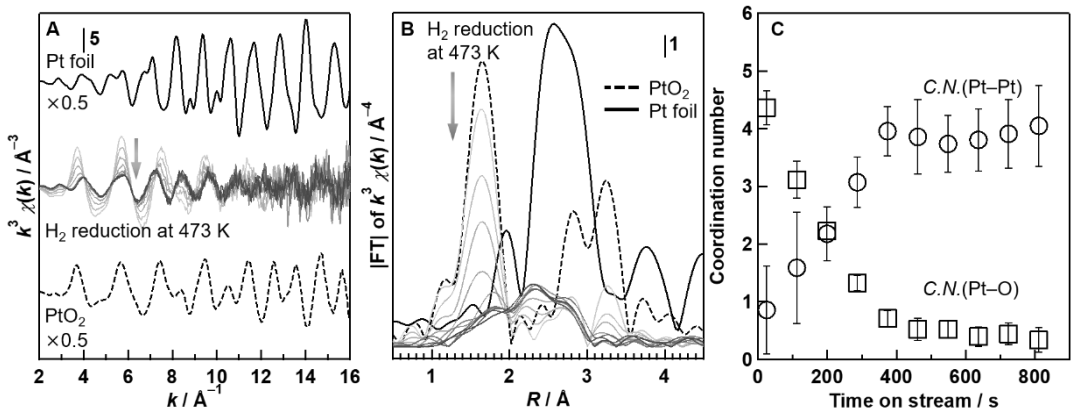

Figure 9. (A) A series of Pt L_3-edge EXAFS oscillations of PtO_x/Al_2O_3 during *in situ* reduction with 500 ppm H_2/He at 473 K. Solid line; Pt L_3-edge EXAFS oscillation of Pt foil acquired at room temperature, dashed line; Pt L_3-edge EXAFS oscillation of PtO_2 acquired at room temperature. **(B)** A series of Fourier-transformed Pt L_3-edge EXAFS oscillations of PtO_x/Al_2O_3 during *in situ* reduction with 500 ppm H_2/He at 473 K. Solid line; Fourier-transformed Pt L_3-edge EXAFS oscillation of Pt foil acquired at room temperature, dashed line; Fourier-transformed Pt L_3-edge EXAFS oscillation of PtO_2 acquired at room temperature. **(C)** The temporal change of the *C.N.*(Pt–O)s (squares) and the *C.N.*(Pt–Pt)s (circles) of PtO_x/Al_2O_3 during *in situ* reduction with 500 ppm H_2/He at 473 K.

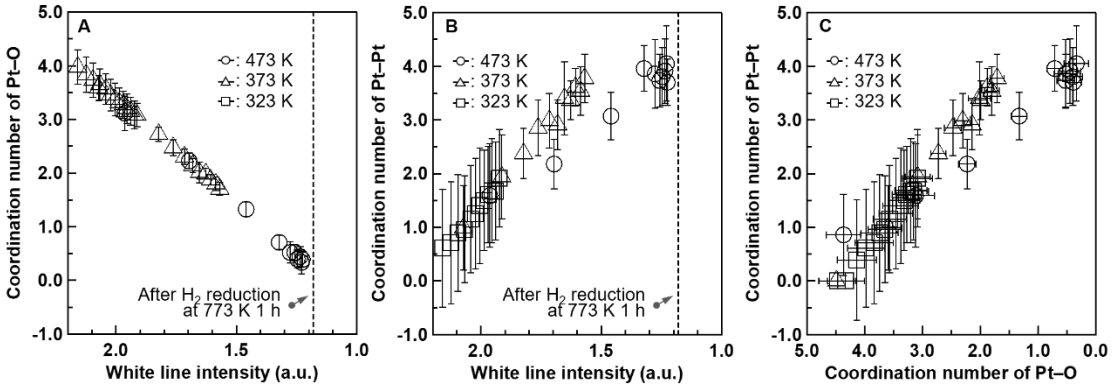

Figure 10. (A) The correlation between the WL intensities and the *C.N.*(Pt–O)s of each Pt L_3-edge XANES spectrum of PtO_x/Al_2O_3 during *in situ* reduction with 500 ppm H_2/He. **(B)** The correlation between the WL intensities and the *C.N.*(Pt–Pt)s of each Pt L_3-edge XANES spectrum of PtO_x/Al_2O_3 during *in situ* reduction with 500 ppm H_2/He. **(C)** The correlation between the *C.N.*(Pt–O)s and the *C.N.*(Pt–Pt)s of each Pt L_3-edge XANES spectrum of PtO_x/Al_2O_3 during *in situ* reduction with 500 ppm H_2/He. Red circles; reduced at 473 K, blue triangles; reduced at 373 K, green squares; reduced at 323 K.

It can be seen from **Figure 10(C)** that the *C.N.*(Pt–Pt) exhibited a linear increase with decrease in the *C.N.*(Pt–O) as the reduction of PtO_x particles proceeded. The *C.N.*(Pt–O) remained unchanged after *in situ* reduction below 373 K, suggesting that the reduction of PtO_x species insufficiently proceeded. As mentioned previously, the insufficient reduction of PtO_x at 373 K suggested that the net *C.N.*(Pt–Pt) of reduced Pt^0 species was higher than 3.8. On the other hand, the *C.N.*(Pt–O) completely disappeared during the *in situ* reduction at 473 K. The reduced Pt particles at 473 K exhibited a *C.N.*(Pt–Pt) of 4.0, which was lower than the *C.N.*(Pt–Pt) value estimated when the three-dimensional hemi-cuboctahedron model of Pt particle was assumed. Thus, the low-coordinated Pt species were expected to form during the reduction at 473 K, whereas the reduction at 373 K resulted in the high *C.N.*(Pt–Pt) of Pt species. Furthermore, the linear increase for Pt–Pt bonds with a different inclination at 473 K from those at 323 and 373 K indicated that the reduction of both interfacial and other PtO_x species simultaneously proceeded accompanied by the dissociation of Pt–O bonds at the interface with Al_2O_3 surface.

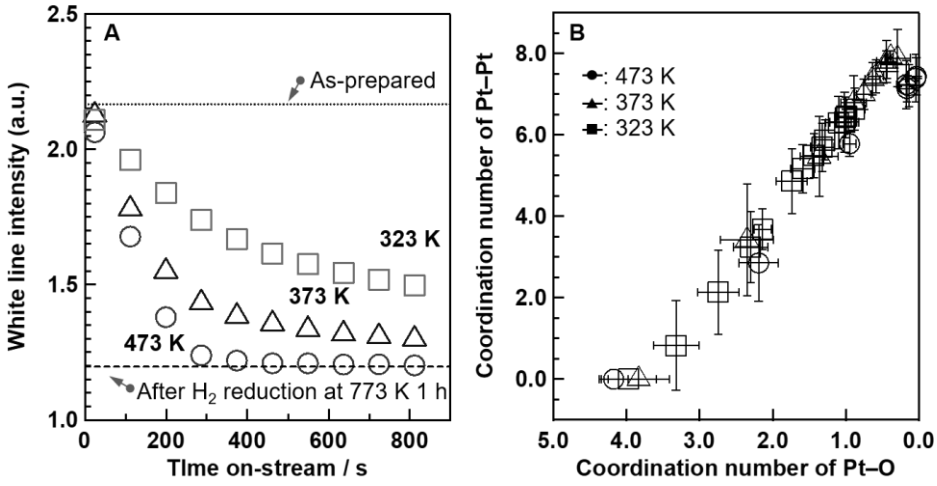

Figure 11. (A) The temporal change of the WL intensities of Pt L_3-edge XANES spectra of PtO_x/SiO_2 during *in situ* reduction with 500 ppm H_2/He. Red circles; reduced at 473 K, blue triangles; reduced at 373 K, green squares; reduced at 323 K, and purple rhombus; reduced at 573 K. Dotted line; WL intensity of Pt L_3-edge XANES spectrum of as prepared PtO_x/SiO_2, dashed line; WL intensity of Pt L_3-edge XANES spectrum of PtO_x/SiO_2 after 500 ppm H_2 reduction at 773 K 1h. **(B)** The correlation between the *C.N.*(Pt–O)s and the *C.N.*(Pt–Pt)s of each Pt L_3-edge XANES spectra of PtO_x/SiO_2 during *in situ* reduction with 500 ppm H_2/He. Red circles; reduced at 473 K, blue triangles; reduced at 373 K, green squares; reduced at 323 K.

For the *in situ* reduction of PtO_x/SiO_2, the trends shown in PtO_x/Al_2O_3 system were partly observed. **Figure 11(A)** displays the temporal change of the WL intensities of Pt L_3-edge XANES spectra during the *in situ* reduction of PtO_x/SiO_2 at 323, 373, and 473 K. At these temperatures, a fast decrease was observed as compared to those of PtO_x/Al_2O_3. At 473 K, the WL intensities rapidly decreased, and after 286.5 s of H_2 injection, reached the same extent as that of PtO_x/SiO_2 reduced at 773 K. For the *in situ* reduction at 323 and 373 K, the insufficient decay of the WL intensities indicated that a part of PtO_x species remained. In addition, from the H_2-TPR profile in **Figure 3(ii)**, we can understand that the PtO_x species, stabilized by the interaction between PtO_x particles and SiO_2 surface, were insufficiently reduced at these temperatures.

Figure 11(B) shows the correlation between the *C.N.*(Pt–O) and the *C.N.*(Pt–Pt) during the *in situ* reduction of PtO_x/SiO_2 at 323, 373, and 473 K. The linear correlation between the *C.N.*(Pt–O) and the *C.N.*(Pt–Pt) at the reduction temperatures indicated that as the reduction proceeded the formation of Pt–Pt bonds was accompanied by the dissociation of Pt–O bonds. For the *in situ* reduction at 373 K, the *C.N.*(Pt–Pt) increased to 7.9 and the *C.N.*(Pt–O) decreased to 0.4. *C.N.*(Pt–Pt) reached 7.4 when the PtO_x species completely reduced to Pt^0 species. This *C.N.*(Pt–Pt) was lower than the *C.N.*(Pt–Pt) estimated by CO pulse titration at a reduction temperature of 473 K: the hemi-cuboctahedron model for Pt nanoparticles with a 38% dispersion are estimated to show the *C.N.*(Pt–Pt) of 9.1 (**Table 3**). The *C.N.*(Pt–Pt) (7.4) of the reduced PtO_x/SiO_2 at 473 K was slightly lower than that at 373 K (7.9), although it was insignificant when compared to that observed for PtO_x/Al_2O_3 system, which was likely due to the large particle size.

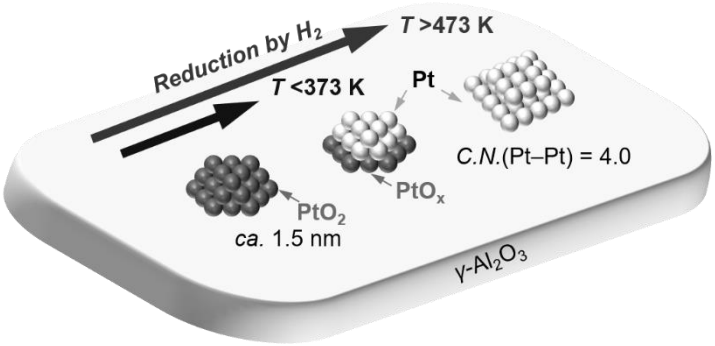

Figure 12. The schematic view of reduction of PtO_x particle supported on Al_2O_3 by H_2 reductant.

As observed in PtO_x/Al_2O_3 system, the formation of Pt particles with low-coordinated Pt species was accompanied by the reduction of the interfacial PtO_x species. We consider the low value of *C.N.*(Pt–Pt) of Pt particles obtained during reduction at 473 K to be a result of the morphology change into two-dimensional low-coordinated structure, as illustrated in **Figure 12**. At reduction temperatures below 373 K, the reduction of PtO_x species proceeded inadequately, and the interfacial PtO_x species with Al_2O_3 surface remained. In addition, the net *C.N.*(Pt–Pt) higher than 3.8 suggested that the three-dimensional structure of PtO_x particles were maintained throughout the reduction at 373 K. Conversely, the PtO_x species were completely reduced at 473 K. The *C.N.*(Pt–Pt) of reduced PtO_x/Al_2O_3 at 473 K was lower than that estimated with the assumption of three-dimensional structure, suggesting the morphology change into two-dimensional structure.

Koningsberger et al. previously proposed the morphology change of Pt particles from three-dimensional structure to two-dimensional raft-like structure after reduction by H_2 using the static XAS observation of Pt/γ-Al_2O_3, which was prepared by the impregnation of 1 wt% H_2PtCl_6 precursors. The reduction by H_2 at 723 K resulted in a raft-like structure with an average *C.N.*(Pt–Pt) of 3.8, whereas three-dimensional 11 Pt atoms were obtained after reduction at 573 K.[13] Moreover, their coordination-shell modeling with (100) thin layer was well matched to the EXAFS fitting results for the first, second, and third shell as compared to that with (111) layer, suggesting the formation of the Pt(100)-like two-dimensional structure. Furthermore, this morphology change was negligibly observed in neutral and acidic zeolites with cavities, indicating that the structure and/or surface hydroxyl groups of γ-Al_2O_3 were likely attributable for the two-dimensional morphology. With the CO pulse titration results of reduced Pt particles (**Table 2**), we assumed a three-dimensional hemisphere model; however, a Pt(100)-like two-dimensional model shown in **Figure 12** also satisfied both of the dispersion of 72% and the low *C.N.*(Pt–Pt) of 4.0. Thus, we consider that the formation of two-dimensional structure of Pt particles proceeded upon the reduction of the interfacial PtO_x species with Al_2O_3 surface. In addition, the morphology change from the three-dimensional PtO_x particles to the low-coordinated Pt particles was likely due to the bond dissociation between the interfacial PtO_x species and the Al_2O_3 surface.

In summary, our *in situ* time-resolved XAS study on the reduction mechanism of PtO_2 particles over Al_2O_3 support observed the behavior of morphology change from three-dimensional PtO_x particles to two-dimensional low-coordinated structure upon reduction of the interfacial PtO_x

species stabilized by Al_2O_3 surface. Our findings indicated that the bond dissociation between the interfacial PtO_x species and the support surface was crucial to the morphology change of Pt particles. However, a combination of direct observations of *in situ* morphology change by high-resolution TEM apparatus and space-resolved spectroscopies is essential to further detailed discussions. The bond formation between the interfacial PtO_x species and the support surface is co-related to the states and densities of hydroxyl groups and oxygen vacancy sites. Further investigation focused on the rates and activation energies of their bond dissociation would help us to develop methodologies for controlling the morphology of Pt particles.

Conclusions

H_2-TPR profile of PtO_x/Al_2O_3 suggested that the PtO_x particles were stabilized by the Al_2O_3 surface as compared to the bulk PtO_2 powder. The combination of H_2-TPR operation with XAS observation revealed that the interfacial PtO_x species on Al_2O_3 surface reduced at higher temperatures than the other PtO_x species. Furthermore, *in situ* time-resolved XAS observations revealed that the interfacial PtO_x species and the other surface and bulk PtO_x species, simultaneously reduced to Pt^0 species during *in situ* reduction at 473 K, whereas the interfacial PtO_x species remained at 373 K. During the *in situ* reduction at 473 K, the three-dimensional morphology of PtO_x particles changed to two-dimensional low-coordinated Pt particles. We concluded that this morphology change was because of the bond dissociation between interfacial PtO_x species and Al_2O_3 surface. Further investigation focused on the rates and activation energies of their bond dissociation would help us to develop methodologies for controlling the morphology of Pt particles.

References

1 M. C. J. Bradford and M. A. Vannice, *Catal. Rev.*, 1999, **41**, 1–42.

2 C. Ratnasamy and J. P. Wagner, *Catal. Rev.*, 2009, **51**, 325–440.

3 J. Wang, H. Chen, Z. Hu, M. Yao and Y. Li, *Catal. Rev.*, 2014, **57**, 79–144.

4 Y. Zhai, D. Pierre, R. Si, W. Deng, P. Ferrin, A. U. Nilekar, G. Peng, J. A. Herron, D. C. Bell and H. Saltsburg, *Science*, 2010, **329**, 1633–1636.

5 M. Cargnello, V. V. Doan-Nguyen, T. R. Gordon, R. E. Diaz, E. A. Stach, R. J. Gorte, P. Fornasiero and C. B. Murray, *Science*, 2013, **341**, 771–773.

6 E. Lira, L. R. Merte, F. Behafarid, L. K. Ono, L. Zhang and B. Roldan Cuenya, *ACS Catal.*, 2014, **4**, 1875–1884.

7 M. Ahmadi, H. Mistry and B. Roldan Cuenya, *J. Phys. Chem. Lett.*, 2016, **7**, 3519–3533.

8 S. Tauster, S. Fung and R. L. Garten, *J. Am. Chem. Soc.*, 1978, **100**, 170–175.

9 S. Bernal, J. Calvino, M. Cauqui, J. Gatica, C. Larese, J. P. Omil and J. Pintado, *Catal. Today*, 1999, **50**, 175–206.

10 T. Tsuchida, R. Furuichi and T. Ishii, *Z. Anorg. Allg. Chem.*, 1975, **415**, 175–184.

11 K. Trumble, *Acta Metall, Mater*, 1992, **40**, 105–110.

12 A. Mansour, J. Cook Jr, D. Sayers, R. Emrich and J. Katzer, *J. Catal.*, 1984, **89**, 462–469.

13 M. Vaarkamp, J. T. Miller, F. S. Modica and D. C. Koningsberger, *J. Catal.*, 1996, **163**, 294–305.

14 J. H. Kwak, J. Hu, D. Mei, C.-W. Yi, D. H. Kim, C. H. Peden, L. F. Allard and J. Szanyi, *Science*, 2009, **325**, 1670–1673.

15 S. I. Sanchez, L. D. Menard, A. Bram, J. H. Kang, M. W. Small, R. G. Nuzzo and A. I. Frenkel, *J. Am. Chem. Soc.*, 2009, **131**, 7040–7054.

16 D. Mei, J. H. Kwak, J. Hu, S. J. Cho, J. Szanyi, L. F. Allard and C. H. Peden, *J. Phys. Chem. Lett.*, 2010, **1**, 2688–2691.

17 J. Matos, L. K. Ono, F. Behafarid, J. R. Croy, S. Mostafa, A. T. DeLaRiva, A. K. Datye, A. I. Frenkel and B. Roldan Cuenya, *Phys. Chem. Chem. Phys.*, 2012, **14**, 11457–11467.

18 L. Li, L. L. Wang, D. D. Johnson, Z. Zhang, S. I. Sanchez, J. H. Kang, R. G. Nuzzo, Q. Wang,

A. I. Frenkel, J. Li*, et al.*, *J. Am. Chem. Soc.*, 2013, **135**, 13062–13072.

19 K. Murata, Y. Mahara, J. Ohyama, Y. Yamamoto, S. Arai and A. Satsuma, *Angew. Chem. Int. Ed. Engl.*, 2017, **56**, 15993–15997.

20 C. Dessal, T. Len, F. Morfin, J.-L. Rousset, M. Aouine, P. Afanasiev and L. Piccolo, *ACS Catal.*, 2019, **9**, 5752–5759.

21 C. Dessal, A. Sangnier, C. Chizallet, C. Dujardin, F. Morfin, J.-L. Rousset, M. Aouine, M. Bugnet, P. Afanasiev and L. Piccolo, *Nanoscale*, 2019, **11**, 6897–6904.

22 K. Murata, E. Eleeda, J. Ohyama, Y. Yamamoto, S. Arai and A. Satsuma, *Phys. Chem. Chem. Phys.*, 2019, **21**, 18128–18137.

23 C. Carrillo, T. R. Johns, H. Xiong, A. DeLaRiva, S. R. Challa, R. S. Goeke, K. Artyushkova, W. Li, C. H. Kim and A. K. Datye, *J. Phys. Chem. Lett.*, 2014, **5**, 2089–2093.

24 M. A. van Spronsen, J. W. M. Frenken and I. M. N. Groot, *Nat. Commun.*, 2017, **8**, 429–436.

25 E. Groppo, C. Lamberti, S. Bordiga, G. Spoto and A. Zecchina, *J. Catal.*, 2006, **240**, 172–181.

26 H. Yoshida, R. Kakei, A. Fujiwara, Y. Uchida and M. Machida, *J. Phys. Chem. C*, 2018, **122**, 28173–28181.

27 J. Singh, C. Lamberti and J. A. van Bokhoven, *Chem. Soc. Rev.*, 2010, **39**, 4754–4766.

28 H. Asakura, S. Hosokawa, T. Ina, K. Kato, K. Nitta, K. Uera, T. Uruga, H. Miura, T. Shishido, J. Ohyama*, et al.*, *J. Am. Chem. Soc.*, 2018, **140**, 176–184.

29 M. A. Newton, D. Ferri, G. Smolentsev, V. Marchionni and M. Nachtegaal, *J. Am. Chem. Soc.*, 2016, **138**, 13930–13940.

30 T. Shishido, H. Asakura, F. Amano, T. Sone, S. Yamazoe, K. Kato, K. Teramura and T. Tanaka, *Catal. Lett.*, 2009, **131**, 413–418.

31 J. Ohyama, A. Yamamoto, K. Teramura, T. Shishido and T. Tanaka, *ACS Catal.*, 2011, **1**, 187–192.

32 T. Shishido, H. Nasu, L. Deng, K. Teramrua and T. Tanaka, *J. Phys. Conf.*, 2013, **430**, 12060–12063.

33 S. Yamashita, Y. Yamamoto, M. Katayama and Y. Inada, *Bull. Chem. Soc. Jpn.*, 2015, **88**, 1629–1635.

34 T. Yamamoto, A. Suzuki, Y. Nagai, T. Tanabe, F. Dong, Y. Inada, M. Nomura, M. Tada and Y.

Iwasawa, *Angew. Chem. Int. Ed. Engl.*, 2007, **46**, 9253–9256.

35 Y. Nagai, K. Dohmae, Y. Ikeda, N. Takagi, T. Tanabe, N. Hara, G. Guilera, S. Pascarelli, M. A. Newton, O. Kuno*, et al.*, *Angew. Chem. Int. Ed. Engl.*, 2008, **47**, 9303–9306.

36 M. Kimura, Y. Niwa, K. Uemura, T. Nagai, Y. Inada and M. Nomura, *Mater. Trans.*, 2013, **54**, 246–254.

37 Y. Mahara, K. Murata, K. Ueda, J. Ohyama, K. Kato and A. Satsuma, *ChemCatChem*, 2018, **10**, 3384–3387.

38 T. Uruga, H. Tanida, Y. Yoneda, K. Takeshita, S. Emura, M. Takahashi, M. Harada, Y. Nishihata, Y. Kubozono and T. Tanaka, *J. Synchrotron Radiat.*, 1999, **6**, 143–145.

39 T. Uruga, H. Tanida, K. Inoue, H. Yamazaki and T. Irie, *AIP Conf. Proc.*, 2007, **882**, 914–916.

40 B. Ravel and M. Newville, *J. Synchrotron Radiat.*, 2005, **12**, 537–541.

41 T. Huizinga, J. Van Grondelle and R. Prins, *Appl. Catal.*, 1984, **10**, 199–213.

Chapter 4

A Combined *Operando* XAS-DRIFTS Study Elucidating the Active Sites for Unfavorable CH_4 Formation at Pt–Al_2O_3 Interface During Hydrogenation of CO_2

Abstract

We elucidated the active sites for unfavorable CH_4 formation over Al_2O_3-supported Pt catalyst during hydrogenation of CO_2 at ambient pressure, by using a combination of X-ray absorption spectroscopy (XAS) and diffuse reflectance infrared Fourier transform spectroscopy (DRIFTS) with product analysis (*operando* XAS-DRIFTS). The interaction between Pt and Al_2O_3 resulted in the unique morphology of Pt particles with a low coordination number for Pt species as compared to that of SiO_2-supported Pt catalyst. Moreover, Pt L_3- and L_2-edge X-ray absorption near edge structure spectra quantified the unoccupied states of Pt species including the antibonding orbitals, which were formed upon the adsorption of intermediates onto the Pt surface. The combined data of XAS and DRIFTS revealed that CO species co-adsorbed with H on the perimeter Pt sites at the interface between Pt particles and Al_2O_3 surface, and then further hydrogenation of those CO species led to the unfavorable CH_4 formation. This study demonstrates the power of the *operando* XAS-DRIFTS system for unveiling the complex effect of metal-support interaction on the catalytic activity, which is a key for designing the active sites on supported metal catalysts.

Introduction

Supported noble metal catalysts are among the most important heterogeneous catalysts and widely used in industrial processes. To enhance their activities, the particle size, morphology, and electronic state of the active metal species should be carefully controlled.[1-3] The main function of the support materials is dispersing the noble metal particles. However, in many cases the interaction between the metal particles and the support surface, called the metal-support interaction (MSI), leads to unique electronic and geometric characteristics in the loaded metal species and excellent activities.[4-8]

Catalytic hydrogenation of CO_2, which has attracted much attention for recycling CO_2 into chemical feedstocks, requires designed active sites of supported metal catalysts for controlling the selectivity.[9, 10] Many studies have been conducted on the hydrogenation of CO_2 over single-crystalline metal surfaces or simple supported metal catalysts. As a result, the selectivity toward reverse water gas shift (RWGS) reaction ($CO_2 + H_2 \rightarrow CO + H_2O$, $\Delta_r H^\circ_{298\,K} = 41.1$ kJ mol^{-1}) or methanation ($CO_2 + 4H_2 \rightarrow CH_4 + 2H_2O$, $\Delta_r H^\circ_{298\,K} = -164.7$ kJ mol^{-1}) has been relatively well classified by the active metal species.[11-18] However, even for the same active metal species, the choice of support materials affects the product selectivity owing to their different morphology and electronic structures.[19-28] For instance, Matsubu *et al.* revealed that Rh species at a low loading on TiO_2 was mainly composed of atomically dispersed Rh species that inhibited CH_4 formation, although the Rh catalyst tends to favor CH_4 production. Ma *et al.* also reported that dispersed Ir species supported on CeO_2 exhibited selective formation of CO, as distinct from the high selectivity toward CH_4 formation at high Ir loading.[25] Those authors assumed that such an effect is not due to a change in the particle size. Rather, when the Ir species are coordinated by the surface oxygen of CeO_2, the resultant electronic structure leads to a lower capacity for the adsorption of CO, which is an intermediate for CH_4 formation. Moreover, Kattel *et al.* investigated the role of Pt-oxide interface for product selectivity by combined density functional theory calculation and kinetic Monte Carlo simulations. Their results revealed that the synergy between the interfacial Pt atoms and the oxygen vacant sites of the support surface lowered the activation energy for forming the key intermediate species for RWGS reaction and enhanced the activity.[21, 24] Thus, those recent theoretical approaches with well-defined models have gradually revealed the role of MSI in

selectivity control, including the particle morphology, their electronic states, and the interfacial atoms with the support surface. Nevertheless, the current understanding is far from complete.

The surface-adsorbed intermediates are the most useful clues for clarifying the complex roles of the catalysts. Nevertheless, it is difficult to experimentally monitor all the intermediates simultaneously. Infrared (IR) spectroscopy has been used to elucidate the reaction mechanisms. The behavior of adsorbed hydrogen species, however, has been poorly studied despite their involvement in many key reactions (such as hydrogenation, hydrodesulfurization, reforming process, and ammonia synthesis): even for the Pt–H vibrations that display IR absorption bands, their assignments are still under debate owing to the very small absorption cross section and/or possible interfering bands of contaminated CO species.[29-31] Normally, X-ray absorption spectroscopy (XAS) as a characterization technique is considered non-surface-sensitive. However, in the case of nanoparticle catalysts, the XAS spectra can reflect the influence of surface adsorbates owing to the high proportion of surface atoms in each particle. Originally, Asakura *et al*. found that the Pt L_3-edge X-ray absorption near-edge structure (XANES) spectra quantitively reflect the H species adsorbed on small Pt particles.[32, 33] Since then, the density of states for Pt species has been analyzed through XANES spectra to quantify species adsorbed on Pt nanoparticles.[34-42]

Pt catalysts are known to be effective for the RWGS reaction, and thus they are desired for high selectivity toward CO.[21, 43-45] During hydrogenation of CO_2 over supported Pt catalysts, the product selectivity is closely related to the adsorbates (namely, H and CO) on the metal active sites, support surface, and the metal-support interface. Pt L-edge XAS is expected to be useful for monitoring species adsorbed on the surface of Pt particles during hydrogenation of CO_2. In particular, the simultaneous use of *in-situ* XAS with *in-situ* IR spectroscopy (*operando* XAS-IR) could distinguish the Pt atoms with attached H and CO species.[41, 46]

Among the various combinations of metal species and support materials, the interaction between Al_2O_3 and Pt is known to induce highly dispersed Pt particles, whereas Pt supported on SiO_2 surface forms relatively large particles.[5, 7, 47-52] In addition, Pt particles supported on γ-Al_2O_3 exhibit two-dimensional morphology with a low coordination number of the Pt species, owing to strong interaction with the penta-coordinated Al^{3+} sites on the γ-Al_2O_3 surface.[5, 7, 48, 53, 54] This unique interaction with the γ-Al_2O_3 surface would affect the product selectivity during hydrogenation of CO_2

over supported Pt particles.

In the current study, Pt catalysts supported on γ-Al_2O_3 or SiO_2 were prepared separately by impregnation. During hydrogenation of CO_2 at ambient pressure, γ-Al_2O_3-supported Pt (Pt/ Al_2O_3) displayed undesirable CH_4 production, whereas over SiO_2-supported Pt (Pt/SiO_2) CO was produced selectively but with a low efficiency. For the two Pt catalysts with different product selectivity, we carried out *operando* study with Pt L-edge XAS and diffuse reflectance infrared Fourier transform spectroscopy (DRIFTS). The results provide useful guidelines for controlling the selectivity during hydrogenation of CO_2, in addition to clearly elucidating the role of MSI effect between the loaded Pt particles and γ-Al_2O_3 surface for the catalytic activity.

Experimental

Supported Pt catalysts were prepared by impregnation with an aqueous solution of $Pt(NH_3)_2(NO_2)_2$ (Furuya metal Co. Ltd., Japan) at 353 K. The support materials were Al_2O_3 (JRC-ALO-7 supplied from the Catalysis Society of Japan; γ-Al_2O_3, S_{BET} = 163.5 m^2 g^{-1}) or SiO_2 (JRC-SIO-13 supplied from the Catalysis Society of Japan; amorphous SiO_2, S_{BET} = 284.7 m^2 g^{-1}). After impregnation, the catalysts were calcined at 673 K for 5 h. For *operando* experiments, catalytic-activity tests, and characterizations, the catalysts were reduced at 773 K for 30 min under 5% H_2 at a flow rate of 50 mL min^{-1}.

All *operando* experiments of combined XAS-DRIFTS were carried out on the BL01B1[55] beamline in SPring-8 (Japan Synchrotron Radiation Research Institute, Hyogo, Japan; 8 GeV, 100 mA). The XAFS spectra were collected using a double-crystal Si(111) monochromator. Higher harmonic X-rays were rejected by setting the glancing angle of the Rh-coated mirrors to 3.0 mrad. The incident (I_0) and transmitted (I_1) X-ray fluxes were measured using ionization chambers filled with N_2 (85%)/Ar (15%) and Ar (100%), respectively. Pt L_3- and L_2-edge XAFS spectra (absorption edge: 11564 and 13274 eV, respectively) were acquired in a transmittance mode with a Quick XAFS system.[56] The photon energy was calibrated at the inflection point of the Pt L_3-edge XANES spectra of reference Pt metal foil (11564 eV). The data reduction was performed using Athena and Artemis software ver. 0.9.25 included in Ifeffit 1.2.12 package.[57] The k^3-weighted extended X-ray absorption fine structure

(EXAFS) oscillation in the range of 3−14 $Å^{-1}$ was Fourier transformed. The curve fitting analysis was performed in the range of 1.8−3.0 Å in *R* space. The backscattering factor and the phase shift of each scattering path were calculated with FEFF6L using the crystal structures of fcc Pt metal (*Fm*−3*m*). The amplitude reduction factor (S_0^2) was also estimated by fitting the reference spectrum of Pt foil with the parameters calculated with FEFF. According to Mansour *et al.*, the unoccupied states of Pt samples, h_T, was estimated using the following equation:[58, 59]

$$h_T = (1+f_d)h_r \quad (1)$$

where h_r is the unoccupied *d*-electron states of bulk Pt (Pt foil), which is reported to be 0.30−0.40.[60, 61] f_d, the indicator of unoccupied states of Pt samples, is expressed as:

$$f_d = (\Delta A_3 + 1.11\Delta A_2) / (A_{3r} + 1.11A_{2r}) \quad (2)$$

$$\Delta A_3 = A_3 - A_{3r}, \Delta A_2 = A_2 - A_{2r} \quad (3)$$

where A_3 and A_2 are the areas of normalized Pt L_3- and L_2-edge XANES spectra from 10 eV below to 13 eV above the X-ray absorption edge. A_{3r} and A_{2r} are those of the reference Pt foil.

All *in-situ* measurements were performed using an XAS-DRIFTS cell equipped with a heater and thermocouples (S.T. Japan Inc., Japan, **Figure 1(A)** and **(B)**). Products at the outlet of the reactor were analyzed by dual channel μGC (490 Micro GC, Agilent Technologies Inc., U.S.), which was placed at downstream and equipped with two thermal conductivity detectors (TCDs) along with a 5Å Molecular Sieve and Pora PLOT Q column and He as the carrier gas (**Figure 1(C)**). The X-ray beam was transmitted through the Kapton® membrane and samples (27 mg) mounted in a sample cup (inner diameter: 7 φ) of Al_2O_3. The IR beam through a CaF_2 window was reflected at the sample surface and detected by a mercury cadmium telluride (MCT) detector through a catadioptric optical system (Pike Technologies, U.S.). The IR spectra were collected by an IR spectrometer (Bruker Vertex 70, Bruker, U.S.) by summing 40 scans with a resolution of 4 cm^{-1}. A background IR spectrum was collected under a flow of He at 100-K temperature intervals during the cooling, after H_2 pretreatment at 773 K for 30 min. After cooling the XAS-DRIFTS cell to 303 K, 10% CO_2 was introduced for 20 min and then 40% H_2 was added for 20 min. After recording the XAS and DRIFTS data and the product analysis (which started after 15 min of gas introduction for complete gas replacement), the cell was heated to 373 K. Then, the temperature was raised to 773 K in steps of 100 K with 15 min waiting at each temperature, before the XAS, DRIFTS, and product analysis (**Figure 1(D)**). The same pretreatment was also

performed prior to measurement under 4% H_2 or 1% CO flow with the same temperature profile.

Hydrogenation of CO_2 was carried out in the laboratory over supported Pt catalysts (27 mg, MgO, TiO_2, SiO_2, SiO_2-Al_2O_3, Al_2O_3, CeO_2, and ZrO_2) in a fixed bed flow reactor (inner diameter: 8 φ) at ambient pressure. Following H_2 pretreatment, the catalyst was exposed to 50 mL min^{-1} flow of mixed gas containing 10% CO_2, 40% H_2, 0.5% N_2 as the internal standard, and He as the balance. The catalytic activity was measured at 25 K intervals between 673 and 823 K. The produced CO and CH_4 were analyzed by gas chromatography (GC) using two GC-8A chromatographs (Shimadzu Corp., Japan) equipped with a TCD and a flame ionization detector (FID), along with a 5Å Molecular Sieve column (Shimadzu Corp., Japan) and He as the carrier gas. Based on the gas composition at the reactor outlet, the yields of CO (Y_{CO}) and CH_4 (Y_{CH4}) were calculated using the following equation:

$$Y_{CH4\ or}\ Y_{CO} = 100 \times (F_{CH4,\ out\ or}\ F_{CO,\ out})/F_{CO2,\ in} \qquad (4)$$

where F_i is the molar ratio of component i at the inlet or outlet of the reactor.

CO pulse titration was performed by a flow-type chemical adsorption measuring apparatus (BELCAT-II, MicrotracBEL Corp., Japan). After reduction treatment with 5% H_2/He at 773 K for 30 min, the reaction tube containing 50 mg catalyst was injected with CO carried by H_2 gas at 323 K. The amount of CO consumed was monitored with a TCD contained in the BELCAT-II system. The number of surface metal atoms was estimated by using the adsorbed amount of CO from pulse titration at 323 K, assuming a chemisorption stoichiometry of CO:Pt = 1. The average particle size was estimated from the adsorbed amount of CO using the hemispherical model.

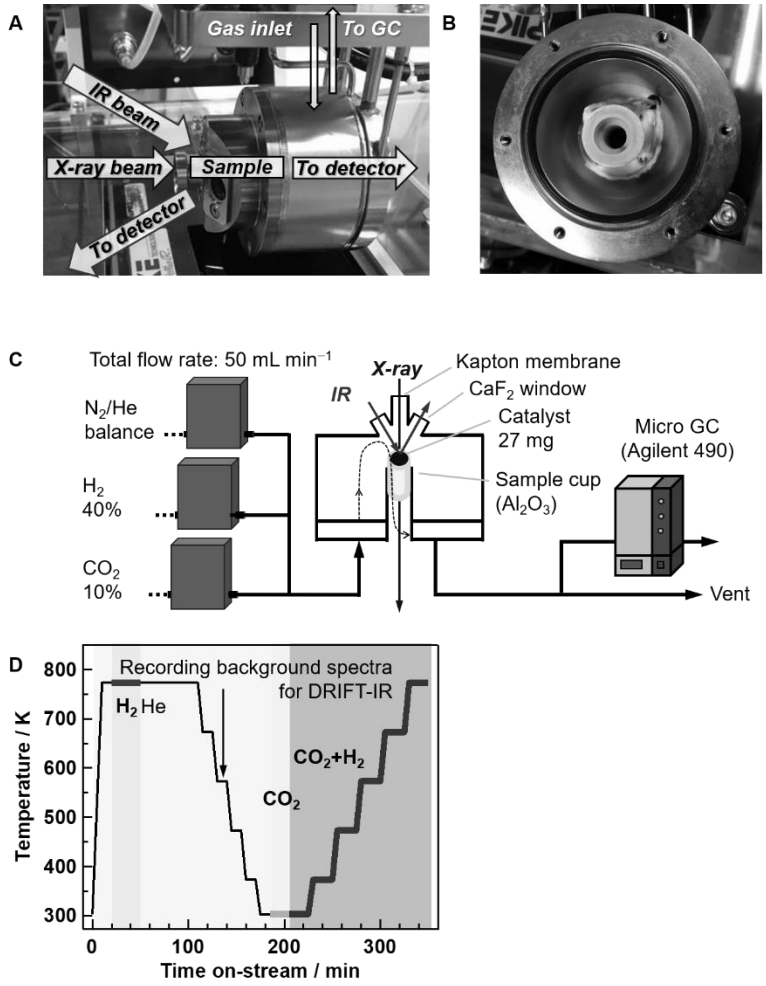

Figure 1. Experimental setup for *operando* XAS-DRIFTS measurement at the SPring-8 BL01B1 beamline. **(A)** External side view of the XAS-DRIFTS cell. **(B)** Internal top view of the XAS-DRIFTS cell. **(C)** Experimental setup for the measurement. **(D)** Typical experimental scheme.

Results and discussion

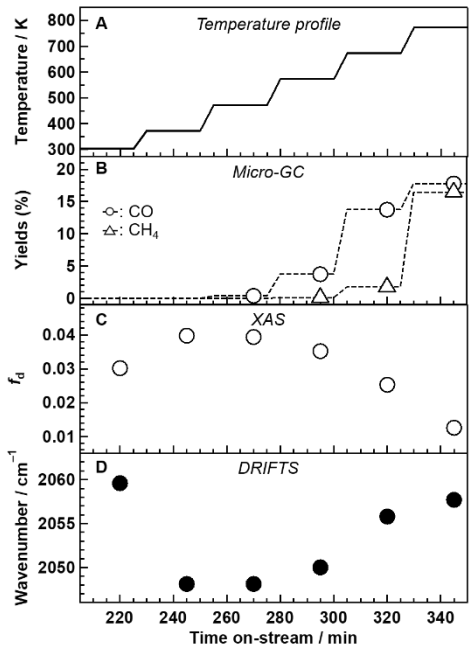

Figure 2. Time profiles of *operando* XAS-DRIFTS data during hydrogenation of CO_2 over Pt/Al_2O_3. **(A)** Temperature profile as a function of time on-stream. **(B)** Yields of hydrogenation products at the reactor outlet measured by μGC placed at downstream. **(C)** f_d values estimated from Pt L_3- and L_2-edge XANES. **(D)** Peak-top frequencies of the IR absorption band of CO species adsorbed on Pt surface.

Figure 2 shows a time profile of data obtained from *operando* XAS-DRIFTS during hydrogenation of CO_2 over Pt/Al_2O_3. The cell temperature was raised to 773 K in steps of 100 K with 20-min waiting at each temperature. The reaction products, XAFS data, and DRIFTS data were recorded 15 min after raising the temperature.

Figure 3(A) shows the reaction products during hydrogenation of CO_2 over Pt/Al_2O_3 and Pt/SiO_2 catalysts in the *operando* XAS-DRIFTS setup. Over Pt/Al_2O_3, a considerable amount of CH_4 was produced together with CO, resulting in a 52% selectivity toward CO. In contrast, Pt/SiO_2 exhibited higher yields of CO (97% selectivity) while the formation of CH_4 was suppressed. When the same reaction was carried out in the quartz tube fixed bed reactor in the laboratory, the same trends were observed although the detailed yields were different from those in the *operando* XAS-DRIFTS cell (**Figure 4** and **Table 1**). CH_4 was formed when using Al_2O_3, ZrO_2, or CeO_2 as the support material, whereas the selective formation of CO was achieved when using MgO, TiO_2, SiO_2, and SiO_2-Al_2O_3.

The CH_4 formation over CeO_2-supported Pt catalyst is consistent with that reported by Amal *et al.*[27] Moreover, the product selectivity and turnover frequencies were totally different for Pt catalysts on different supports, clearly showing that the MSI played a significant role in the hydrogenation of CO_2 over supported Pt catalysts.

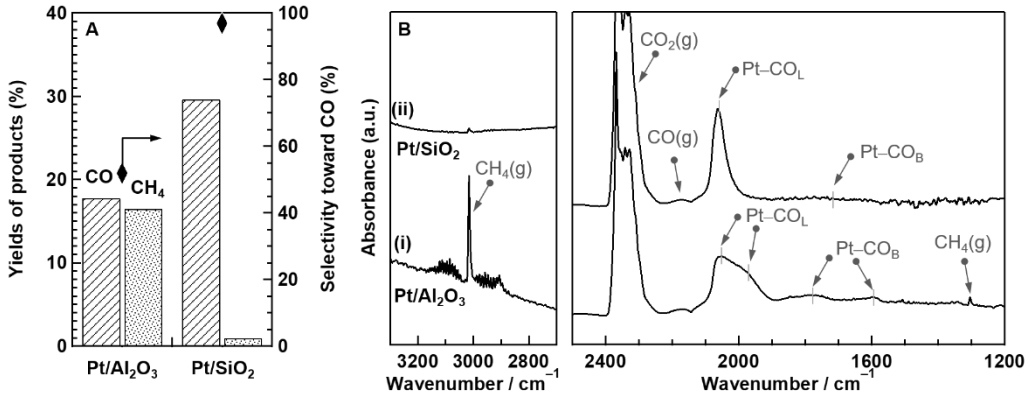

Figure 3. (A) Yields of products (hatched: CO, dotted: CH_4) and selectivity toward CO (black diamond) during hydrogenation of CO_2 at 773 K over 5wt% Pt/Al_2O_3 and Pt/SiO_2 catalysts. m_{cat} = 27 mg, 10% CO_2 and 40% H_2 in He (total flow rate = 50 mL min^{-1}). **(B)** DRIFT-IR spectra of adsorbed species during hydrogenation at 773 K over (i) Pt/Al_2O_3 and (ii) Pt/SiO_2 catalysts. The reduction pretreatment was performed at 773 K for 30 min, prior to measurement in *operando* XAS-DRIFT cell. The background spectrum was recorded under He flow at 773 K after pretreatment. The products at the reactor outlet were analyzed by μGC placed at downstream.

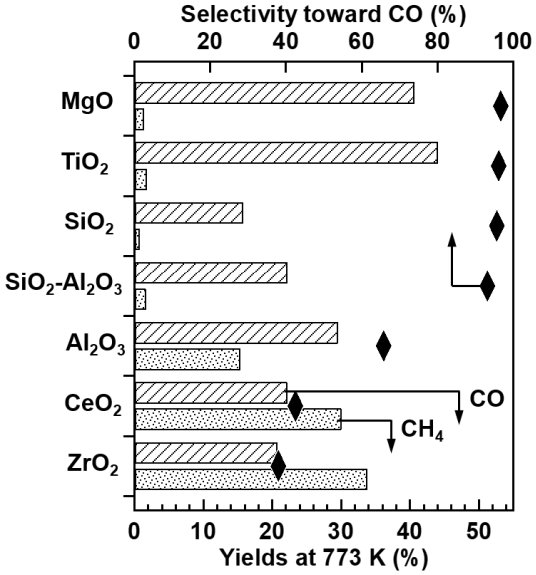

Figure 4. Yields of products (hatched: CO, dotted: CH_4) and selectivity toward CO (diamonds) during hydrogenation of CO_2 at 773 K over supported Pt catalysts in the fixed bed reactor in the laboratory. The total amount of the metal species was fixed at 5wt%. m_{cat} = 27 mg, 10% CO_2 and 40% H_2 in He (total flow rate = 50 mL min^{-1}).

Table 1. Hydrogenation of CO_2 over supported Pt catalysts measured in the fixed bed reactor in the laboratory. The total amount of metal species was fixed at 5wt%. m_{cat} = 27 mg, 10% CO_2 and 40% H_2 in He (total flow rate = 50 mL min^{-1}). The reaction temperature was 773 K.

Support[a] (5wt% Pt)	CO adsorption[b] / μmol g_{cat}^{-1}	Dispersion[b] / %	TOF_{CH4}[c] / mmol mol_{Pt}^{-1} s^{-1}	TOF_{CO}[c] / mmol mol_{Pt}^{-1} s^{-1}	Selectivity toward CO[b]/ %
MgO	52.4	20	3.7×10	106.8×10	97
TiO_2	20.6	-	-	-	96
SiO_2	84.6	33	1.2×10	25.7×10	96
SiO_2-Al_2O_3	96.0	37	2.3×10	31.8×10	93
Al_2O_3	138.5	54	15.3×10	29.4×10	66
CeO_2	98.1	-	-	-	42
ZrO_2	68.1	27	68.4×10	41.9×10	38

[a] The supported Pt catalysts were prepared by impregnation with an aqueous solution of $Pt(NH_3)_2(NO_2)_2$, the same as with the Al_2O_3- and SiO_2-supported Pt catalysts. Support materials: MgO (JRC-MGO-4 supplied from the Catalysis Society of Japan), TiO_2 (ST-01 purchased from Ishihara Sangyo Kaisya. Ltd., Japan), SiO_2-Al_2O_3 (JRC-SAL-1 supplied from the Catalysis Society of Japan), CeO_2 (CEO-2 supplied from the Catalysis Society of Japan), and ZrO_2 (JRC-ZRO-6 supplied from the Catalysis Society of Japan). For TiO_2- and CeO_2-supported catalysts, only the amount of CO adsorption and selectivity toward CO were displayed, since the strong MSI effect and/or the spillover of CO to support surface could occur.

[b] The amount of exposed Pt atoms was estimated by using CO pulse titration data at 323 K, assuming a chemisorption stoichiometry of CO:Pt = 1.

[c] Product formation rates per surface-metal atom (TOF_{CH4} or TOF_{CO}) were calculated as

$$TOF \text{ (mol } mol_{Pt}^{-1} s^{-1}) = TF \text{ (mol } s^{-1}) \times F / (N_{surf} \text{ (mol } g_{cat}^{-1}) \times 0.027 \text{ (g))}$$

where TF, F, and N_{surf} are the total flow at reactor outlet expressed in mol s^{-1}, the molar ratio of CH_4 or CO at reactor outlet, and the estimated mole of exposed Pt atoms per 1.0 g of catalyst, respectively.

The DRIFT spectra (**Figure 3(B)**) reveal the surface-adsorbed species and gas phase products over the Pt catalysts. For Pt/Al_2O_3, absorption bands attributed to CH_4 (1306 and 3016 cm^{-1}) and CO (2050 to 2200 cm^{-1}) molecules in the gas phase appeared, accompanied by that of CO_2 substrate (2200 to 2400 cm^{-1}). In contrast, the spectrum over Pt/SiO_2 showed weak band of CH_4 at 3016 cm^{-1} and considerable absorption band of CO molecules in the gas phase, which was consistent with the quantification results of products. The different product selectivity between Pt/Al_2O_3 and Pt/SiO_2

would be attributed to the particle size, morphologies, and the electronic states of the supported Pt species, and these aspects are reflected in the species adsorbed on the catalyst surface during the reaction. For Pt/Al_2O_3, CO species on the Pt surface had the linear form (CO_L species, 1900 to 2100 cm^{-1}) and the bridged form (CO_B species, 1600 to 1900 cm^{-1}).[43, 62-64] Pt/SiO_2 also exhibited the absorption bands of CO_L and CO_B. However, the CO_L band on Pt/SiO_2 was narrower than that on Pt/Al_2O_3, indicating that the unique electronic structure of Pt species on Al_2O_3 affected the C=O bond energy of CO attached on Pt, or that some other species was formed on the Pt surface during CH_4 production. To identify the absorbed species during the reaction (which would determine the product selectivity) Pt L-edge XANES spectra were simultaneously monitored *in situ*, namely under the *operando* XAS-DRIFTS condition.

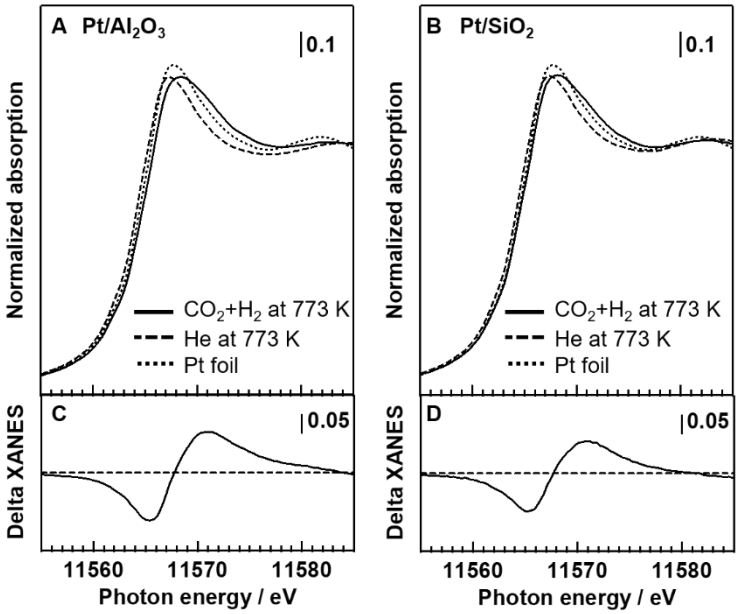

Figure 5. Pt L_3-edge XANES spectra from *operando* XAS-DIRIFTS observation for **(A)** Pt/Al_2O_3 and **(B)** Pt/SiO_2 during hydrogenation of CO_2 at 773 K (solid line) and that under He at 773 K after pretreatment (dashed line). Dotted line: reference spectrum of Pt foil measured at room temperature. **(C)** and **(D)** The delta XANES spectra (the difference between hydrogenation condition and under He flow) over Pt/Al_2O_3 and Pt/SiO_2, respectively.

Figure 5 shows the Pt L_3-edge XANES spectra of Pt/Al_2O_3 and Pt/SiO_2 under *operando* XAS-DRIFT observation. After reduction pretreatment at 773 K, the spectra of Pt/Al_2O_3 and Pt/SiO_2 were identical to that of Pt foil, and their slightly lower absorption peaks compared to Pt foil is attributed to

the different electronic states of nanoparticles from that of bulk Pt.[58, 59, 65-67] For Pt/Al_2O_3, the spectrum under hydrogenation condition was shifted to higher energy owing to the change in the unoccupied states of Pt species by interaction with the adsorbed intermediates, and this is clearly shown in the difference spectrum (delta XANES spectrum, **Figure 5(C)**). Pt/SiO_2 also showed a spectral change between hydrogenation condition and under He. However, the amplitude of the delta XANES spectrum was less than that of Pt/Al_2O_3. The amount of surface Pt atoms over Pt/Al_2O_3 catalyst estimated by CO pulse titration (138.5 μmol g_{cat}^{-1}) was larger than that of Pt/SiO_2 (84.6 μmol g_{cat}^{-1}). This is one plausible reason for the different spectral changes. However, a difference in the adsorbed intermediates would also affect the unoccupied states of Pt species and the X-ray spectra. In many cases, the morphology and electronic states of Pt particles would also significantly influence the adsorption of intermediates. Thus, below we further examine the geometric and electronic states of the Pt particles supported on Al_2O_3 and SiO_2.

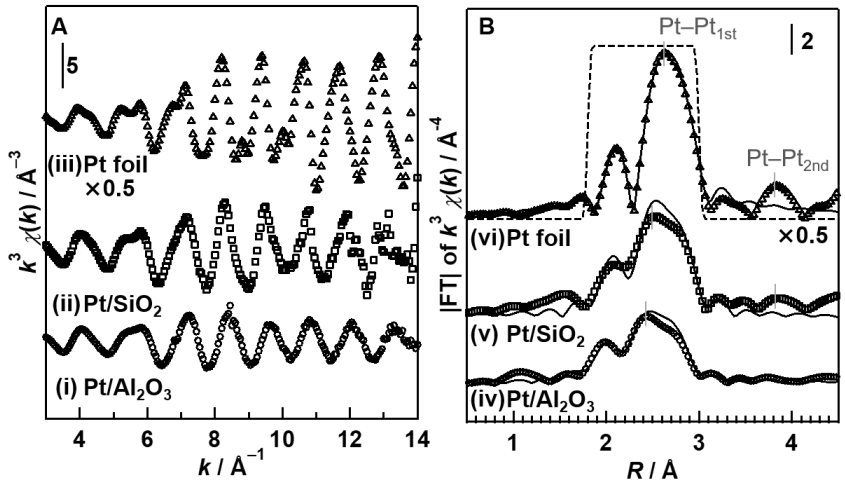

Figure 6. (A) Pt L_3-edge EXAFS oscillations of (i) Pt/Al_2O_3 (circles), (ii) Pt/SiO_2 (squares), and (iii) reference Pt foil (triangles). The spectra of Pt-loaded catalysts were obtained at 303 K under He flow after reduction pretreatment. **(B)** Pt L_3-edge Fourier-transformed EXAFS oscillations of (iv) Pt/Al_2O_3 (circles), (v) Pt/SiO_2 (squares), and (vi) reference Pt foil (triangles). Fitting results in the range of 1.8−3.0 Å in *R* space are shown as solid lines. The dashed line depicts the fitting window.

Table 2. Fitting results of EXAFS oscillations performed in *R* space [a].

Sample	*C.N.*	*r* / Å	Δ*E* /eV	σ^2 (10^{-3})	*R*-factor
Pt/Al_2O_3	6.9 (0.5)	2.68 (0.01)	5.83 (0.73)	9.54 (0.43)	0.004
Pt/SiO_2	9.6 (0.8)	2.73 (0.01)	8.90 (0.95)	8.63 (0.42)	0.005
Pt foil	12 (fixed)	2.76 (0.01)	9.11 (0.31)	4.92 (0.11)	0.001

[a] *C.N.*: coordination number; *r*: bond distance; Δ*E*: energy shift of the absorption edge; σ^2: Debye-Waller factor.
The amplitude reduction factor (S_0^2) value of 0.864 was determined by fitting data for the Pt foil. Numbers in parentheses represent uncertainties for the fits. The reliability factor (*R*-factor) is defined as $\Sigma[k^3\chi_{obs}(k) - k^3\chi_{cal}(k)]^2 / \Sigma[k^3\chi_{obs}(k)]^2$, where χ_{obs} and χ_{cal} correspond to the observed and calculated data, respectively.

Figure 6(A) shows the Pt L_3-edge EXAFS oscillations of Pt-loaded catalysts after reduction pretreatment, measured at 303 K under He flow. Both Pt/Al_2O_3 and Pt/SiO_2 exhibited oscillation shapes similar to that of reference Pt foil, although the oscillation amplitude of Pt/Al_2O_3 was smaller than that of Pt/SiO_2. In the corresponding Fourier transforms (**Figure 6(B)**), Pt foil exhibited peaks at around 2.0–3.0 and 3.8 Å, which were assignable to the scattering of the first and second coordination of Pt–Pt shell, respectively. For the first coordination in Pt/Al_2O_3, the peak top of the Pt–Pt scattering is located at a shorter distance than those of Pt/SiO_2 and Pt foil, indicating different location of Pt atoms in the Pt/Al_2O_3 catalyst. In addition, there was only a negligible scattering peak for the second coordination of Pt–Pt shell at 3.8 Å, while it was obvious in the oscillations of Pt/SiO_2. The curve fitting analysis was performed in the range of 1.8−3.0 Å in *R* space, and the results are shown as solid lines in **Figure 6(B)** (the parameters are summarized in **Table 2**). The obtained coordination number of Pt–Pt shell of Pt/Al_2O_3 (*C.N.*(Pt–Pt) = 6.9) was much smaller than that of Pt/SiO_2, and this result is consistent with the particle dispersion estimated from CO pulse titration. However, the value of *C.N.*(Pt–Pt) in Pt/Al_2O_3 was also curiously low compared to that estimated by using the hemi-cuboctahedron model of a three-dimensional particle: the hemi-cuboctahedral Pt nanoparticle at a dispersion of 50% is composed of 185 Pt atoms with an averaged *C.N.*(Pt–Pt) = 8.0 (detailed numbers of atoms are shown in **Table 3**). In contrast, Pt/SiO_2 exhibited *C.N.*(Pt–Pt) = 9.6, which is consistent with the estimated value of 9.4 from the three-dimensional hemi-cuboctahedron model at a dispersion

of 34%. Vaarkamp *et al.* proposed a morphology change in the Pt particles from three-dimensional to two-dimensional raft-like upon H_2 reduction of Pt/γ-Al_2O_3, prepared by the impregnation of 1wt% H_2PtCl_6 precursor.[53] we observed the morphology change of three-dimensional PtO_x particles into two-dimensional Pt particles with a low coordination number for Pt species during reduction by using *in situ* time-resolved XAS technique (Chapter 3). Thus, we consider the low-coordinated Pt species in Pt/γ-Al_2O_3 as evidence for the formation of two-dimensional raft-like Pt particles. The shorter first-shell Pt–Pt distance and low-energy edge shift of Pt/Al_2O_3 as compared to Pt/SiO_2 and Pt foil would be attributed to the characteristic structure of Pt particle on the Al_2O_3 surface.

Table 3. Structure model of hemi-cuboctahedron particle [a]

Num. of atoms on each side	Num. of contained atoms	Num. of surface atoms	Num. of perimeter atoms	Dispersion (%)	*C.N.*(Pt–Pt)
5	185	93	24	50	8.0
7	525	199	36	38	-
8	792	267	42	34	9.4
9	1137	345	48	30	

[a] The model of supported Pt particle was assumed to be hemi-cuboctahedron with n atoms on each side. The numbers of total contained atoms ($A_{total}(n)$), surface atoms ($A_{surface}(n)$), interfacial atoms with the support surface ($A_{interface}(n)$), perimeter atoms at the interface ($A_{perimeter}(n)$), and the bonding between atoms are expressed in the following equations:

$$A_{total}(n) = 1/3\ n\ (5n^2-3n+1)$$
$$A_{surface}(n) = A_{total}(n)-A_{total}(n-1) = 5n^2-7n+3$$
$$A_{interface}(n) = 3n^2-3n+1$$
$$A_{perimeter}(n) = A_{interface}(n)-A_{interface}(n-1) = 6(n-1)$$
$$N_{bonding}(n) = 4(5n^3-12n^3+10n-3)$$

The dispersion of Pt atoms was calculated by $A_{surface}(n)/A_{total}(n)$. The average coordination number is $A_{total}(n)/N_{bonding}(n)$.

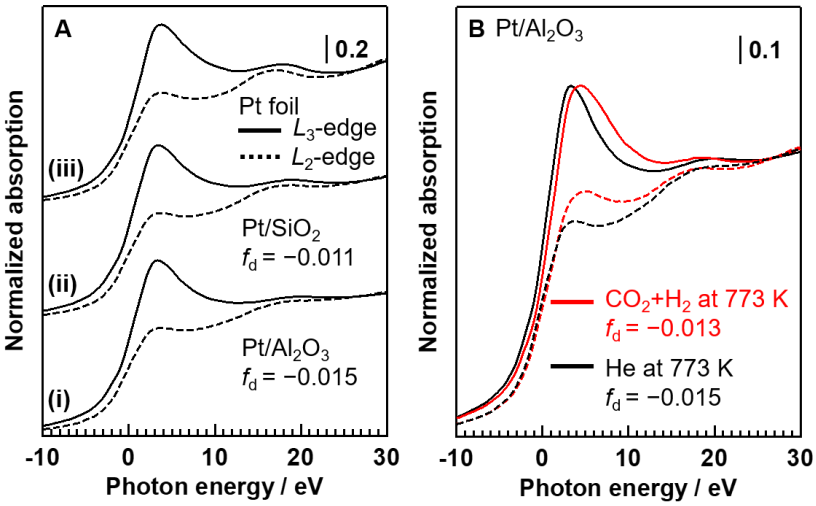

Figure 7. (A) Pt L_3- (solid lines) and L_2-edge (dashed lines) XANES spectra of (i) Pt/Al_2O_3, (ii) Pt/SiO_2, and (iii) reference Pt foil. The spectra of Pt/Al_2O_3 and Pt/SiO_2 were obtained at 773 K under He flow after reduction pretreatment. (B) Pt L_3- and L_2-edge XANES spectra of Pt/Al_2O_3 obtained at 773 K under He flow (black lines) and during hydrogenation of CO_2 (10% CO_2+40% H_2, red lines). The energy offsets were 11564 eV for L_3-edge and 13274 eV for L_2-edge.

To evaluate the unoccupied states of Pt species, we also measured Pt L_2-edge XANES spectra of supported Pt catalysts after reduction (**Figure 7(A)**). Whereas the absorptions of L_3-edge transition ($2p_{3/2}\rightarrow5d_{5/2}$, $5d_{3/2}$) exibited large peaks owing to the unoccupied states of Pt $5d_{5/2}$, small absorption peaks appeared in L_2-edge XANES spectra ($2p_{1/2}\rightarrow5d_{3/2}$).[35] The f_d value of Pt species for Pt/Al_2O_3 estimated using the method of Mansour *et al.*[58, 59] was −0.015, indicating that the Pt species on Al_2O_3 was rich in *d*-electrons as compared to bulk Pt. This f_d value is reasonable compared to that of Pt/Al_2O_3 prepared by Yazawa *et al.* in a similar method.[66] For Pt/SiO_2, the f_d value of −0.011 was higher than that of Pt/Al_2O_3, namely, Pt species supported on SiO_2 had lower *d*-electron density than that on Al_2O_3. The order in the f_d of Pt species (Pt/Al_2O_3 > Pt/ SiO_2 > Pt foil) matches the order of *C.N.*(Pt–Pt) in **Table 2**. Naturally, Pt particles supported on Al_2O_3 with rich in dangling bonds exhibited high *d*-electron density on Pt. Mansour *et al.* reported the electron transfer from Pt to Al_2O_3 support after reduction at 473 K.[58] However, such electron-donating Pt species were not observed in our system with high-temperature reduction. Thus, among the three samples (Pt/Al_2O_3, Pt/SiO_2, and Pt foil), the particle size or particle morphology, rather than the electron transfer between metal and support surface, had a stronger effect on the *d*-electron density. From the values of *C.N.*(Pt–Pt) and f_d values, Pt species supported on Al_2O_3 formed two-dimensional raft-like Pt particles with a high electron density mainly

due to the small particle size, whereas those on SiO_2 maintained a three-dimensional form with relatively large particle size.

Figure 7(B) displays the Pt L_3- and L_2-edge XANES spectra of Pt/Al_2O_3 under He flow and during hydrogenation of CO_2 at 773 K. In addition to the high energy shift of L_3-edge XANES spectrum upon adsorption of intermediates (**Figure 5(A)**), the white line intensity of L_2-edge XANES spectrum during hydrogenation increased as compared to that under He. The estimated f_d value of −0.013 was slightly higher than that of Pt particles on Al_2O_3 without adsorbed species. This increase in the apparent *d*-electron density upon adsorption of intermediates was due to an increase in the unoccupied states that resulted from the formation of bonding and antibonding orbitals. For instance, a surface Pt orbital and a chemisorbed H 1*s* orbital form an occupied bonding orbital more localized on H, and an antibonding orbital more localized on Pt.[35, 68] The bonding of chemisorbed H species pushes part of the Pt density of states (DOS) from below the Fermi level to just above the valence band into the antibonding states, resulting in the high energy shift of the absorption edge of L_3-edge transition ($2p_{3/2} \rightarrow 5d_{5/2}$, $5d_{3/2}$).[35] Moreover, the chemisorption of H species on Pt surface results shifts the Pt $5d_{3/2}$ component of antibonding states below the Fermi level of Pt, [68] which likely leads an increased L_2-edge absorption ($2p_{3/2} \rightarrow 5d_{3/2}$). The high energy shift of L-edge XANES upon CO chemisorption was also attributed to the formation of antibonding states by the overlap of Pt *d*-orbital with the $2\pi^*$ orbital of C species.[40, 69]

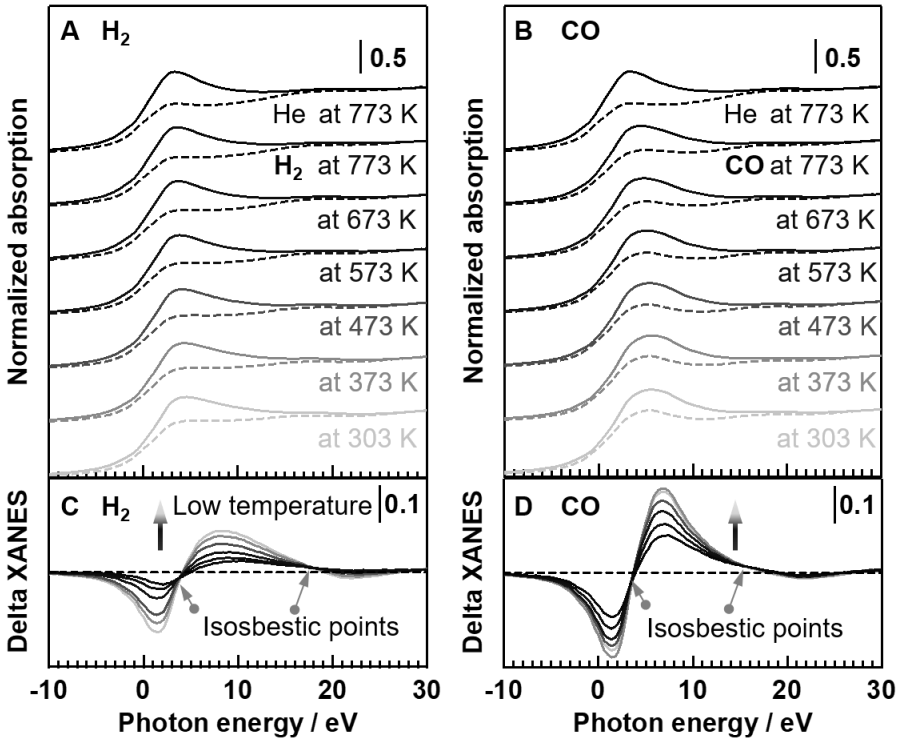

Figure 8. Pt L_3- (solid lines) and L_2-edge (dashed lines) XANES spectra of Pt/Al_2O_3 under **(A)** 4% H_2 and **(B)** 1%CO flow at various temperatures. Black line: spectrum obtained at 773 K under He flow after reduction pretreatment. A series of spectra were measured from 303 K to 773 K under each gas flow. The corresponding difference spectra of Pt L_3-edge XANES under **(C)** H_2 and **(D)** CO flow from that under He flow, respectively.

We monitored the change in the unoccupied states of Pt species as an indicator of the amount of surface-adsorbed species during reaction. The f_d values during reaction was compared with those under H_2 and CO flow to estimate the surface-adsorbed species during hydrogenation. First, **Figure 8(A)** and **(B)** show the Pt L_3- and L_2-edge XANES spectra of Pt/Al_2O_3 under H_2 and CO flow at various temperatures, respectively. To clearly see the temperature dependence, **Figures 8(C)** and **(D)** display the corresponding difference spectra against that under He flow (delta XANES spectra). The spectra under H_2 flow exhibited large shifts in absorption with decreasing temperature, showing the isosbestic point. Those are consistent with the results Asakura *et al.* reported in their quantitative evaluation of the amount of H species adsorbed on Pt surface from delta L_3-edge XANES.[32, 33] The spectra under CO flow also showed similar trend at various temperatures, although the absorption difference was larger than that under H_2. We evaluated the unoccupied states of Pt species including the antibonding orbitals under a series of conditions based on eqs. (1–3).

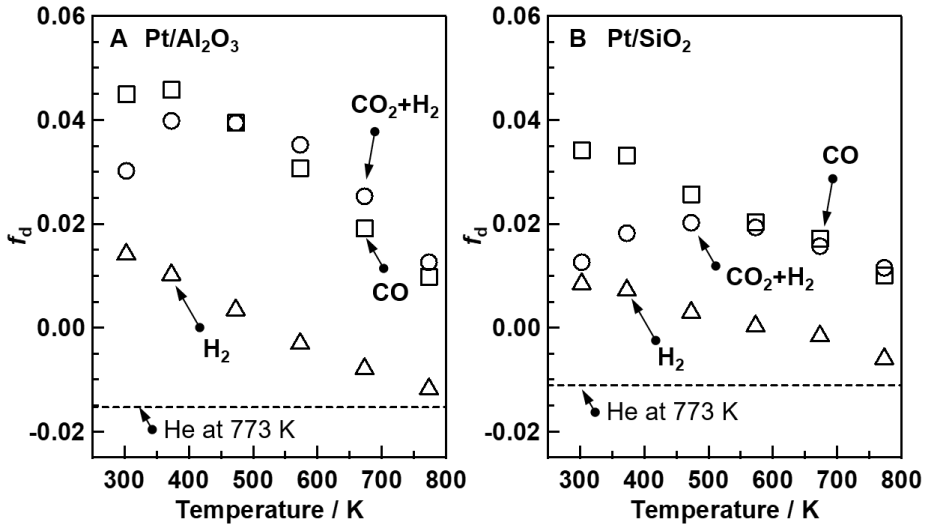

Figure 9. Estimated f_d values of Pt species for **(A)** Pt/Al_2O_3 and **(B)** Pt/SiO_2 at various temperatures during hydrogenation of CO_2 (10% CO_2+40% H_2, circles), under 4% H_2 flow (triangles), and under 1% CO flow (squares). Dashed lines are the f_d values of each catalyst at 773 K under He flow after reduction pretreatment.

Figure 9(A) and **(B)** display the estimated f_d values of Pt species in Pt/Al_2O_3 and Pt/SiO_2 at different temperatures, respectively. These values are higher than those under He at 773 K (namely, Pt particles with clear surface), owing to the formation of empty orbitals by chemisorption as mentioned above. Pt/Al_2O_3 under CO flow at 303 K exhibited $f_d = 0.045$ and it was maintained even at 373 K, suggesting that the Pt surface was fully covered by CO species at 373 K. The f_d value decreased with ramping temperature and reached 0.010 at 773 K. Under H_2 flow, the f_d value linearly decreased with ramping temperature, from 0.014 at 303 K to −0.012 at 773 K. In a previously reported temperature-programmed desorption profile of H_2 over Pt/Al_2O_3, the desorption of H species on Pt was observed at above 373 K.[70] So, we consider that a Pt surface fully covered with H species was obtained at 303 K. Thus, the difference of f_d from that of clear Pt surface reflects the amount of adsorbed CO and H species.

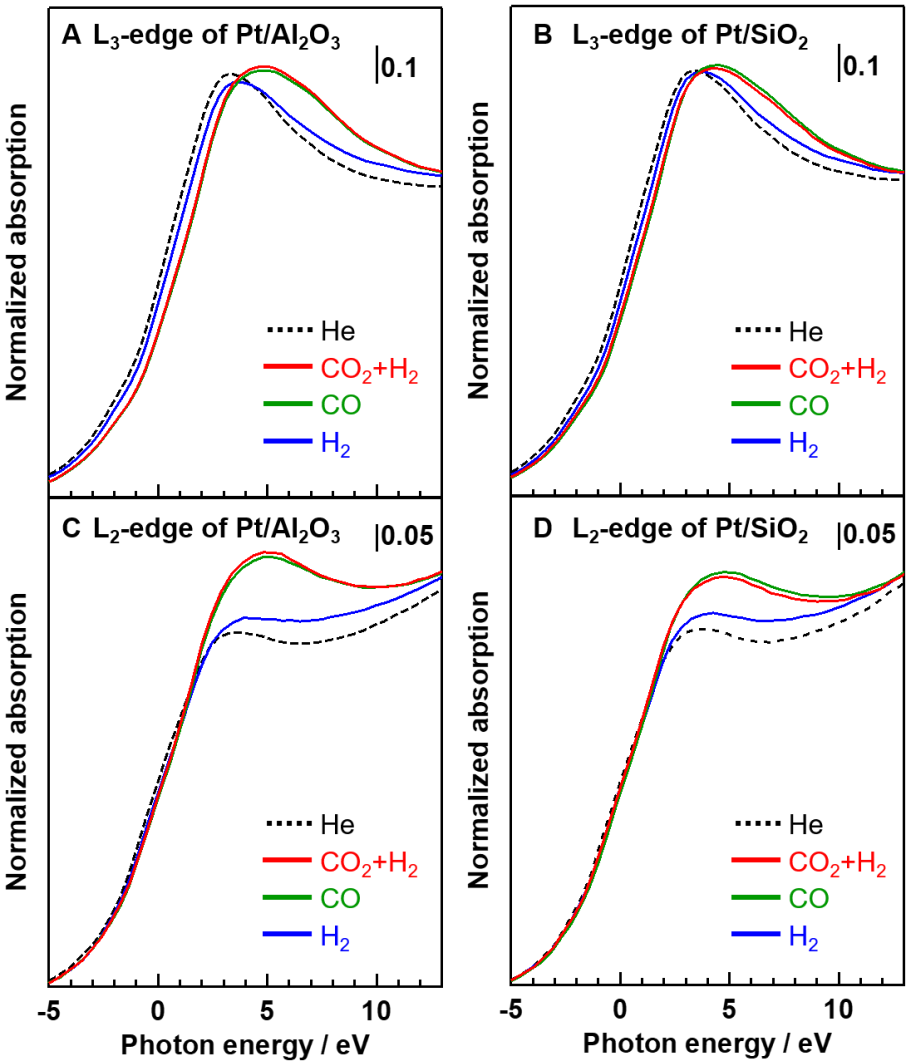

Figure 10. Pt L_3-edge XANES spectra of **(A)** Pt/Al_2O_3 and **(B)** Pt/SiO_2 under various gas flows at 673 K. Pt L_2-edge XANES spectra of **(C)** Pt/Al_2O_3 and **(D)** Pt/SiO_2 under various gas flows at 673 K. Dashed black line: He flow, red solid line: 10% CO_2+40% H_2, blue solid line: 4% H_2, red solid line: 1% CO.

Under hydrogenation, the f_d value of Pt/Al_2O_3 was 0.030 at 303 K and increased to 0.04 at 373 K. Above 473 K, f_d decreased with increasing temperature to 0.013 at 773 K. Notably, Pt/Al_2O_3 under hydrogenation at 573–773 K has higher f_d values than those under CO flow at the corresponding temperatures. Here, the f_d value at 673 K (when all available adsorption sites of Pt were filled with CO species) was 0.019, whereas that under hydrogenation at 673 K was 0.025. We attribute this high f_d value under hydrogenation to the adsorption of H species in addition to that of CO species. In contrast, Pt/SiO_2 under hydrogenation at 673 K exhibited a lower f_d value than that under CO at the same temperature, i.e., a relatively smaller amount of H species was adsorbed on Pt/SiO_2. From the raw

spectra at 673 K in **Figure 10**, the L_3- and L_2-edge of XANES spectra for Pt/Al_2O_3 under hydrogenation were indeed slightly higher than those under CO flow, whereas for Pt/SiO_2 they were lower under hydrogenation than under CO flow. Thus, Pt/Al_2O_3 and Pt/SiO_2 exhibited totally different trends in the f_d values during hydrogenation. We consider the adsorption of H species with CO species to be a key to the formation of CH_4 over Al_2O_3-supported Pt catalysts. In other words, co-adsorbed H species induced the hydrogenation of adsorbed CO species toward CH_4.

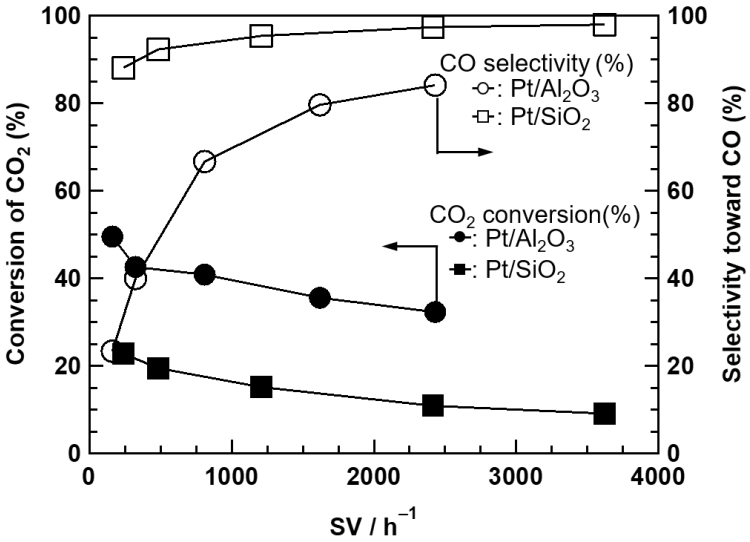

Figure 11. Results for hydrogenation of CO_2 at various total flow rates of feed gas (10, 20, 50, 100, and 150 mL min^{-1}) over 5wt% Pt/Al_2O_3 and Pt/SiO_2 catalysts. m_{cat} = 27 mg, 10% CO_2 and 40% H_2 in He. The space velocity (h^{-1}) was determined by the volume estimated using sample tube.

To reveal the stepwise hydrogenation of adsorbed CO toward CH_4, the reaction was performed under different flow rates, and the results are shown in **Figure 11**. The conversion of CO_2 increased with decreasing space velocity (SV) over both Pt/Al_2O_3 and Pt/SiO_2. The selectivity toward CO over Pt/Al_2O_3 dramatically decreased at lower SV, whereas that over Pt/SiO_2 had insignificant dependence on SV. Thus, Pt species supported on Al_2O_3 induced the stepwise hydrogenation of CO produced in the gas phase towards CH_4, whereas that supported on SiO_2 was inactive for these reaction steps. Moreover, the formation of CH_4 over Pt/Al_2O_3 was relatively durable, although a slight decrease in the selectivity toward CH_4 was observed (**Figure 12**). Since the activity for forming CH_4 recovered through the H_2 treatment, we consider that the surface-deposited carbon species prevents the methanation of adsorbed CO species, as established mechanism in methanation of over Ni catalysts.[71,

[72] These results strongly suggest the subsequent hydrogenation of adsorbed CO species toward CH_4 over Pt surface.

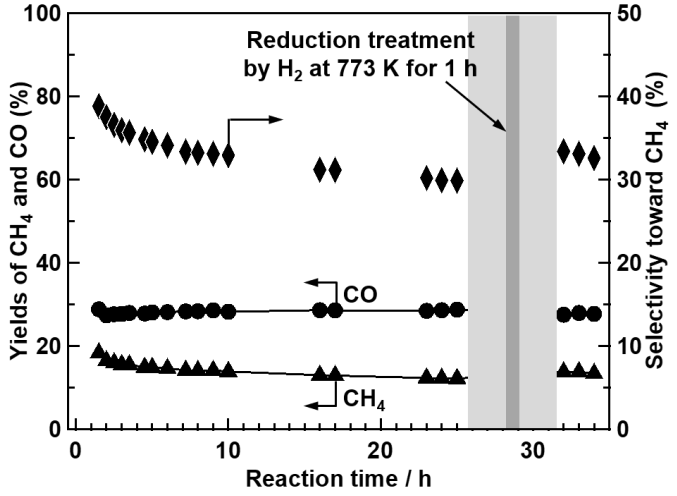

Figure 12. Time course of the product yields (CH_4: triangles, CO: circles) over Pt/Al_2O_3 at 773 K measured in the fixed bed reactor in the laboratory. The selectivity toward CH_4 is shown in the right axis (diamonds). m_{cat} = 100 mg, 10% CO_2 and 40% H_2 in He (total flow rate = 50 mL min^{-1}). Reduction treatment by 5% H_2/He at 773 K for 1 h was conducted after 25 h of reaction.

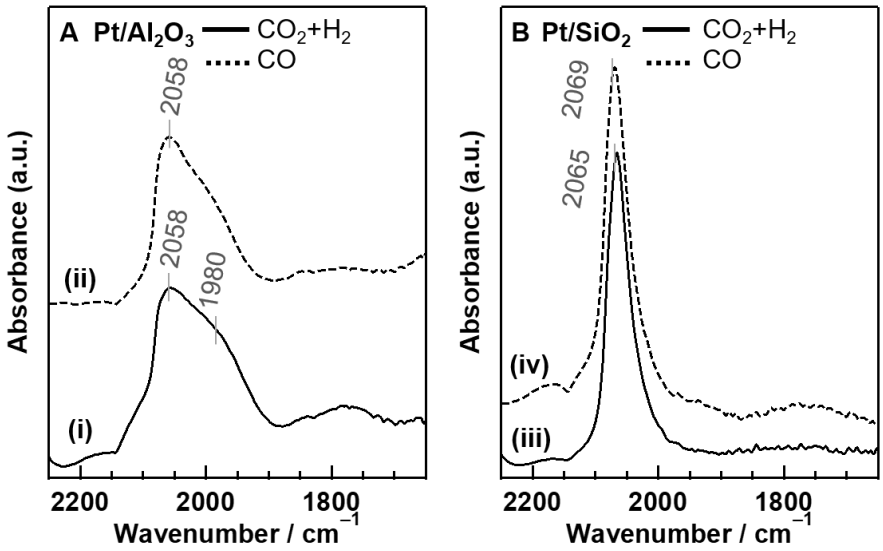

Figure 13. (A) DRIFT-IR spectra of adsorbed species at 673 K on Pt/Al_2O_3 (i) during hydrogenation (10% CO_2+40% H_2) and (ii) under 1% CO flow. **(B)** DRIFT-IR spectra at 773 K over Pt/SiO_2 (iii) during hydrogenation (10% CO_2+40% H_2) and (iv) under 1% CO flow. The background spectrum was recorded under He flow at 673 K after pretreatment. The spectral intensities were normalized by that of the strongest band of adsorbed CO species.

A remaining issue is identifying the active sites for the unfavorable methanation of CO species over Pt/Al_2O_3 catalyst. **Figure 13** shows the DRIFT-IR spectra of the adsorbed species at 673 K during hydrogenation and under CO flow. During hydrogenation over Pt/Al_2O_3, a broad absorption band of CO species adsorbed on Pt exhibited a peak top at 2058 cm^{-1} with a large shoulder peak at 1980 cm^{-1}. Under CO flow, the peak at 2058 cm^{-1} and a relatively smaller shoulder peak at lower frequency were observed. In contrast, Pt/SiO_2 (**Figure 13(B)**) exhibited a narrower absorption band both during hydrogenation and under CO flow. The slight peak shift to low frequency over Pt/SiO_2 during hydrogenation as compared to that under CO flow was because of a decrease in the dipole-dipole interaction at low coverage, consistent with the XANES analysis in **Figure 9(B)**. Here, the absorption bands were obviously different between Pt/Al_2O_3 and Pt/SiO_2 even under CO flow. Ferri *et al.* assigned this shoulder peak of C–O stretching mode at low frequency to CO species attached at the boundary sites between Pt particles and Al_2O_3 thin film.[43] Thus, we consider that the broad absorption band over Pt/Al_2O_3 represented the C–O stretching mode of CO attached on two kinds of Pt sites: the perimeter Pt atoms (i.e., those at the interface between Pt particles and Al_2O_3 surface) and other Pt atoms. The lowered frequency of C–O stretching of CO species attached onto perimeter Pt atoms was likely owing to a large electron backdonation derived from the abundant dangling bond of the perimeter atoms,[73] or an electronic interaction with oxygen atoms or surface hydroxyl groups of Al_2O_3 surface.[74]

In addition, we attribute the large shoulder peak of CO species over Pt/Al_2O_3 under hydrogenation to the low energy shift in the absorption band of CO species upon co-adsorption of H species, although there is also the possible contribution of Pt–H vibration. Such a shift of C–O stretching mode to low frequency upon co-adoption of H species was reported as “formyl species” over supported Ru catalysts.[75, 76] Here, we consider the formation of formyl species at the perimeter atoms on Pt/Al_2O_3 to induce to further hydrogenation of adsorbed CO species into CH_4.

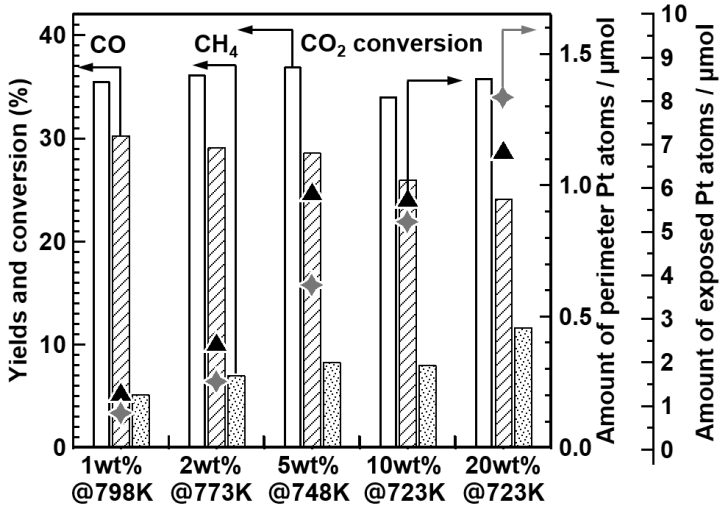

Figure 14. Conversion of CO_2 (blank bar) and yields of products (hatched bar: CO, dotted bar: CH_4) during hydrogenation of CO_2 over Pt/Al_2O_3 at various loadings, measured in the fixed bed flow reactor in the laboratory. The triangles and stars are the amounts of perimeter Pt atoms at the interface between Pt particle and Al_2O_3 surface and the amounts of exposed Pt atoms, which were estimated by CO pulse titration, respectively (right y-axis). m_{cat} = 27 mg, 10% CO_2 and 40% H_2 in He. The catalytic activity was measured at 25 K intervals between 673 and 823 K, and displayed at the temperature with approximately the same CO_2 conversion level.

The reaction results over Pt/Al_2O_3 at various Pt loadings also clearly showed the active sites for methanation. **Figure 14** displays the CO and CH_4 yields for catalysts with different Pt loadings and at temperatures with comparable CO_2 conversions. At 1wt% Pt loading, a CH_4 yield of 5.2% was obtained (CO_2 conversion: 35.5%, 798 K), while the 20wt% Pt/Al_2O_3 exhibited a CH_4 yield of 11.7% (CO_2 conversion: 35.9%, 723 K). Here, we estimated the amount of perimeter Pt atoms by assuming a hemi-cuboctahedral model particle. At a dispersion of 50%, this particle is composed of 185 Pt atoms including 24 perimeter ones (**Table 3**). The actual dispersions of Pt atoms determined by CO pulse titration were 56%, 55%, 54%, 38%, and 29% for 1wt%, 2wt%, 5wt%, 10wt%, and 20wt% Pt, respectively. The amount of perimeter Pt atoms in each Pt catalyst relatively well matched the trend in CH_4 yields. Of course, it should be noted that the morphology of Pt was different from the three-dimensional particle. In contrast, the amount of exposed Pt atoms totally mismatched the CH_4 yield. Thus, the perimeter Pt sites are plausible active sites for methanation over Pt/Al_2O_3 catalysts.

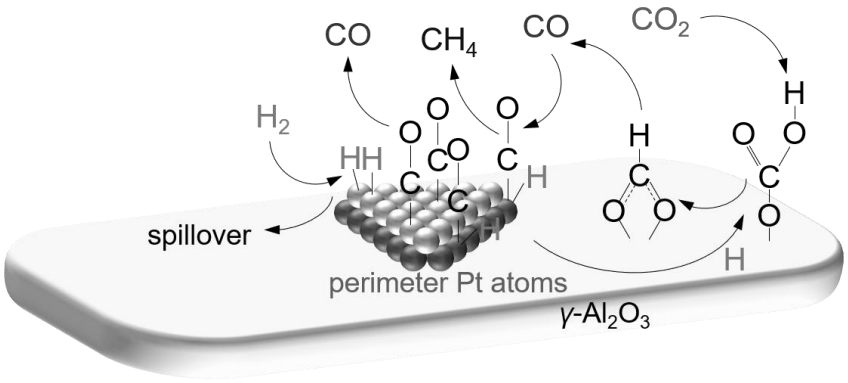

Figure 15. Illustration of the mechanism of CH_4 formation during hydrogenation of CO_2 over two-dimensional Pt particle supported on Al_2O_3.

To summarize, the unfavorable formation of CH_4 over Pt/Al_2O_3 proceeded thorough CO species attached on the perimeter Pt atoms at the interface between the Pt particle and Al_2O_3 surface, which co-adsorbed dissociated hydrogen as illustrated in **Figure 15**. In general, the CO species are considered to stem from either hydrogenation of CO_2 through the formate species on the support, or direct dissociation over metal surface.[12, 18, 77, 78] Since CO species on Pt frequently causes unwanted inhibition of adsorption in other surface reactions, we consider the production of CO to be mainly through the formate route. Namely, bicarbonate species are formed on the Al_2O_3 surface upon adsorption of CO_2 at the surface hydroxyl groups of Al_2O_3.[77, 79] Those bicarbonate species are hydrogenated toward CO by hydrogen spillover from Pt surface as the dissociation sites of H_2. Our *operando* XAS-DRIFTS study suggested that a part of the CO species are temporally adsorbed onto the Pt surface. Moreover, CO species on the perimeter Pt atoms co-adsorbed with H species are subsequently hydrogenated toward CH_4. In addition, the trend in selectivity toward CH_4 over catalysts with various Pt loadings robustly supported that perimeter Pt atoms with the Al_2O_3 surface act as the active sites for unfavorable CH_4 formation.

Our *operando* XAS-DRIFTS study revealed the active sites for undesirable CH_4 formation over Al_2O_3-supported Pt catalysts, leading to novel insights into the MSI effect between Pt particles and Al_2O_3 surface on the catalytic activity during hydrogenation of CO_2. Some questions still remain, such as why such perimeter Pt atoms with unique electronic states were derived in Pt/Al_2O_3 as opposed to Pt/SiO_2. Further studies on the formation mechanism of two-dimensional particles over Al_2O_3 supports would reveal the role of MSI during particle formation, and provide a methodology for

controlling the electronic and geometric states of supported metal particles. Moreover, a more thorough understanding of the role of hydroxyl groups on the support surface and the dynamics of protons over metal and support surface is needed, since these factors are strongly relevant to the hydrogenation of CO_2.

Conclusions

A combined X-ray absorption spectroscopy and diffuse reflectance infrared Fourier transform spectroscopy approach with product analysis was performed over Al_2O_3- and SiO_2-supported Pt catalysts during hydrogenation of CO_2. These two catalysts have totally different product selectivities despite using the same active metal species: Pt/Al_2O_3 exhibits undesirable CH_4 production whereas Pt/SiO_2 selectively produces CO. From the results of EXAFS analysis and estimated *d*-electron density of Pt, Pt species supported on Al_2O_3 formed two-dimensional raft-like Pt particles with a high *d*-electron density mainly due to the small particle size, whereas those on SiO_2 were larger three-dimensional particles. Moreover, Pt/Al_2O_3 had a higher density of unoccupied states of Pt under hydrogenation of CO_2, and this indicates the co-adsorption of H species and CO species that likely induced further hydrogenation of adsorbed CO toward CH_4. From the strong absorption bands of CO species attached onto both the perimeter and other Pt sites and the CH_4 selectivity over Pt/Al_2O_3 at various loadings, the perimeter Pt atoms with the Al_2O_3 surface acted as the active sites for unfavorable CH_4 formation. We believe that this study provides novel insights for designing effective active sites for selective CO production through hydrogenation of CO_2. The results also add to fundamental understanding of the interaction between metal particles and the support surface.

References

1 M. C. J. Bradford and M. A. Vannice, *Catal. Rev.*, 1999, **41**, 1–42.

2 C. Ratnasamy and J. P. Wagner, *Catal. Rev.*, 2009, **51**, 325–440.

3 J. Wang, H. Chen, Z. Hu, M. Yao and Y. Li, *Catal. Rev.*, 2014, **57**, 79–144.

4 D. Kubička, N. Kumar, T. Venäläinen, H. Karhu, I. Kubičková, H. Österholm and D. Y. Murzin, *J. Phys. Chem. B*, 2006, **110**, 4937–4946.

5 J. H. Kwak, J. Hu, D. Mei, C.-W. Yi, D. H. Kim, C. H. Peden, L. F. Allard and J. Szanyi, *Science*, 2009, **325**, 1670–1673.

6 Y. Zhai, D. Pierre, R. Si, W. Deng, P. Ferrin, A. U. Nilekar, G. Peng, J. A. Herron, D. C. Bell and H. Saltsburg, *Science*, 2010, **329**, 1633–1636.

7 M. Ahmadi, H. Mistry and B. Roldan Cuenya, *J. Phys. Chem. Lett.*, 2016, **7**, 3519–3533.

8 K. Murata, Y. Mahara, J. Ohyama, Y. Yamamoto, S. Arai and A. Satsuma, *Angew. Chem. Int. Ed. Engl.*, 2017, **56**, 15993–15997.

9 W. Wang, S. Wang, X. Ma and J. Gong, *Chem. Soc. Rev.*, 2011, **40**, 3703–3727.

10 W. Zhou, K. Cheng, J. Kang, C. Zhou, V. Subramanian, Q. Zhang and Y. Wang, *Chem. Soc. Rev.*, 2019, **48**, 3193–3228.

11 B. Sexton and G. Somorjai, *J. Catal.*, 1977, **46**, 167–189.

12 F. Solymosi and A. Erdőhelyi, *J. Mol. Catal.*, 1980, **8**, 471–474.

13 G. D. Weatherbee and C. H. Bartholomew, *J. Catal.*, 1981, **68**, 67–76.

14 G. D. Weatherbee and C. H. Bartholomew, *J. Catal.*, 1982, **77**, 460–472.

15 D. Peebles, D. Goodman and J. White, *J. Phys. Chem.*, 1983, **87**, 4378–4387.

16 C. K. Vance and C. H. Bartholomew, *Appl. Catal.*, 1983, **7**, 169–177.

17 G. D. Weatherbee and C. H. Bartholomew, *J. Catal.*, 1984, **87**, 352–362.

18 F. Solymosi, *J. Mol. Catal.*, 1991, **65**, 337–358.

19 M. D. Porosoff and J. G. Chen, *J. Catal.*, 2013, **301**, 30–37.

20 J. C. Matsubu, V. N. Yang and P. Christopher, *J. Am. Chem. Soc.*, 2015, **137**, 3076–3084.

21 S. Kattel, B. Yan, J. G. Chen and P. Liu, *J. Catal.*, 2016, **343**, 115–126.

22 S. Kattel, B. Yan, Y. Yang, J. G. Chen and P. Liu, *J. Am. Chem. Soc.*, 2016, **138**, 12440–12450.

23 F. Wang, S. He, H. Chen, B. Wang, L. Zheng, M. Wei, D. G. Evans and X. Duan, *J. Am. Chem. Soc.*, 2016, **138**, 6298–6305.

24 S. Kattel, P. Liu and J. G. Chen, *J. Am. Chem. Soc.*, 2017, **139**, 9739–9754.

25 S. Li, Y. Xu, Y. Chen, W. Li, L. Lin, M. Li, Y. Deng, X. Wang, B. Ge, C. Yang*, et al.*, *Angew. Chem. Int. Ed. Engl.*, 2017, **56**, 10761–10765.

26 Y. Guo, S. Mei, K. Yuan, D.-J. Wang, H.-C. Liu, C.-H. Yan and Y.-W. Zhang, *ACS Catal.*, 2018, **8**, 6203–6215.

27 Y. Wang, H. Arandiyan, J. Scott, K.-F. Aguey-Zinsou and R. Amal, *ACS Appl. Energy Mater.*, 2018, **1**, 6781–6789.

28 M. M. Millet, G. Algara-Siller, S. Wrabetz, A. Mazheika, F. Girgsdies, D. Teschner, F. Seitz, A. Tarasov, S. V. Levchenko, R. Schlogl*, et al.*, *J. Am. Chem. Soc.*, 2019, **141**, 2451–2461.

29 M. Primet, J. Basset, M. Mathieu and M. Prettre, *J. Catal.*, 1973, **28**, 368–375.

30 Y. Dong, G. Hu, X. Hu, G. Xie, J. Lu and M. Luo, *J. Phys. Chem. C*, 2013, **117**, 12537‑12543.

31 D. Palecek, G. Tek, J. Lan, M. Iannuzzi and P. Hamm, *J. Phys. Chem. Lett.*, 2018, **9**, 1254–1259.

32 T. Kubota, K. Asakura, N. Ichikuni and Y. Iwasawa, *Chem. Phys. Lett.*, 1996, **256**, 445–448.

33 K. Asakura, T. Kubota, W. J. Chun, Y. Iwasawa, K. Ohtani and T. Fujikawa, *J. Synchrotron Radiat.*, 1999, **6**, 439–441.

34 B. L. Mojet, J. T. Miller and D. C. Koningsberger, *J. Phys. Chem. B*, 1999, **103**, 2724–2734.

35 D. E. Ramaker, B. L. Mojet, M. T. G. Oostenbrink, J. T. Miller and D. C. Koningsberger, *Phys. Chem. Chem. Phys.*, 1999, **1**, 2293–2302.

36 D. Koningsberger, M. Oudenhuijzen, J. Bitter and D. Ramaker, *Top. Catal.*, 2000, **10**, 167–177.

37 A. L. Ankudinov, J. J. Rehr, J. Low and S. R. Bare, *Phys. Rev. Lett.*, 2001, **86**, 1642–1645.

38 M. Oudenhuijzen, J. Bitter and D. Koningsberger, *J. Phys. Chem. B*, 2001, **105**, 4616–4622.

39 J. Singh, C. Lamberti and J. A. van Bokhoven, *Chem. Soc. Rev.*, 2010, **39**, 4754–4766.

40 J. van Bokhoven, *Phys. Chem. Chem. Phys.*, 2010, **12**, 5514–5534.

41 C. Brieger, J. Melke, N. van der Bosch, U. Reinholz, H. Riesemeier, A. Guilherme Buzanich, M. K. Kayarkatte, I. Derr, A. Schökel and C. Roth, *J. Catal.*, 2016, **339**, 57–67.

42 M. A. Newton, D. Ferri, G. Smolentsev, V. Marchionni and M. Nachtegaal, *J. Am. Chem. Soc.*,

2016, **138**, 13930–13940.

43 D. Ferri, T. Bürgi and A. Baiker, *Phys. Chem. Chem. Phys.*, 2002, **4**, 2667–2672.

44 A. Goguet, F. C. Meunier, D. Tibiletti, J. P. Breen and R. Burch, *J. Phys. Chem. B*, 2004, **108**, 20240–20246.

45 S. Kikkawa, K. Teramura, H. Asakura, S. Hosokawa and T. Tanaka, *J. Phys. Chem. C*, 2019, **123**, 23446–23454.

46 A. Urakawa, *Curr. Opin. Chem. Eng.*, 2016, **12**, 31–36.

47 A. Borgna, T. Garetto, C. Apesteguıa, F. Le Normand and B. Moraweck, *J. Catal.*, 1999, **186**, 433–441.

48 D. Mei, J. H. Kwak, J. Hu, S. J. Cho, J. Szanyi, L. F. Allard and C. H. Peden, *J. Phys. Chem. Lett.*, 2010, **1**, 2688–2691.

49 J. Matos, L. K. Ono, F. Behafarid, J. R. Croy, S. Mostafa, A. T. DeLaRiva, A. K. Datye, A. I. Frenkel and B. Roldan Cuenya, *Phys. Chem. Chem. Phys.*, 2012, **14**, 11457–11467.

50 L. Deng, H. Miura, T. Shishido, S. Hosokawa, K. Teramura and T. Tanaka, *Chem. Commun.*, 2017, **53**, 6937–6940.

51 C. Dessal, T. Len, F. Morfin, J.-L. Rousset, M. Aouine, P. Afanasiev and L. Piccolo, *ACS Catal.*, 2019, **9**, 5752–5759.

52 C. Dessal, A. Sangnier, C. Chizallet, C. Dujardin, F. Morfin, J.-L. Rousset, M. Aouine, M. Bugnet, P. Afanasiev and L. Piccolo, *Nanoscale*, 2019, **11**, 6897–6904.

53 M. Vaarkamp, J. T. Miller, F. S. Modica and D. C. Koningsberger, *J. Catal.*, 1996, **163**, 294–305.

54 W. Sinkler, S. I. Sanchez, S. A. Bradley, J. Wen, B. Mishra, S. D. Kelly and S. R. Bare, *ChemCatChem*, 2015, **7**, 3779–3787.

55 T. Uruga, H. Tanida, Y. Yoneda, K. Takeshita, S. Emura, M. Takahashi, M. Harada, Y. Nishihata, Y. Kubozono and T. Tanaka, *J. Synchrotron Radiat.*, 1999, **6**, 143–145.

56 T. Uruga, H. Tanida, K. Inoue, H. Yamazaki and T. Irie, *AIP Conf. Proc.*, 2007, **882**, 914–916.

57 B. Ravel and M. Newville, *J. Synchrotron Radiat.*, 2005, **12**, 537–541.

58 A. Mansour, J. Cook Jr and D. Sayers, *J. Phys. Chem.*, 1984, **88**, 2330–2334.

59 A. Mansour, J. Cook Jr, D. Sayers, R. Emrich and J. Katzer, *J. Catal.*, 1984, **89**, 462–469.

60 M. Brown, R. Peierls and E. Stern, *Phys. Rev. B*, 1977, **15**, 738–744.

61 L. Mattheiss and R. Dietz, *Phys. Rev. B*, 1980, **22**, 1663–1676.

62 R. Barth and A. Ramachandran, *J. Catal.*, 1990, **125**, 467–471.

63 L.-C. de Ménorval, A. Chaqroune, B. Coq and F. Figueras, *J. Chem. Soc., Faraday Trans.*, 1997, **93**, 3715–3720.

64 E. V. Benvenutti, L. Franken, C. C. Moro and C. U. Davanzo, *Langmuir*, 1999, **15**, 8140–8146.

65 T. M. Salama, H. Hattori, H. Kita, K. Ebitani and T. Tanaka, *J. Chem. Soc., Faraday Trans.*, 1993, **89**, 2067–2073.

66 Y. Yazawa, H. Yoshida, S. Komai and T. Hattori, *Appl. Catal. A*, 2002, **233**, 113–124.

67 J. A. van Bokhoven and J. T. Miller, *J. Phys. Chem. C*, 2007, **111**, 9245–9249.

68 B. Hammer and J. Norskov, *Nature*, 1995, **376**, 238–240.

69 O. V. Safonova, M. Tromp, J. A. Van Bokhoven, F. M. De Groot, J. Evans and P. Glatzel, *J. Phys. Chem. B*, 2006, **110**, 16162–16164.

70 J. Miller, B. Meyers, F. Modica, G. Lane, M. Vaarkamp and D. Koningsberger, *J. Catal.*, 1993, **143**, 395–408.

71 S. Fujita, H. Terunuma, H. Kobayashi and N. Takezawa, *React. Kinet. Catal. Lett.*, 1987, **33**, 179–184.

72 S. Fujita, M. Nakamura, T. Doi and N. Takezawa, *Appl. Catal. A*, 1993, **104**, 87–100.

73 G. Blyholder, *J. Phys. Chem.*, 1964, **68**, 2772–2777.

74 F. C. Meunier, R. Kdhir, N. Potrzebowska, N. Perret and M. Besson, *Inorg. Chem.*, 2019, **58**, 8021–8029.

75 M. P. Andersson, F. Abild-Pedersen, I. N. Remediakis, T. Bligaard, G. Jones, J. Engbæk, O. Lytken, S. Horch, J. H. Nielsen and J. Sehested, *J. Catal.*, 2008, **255**, 6–19.

76 S. Eckle, H. G. Anfang and R. J. Behm, *J. Phys. Chem. C*, 2011, **115**, 1361–1367.

77 M. A. A. Aziz, A. A. Jalil, S. Triwahyono and A. Ahmad, *Green Chem.*, 2015, **17**, 2647–2663.

78 K. Jalama, *Catal. Rev.*, 2017, **59**, 95–164.

79 Q. Pan, J. Peng, T. Sun, S. Wang and S. Wang, *Catal. Commun.*, 2014, **45**, 74–78.

Part III

Photocatalytic and Electrocatalytic Reduction of CO_2 Toward CO over Ag Species

Chapter 5

Development of Rh-Doped Ga_2O_3 Photocatalysts for Reduction of CO_2 by H_2O as an Electron Donor at a More than 300 nm Wavelength

Abstract

Rhodium-doped gallium oxide (Ga_2O_3:Rh) that was prepared by the simple coprecipitation method exhibited the activity for the photocatalytic conversion of CO_2 by H_2O under photoirradiation with light of >300 nm wavelength. Although Ga_2O_3 is a wide band gap photocatalyst that is active only under photoirradiation with <300 nm light, the absorption edge shifted to >300 nm as a result of Rh doping. Ag–Cr-loaded Ga_2O_3:Rh (0.7 mol%) showed activity for the production of CO (3.9 μmol h^{-1}) as a reduction product of CO_2. The formation of stoichiometric amount of O_2 indicated that H_2O acts as an electron donor for the photocatalytic conversion of CO_2. Characterization using several techniques such as X-ray absorption spectroscopy (XAS) revealed that after doping in Ga_2O_3, the trivalent Rh species substituted not for the tetrahedral Ga site but for the octahedral Ga site of β-Ga_2O_3. From the result of DFT calculations, the new energy level owing to Rh^{3+} was within the Ga_2O_3 band gap. It was concluded that the new absorption due to the Rh d t_{2g} orbital to the conduction band contributed to the activity of photocatalytic conversion of CO_2 by H_2O under photoirradiation with light of >300 nm wavelength.

Introduction

The photocatalytic conversion of CO_2 is widely investigated as a means to convert it to valuable chemical feedstocks, such as CO, HCOOH, CH_4, and CH_3OH, which is called as artificial photosynthesis.[1-8] Due to the thermodynamic stability of CO_2, the reduction of CO_2 requires high-energy reductants, such as H_2 or hydrocarbons, and high temperatures in carbon cycling systems, such as Fischer-Tropsch synthesis or dry reforming reaction.[3, 9, 10] However, H_2O is a more desirable and favorable reductant because it is harmless and abundant on the earth. Recently, several oxide semiconductors have been reported to have photocatalytic activity for CO production as the reduction products of CO_2 using H_2O as the reductant, such as Ag-loaded $ALa_4Ti_4O_{15}$ (A:Ca, Sr and Ba),[11] Ag-loaded $KCaSrTa_5O_{15}$,[12] Ag-loaded $La_2Ti_2O_7$ (CO formation rate = 5.2 μmol h^{-1}),[13] Ag-loaded Sr-modified Ta_2O_5 (6.8 μmol h^{-1}),[14] Ag-loaded $ZnGa_2O_4$-modified Ga_2O_3 (147 μmol h^{-1}),[15, 16] Ag-loaded $ZnTa_2O_6$ (21.9 μmol h^{-1}),[17] Ag-loaded $Sr_2KTa_5O_{15}$ (65.5 μmol h^{-1}),[18] Ag-loaded $CaTiO_3$ (54 μmol h^{-1}),[19] and Ag-loaded $NaTaO_3$:Sr (176 μmol h^{-1}).[20] Especially, we recently reported that Ag–Cr core-shell cocatalyst-loaded Ga_2O_3 exhibits a high CO formation rate of 480 μmol h^{-1}.[21]

The photocatalytic water splitting, one promising process of artificial photosynthesis, proceeds using solar energy, which is called as solar H_2 production.[22-24] Unfortunately, the photocatalysts for the photocatalytic conversion of CO_2 reported thus far only function effectively under photoirradiation with UV light or produce only insignificant amounts of products under sun light. Thus, new photocatalysts are required, which can be active under photoirradiation with light of a wide range of wavelengths. To design the photocatalysts that exhibit the activity for the photocatalytic reduction of CO_2 in an aqueous solution, the relationship between the standard potential for CO_2 (i.e., $E^{\circ}(CO_2/CO)$ = −0.11 V vs. NHE at pH = 0)[25] and the potentials of photoexcited electrons should be considered. It is difficult to reduce CO_2 toward CO because of the competition with the reduction of a proton (i.e., $E^{\circ}(H^+/H_2)$ = 0.0 V vs. NHE).[26] Additionally, photogenerated holes should induce the oxidation of H_2O (i.e., $E^{\circ}(O_2/H_2O)$ = 1.23 V vs. NHE at pH = 0). Ga_2O_3 and Ta_2O_5,[27, 28] which produce photogenerated electrons with a high potential energy, can induce the two-electron reduction of CO_2 and oxidation of H_2O toward O_2 evolution. Unfortunately, UV light irradiation (λ <300 nm) was required for the photoexcitation of these photocatalysts.

Although photoelectrochemical systems enable to solve this problem by applying external voltages to reach enough potential energy of electron and holes under visible light irradiation,[5, 8] simple semiconductive photocatalysts without any external voltages would be preferable.

Thus, controlling the band energy of photocatalysts is one of the possible strategies for development of photocatalysts that will be active under irradiation with light with a wide range of wavelengths. Doping a wide-band-gap oxide semiconductor with a foreign element is a well-known approach to produce a visible-light-driven water splitting photocatalyst. Various oxide materials, such as TiO_2,[29, 30] $SrTiO_3$,[29, 31, 32] $La_2Ti_2O_7$,[33] $CaTiO_3$,[34] $BaTiO_3$,[35] and $ZnGa_2O_4$[36] have been employed as host materials. Follow-up studies indicated that several oxides doped with Rh are active under longer wavelengths than the corresponding undoped oxides. Specifically, the Rh^{3+} ion in a regular octahedral coordination forms fully occupied t_{2g}^6 and empty e_g^0 orbitals, resulting in a donor level in their band gap.[36]

In this study, we chose the β-Ga_2O_3 photocatalyst as a host material for introducing Rh^{3+} because of the following reasons. Octahedrally coordinated Rh^{3+} ions are expected to be easy to replace to octahedrally coordinated Ga^{3+} ions in the lattice of an α-corundum structure of Ga_2O_3 because of similarity of ionic radius.[37, 38] The band-gap of Ga_2O_3 is 4.7 eV and potential energies of the top of the conduction band and the bottom of the valence band are thermodynamically sufficient for reduction of CO_2 to CO and oxidation of H_2O to O_2, respectively.[39] The midgap states in the forbidden band of Ga_2O_3 would be possibly formed by Rh t_{2g}^6 and empty e_g^0 orbitals of Rh^{3+} introduced at the Ga^{3+} site. Thus, we designed a Rh-doped Ga_2O_3-based photocatalyst with a high-energy-level conduction band and investigated their activity for the photocatalytic conversion of CO_2 by H_2O under photoirradiation with >300 nm light.

Experimental

Rh-doped Ga_2O_3 was prepared by a co-precipitation method using a $Ga(NO_3)_3 \cdot nH_2O$ precursor (Kojundo Chemical Laboratory Co., Ltd) and $RhCl_3 \cdot 3H_2O$ precursor (Wako Pure Chemicals Co. Ltd.). An aqueous solution of NH_3 was dropped into a mixed solution of $Ga(NO_3)_3$ and $RhCl_3$. Rh-doped Ga_2O_3 was obtained by calcination of the precipitate at 1173 K for 6 h. Ag–Cr cocatalyst was loaded by an impregnation method. The prepared powder was dispersed in an aqueous solution of $AgNO_3$ (Wako Pure Chemicals Co. Ltd.) and $Cr(NO_3)_3$ (Kanto Chemicals Co. Ltd.), followed by calcination at 723 K for 2 h. The molar ratio of Ag/Cr was 1 and total amount of the metal species was 1.0 wt%, which were optimized values for the activity of CO production as summarized in **Table 1**.

Table 1. The activity for the photocatalytic conversion of CO_2 in water over Ag–Cr/Ga_2O_3:Rh (0.7 mol%) after 5 h of more than 300 nm of UV light irradiation.

Entry	Ag/Cr ratio	Total amount of Ag–Cr (wt%)	Formation rates (μmol h^{-1})			Selectivity toward CO (%)
			H_2	O_2	CO	
1	Ag only	1.0	1.0	0.1	0.4	27.3
2	3	1.0	19.3	9.3	2.5	11.3
3	1	1.0	10.3	6.5	3.9	27.6
4	1/3	1.0	6.9	4.9	3.1	31.0
5	Cr only	1.0	3.3	2.0	0.6	14.7
6	1	0.5	21.3	11.6	3.0	12.3
7	1	2.0	6.0	4.1	2.6	30.5
8	1	5.0	2.5	3.0	1.2	32.2

X-ray diffraction (XRD) patterns of the prepared catalysts were collected by using an X-ray diffractometer (Multiflex, Rigaku) using Cu K_α radiation at an acceleration voltage of 40 kV. UV-vis diffuse reflectance spectra of the samples were measured by a UV-visible spectrometer (V-670, JASCO) equipped with an integrated sphere accessory. The energy gap (hereinafter "$\boldsymbol{E_{BG}}$") of a series of Ga_2O_3 and Ga_2O_3:Rh samples was determined by using the Davis-Mott equation[40] with the Kubelka-Munk function $\boldsymbol{F(R_\infty)}$ obtained from the diffuse reflectance spectrum,

$$[F(R_\infty)hv]^{-n} = A\,(hv - E_g)$$

where h, v, and A are the Planck's constant, frequency of vibration, and proportional constant,

respectively. The X-ray absorption structure (XAFS) at the Ga K-edge or Rh K-edge was measured at the beam line BL01B1 of SPring-8. The XAFS spectra were recorded in a transmittance mode at room temperature, using Si(111) and Si(311) double crystal monochromators for the measurements at the Ga K-edge and Rh K-edge, respectively. The density of state of Ga_2O_3 and Ga_2O_3:Rh was simulated by the ab initio full-potential linearized augmented plane-wave (FP-LAPW) method within the density functional theory (DFT) as implemented in the WIEN2k code.[41] Basic parameters were chosen as follows: kinetic energy cut-off = 380 eV and SCF tolerance = 5.0×10^{-7} eV atom^{-1}. The *k* points of 4×10×19 meshes are summed in all Brillouin zone in the reciprocal space. A 2 × 2 × 2 Ga_2O_3 supercell was used with one of the Ga^{3+} sites substituted by a Rh^{3+} ion, corresponding to a doping level of 1.5 mol%.

The photocatalytic conversion of CO_2 by H_2O as an electron donor over Ag–Cr-loaded Ga_2O_3:Rh (Ag–Cr/Ga_2O_3:Rh) was performed with an inner-irradiation type reactor. 0.5 g of photocatalyst was dispersed in an aqueous solution of $NaHCO_3$ (0.1 M, 1.0 L). The suspension was irradiated under a 400 W high-pressure mercury lamp though a Pyrex® glass filter equipped with a cooling water system. CO_2 gas (99.999 %) was bubbled into the solution at a flow rate of 30 mL min^{-1}. Isotopic experiment was performed with ^{13}C-labeled $^{13}CO_2$ gas (99.9%) as a substrate. CO, H_2 and O_2, as products were analyzed by TCD-GC using a GC-8A chromatograph (Shimadzu Corp.) equipped with a Molecular Sieve 5A column with Ar as the carrier gas and by FID-GC (Shimadzu Corp.) with a methanizer using a Shincarbon ST column with N_2 as the carrier gas. The selectivity toward CO evolution compared to H_2 evolution and the balance between consumed electrons ($\boldsymbol{e}^-$) and holes ($\boldsymbol{h}^+$) can generally be described using the formulae shown below:

$$\text{Selectivity toward CO evolution (\%)} = 100 \times \boldsymbol{R}_{\mathbf{CO}}/(\boldsymbol{R}_{\mathbf{CO}} + \boldsymbol{R}_{\mathbf{H2}})$$

$$\text{Consumed } \boldsymbol{e}^-/\boldsymbol{h}^+ = (\boldsymbol{R}_{\mathbf{CO}} + \boldsymbol{R}_{\mathbf{H2}})/(2 \times \boldsymbol{R}_{\mathbf{O2}})$$

where $\boldsymbol{R}_{\mathbf{CO}}$, $\boldsymbol{R}_{\mathbf{H2}}$, and $\boldsymbol{R}_{\mathbf{O2}}$ represent the rates of formation of CO, H_2, and O_2, respectively.

The photocatalytic reaction under a Xe lamp equipped with a cut-off filter was carried out in a closed circulation system connected to a vacuum line with an external-irradiation type reactor. 0.3 g of the photocatalyst (Ag–Cr/Ga_2O_3:Rh or Ag–Cr/Ga_2O_3) was dispersed in a 10% methanol aqueous solution. After 5 h of photoirradiation with a UV-29 cut-off filter, the photocatalytic activity for H_2 production was examined by using cut-off filters (UV-29, -31, 33, 35, 37, 39, L-42, Y-52). The

amount of H_2 was measured by TCD-GC equipped with the Molecular Sieve 5A column.

Results and discussion

Table 2. The activity for the photocatalytic conversion of CO_2 in water over Ag–Cr/Ga_2O_3:Rh and Ag–Cr/Ga_2O_3 after 5 h of UV light irradiation.

Entry	Photocatalyst	Light source	Formation rates (μmol h^{-1})			Selectivity toward CO (%)	Consumed e^-/h^+ ratio
			H_2	O_2	CO		
1	Ag–Cr/Ga_2O_3	400 W Hg lamp	132.3	193.6	271.0	67.2	1.04
2	Ag–Cr/Ga_2O_3	400 W Hg lamp with Pyrex filter (λ >300 nm)	trace	n.d.	trace	-	-
3	Ag–Cr/Ga_2O_3:Rh (0.7 mol%)	400 W Hg lamp	338.6	169.3	8.3	2.4	1.02
4	Ag–Cr/Ga_2O_3:Rh (0.7 mol%)	400 W Hg lamp with Pyrex filter (λ >300 nm)	10.3	6.5	3.9	27.6	1.09

Table 2 shows the formation rates of CO and H_2 and the selectivity toward CO evolution for the photocatalytic conversion of CO_2 over Ga_2O_3 and Rh-doped Ga_2O_3 with the Ag–Cr core-shell cocatalyst after 5 h of reaction. Under UV light irradiation, Ag–Cr/Ga_2O_3 exhibited a high formation rate of CO as a reduction product of CO_2 at the rate of 271.0 μmol h^{-1} (Entry 1). H_2 was also generated as a byproduct derived from the reduction of protons, with the selectivity toward CO evolution being 67%. O_2 was generated as the oxidation product of H_2O. The consumed $\boldsymbol{e^-/h^+}$ ratio was approximately 1.0, indicating that stoichiometric reduction and oxidation successfully proceeded. In contrast, only trace amount of CO and H_2 were generated under >300 nm photoirradiation (Entry 2). The band gap of Ga_2O_3 was too large to harvest the photons using light in this wavelength range.

An increase in the activity was observed upon doping with 0.7 mol% of Rh (hereinafter, Ga_2O_3:Rh (0.7mol%)). The formation rates of H_2, O_2, and CO were 10.3, 6.5, and 3.9 μmol h^{-1}, respectively (Entry 4). The selectivity for CO evolution among reduction products was lower than that of undoped Ga_2O_3. The stoichiometric amount of O_2 was definitely generated. These results indicate that doping with Rh species contributes to photocatalytic activity for the conversion of CO_2 by H_2O as the electron donor under >300 nm photoirradiation. Under UV light irradiation, Ga_2O_3:Rh

showed a high activity for H_2 formation under UV light irradiation at the rate of 338.6 μmol h^{-1} (Entry 3). This result suggested that doped Rh species might work as reaction sites for H_2 formation.

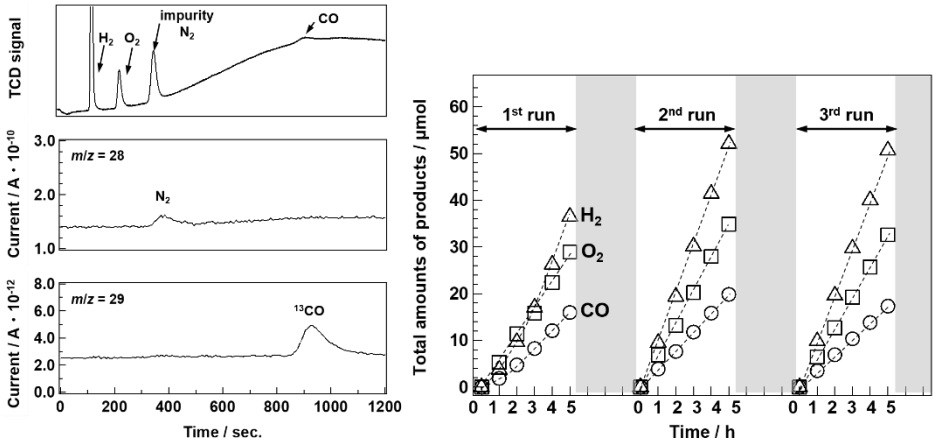

Figure 1. (A) Gas chromatogram and mass spectra (m/z = 28 and 29) in the photocatalytic conversion of $^{13}CO_2$ by H_2O over Ag–Cr/Ga_2O_3:Rh (0.7 mol%). Reaction conditions are the same as those in **Table 1**. **(B)** Time courses of the formation rate of products (CO: circles, H_2: triangles, O_2: squares for 15 h of photoirradiation over Ag–Cr/Ga_2O_3:Rh (0.7 mol%).

Figure 1(A) shows the results obtained from isotopic experiments over Ag–Cr/Ga_2O_3:Rh (0.7mol%). The products were detected by the gas chromatogram and mass spectra (m/z = 28 and 29) during the photocatalytic conversion of $^{13}CO_2$ by H_2O. We introduced the sampling gas into the mass spectrometer after the separation by TCD-GC with the Molecular Sieve 5A column. Four peaks were observed at approximately 100, 200, 400 and, 900 s in the GC chromatogram. These peaks corresponded to H_2, O_2, impurity N_2 contained in $^{13}CO_2$ gas, and CO. The peak observed at *m*/*z* = 29 was located at the same position as that assigned to CO in the GC chromatogram, indicating that ^{13}C-labeled CO was generated as the reduction products of $^{13}CO_2$. On the other hand, no peak was observed at *m*/*z* = 28 at the same position, indicating that unlabeled CO was not formed during the photocatalytic reaction. This result clearly proves that the evolved CO in this reaction did not originate from carbon residues on the catalyst surface but did from CO_2 substrates. **Figure 1(B)** shows the time course of the activity over Ag–Cr/Ga_2O_3:Rh (0.7 mol%) under >300 nm photoirradiation for 15 h. For a few hours in the beginning of the reaction, the total amount of CO and H_2 evolved did not increase linearly, although that of O_2 increased linearly with photoirradiation time. On the other hand, the total formation rates of CO, H_2, and, O_2 increased lineally with time in

the 2nd and 3rd runs. The induction period in the 1st run was attributed to the consumption of generated electrons to reduce Ag or Cr species and to form the Ag–Cr core-shell cocatalyst. [21] The silver oxide and CrO_3 species of as-prepared Ag–Cr/Ga_2O_3 changed into metallic silver and chromium hydroxide-like species, such as $Cr(OH)_3$ and $CrOHCO_3$, respectively, as shown in Ag K-edge and Cr K-edge XANES spectra (**Figure 2**).

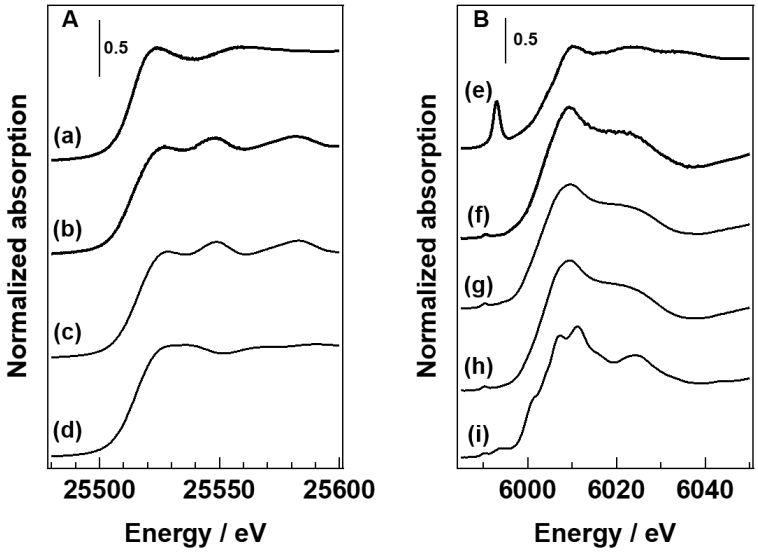

Figure 2. (A) Ag K-edge XANES spectra of Ag–Cr/Ga_2O_3:Rh ((a) as synthesized (b) after 15 h of reaction) and reference samples, (c) Ag-foil and (d) AgO. **(B)** Cr K-edge XANES spectra of Ag–Cr/Ga_2O_3:Rh ((e) as synthesized (f) after 15 h of reaction) and reference samples, (g) $CrOHCO_3$, (h) $Cr(OH)_3$ and (i) Cr_2O_3.

Figure 3(A) shows UV-vis DRS of Rh-doped Ga_2O_3 samples. The undoped Ga_2O_3 exhibited an absorption edge at 270 nm (E_{BG} = 4.6 eV), assignable to direct transitions from the valence band formed by the O 2p orbital to the conduction band consisting of the empty 4s and 4p orbitals of Ga.[42] In contrast, Rh-doped Ga_2O_3 had a new broad absorption between 400 and 500 nm. Additionally, the absorption edge of Ga_2O_3 shifted to 370 nm. The intensity of these two absorptions became stronger with increasing concentration of the Rh dopant. These absorptions originated from new energy levels resulting from doping with Rh.

Figure 3(B) shows UV-vis DRS of Ga_2O_3:Rh (0.7 mol%) and bare-Ga_2O_3 and the H_2 formation rates when using Ag–Cr/Ga_2O_3:Rh (0.7mol%) and undoped Ag–Cr/Ga_2O_3 with cut-off filters (from UV-29 to Y-52). The undoped Ag–Cr/Ga_2O_3 exhibited a low photocatalytic activity

under photoirradiation at λ >290 nm. The evolution of H_2 was observed over Ag–Cr/Ga_2O_3:Rh (0.7 mol%) when cut-off filters from UV-29 to UV-37 were employed. The produced H_2 was derived from the reduction of proton. In case of a reaction system with methanol as a sacrificial reagent, it should be taken into account that protons were derived from the both of the aqueous solution and/or the oxidation of methanol.[43] Thus, it is considered that the photo-exited electrons and holes were consumed to induce the reduction of proton and the oxidation of methanol using the absorption edge below 370 nm, respectively. In contrast, the activity was negligible when a cut-off filter of λ >390 nm was used. In addition, the photocatalytic activity depended on the absorption of Ga_2O_3:Rh in UV-vis DRS, indicating that the photocatalytic activity of Ag–Cr/Ga_2O_3:Rh results from the electron transition using the absorption edge below 370 nm.

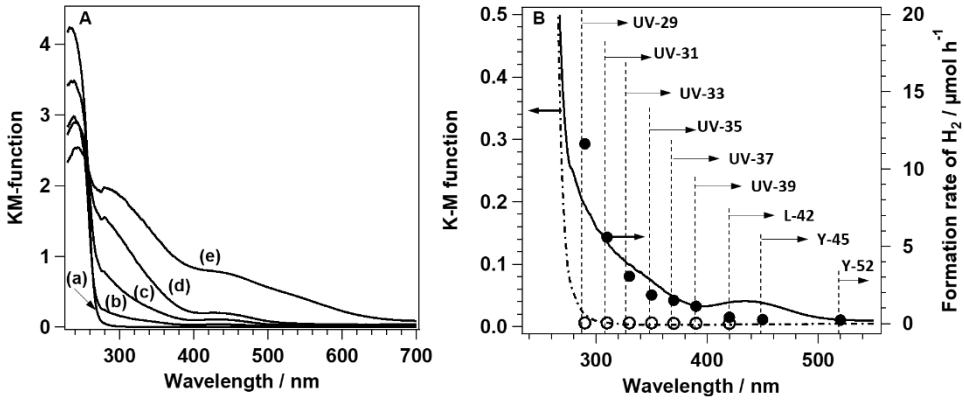

Figure 3. (A) UV-vis DRS of (a) undoped-Ga_2O_3 and Ga_2O_3:Rh (*n* mol%) (*n* = (b) 0.7, (c) 1.3, (d) 3.2, and (e) 6.1 collected by a UV-visible Spectrometer (V-670, JASCO) equipped with an integrated sphere accessory. **(B)** UV-vis DRS of Ga_2O_3:Rh (0.7 mol%) (solid line) and Ga_2O_3 (dotted line) and the formation rate of H_2 in 10 % MeOH aqueous solution as a function of the cut-off wavelength for irradiation over Ag–Cr/Ga_2O_3:Rh (0.7 mol%) (closed circles) and Ag–Cr/Ga_2O_3 (open circles).

As summarized in **Table 3**, the photocatalytic conversions of CO_2 under >300 nm photoirradiation were performed over Ga_2O_3 doped with various molar amounts of Rh and with the Ag–Cr cocatalyst. At the doping amount of 0.1 or 0.3 mol%, reduction products, H_2 and CO, were almost not observed as in the case of undoped Ga_2O_3. Ga_2O_3:Rh (0.7mol%) exhibited the highest formation rate of CO among Ga_2O_3 photocatalysts with various amounts of Rh dopants. At the concentrations of Rh dopants higher than 1.0 mol%, the formation rate of CO began to drop. The

formation rate of H_2 increased with an increase in the doping amount to reach a maximum at 1.3 mol% doping, beyond which it began to drop. As a result, the selectivity toward CO evolution decreased with an increase in the doping amount. It has been reported that Rh species work as a cocatalyst for photocatalytic decomposition of water.[44-46] Ida *et al.* reported that the RhO_6 unit in the lattice of calcium niobate nanosheet functions as a site for H_2 formation from H_2O.[46] As shown in **Table 2** (Entry 3), a significant amount of H_2 gas was produced over Ga_2O_3:Rh under UV light irradiation, indicating that doped Rh species could work as the active sites for H_2 formation. The decrease in the activity at the high concentrations of Rh dopants would be due to the excessive amounts of doped Rh species that work as the recombination centers between photogenerated electrons and holes. The low formation rates of reduction products in the case of Rh doping amounts from 0 to 0.3 mol% were caused by the consumption of photogenerated electrons in order to form the Ag–Cr core-shell cocatalyst, as in the case with **Figure 1(B)**.

Table 3. The activity for the photocatalytic conversion of CO_2 in water over Ag–Cr/Ga_2O_3:Rh (*n* mol%) after 5 h under >300 nm of UV light irradiation.

Entry	Amount of Rh doped (mol%)	Formation rates (μmol h^{-1})			Selectivity toward CO (%)
		H_2	O_2	CO	
1	0	trace	n.d.	trace	-
2	0.1	trace	0.6	0.2	-
3	0.3	4.5	5.2	4.0	46.9
4	0.7	10.3	6.5	3.9	27.6
5	1.0	10.8	6.4	2.7	20.2
6	1.3	4.3	2.7	1.2	21.1
7	1.9	1.9	1.8	0.6	24.4
8	3.2	0.2	0.9	trace	-
9	6.1	trace	n.d.	trace	-

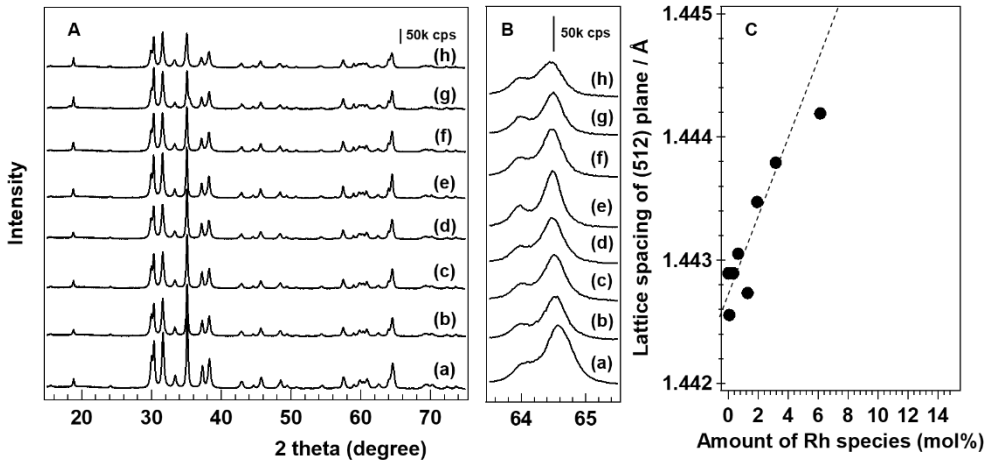

Figure 4. XRD patterns of (a) undoped-Ga_2O_3 and Ga_2O_3:Rh (*n* mol%) (*n* = (b) 0.1, (c) 0.3, (d) 0.7, (e) 1.3, (f) 1.9, (g) 3.2, and (h) 6.1 collected in **(A)** wide range scan and **(B)** narrow range scan. **(C)** Relationship between Amount of Rh species to the change of lattice plane of (512) facet at around 64 °.

Figure 4(A) shows the X-ray diffraction (XRD) patterns of the prepared Ga_2O_3:Rh photocatalysts. Undoped Ga_2O_3 exhibited the diffraction peaks corresponding to β-Ga_2O_3.[38] These diffraction peaks derived from β-Ga_2O_3 were still observed in the XRD patterns of Ga_2O_3:Rh. For further detailed analysis, diffraction peaks between 2θ = 63°-66° are shown in **Figure 4(B).** The position of the diffraction peak assigned to the (512) facet of β-Ga_2O_3 at around 65° shifted to a lower angle, with increasing amount of Rh. Shannon *et al.* reported that the ionic radius of Rh trivalent cation of 6 oxygen coordination environment is 0.665 Å. On the other hand, Ga trivalent cation of 4 and 6 oxygen coordination environment are 0.470 Å and 0.620 Å, respectively.[37] An α-corundum structure of Ga_2O_3 has octahedrally- and tetrahedrally-coordinated Ga^{3+} ions. The peak shift to low angle would be due to the lattice expansion by the substitution of Rh^{3+} ion for Ga^{3+} ion. As shown in **Figure 4(C)**, the lattice spacing of the (512) facet increased linearly with the amount of Rh from 0 to 3.2 mol%. These results indicated that Rh species were doped into the lattice of β-Ga_2O_3. At a concentration of 6.1 mol% of Rh, the peak position corresponding to the (512) facet did not exhibit a linear tendency, suggesting that the excess amount of Rh species in the solution at coprecipitation step remained on the surface without doping in the lattice of Ga_2O_3

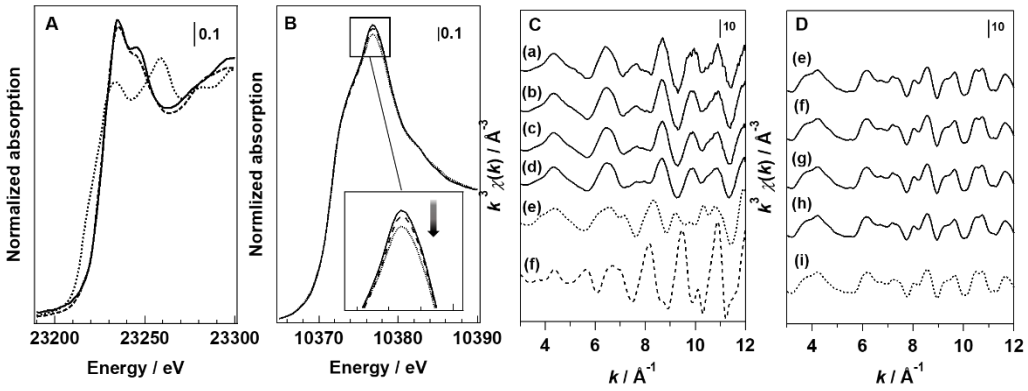

Figure 5. (A) Rh K-edge XANES spectra of Ga_2O_3:Rh (n = 0.7, solid line) and reference samples, Rh_2O_3 (dashed line) and Rh-foil (dotted line). **(B)** Ga K-edge XANES spectra of Ga_2O_3:Rh (n mol%) (n = 0.7 (solid line), 3.2 (dashed line), and 6.1 (dotted line)). **(C)** Rh K-edge EXAFS of Ga_2O_3:Rh (n mol%) (n = (a) 0.7, (b) 1.9, (c) 3.2, and (d) 6.1), (e) Rh_2O_3, and (f) Rh-foil. **(D)** Ga K-edge EXAFS of Ga_2O_3:Rh (n mol%) (n = (e) 0.7, (f) 1.9, (g) 3.2, and (h) 6.1 and (i) undoped-Ga_2O_3.

Figure 5(A) shows Rh K-edge XANES spectra of Ga_2O_3:Rh (0.7 mol%). The Rh species in Ga_2O_3:Rh were considered to be trivalent because the white line absorption edge was almost identical with that of Rh_2O_3. With increasing amount of Rh species, no changes in spectra were observed. The XANES spectrum after 15 h of photoirradiation was similar to that of the as-prepared sample; therefore, the doped-Rh species remained trivalent during the reaction. **Figure 5(B)** shows Ga K-edge XANES spectra of Ga_2O_3:Rh (0.7, 3.2, and 6.1 mol% of Rh were added). A peak top of these spectra slightly decreased with an increase in the amount of the Rh species. Yoshida *et al.* reported that the Ga K-edge XANES spectra of Ga_2O_3 supported on SiO_2 showed two distinct peaks: the lower- and higher-energy peaks were assigned to GaO_4 tetrahedral (Ga(t)) and GaO_6 octahedral (Ga(o)), respectively.[47] β-Ga_2O_3 has these two coordination types of Ga species, Ga(t) and Ga(o), at a ratio in 1:1.[38] The decrease in the higher energy part of the white line of Ga K-edge XANES suggests that the Rh species substituted for some Ga(o) species. EXAFS oscillation also suggested that Rh species in Ga_2O_3 selectively replaced Ga(o). The EXAFS oscillation of the Ga K-edge of Ga_2O_3:Rh differs from Rh K-edge in the oscillation periods (**Figure 5(C)** and **Figure 5(D)**). If Rh species substituted for both Ga(t) and Ga(o) equally, EXAFS of Rh K-edge oscillation should be similar to that of Ga K-edge. Thus, it is plausible that Rh species selectively substituted for Ga(t) or Ga(o). **Figure 6** shows the curve fitting result of Rh K-edge EXAFS spectrum of Ga_2O_3:Rh (0.7 mol%). The

first shell was fitted well with a model doped Rh species substituted to the octahedral Ga sites. The coordination number of Rh was estimated to be 7.1 ± 0.7. A slightly higher coordination number for the first shell might be due to the structure model without consideration of the lattice expansion of Ga_2O_3 by Rh-doping. On the other hand, another curve fitting analysis based on tetrahedral model did not give reasonable physical parameters. Those curve fitting analysis clearly suggested that Rh species selectively substituted for Ga(*o*) sites.

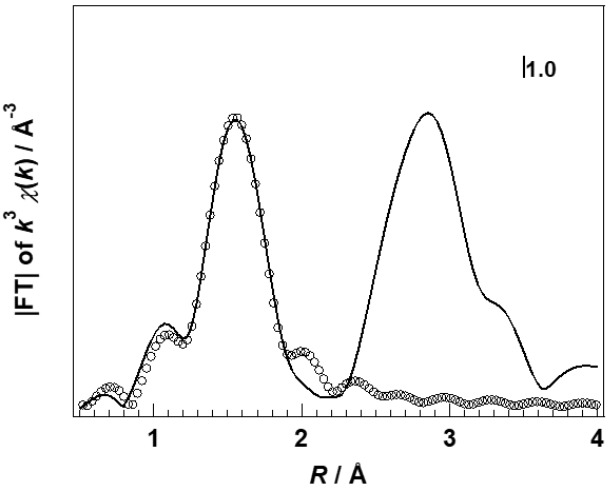

Figure 6. Results of the curve-fitting analysis of Rh K-edge EXAFS of Ga_2O_3:Rh (0.7 mol%). Solid line shows measured Fourier-transformed EXAFS spectrum and circles are the result of curve fitting of the first coordination shell (1< ***R*** <2). The scattering path of Rh-O was estimated from the structure model which doped Rh species substituted to the octahedral Ga sites of β-Ga_2O_3 using FEFF6L code. The local structural parameters determined by the curve fitting are as follows: the coordination number is 7.1 ± 0.7, the inter atomic distance of Rh-O is 2.04 ± 0.01 Å, the Debye-Waller factor is 0.0021 ± 0.0007, and the reliability factor is 0.005. The reliability factor (*r*) is defined as below:

$r = \Sigma[k^3\chi_{obs}(k) - k^3\chi_{cal}(k)]^2 / \Sigma[k^3\chi_{obs}(k)]^2$.

The model doped Rh species substituted to the tetrahedral Ga sites did not give the reasonable physical parameters.

As mentioned above, Rh^{3+} substituted for the octahedral Ga^{3+} in Ga_2O_3. The shift of the absorption edge and new absorption band were observed in the UV-vis DRS of Ga_2O_3:Rh, as shown in **Figure 3**. Density of states of Ga_2O_3 was calculated on 1×1×1 cell of β-Ga_2O_3 by WIEN2k based on DFT, as shown in **Figure 7(A)(a)**. The result was in good agreement with literature data collected by using other calculation software, such as VASP and CASTEP.[39, 48] The midgap state was not observed in the energy gap of Ga_2O_3. In contrast, Ga_2O_3:Rh showed some energy levels in the energy

gap (**Figure 7(A)**(b)). Projected density of states (PDOS) derived from the orbital of Rh of Ga_2O_3:Rh is showed in **Figure 7(B)**. This result suggested that the new two dopant levels in the band gap of Ga_2O_3 corresponded to the d t_{2g} and e_g orbitals of octahedrally coordinated Rh^{3+} species.

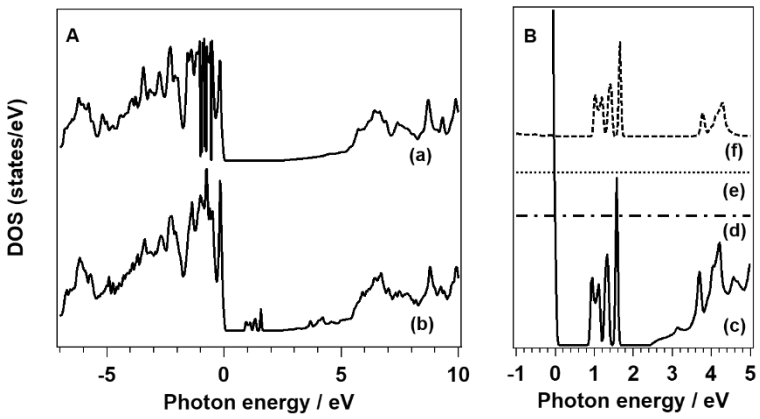

Figure 7. (A) Density of state of (a) Ga_2O_3 and (b) Ga_2O_3:Rh. **(B)** (c) total density of state of Ga_2O_3:Rh and partial density of state of (d) Rh s-orbital and (e) p-orbital (f) d-orbital obtained by first-principles calculation. The energy level was normalized at the top of valence band.

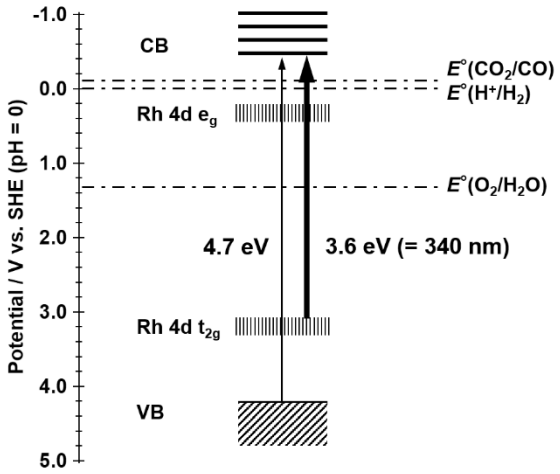

Figure 8. Proposed energy diagram of Ga_2O_3:Rh photocatalyst estimated from UV-vis DRS and DFT calculations.

The proposed energy diagram of Ga_2O_3:Rh is illustrated in **Figure 8**. The band-gap energy of Ga_2O_3 was estimated to be 4.7 eV. UV-vis DRS of Ga_2O_3:Rh suggested that two new absorption were generated, which correspond to ca.3.6 eV and 2.9 eV (**Figure 9**). The octahedrally-coordinated

Rh^{3+} species has fully occupied t_{2g} and empty e_g sets because of ligand field splitting of octahedrally coordinated Rh^{3+}.[36] Thus, possible electron excitations were those from the valence band to Rh 4d e_g^0, from Rh 4d t_{2g}^6 to the conduction band, and from Rh 4d t_{2g}^6 to Rh 4d e_g^0. As shown in **Figure 7(B)**, the energy gap of d-d transition of Rh 4d was ca. 2.9 eV. Additionally, H_2 production was not observed under >390 nm photoirradiation, as shown in **Figure 7(B)**. This result indicated that the potential energy of the Rh 4d e_g orbital is not enough to induce the reduction of proton to H_2. Thus, the electrons generated in the conduction band reduce water to H_2, and these electrons were generated by electron transition from Rh 4d t_{2g}^6.

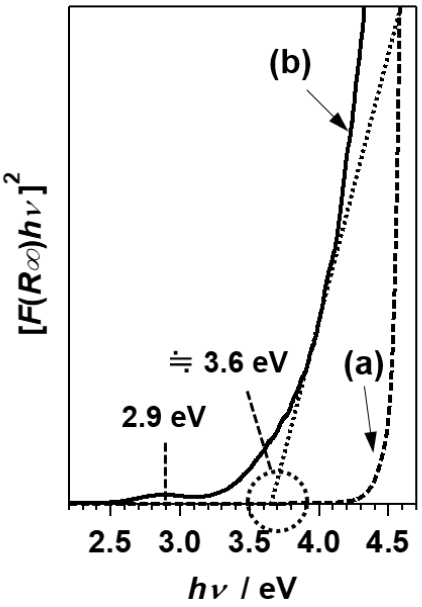

Figure 9. Tauc plot of (a) undoped-Ga_2O_3 and (b) Ga_2O_3:Rh based on the results of UV-vis diffused reflection spectra.

We provided the new system for the photocatalytic conversion of CO_2 by H_2O under oxygen evolution with light of >300 nm wavelength. The formation rate of CO (3.9 μmol h^{-1}) is comparable to reported systems of the reduction of CO_2 induced by >300 nm photoirradiation thus far. [6] The trivalent Rh species were successfully doped into the GaO_6 octahedral site of β-Ga_2O_3 due to the good matching of ionic radius. The doped Rh species are chemically stable in the lattice of Ga_2O_3 during reaction. The role of doped Rh species is the creation of midgap state, resulting in the availability of the electron transition from Rh 4d t_{2g}^6 to the conduction band, which would be similar to the other Rh-doped photocatalysts for water splitting. [32, 36]

Conclusion

Rh-doped Ga_2O_3 acted as a photocatalyst for the reduction of CO_2 at >300 nm wavelength of light. Ag–Cr/Ga_2O_3:Rh (0.7 mol%) showed the activity for the production of CO (3.9 μmol h^{-1}) as a reduction product of CO_2. The formation of the stoichiometric amount of O_2 as the oxidation product of H_2O indicated that H_2O acts as an electron donor. Isotopic experiment results revealed that the CO produced over Ga_2O_3:Rh was definitely derived from CO_2 as the substrate. The absorption edge of UV-vis DRS shifted from 270 nm to more than 300 nm as a result of the Rh doping. The XRD patterns and XANES spectra clarified that Rh^{3+} is substituted for the octahedral Ga^{3+} in Ga_2O_3. DFT calculation results revealed that the new doping levels derived from the Rh d orbitals were generated in the band gap of Ga_2O_3. It was concluded that Ga_2O_3 exhibited the activity for the reduction of CO_2 by doping of Rh with using the absorption derived from Rh d t_{2g} orbital to conduction band.

References

1 T. Inoue, A. Fujishima, S. Konishi and K. Honda, *Nature*, 1979, **277**, 637–638.

2 G. Centi, E. A. Quadrelli and S. Perathoner, *Energy Environ. Sci.*, 2013, **6**, 1711–1731.

3 E. V. Kondratenko, G. Mul, J. Baltrusaitis, G. O. Larrazábal and J. Pérez-Ramírez, *Energy Environ. Sci.*, 2013, **6**, 3112–3135.

4 W. Kim, G. Yuan, B. A. McClure and H. Frei, *J. Am. Chem. Soc.*, 2014, **136**, 11034–11042.

5 T. Arai, S. Sato and T. Morikawa, *Energy Environ. Sci.*, 2015, **8**, 1998–2002.

6 P. Li, Y. Zhou, H. Li, Q. Xu, X. Meng, X. Wang, M. Xiao and Z. Zou, *Chem. Commun.*, 2015, **51**, 800–803.

7 H. Li, Y. Gao, Y. Zhou, F. Fan, Q. Han, Q. Xu, X. Wang, M. Xiao, C. Li and Z. Zou, *Nano Lett.*, 2016, **16**, 5547–5552.

8 X. Zhou, R. Liu, K. Sun, Y. Chen, E. Verlage, S. A. Francis, N. S. Lewis and C. Xiang, *ACS Energy Lett.*, 2016, **1**, 764–770.

9 W. Wang, S. Wang, X. Ma and J. Gong, *Chem. Soc. Rev.*, 2011, **40**, 3703-3727.

10 M. S. Fan, A. Z. Abdullah and S. Bhatia, *ChemCatChem*, 2009, **1**, 192–208.

11 K. Teramura, S. Okuoka, H. Tsuneoka, T. Shishido and T. Tanaka, *Appl. Catal. B: Environ.*, 2010, **96**, 565–568.

12 T. Takayama, K. Tanabe, K. Saito, A. Iwase and A. Kudo, *Phys. Chem. Chem. Phys.*, 2014, **16**, 24417–24422.

13 Z. Wang, K. Teramura, S. Hosokawa and T. Tanaka, *Appl. Catal. B: Environ.*, 2015, **163**, 241–247.

14 K. Teramura, H. Tatsumi, Z. Wang, S. Hosokawa and T. Tanaka, *Bull. Chem. Soc. Jpn*, 2015, **88**, 431–437.

15 K. Teramura, Z. Wang, S. Hosokawa, Y. Sakata and T. Tanaka, *Chem. Eur. J.*, 2014, **20**, 9906–9009.

16 Z. Wang, K. Teramura, Z. Huang, S. Hosokawa, Y. Sakata and T. Tanaka, *Catal. Sci. Technol.*, 2016, **6**, 1025–1032.

17 S. Iguchi, K. Teramura, S. Hosokawa and T. Tanaka, *Catal. Sci. Technol.*, 2016, **6**, 4978–4985.

18 Z. Huang, K. Teramura, S. Hosokawa and T. Tanaka, *Appl. Catal. B: Environ.*, 2016, **199**, 272–281.

19 A. Anzai, N. Fukuo, A. Yamamoto and H. Yoshida, *Catal. Commun.*, 2017, **100**, 134–138.

20 H. Nakanishi, K. Iizuka, T. Takayama, A. Iwase and A. Kudo, *ChemSusChem*, 2017, **10**, 112–118.

21 R. Pang, K. Teramura, H. Tatsumi, H. Asakura, S. Hosokawa and T. Tanaka, *Chem. Commun.*, 2018, **54**, 1053–1056.

22 J. A. Turner, M. C. Williams and K. Rajeshwar, *Electrochem. Soc. Interface*, 2004, **25**, 24–30.

23 A. Kudo and Y. Miseki, *Chem. Soc. Rev.*, 2009, **38**, 253–278.

24 M. Kurihara, F. Hayashi, K. Shimizu, H. Wagata, T. Hirano, Y. Nakajima, H. Nishikiori, S. Oishi, K. Domen and K. Teshima, *CrystEngComm*, 2016, **18**, 3612–3616.

25 A. J. Bard, R. Parsons and J. Jordan, *Standard Potentials in Aqueous Solution*, Marcel Dekker, New York and Basel, 1985.

26 K. Teramura and T. Tanaka, *Phys. Chem. Chem. Phys.*, 2018, **20**, 8423–8431.

27 S. Iguchi, Y. Hasegawa, K. Teramura, S. Kidera, S. Kikkawa, S. Hosokawa, H. Asakura and T.

Tanaka, *Sustain. Energ. Fuels*, 2017, **1**, 1740–1747.

28 S. Iguchi, S. Kikkawa, K. Teramura, S. Hosokawa and T. Tanaka, *Phys. Chem. Chem. Phys.*, 2016, **18**, 13811–13819.

29 H. Kato and A. Kudo, *J. Phys. Chem. B*, 2002, **106**, 5029–5034.

30 R. Niishiro, R. Konta, H. Kato, W. J. Chun, K. Asakura and A. Kudo, *J. Phys. Chem. C*, 2007, **111**, 17420–17426.

31 T. Ishii, H. Kato and A. Kudo, *J. Photochem. Photobiol. A: Chem.*, 2004, **163**, 181–186.

32 R. Konta, T. Ishii, H. Kato and A. Kudo, *J. Phys. Chem. B*, 2004, **108**, 8992–8995.

33 D. W. Hwang, H. G. Kim, J. S. Lee, J. Kim, W. Li and S. H. Oh, *J. Phys. Chem. B*, 2005, **109**, 2093–2102.

34 S. Nishimoto, M. Matsuda and M. Miyake, *Chem. Lett.*, 2006, **35**, 308–309.

35 K. Maeda, *ACS Appl. Mater. Interfaces*, 2014, **6**, 2167–2173.

36 N. Kumagai, L. Ni and H. Irie, *Chem. Commun.*, 2011, **47**, 1884–1886.

37 R. D. Shannon, *Acta cryst.* , 1976, **32**, 751‑767.

38 S. Geller, *JChPh*, 1960, **33**, 676–684.

39 M.-G. Ju, X. Wang, W. Liang, Y. Zhao and C. Li, *J. Mater. Chem. A*, 2014, **2**, 17005–17014.

40 E. A. Davis and N. F. Mott, *Philos. Mag.*, 1970, **22**, 0903–0922.

41 P. Blaha, K. Schwarz and P. Sorantin, *Comput. Phys. Commun.*, 1990, **59**, 399–415.

42 Y. Hou, L. Wu, X. Wang, Z. Ding, Z. Li and X. Fu, *J. Catal.*, 2007, **250**, 12–18.

43 J. Schneider and D. W. Bahnemann, *J. Phys. Chem. Lett.*, 2013, **4**, 3479–3483.

44 K. Yamaguti and S. Sato, *J. Chem. Soc., Faraday Trans.*, 1985, **81**, 1237–1246.

45 K. Maeda, K. Teramura, D. Lu, N. Saito, Y. Inoue and K. Domen, *Angew. Chem. Int. Ed. Engl.*, 2006, **45**, 7806–7809.

46 Y. Okamoto, S. Ida, J. Hyodo, H. Hagiwara and T. Ishihara, *J. Am. Chem. Soc.*, 2011, **133**, 18034–18037.

47 K. Nishi, K. Shimizu, M. Takamatsu, H. Yoshida, A. Satsuma, T. Tanaka, S. Yoshida and T. Hattori, *J. Phys. Chem. B*, 1998, **102**, 10190–10195.

48 Y. Zhang, J. Yan, G. Zhao and W. Xie, *Physica B*, 2010, **405**, 3899–3903.

Chapter 6

Photoelectrochemical Investigation of the Role of Surface-Modified Yb Species in the Photocatalytic Conversion of CO_2 by H_2O over Ga_2O_3 Photocatalysts

Abstract

Modification of Ga_2O_3 photocatalysts with rare earth elements is known to enhance the activity and selectivity of CO formation during the photocatalytic conversion of CO_2 by H_2O as an electron donor, but the role of the rare earth species requires clarification. Photocurrent measurements revealed that modification with Yb species *via* hydrothermal treatment enhanced the anodic photocurrent of the Ga_2O_3 photoelectrode in CO_2-saturated $NaHCO_3$ aqueous solution while maintaining the onset potential of the anodic photocurrent. Impedance measurements revealed that the band structure of Ga_2O_3 was maintained following Yb modification, suggesting that the enhanced anodic photocurrent was due to the surface properties. The anodic photocurrent values of the Yb-modified Ga_2O_3 photoelectrode increased with an increase in the surface adsorption ability of CO_2. The positive relationship between the anodic photocurrent value and the concentration of HCO_3^- species, as measured in two-component $NaHCO_3$ and Na_3PO_4 electrolytes, indicated that the concentration of HCO_3^- species near the surface strongly influenced the anodic O_2-formation activity of the Yb-modified Ga_2O_3 photoelectrode. We concluded that Yb modification improved the oxidation activity of H_2O on the surface of Ga_2O_3 by enhancing the affinity for intermediate HCO_3^- species, resulting in a high activity for the photocatalytic conversion of CO_2 by H_2O.

Introduction

Carbon dioxide (CO_2), one of the major greenhouse gases, is emitted by the consumption of fossil fuels. It is imperative to address climate change through the introduction of neutral carbon cycles that convert CO_2 to other valuable compounds, such as carbon monoxide (CO), formic acid (HCOOH), formaldehyde (HCHO), methanol (CH_3OH), and methane (CH_4). Among CO_2 conversion techniques, the photocatalytic conversion of CO_2 using H_2O as an electron donor, called artificial photosynthesis, has received significant attention[1-4]. In such a process, it is important to achieve stoichiometric oxidation of H_2O, which means that the number of holes consumed to evolve O_2 *via* a four-electron oxidation process is equivalent to the number of electrons consumed to produce the reduction products[5]. Several studies on the photocatalytic conversion of CO_2 by H_2O have reported that various metal oxide photocatalysts with a Ag cocatalyst exhibit activity for CO_2 reduction and water splitting with the stoichiometric evolution of O_2[5-17]. In addition, the selective consumption of photoexcited electrons for the reduction of CO_2 is required to suppress the competitive reduction of the oxonium cation (H_3O^+) in aqueous solution. However, achieving the selective reduction of CO_2 while suppressing the evolution of H_2 is difficult because the standard potential for H^+/H_2 ($E^{\circ\prime} = -0.41$ V *vs.* SHE at pH = 7) is more positive than that of CO/CO_2 ($E^{\circ\prime} = -0.52$ V *vs.* SHE at pH = 7)[18].

Previously, our group has reported that the modification of Ta_2O_5 photocatalysts with alkaline earth metals, such as Mg, Ca, Sr, or Ba, improves the selectivity toward CO while maintaining the formation rate of O_2[8]. In addition, we have also reported that, in some cases, surface modification of the photocatalysts improves the overall activity, as represented by the formation rate of O_2. For example, rare earth metal elements, such as Y, Pr, Nd, Sm, Gd, Dy, Ho, Er, Yb, or Lu, improved the formation rates of CO and H_2, resulting in an increase in the formation rate of O_2[19, 20]. Therefore, rare earth metal elements on the surface of Ga_2O_3 photocatalysts not only promoted the selectivity of CO formation but also improved the activity itself. We consider the high selectivity toward CO to be a result of enhanced CO_2 adsorption on the surface. In fact, the CO_2 adsorption amount on Pr-modified Ga_2O_3 was fifty times higher than that on bare Ga_2O_3[19]. In addition, *in situ* infrared spectroscopy studies revealed that CO_2 molecules react with hydroxyl groups on the surface of Ga_2O_3, resulting in the formation of bidentate carbonate species[21]. Thus, we consider the improved adsorption ability of

CO_2 in aqueous solution to lead to high selectivity toward CO formation. However, there is no plausible explanation for why surface modification with Yb results in high activity for O_2 evolution. Thus, to establish an efficient system for the photocatalytic conversion of CO_2 by H_2O, it is essential to identify the role of the rare earth species on the Ga_2O_3 surface.

During photocatalytic water splitting, the four-electron oxidation of H_2O is considered more difficult to achieve than the two-electron reduction of H_3O^+ to H_2[22-24]. There are many approaches for improving the activity and elucidating the mechanisms of these processes over photocatalytic and photoelectrochemical water oxidation catalysts[22, 25-32]. In particular, during photoelectrochemical water oxidation over an *n*-type photoanode, photoelectrochemical analysis is an effective method for elucidating the carrier dynamics of photogenerated holes in the photoanode under *in situ* conditions in aqueous solution[26, 29, 31, 32]. Half reactions using an oxidation reagent such as $AgNO_3$ or $Ce(SO_4)_2$ are commonly employed to evaluate the net oxidation activity of powder-type photocatalysts[33], but such processes are not suitable for the photocatalytic conversion of CO_2 in H_2O because undesirable reactions occur over the reductive-deposited species, such as Ag metal or $Ce(OH)_3$. Thus, in this study, to elucidate the role of surface-modified Yb species during the photocatalytic conversion of CO_2 by H_2O, the net oxidation ability of the holes was evaluated using a photoelectrochemical system with a Pt counter electrode. As Ga_2O_3 is an *n*-type semiconductive oxide, electrons photogenerated on the Ga_2O_3 photoanode were rapidly transferred to the Pt counter electrode and then consumed to reduce H_3O^+. In addition, impedance measurements were performed to reveal the band structure of surface-modified Ga_2O_3 photocatalysts. Moreover, the relationships between the anodic photocurrent and the concentration of CO_2-related species in aqueous solution were investigated by measuring the anodic photocurrent in mixed electrolytes of $NaHCO_3$ and Na_3PO_4. This study provided electrochemical and photoelectrochemical insights into the role of surface-modified Yb species on Ga_2O_3 in the effective photocatalytic conversion of CO_2 by H_2O.

Experimental

Gallium hydroxide ($Ga(OH)_3$) was prepared by hydrolyzing $Ga(NO_3)_3{\cdot}nH_2O$ (99.9%, Kojundo Chemical Laboratory Co., Ltd) with an aqueous solution of NH_3. Ga_2O_3 was synthesized by

calcination of $Ga(OH)_3$ at 1273 K for 6 h. Yb-modified Ga_2O_3 was prepared using a hydrothermal method. Ga_2O_3 was suspended in an aqueous solution of $Yb(NO_3)_3 \cdot nH_2O$ (99.9%, Wako Pure Chemicals Co., Ltd.). The suspension was aged at 393 K for 24 h under hydrothermal conditions in a stainless steel autoclave equipped with an inner Teflon vessel. The resulting precipitate was collected by filtration, washed with ultrapure water, and then dried at room temperature in air. To test the photocatalytic activity for the conversion of CO_2, the Ga_2O_3 photocatalyst was modified with 1.0 wt% Ag cocatalyst using a typical photodeposition method. The photocatalysts were dispersed in an aqueous solution of $AgNO_3$ and then illuminated using a 400 W high-pressure Hg lamp through a quartz glass filter equipped with a cooling water system for 2 h under flowing Ar[19, 20].

For the electrochemical and photoelectrochemical measurements, surface-modified Ga_2O_3 electrodes were prepared on fluorine-doped tin oxide (FTO) glass (AGC Fabritech Co., Ltd.) *via* an electrophoresis deposition process. The Ga_2O_3-based photocatalyst (50 mg) was added to 50 mL of an acetone solution containing 10 mg of iodine (99.8%, Wako Pure Chemicals Co., Ltd.) as an electrolyte, and then the powder was dispersed by ultrasonication in a cooling bath (~273 K). Prior to use, the FTO glass was washed successively with acetone and 2-propanol. Two FTO glasses were immersed in the photocatalyst solution facing each other, and a direct current of 0.1 mA was applied between the two FTO glasses using an electrochemical measurement system (HZ-5000, Hokuto Denko Corp.) for 2 min. After drying at room temperature in air, the prepared electrode was annealed at 773 K for 30 min to remove any residual iodine. Hereinafter, these electrodes are called Ag/*x*Yb/Ga_2O_3/FTO, where *x* is the molar ratio of Yb species relative to the total amount of cations (Ga and Yb species).

Impedance measurements were performed using a three-electrode electrochemical cell consisting of a series of surface-modified Ga_2O_3/FTO electrodes, a standard Ag/AgCl electrode, and a Pt wire as the working electrode, reference electrode, and counter electrode, respectively. In all the electrochemical measurements, the area of the electrode immersed in the electrolyte solution was fixed at 8 cm^2. Prior to the measurements, air dissolved in the electrolyte solution was completely removed using an Ar gas flow at pH = 6.2. The imaginary component of the impedance (Z'') of the equivalent circuit including the Ga_2O_3/FTO electrode was evaluated at alternating current frequencies of 79.4, 63.0, and 50.1 kHz while sweeping the applied voltage from 0.3 to −0.5 V *vs*. Ag/AgCl using an electrochemical measurement system (HZ-5000, Hokuto Denko Corp.) equipped with a frequency

response analyzer (FRA5095, NF Corporation). As a reference sample, a TiO_2 electrode (ST-01, Ishihara Sangyo Kaisha, Ltd) exhibited a reasonable flat band potential (E_{FB}), as shown in our previous report[11]. The E_{FB} values were determined in the following manner.

The capacitance (C) of the circuit was calculated from the imaginary component of the impedance (Z'') using the relationship:

$$\left|Z''\right| = 1/\left(2\pi fC\right) \tag{1}$$

where π and f are the circumference ratio and the frequency of the alternating current, respectively. The E_{FB} value of the working electrode was estimated using the obtained C value in accordance with the Mott–Schottky equation:

$$C^{-2} = \left(2/\varepsilon\varepsilon_{\circ}A^2eN_{\mathrm{D}}\right)\ \left(V - E_{\mathrm{FB}} - k_{\mathrm{B}}T/e\right) \tag{2}$$

where C and A are the interfacial capacitance and area, respectively, N_D is the number of carriers, V is the applied voltage, k_B is Boltzmann's constant, T is the absolute temperature, ε is the dielectric constant of the semiconductor, ε_o is the permittivity of free space, and e is the electronic charge. Therefore, the value of E_{FB} can be obtained from the x-axis intercept of the plot of C^{-2} *vs.* V. For the Ga_2O_3 photocatalysts in the present study, the band gap energy, the potential energy of the bottom of the conduction band, and the potential energy of the top of the valence band are called E_{BG}, E_{CB}, and E_{VB}, respectively. The effect of the pH of the electrolyte solution on the potential was determined using the Nernst equation, as follows:

$$E^{\circ\prime}_{(pH=a)} = E^{\circ\prime\prime}_{(pH=b)} - 0.059 \times \left(a - b\right) \tag{3}$$

where $E^{\circ\prime}_{(\mathrm{pH}=a)}$ and $E^{\circ\prime\prime}_{(\mathrm{pH}=b)}$ are the values of the potential at pH = a and b, respectively. For example, a potential of 0.00 V at pH = 0.0 corresponds to a potential of 0.41 V at pH = 7.0. In addition, the potentials against Ag/AgCl were converted to standard electrode potentials (normal hydrogen electrode (NHE) and reversible hydrogen electrode (RHE)) using the following equations:

$$E\left(vs.\ \mathrm{NHE}\right) = E\left(vs.\ \mathrm{Ag/AgCl}\right) + 0.199\,\mathrm{V} \tag{4}$$

$$E\left(vs.\ \mathrm{RHE}\right) = E\left(vs.\ \mathrm{Ag/AgCl}\right) + 0.199\,\mathrm{V} + 0.059\times\mathrm{pH} \tag{5}$$

Transient photocurrents in the absence of an external bias were measured in a two-electrode H-type electrochemical cell using an electrochemical measurement system (HZ-5000, Hokuto Denko Corp.). The prepared photoelectrode and Pt wire were used as the working electrode in the anode chamber and the counter electrode in the cathode chamber, respectively. The anode and cathode

chambers were separated by a cation exchange membrane filter (Nafion® perfluorinated membrane, Nafion® 117, Sigma Aldrich) to maintain the same pH in both chambers. The immersed photoelectrode was irradiated through the quartz window using a 200 W Hg–Xe lamp (SAN-EI Electric Co., Ltd.) with a chopper used to switch photoirradiation on or off every 10 s. Prior to measurements, the electrolyte solution (0.1 M Na_2SO_4) was degassed using CO_2 (at pH = 4.3) or Ar (at pH = 6.2).

Linear sweep voltammograms were collected using a three-electrode electrochemical cell consisting of a series of prepared surface-modified Ga_2O_3/FTO electrodes, a Ag/AgCl electrode, and a Pt wire as the working electrode, reference electrode, and counter electrode, respectively. The photoelectrode was irradiated through the quartz window using a 200 W Hg–Xe lamp with a chopper used to switch photoirradiation on or off every 3 s. During photoirradiation, the photocurrent was collected by an electrochemical measurement system (HZ-5000, Hokuto Denko Corp.) under an applied voltage that was swept linearly from −1.4 to 1.0 V *vs*. Ag/AgCl at a scanning rate of 5 mV s^{-1}. A series of mixed $NaHCO_3$ and Na_3PO_4 aqueous electrolyte solutions, in which the concentration of counter cations was fixed at 0.1 M, was degassed using CO_2. The concentration of CO_2-related species in the electrolyte solutions, such as hydrated CO_2 molecules (CO_2(aq)), carbonic acid (H_2CO_3), bicarbonate (HCO_3^-), and carbonate ions (CO_3^{2-}), were calculated from the pH of the mixed $NaHCO_3$ and Na_3PO_4 aqueous solution, as described in our previous report (**Table 1**)[21]. Namely, considering the low hydration equilibrium constant, the total concentration of CO_2-related species and the dissociation constants of carbonic acid can be estimated using the following equations:

$$\left[CO_2(aq)\right] = \left(\frac{\left[H^+\right]^2}{\left[H^+\right]^2 + K_1\left[H^+\right] + K_1K_2} \right) S \tag{6}$$

$$\left[HCO_3^-\right] = \left(\frac{K_1\left[H^+\right]}{\left[H^+\right]^2 + K_1\left[H^+\right] + K_1K_2} \right) S \tag{7}$$

$$\left[CO_3^{2-}\right] = \left(\frac{K_1K_2}{\left[H^+\right]^2 + K_1\left[H^+\right] + K_1K_2} \right) S \tag{8}$$

where S is the total concentration of CO_2-related species and K_1 and K_2 are the first and second

dissociation constants of carbonic acid, respectively. Considering electrical neutrality and the equilibrium of phosphate species, the total concentration of CO_2-related species, S, can be obtained as follows:

$$S = \left(\left[Na^+ \right] + \left[H^+ \right] - \frac{K_W}{\left[H^+ \right]} - \left[H_2PO_4^- \right] - 2\left[HPO_4^{2-} \right] - 3\left[PO_4^{3-} \right] \right) \left(\frac{\left[H^+ \right]^2 + K_1 \left[H^+ \right] + K_1 K_2}{K_1 \left[H^+ \right] + 2K_1 K_2} \right) \quad (9)$$

where K_W is the self-ionization constant of water, and $[H_2PO_4^-]$, $[HPO_4^{2-}]$, and $[PO_4^{3-}]$ are calculated by using the total concentration of phosphate species and their dissociation constants.

Table 1. Concentrations of $NaHCO_3$, Na_3PO_4, and CO_2-related species in aqueous solution as calculated from the solution pH.

Entry	Concentration of additives[a] (mM)		CO_2-related species[b] (mM)			pH	Anodic photocurrent[c]
	$NaHCO_3$	Na_3PO_4	$[CO_2(aq.)]$	$[HCO_3^-]$	$[CO_3^{2-}]$		($\mu A\ cm^{-2}$)
1	10.0	30.0	165.8	68.3	2.9×10^{-3}	5.97	36.4
2	20.0	26.7	122.4	71.2	4.3×10^{-3}	6.12	83.4
3	40.0	20.0	88.2	77.8	7.2×10^{-3}	6.30	92.9
4	50.0	16.7	74.8	81.0	9.2×10^{-3}	6.39	128.6
5	60.0	13.3	63.4	84.5	11.8×10^{-3}	6.48	165.2
6	80.0	6.7	52.3	91.9	16.9×10^{-3}	6.60	168.6
7	90.0	3.3	43.3	95.9	22.2×10^{-3}	6.70	163.9
8	100.0	0	35.9	99.9	29.1×10^{-3}	6.80	163.1

[a] Total concentration of Na^+ was maintained at 100 mM.

[b] For calculations, the following values were applied (298.15 K and ionic strength = 0): $K_1 = 4.42 \times 10^{-7}$, $K_2 = 4.69 \times 10^{-11}$, and $K_W = 1.0 \times 10^{-14}$. The first, second, and third dissociation constants of phosphoric acid are $Kp_1 = 7.23 \times 10^{-3}$, $Kp_2 = 6.31 \times 10^{-8}$, and $Kp_3 = 4.59 \times 10^{-13}$, respectively.

[c] Photocurrent values were collected at an applied bias of 1.1 V *vs*. RHE.

In this study, we only focused on $CO_2(aq)$ and HCO_3^- as the species related to the activity of water oxidation. For instance, **Figure 1** shows the concentrations of CO_2-related species as a function of pH in the mixed solution of 40 mM $NaHCO_3$ and 20 mM Na_3PO_4 under typical reaction conditions (298.15 K and 101.325 kPa of CO_2). At the experimental pH value of 6.30, $[CO_3^{2-}]$ was much lower than $[CO_2(aq)]$ and $[HCO_3^-]$.

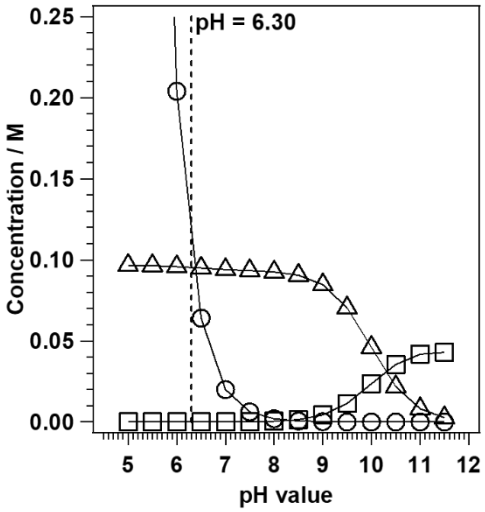

Figure 1. Calculated concentrations of CO_2(aq) (circles), HCO_3^- (triangles), and CO_3^{2-} (squares) in a mixed solution of 40 mM $NaHCO_3$ and 20 mM Na_3PO_4 at 303 K under 101.325 kPa of CO_2 (**Table 1**, Entry 3).

The photocatalytic conversion of CO_2 by H_2O as an electron donor over Ag-loaded xYb/Ga_2O_3 was performed in an inner-irradiation-type reactor in the same manner as in our previous reports[19, 20]. The photocatalyst powder (0.5 g) was dispersed in an aqueous solution of $NaHCO_3$ (0.1 M, 1.0 L). The suspension was irradiated using a 400 W high-pressure Hg lamp through a quartz glass filter equipped with a cooling water system. CO_2 gas (99.999%) was bubbled into the solution at a flow rate of 30 mL min^{-1}. As products, CO, H_2, and O_2 were analyzed by gas chromatography equipped with a thermal conductivity detector using a GC-8A chromatograph (Shimadzu Corp.) equipped with a Molecular Sieve 5A column with Ar as the carrier gas and gas chromatography equipped with a flame ionization detector (Shimadzu Corp.) with a methanizer using a Shincarbon ST column with N_2 as the carrier gas.

The selectivity toward CO evolution over H_2 evolution and the balance between consumed electrons (e^-) and holes (h^+) can be described generally as follows:

$$\text{Selectivity toward CO evolution } (\%) = 100 \times 2R_{CO} / \left(2R_{CO} + 2R_{H_2}\right) \quad (10)$$

$$\text{Consumed } e^- / h^+ = \left(2R_{CO} + 2R_{H_2}\right) / 4R_{O_2} \quad (11)$$

where R_{CO}, R_{CH4}, and R_{O2} represent the rates of formation of CO, H_2, and O_2, respectively.

X-ray diffraction (XRD) patterns of the powder samples and prepared electrodes were collected with an X-ray diffractometer (Multiflex, Rigaku) using Cu K_α radiation at an acceleration

voltage of 40 kV with a step size of 0.02°. Scanning electron microscopy (SEM) images of the electrodes were captured using a field emission scanning electron microscope (SU-8220, Hitachi High-Technologies) at an acceleration voltage of 3.0 kV. Local element mapping of the surface-modified Ga_2O_3 photocatalysts was conducted using energy-dispersive X-ray spectroscopy (EDS; EMAX ENERGY EX-250, Horiba).

UV-vis diffuse reflectance spectroscopy (DRS) of the surface-modified Ga_2O_3 photocatalysts was performed using a UV-vis spectrometer (V-670, JASCO) equipped with an integrating sphere accessory. The energy gap (E_{BG}) value of each Ga_2O_3 photocatalyst was determined with the Davis–Mott equation using the Kubelka–Munk function $F(R_\infty)$ obtained from the diffuse reflectance spectrum:

$$\left[F\left(R_\infty\right)h\nu\right]^{-n} = A\left(h\nu - E_{BG}\right) \tag{12}$$

where h, ν, and A are Plank's constant, the frequency of vibration, and the proportionality constant, respectively.

The Brunauer–Emmett–Teller (BET) surface area was measured by N_2 adsorption at 77 K using a volumetric gas adsorption apparatus (BELmini, BEL Japan, Inc.). The temperature-programed desorption (TPD) profile of CO_2 was evaluated using a TPD apparatus (TPD 1-AT, BEL Japan Inc.) equipped with a quadrupole mass spectrometer (Q-MASS). The samples were mounted in a quartz glass tube with internal K-type thermocouples. After pretreatment under flowing He at 723 K for 1 h to remove preadsorbed species, CO_2 gas was introduced and allowed to adsorb on the sample surface at 313 K for 30 min. TPD measurements were then performed at a ramp rate of 5 K min^{-1} under flowing He in the temperature range of 313–1223 K.

Results and discussion

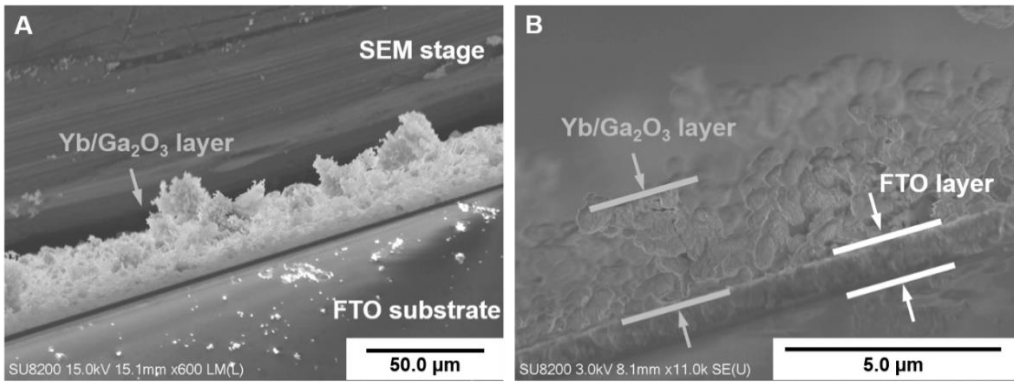

Figure 2. SEM images (side view) of the 9Yb/Ga_2O_3/FTO photoelectrode: (A) wide view at low magnification and (B) narrow view at a magnification of 11.0 k.

Figure 2 shows SEM images of the Ga_2O_3 photocatalyst loaded with 9 mol% Yb and mounted on the FTO substrate (9Yb/Ga_2O_3/FTO), which was fabricated by an electrophoretic method. The Yb/Ga_2O_3 layer, with a thickness of ~3.0 μm, covered the entire FTO substrate and maintained the ellipsoid-like morphology of Ga_2O_3. Mixed diffraction patterns derived from β-Ga_2O_3 and FTO glass were observed in the XRD pattern of a Yb/Ga_2O_3/FTO photoelectrode, suggesting that the structure of Yb/Ga_2O_3 was maintained during the photoelectrode fabrication process (**Figure 3**). Powder XRD patterns (**Figure 4**) of Yb/Ga_2O_3 indicated that the crystal structure of β-Ga_2O_3 was maintained following the hydrothermal treatment. Although the Yb species deposited on Ga_2O_3 were amorphous at less than 3 mol% Yb, modification with higher amounts of Yb resulted in surface-formed Yb-derived species, which is consistent with previous reports on Yb-modified Ga_2O_3 photocatalysts[20]. The Yb species covered the entire surface of Ga_2O_3, as shown by EDS mapping (**Figure 5**). The absorption edge in the UV-vis diffuse reflectance spectrum of 3Yb/Ga_2O_3 is located at 270 nm, which is the same as that of Ga_2O_3, indicating that Yb modification did not affect the photoabsorption properties of Ga_2O_3 (**Figure 6(A)**). For Ag-loaded Yb/Ga_2O_3 (Ag/Yb/Ga_2O_3), the surface plasmon resonance peak was observed in the visible region of the UV-vis diffuse reflectance spectrum, suggested the formation of poorly dispersed Ag nanoparticles [13]. However, the particles were not large enough to be observed by SEM or XRD.

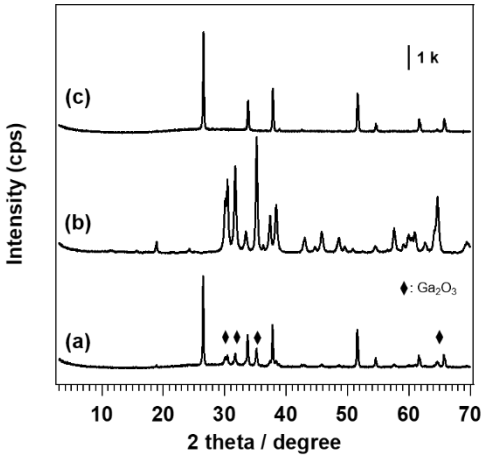

Figure 3. XRD patterns of (a) the 3Yb/Ga_2O_3/FTO composite, (b) the 3Yb/Ga_2O_3 powder, and (c) the bare FTO substrate.

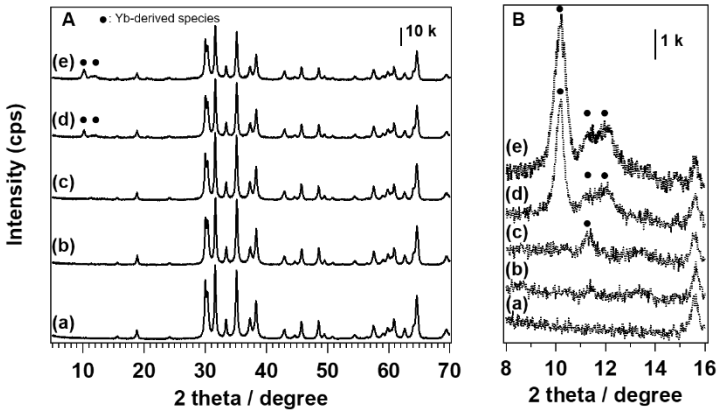

Figure 4. (A) Wide-range and **(B)** narrow-range XRD patterns of powder samples. (a) Ga_2O_3, (b) 1Yb/Ga_2O_3, (c) 3Yb/Ga_2O_3, (d) 5Yb/Ga_2O_3, and (e) 9Yb/Ga_2O_3.

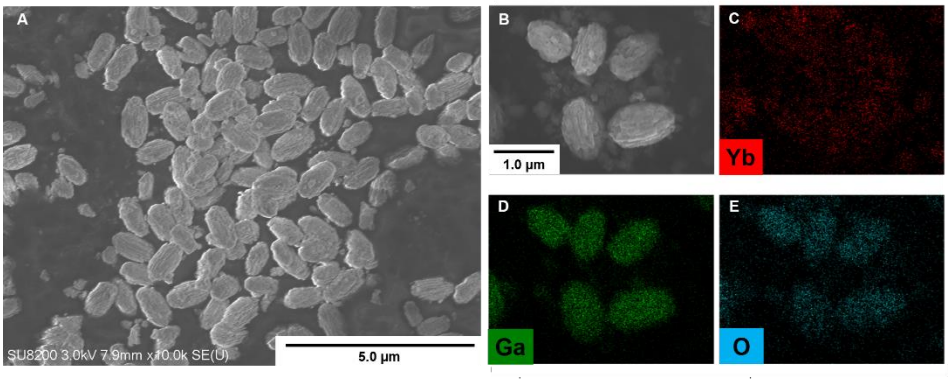

Figure 5. SEM images of **(A)** 9Yb/Ga_2O_3 and **(B)** selected particles of 9Yb/Ga_2O_3, and corresponding elemental maps of **(C)** Yb, **(D)** Ga, and **(E)** O.

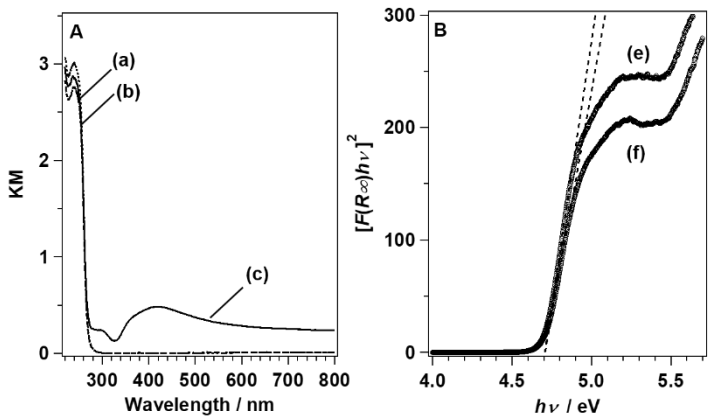

Figure 6. (A) UV-vis diffuse reflectance spectra (DRS) of (a) Ga_2O_3 (b) $3Yb/Ga_2O_3$, and (c) $Ag/3Yb/Ga_2O_3$. **(B)** Tauc plot of (d) Ga_2O_3 and (e) $3Yb/Ga_2O_3$ based on the UV-vis DRS results. The dotted lines are the tangents of the inflection points.

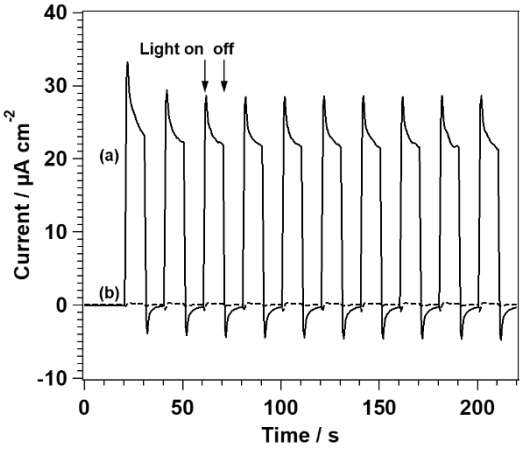

Figure 7. Transient photocurrent response under chopped illumination (photoirradiation turned on or off every 10 s) over (a) $3Yb/Ga_2O_3/FTO$ (solid line) and (b) $Ag/3Yb/Ga_2O_3/FTO$ (dashed line) photoelectrodes. Electrochemical cell: working photoelectrode, Pt wire counter electrode, and 0.1 M Na_2SO_4 aqueous solution (pH 4.3) under flowing CO_2. Photoirradiation: 200 W Hg–Xe lamp through a quartz glass window.

Figure 7 shows the transient photocurrent under chopped illumination with no applied external bias in a two-electrode system. The $3Yb/Ga_2O_3$ photoelectrode exhibited an anodic photocurrent under illumination, with a transient decay following the anodic response. When the irradiation was turned off, the anodic current decreased and then a slight cathodic overshoot was observed. The anodic current was stable during repeated chopped illumination and after this

measurement, the 3Yb/Ga_2O_3 particles mounted on the photoelectrode were still observable in SEM images. These results indicate that surface oxidation of the *n*-type photoelectrode proceeded and that the photoexcited electrons were transferred to the Pt counter electrode. It has previously been suggested that positive transient and negative overshoots are associated with the accumulation of holes in the space charge layer and the recombination of bulk electrons with holes, respectively[29, 34].

The Ag/3Yb/Ga_2O_3 photoelectrode, loaded with a Ag cocatalyst, which is effective for the photocatalytic conversion of CO_2 in water, exhibited a much lower photocurrent than 3Yb/Ga_2O_3. In addition, a cathodic current spike was observed following illumination of the Ag/3Yb/Ga_2O_3 photoelectrode, which transformed into a steady anodic current over the irradiation time. A cathodic spike current for *n*-type photoanodes indicates the presence of reduction sites on the photoelectrodes. We consider the photoexcited electrons to be consumed by reduction over the Ag cocatalyst, even in the presence of the Pt counter electrode. Thus, we compared the anodic currents of the Yb/Ga_2O_3 photoelectrodes without the Ag cocatalyst to evaluate their net oxidation activities.

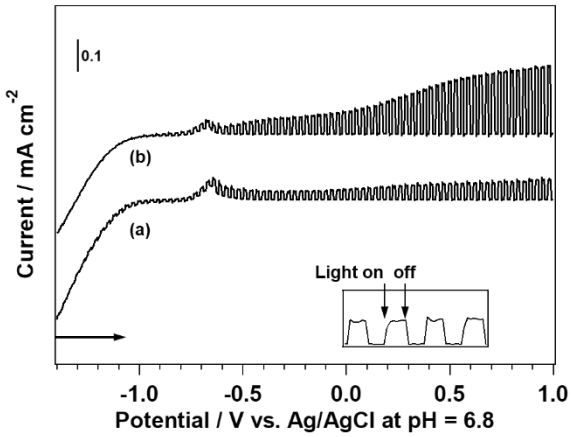

Figure 8. Linear sweep voltammograms of (a) Ga_2O_3/FTO and (b) Yb/Ga_2O_3/FTO photoelectrodes under chopped illumination (photoirradiation turned on or off every 3 s). Electrochemical cell: working photoelectrode, Ag/AgCl reference electrode, Pt wire counter electrode, and 0.1 M $NaHCO_3$ aqueous solution (pH 6.8) under flowing CO_2. Sweep range: −1.4 to 1.0 V *vs*. Ag/AgCl at a scanning rate of 5 mV s^{-1}. Photoirradiation: 200 W Hg–Xe lamp through a quartz glass window.

Figure 8 shows the current–voltage curves of Ga_2O_3 photoelectrodes with and without Yb modification under chopped irradiation. Cathodic polarization was observed on both the photoelectrodes. The Ga_2O_3 photoelectrode exhibited an anodic photocurrent when a voltage more positive than −1.1 V *vs*. Ag/AgCl was applied during photoirradiation, which means that the potential

energy of the holes was sufficiently positive to induce the oxidation reaction on the electrode surface. The modification of Ga_2O_3 with Yb enhanced the anodic current under photoirradiation while maintaining the onset potential of the anodic photocurrent. In a photoelectrochemical system with a Pt counter electrode, the electrons photoexcited on an *n*-type photoanode are rapidly transferred to the Pt counter electrode, where H_2 is smoothly evolved. Thus, the anodic photocurrent values reflect changes in the oxidation activity on the surface or in the bulk properties of the Ga_2O_3 photocatalyst.

The anodic dark current, observed in both voltammograms at approximately −0.65 V, was assigned to the oxidative formation of SnO_x species in the FTO glass (Sn^{2+}/Sn = −0.138 V *vs.* SHE), which were previously reduced at more negative applied potentials. However, negligible deterioration of the anodic photocurrent was observed during cyclic sweeping of the applied potential when the sweeping direction was changed (**Figure 9**).

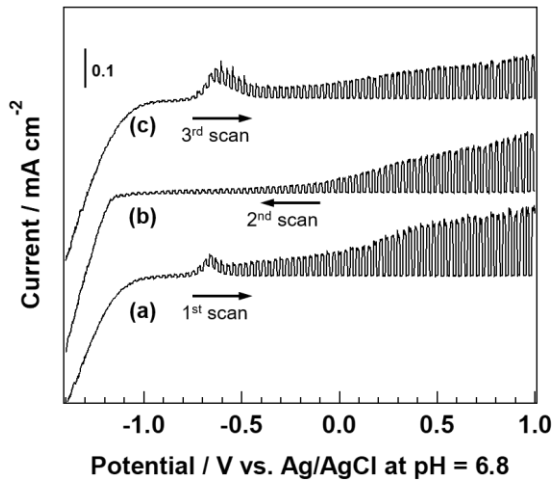

Figure 9. Linear sweep voltammograms of $3Yb/Ga_2O_3$ measured with repeated voltage scanning. Electrochemical cell: working photoelectrode, Ag/AgCl reference electrode, Pt wire counter electrode, and 0.1 M $NaHCO_3$ aqueous solution with flowing CO_2. Sweep range: (a) 1st scan from −1.4 to 1.0 V *vs*. Ag/AgCl, (b) 2nd scan from 1.0 to −1.4 V *vs*. Ag/AgCl, and (c) 3rd scan from −1.4 to 1.0 V *vs*. Ag/AgCl at a scanning rate of 5 mV s^{-1}. Photoirradiation: 200 W Hg–Xe lamp though a quartz glass window (photoirradiation turned on or off every 3 s).

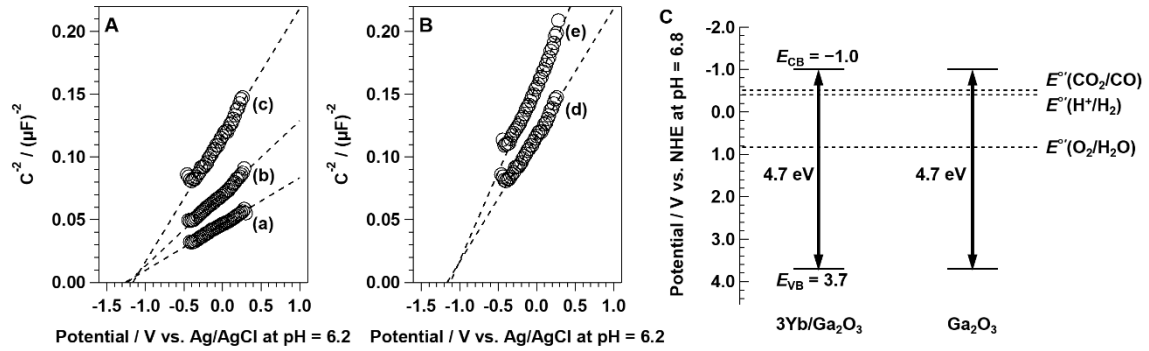

Figure 10. Mott–Schottky plots based on impedance measurement results. (A) Plots for 3Yb/Ga_2O_3/FTO at frequencies of (a) 50.1, (b) 63.0, and (c) 79.4 kHz. (B) Plots for (d) 3Yb/Ga_2O_3/FTO and (e) Ga_2O_3/FTO at a frequency of 79.4 kHz. (C) Electrochemical potentials of the bottom of the conduction bands and the top of the valence bands of 3Yb/Ga_2O_3 and Ga_2O_3 determined from impedance measurements and UV-vis DRS. Electrochemical cell: working photoelectrode, Ag/AgCl reference electrode, Pt wire counter electrode, and 0.1 M Na_2SO_4 aqueous solution (pH 6.2) under flowing Ar. Sweep range: 0.3 to −0.5 V *vs*. Ag/AgCl with alternating current frequencies of 79.4, 63.0, or 50.1 kHz.

Figure 10(A) and **10(B)** display the Mott–Schottky plots of 3Yb/Ga_2O_3/FTO and bare Ga_2O_3/FTO. The capacitance of band bending across a semiconductor–electrolyte junction can be determined using the Mott–Schottky equation. Based on the impedance measurements, the E_{FB} values were estimated by extrapolation to $C^{-2} = 0$ in the C^{-2} *vs.* applied voltage plots. For impedance measurements of 3Yb/Ga_2O_3 at frequencies of 50.1, 63.0, and 79.4 kHz, the extrapolated lines crossed on the *x*-axis, giving an E_{FB} value of −1.2 V *vs*. Ag/AgCl (**Figure 10(A)** (a–c)). The Mott–Schottky plots at 79.4 kHz (**Figure 10(B)**) showed that the E_{FB} values of Ga_2O_3 and 3Yb/Ga_2O_3 were the same. In addition, the slopes of the Mott–Schottky plots of these samples showed the characteristic positive slope of *n*-type semiconductors, indicating that the main carriers were electrons rather than holes. Generally, the E_{FB} of an *n*-type photocatalyst corresponds to the potential of the bottom of the conduction band (E_{CB}). According to the Tauc plot in **Figure 6(B)**, modification with Yb did not affect the band gap energy of Ga_2O_3 (E_{BG} = 4.7 eV). From these results, the top of the valence band (E_{VB}) can be determined, as shown in the band diagrams of 3Yb/Ga_2O_3 and Ga_2O_3 (**Figure 10(C)**). The bottom of the E_{CB} of 3Yb/Ga_2O_3 was −1.0 V *vs*. SHE, which satisfied the potential energy for the two-electron reduction of CO_2 to CO ($E°'$ = −0.51 V *vs*. SHE at pH = 6.8 in 0.1 M $NaHCO_3$ under flowing CO_2), as is the case for bare Ga_2O_3. The top of the E_{VB} of 3Yb/Ga_2O_3, *i.e.*, the potential energy of the

holes, was sufficient to induce the oxidation of H_2O to O_2. These results indicate that the photogenerated electrons and holes in Ga_2O_3 were capable of reducing CO_2 to CO and oxidizing H_2O to O_2, respectively. In addition, modification with Yb species did not affect the band structure of Ga_2O_3. Thus, we consider the high anodic current induced by Yb modification to be derived from improvement of the surface-oxidation activity of the photoanode.

All the Yb-modified Ga_2O_3 photoelectrodes exhibited significant improvements in anodic photocurrent when compared with the bare Ga_2O_3 photoelectrode, as shown in the current–voltage curves under chopped illumination (**Figure 11**). The anodic current values obtained for *x*Yb/Ga_2O_3/FTO are compared in **Figure 12**. The anodic current increased with an increase in the amount of Yb, reaching a maximum at 3.0 mol% and then decreasing. This anodic photocurrent trend represented the order of H_2O oxidation activity on the Yb/Ga_2O_3 surface.

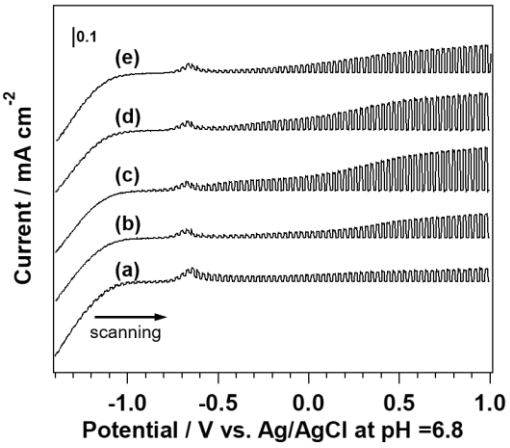

Figure 11. Linear sweep voltammograms of (a) Ga_2O_3, (b) 1Yb/Ga_2O_3, (c) 3Yb/Ga_2O_3, (d) 5Yb/Ga_2O_3, and (e) 9Yb/Ga_2O_3 measured under chopped illumination (photoirradiation turned on or off every 3 s). Electrochemical cell: *x*Yb/Ga_2O_3 working electrode, Ag/AgCl reference electrode, Pt wire counter electrode, and 0.1 M $NaHCO_3$ aqueous solution (pH 6.8) under flowing CO_2. Sweep range: from −1.4 to 1.0 V *vs*. Ag/AgCl at a scanning rate of 5 mV s^{-1}. Photoirradiation: 200 W Hg–Xe lamp though a quartz glass window.

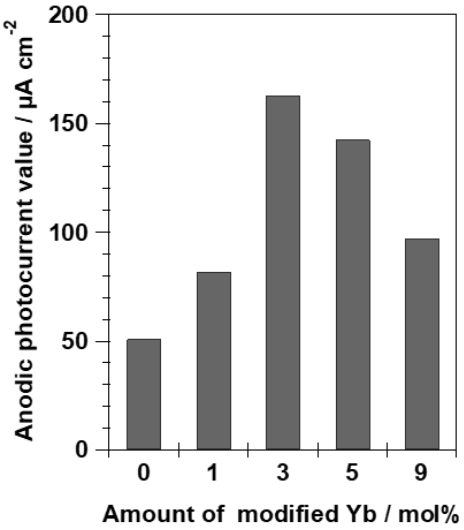

Figure 12. Anodic photocurrents of xYb/Ga_2O_3/FTO photoelectrodes acquired from the current–voltage curves under chopped illumination (photoirradiation turned on or off every 3 s) at an applied potential of 0.5 V *vs*. Ag/AgCl (1.1 V *vs.* RHE). Electrochemical cell: working photoelectrode, Ag/AgCl reference electrode, Pt wire counter electrode, and 0.1 M $NaHCO_3$ aqueous solution (pH 6.8) under flowing CO_2. Sweep range: −1.4 to 1.0 V *vs*. Ag/AgCl at a scanning rate of 5 mV s^{-1}. Photoirradiation: 200 W Hg–Xe lamp through a quartz glass window.

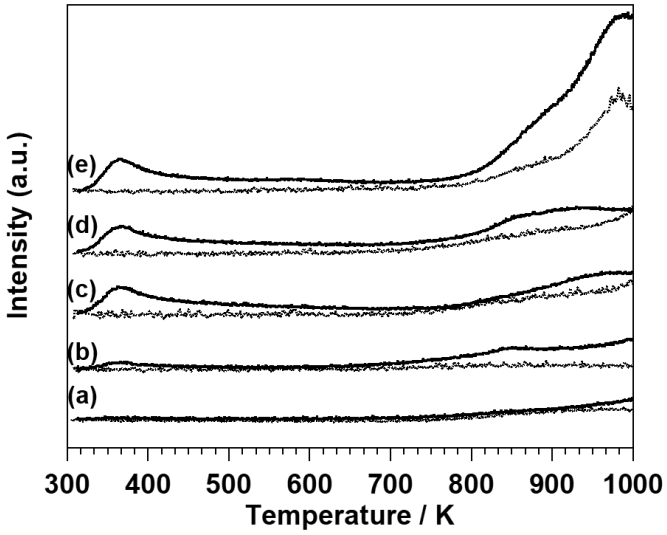

Figure 13. CO_2-temperature-programed desorption (TPD) profiles of (a) Ga_2O_3, (b) 1Yb/Ga_2O_3, (c) 3Yb/Ga_2O_3, (d) 5Yb/Ga_2O_3, and (e) 9Yb/Ga_2O_3. The signals were measured at m/z = 44 and the integrated areas were normalized by the weight of the catalyst. The solid lines correspond to the results with preadsorption of CO_2, whereas the dashed lines correspond to those after pretreatment without preadsorption of CO_2.

The CO_2-TPD profiles of Yb-modified Ga_2O_3 revealed the adsorption properties of the surface-formed Yb species (**Figure 13**). While insignificant CO_2 desorption occurred on the surface of bare Ga_2O_3, the Yb/Ga_2O_3 samples showed two obvious peaks when the sample temperature was elevated. One peak, located below 773 K, was attributed to the desorption of surface-adsorbed CO_2 species[19, 35]. The other peak, located above 773 K, was also observed in the absence of CO_2 preadsorption, indicating that it was derived from the decomposition of surface-formed Yb-derived species, such as carbonate hydrates or hydroxycarbonates[19]. The peak area of the low-temperature CO_2 desorption process increased with an increase in the amount of Yb, reaching a maximum at 3.0 mol% and then remaining constant. As the specific surface areas of the series of Ga_2O_3 photocatalysts were not affected by Yb modification, this increase in CO_2 desorption indicated that the surface of Yb-modified Ga_2O_3 became covered with adsorbed CO_2 species at higher concentrations than bare Ga_2O_3. With CO_2 preadsorption, the peak area of the high-temperature process increased with an increase in the amount of Yb. Thus, we consider the adsorption ability of CO_2 to be related to the oxidation activity of H_2O. In addition, excess modification with Yb species prevented the surface reaction.

Table 2. Activity for the photocatalytic conversion of CO_2 by H_2O over 1.0 wt% Ag cocatalyst-loaded *x*Yb/Ga_2O_3 under UV light irradiation [a].

Entry	Photocatalyst	S_{BET}	Formation rates (μmol h^{-1})			Selectivity	Consumed
		(m^2 g^{-1})	H_2	O_2	CO	toward CO (%)	e^-/h^+ ratio
1	Ga_2O_3	12.9	99.8	95.2	102.1	50.6	0.94
2	1Yb/Ga_2O_3	11.3	112.1	161.5	218.0	66.0	0.98
3	3Yb/Ga_2O_3	10.7	87.6	147.8	211.3	70.1	0.99
4	5Yb/Ga_2O_3	10.6	103.0	140.0	200.0	65.9	0.92
5	9Yb/Ga_2O_3	10.0	136.2	135.4	133.4	49.8	1.00

[a] Photocatalyst weight, 0.5 g; CO_2 flow, 30 mL min^{-1}; solution volume, 1.0 L; additive, 0.1 M $NaHCO_3$; light source, 400 W Hg lamp; irradiation time, 1 h.

Table 2 shows the formation rates of the products obtained by the photocatalytic conversion of CO_2 over Yb-modified Ga_2O_3 photocatalysts after 1 h of photoirradiation. In this study, CO and H_2 were observed as reduction products of CO_2 and H_3O^+, respectively. Other reaction products, such as CH_4, HCOOH, HCHO, and CH_3OH, were not detected by GC or HPLC. Importantly, O_2 was generated as the oxidation product of H_2O. The consumed e^-/h^+ ratio was approximately 1.0, indicating that stoichiometric reduction and oxidation proceeded. Ag/Ga_2O_3 produced CO as the reduction product of CO_2 with a formation rate of 102 μmol h^{-1} (Entry 1). However, H_2 was also generated as an undesired byproduct *via* the reduction of H_3O^+, resulting in a CO selectivity of only 50%. In contrast, an increase in the activity of CO formation was observed by surface modification of Ga_2O_3 with 1.0 mol% of Yb. The formation rate of CO reached 218 μmol h^{-1}, while the formation rate of H_2 was maintained, resulting in an increase of the CO selectivity to 66% (Entry 2). The evolution of O_2 as an oxidation product also increased, which is in accordance with the observation of stoichiometric reduction and oxidation. At Yb amounts higher than 3.0 mol%, the formation rate of CO began to decrease, resulting in a decrease in the formation rate of the oxidation product (Entries 3–5). Although Yb modification enhanced the total activity, *i.e.*, the formation rate of O_2, the activities for photocatalytic conversion of CO_2 exhibited different trends than the anodic photocurrent values. For instance, the formation rate of O_2 over $3Yb/Ga_2O_3$, which exhibited the highest anodic photocurrent, was lower than that over $1Yb/Ga_2O_3$. During the photocatalytic conversion of CO_2 by H_2O, the consumption efficiency of electrons for the reduction of CO_2 and H_3O^+ could also affect the concentration of holes near the surface, which is related to the total activity, resulting in the observed difference between the photocatalytic conversion of CO_2 and the photoelectrochemical measurements. However, the improvement of the anodic oxidation activity on the surface of Ga_2O_3 by Yb modification is a plausible reason for the high activity of the Yb-modified Ga_2O_3 photocatalysts.

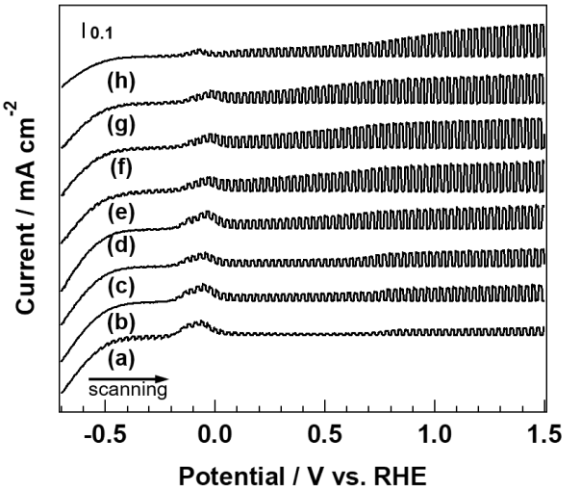

Figure 14. Linear sweep voltammograms of the 3Yb/Ga_2O_3/FTO photoelectrode in a series of mixed $NaHCO_3$ and Na_3PO_4 electrolyte aqueous solutions under chopped illumination (photoirradiation turned on or off every 3 s): (a) 10 mM $NaHCO_3$ and 30 mM Na_3PO_4 at pH = 5.97, (b) 20 mM $NaHCO_3$ and 26.7 mM Na_3PO_4 at pH = 6.12, (c) 40 mM $NaHCO_3$ and 20 mM Na_3PO_4 at pH = 6.30, (d) 50 mM $NaHCO_3$ and 16.7 mM Na_3PO_4 at pH = 6.39, (e) 60 mM $NaHCO_3$ and 13.3 mM Na_3PO_4 at pH = 6.48, (f) 80 mM $NaHCO_3$ and 6.7 mM Na_3PO_4 at pH = 6.60, (g) 90 mM $NaHCO_3$ and 3.3 mM Na_3PO_4 at pH = 6.70, and (h) 100 mM $NaHCO_3$ at pH = 6.80. The electrochemical potentials were converted to the values against RHE using the pH values shown in **Table 1**.

To discuss the dominant factor affecting the oxidation activity on the photoelectrodes in further detail, the photocurrents of 3Yb/Ga_2O_3/FTO were measured in a series of mixed $NaHCO_3$ and Na_3PO_4 electrolyte solutions with a fixed Na^+ concentration of 0.1 M. **Figure 14** shows the linear sweep voltammograms measured under chopped irradiation in the various mixed electrolytes. The potentials of the photoelectrode were converted to the values against RHE using eq. (5). **Table 1** summarizes [CO_2(aq)], [HCO_3^-], and [CO_3^{2-}] in the aqueous phase, as calculated from the pH values of the series of mixed electrolytes using eq. (6)–(9). Within the series of mixed electrolytes, 3Yb/Ga_2O_3 exhibited the same onset potential of the anodic photocurrent (−0.5 V *vs*. RHE). However, the anodic current increased with an increase of the fraction of $NaHCO_3$. As mentioned by Shao-Horn *et al*.,electrocatalytic water oxidation on an oxide surface yields pH-independent activity on the RHE scale [36, 37]. Among the CO_2-related species dissolved in the electrolyte, the concentration of CO_3^{2-} was much lower than those of CO_2(aq) and HCO_3^-. Thus, we consider CO_2(aq) and HCO_3^- as the rate determining factors for the oxidation activity of H_2O.

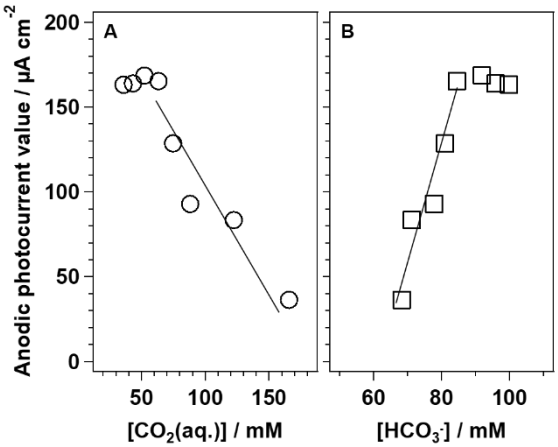

Figure 15. Relationships between the anodic current of the 3Yb/Ga_2O_3/FTO photoelectrode at 1.1 V *vs*. RHE and the concentration of (A) CO_2(aq) and (B) HCO_3^- in electrolyte solutions, as obtained from the linear sweep voltammograms in **Figure 14**. The concentrations of CO_2-related species in the electrolyte and the corresponding pH are summarized in **Table 1**.

Figure 15 shows the relationships between the anodic current of the 3Yb/Ga_2O_3 photoelectrode at an applied voltage of 1.1 V *vs*. RHE and the concentrations of CO_2(aq) and HCO_3^-. As shown in **Figure 15(A)**, the anodic current has a negative correlation with [CO_2(aq)]. In contrast, a positive correlation is observed between the anodic current and [HCO_3^-] (**Figure 15(B)**), indicating that the concentration of HCO_3^- is a key factor in the anodic water oxidation activity. The anodic photocurrent values could be maintained at high HCO_3^- concentrations because of limitations in either the diffusion of HCO_3^- or the charge separation ability on the Ga_2O_3 photoelectrode. The former suggestion is not reasonable because the limitation of the anodic photocurrent during positive scanning was also observed in electrolytes with low HCO_3^- fractions. Thus, in this case, the charge separation at each applied potential limited the anodic photocurrent.

The anodic photocurrent values showed a positive correlation with [HCO_3^-] over the Yb/Ga_2O_3 photoelectrodes. Sayama *et al*. proposed that HCO_3^- acts as an intermediate species during oxidation of H_2O in $NaHCO_3$ aqueous solution over ZrO_2 photocatalysts, as shown by the following equations[38-40].

$$h^+ + HCO_3^- \rightarrow HCO_3^{\cdot} \quad (13)$$

$$HCO_3^{\cdot} \rightleftarrows H^+ + CO_3^{\cdot -} \quad (14)$$

$$2CO_3^{\cdot -} \rightarrow C_2O_6^{2-} \quad (15)$$

$$C_2O_6^{2-} + 2H^+ \rightarrow O_2 + 2CO_2 \quad (16)$$

where h^+ is photogenerated holes. In this mechanism, HCO_3^- ions act as hole traps, resulting in the formation of carbonate radicals ($CO_3^{\bullet}$) and peroxydicarbonate species ($C_2O_6^{2-}$) as intermediate species during O_2 production. The adsorption abilities of CO_2 on a series of Yb/Ga_2O_3 photocatalysts are representative of the amounts of surface basic sites, which we consider to affect the local concentration of HCO_3^- ions near the surface. It is well known that the surface electronegativity, *i.e.*, the basicity of metal oxides, is well correlated with the zeta potential[41, 42]. Basic oxides, such as BaO, MgO, and Y_2O_3, are positively charged in neutral electrolytes. Thus, it is expected that HCO_3^- ions can be concentrated near the surface of the positively charged catalyst. Assuming that the rate is determined by hole trapping by HCO_3^- ions (eq. (13)), the concentrations of photogenerated holes at the surface of the photocatalyst and HCO_3^- ions near the active sites are related to the total activity.

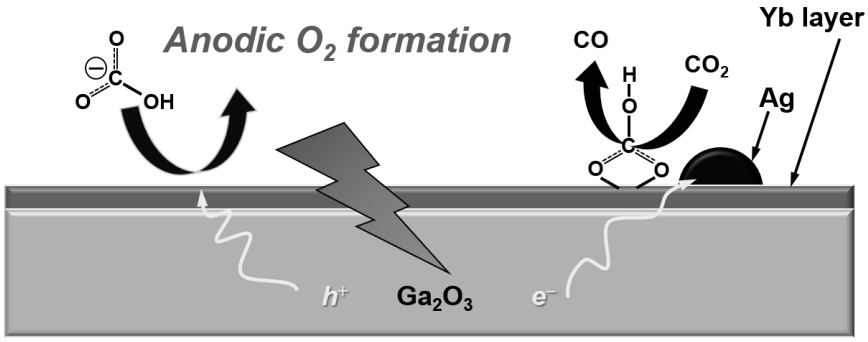

Figure 16. Schematic illustration of the behavior of photogenerated electrons and holes in a Ag/Yb/Ga_2O_3 photocatalyst during the photocatalytic conversion of CO_2 by H_2O.

In **Figure 16**, we present a schematic illustration of the behavior of photogenerated electrons and holes in a Ag/Yb/Ga_2O_3 photocatalyst during the photocatalytic conversion of CO_2 by H_2O. As mentioned in our previous reports, photoexcited electrons were consumed to reduce adsorbed bicarbonate species, formed by the adsorption of CO_2(aq) onto hydroxyl groups, to CO as a reduction product [21]. Modification with Yb improved the adsorption ability of CO_2, resulting in higher selectivity toward CO than that achieved with Ag/Ga_2O_3[19, 20]. The insights provided by our photoelectrochemical investigation indicated that HCO_3^- ions were involved in the O_2 formation process *via* $C_2O_6^{2-}$ ions. The Yb species on the surface of Ga_2O_3 improved the local concentration of HCO_3^- owing to the positive charge derived from their basicity. However, excess Yb modification resulted in the formation of surface-modified Yb species, which prevented oxidative O_2 formation.

Conclusions

The photoelectrochemical measurements on Yb-modified Ga_2O_3 photocatalysts revealed that the modification of Ga_2O_3 with Yb species dramatically improved the anodic photocurrent while maintaining the onset potential of Ga_2O_3. The E_{FB} of Ga_2O_3, estimated using impedance measurements, was not affected by Yb modification, suggesting that the Yb species only affected the surface properties of Ga_2O_3, not the bulk. The relationship between the CO_2 adsorption ability and the anodic photocurrent over the Yb loading amounts indicated that a high concentration of CO_2-adsorption sites on the surface led to the high oxidation activity. In addition, the anodic current values in a series of mixed $NaHCO_3$ and Na_3PO_4 electrolytes showed a positive correlation with the concentration of HCO_3^-. Thus, we concluded that the oxidative formation of O_2, which was related to the concentration of HCO_3^- near the surface, was promoted by Yb modification, resulting in an increase in the activity for the photocatalytic conversion of CO_2 by H_2O. These findings could lead to the establishment of an efficient system for the photocatalytic conversion of CO_2 by H_2O.

References

1 T. Inoue, A. Fujishima, S. Konishi and K. Honda, *Nature*, 1979, **277**, 637–638.

2 G. Centi, E. A. Quadrelli and S. Perathoner, *Energy Environ. Sci.*, 2013, **6**, 1711–1731.

3 E. V. Kondratenko, G. Mul, J. Baltrusaitis, G. O. Larrazábal and J. Pérez-Ramírez, *Energy Environ. Sci.*, 2013, **6**, 3112–3135.

4 T. Arai, S. Sato and T. Morikawa, *Energy Environ. Sci.*, 2015, **8**, 1998–2002.

5 K. Teramura and T. Tanaka, *Phys. Chem. Chem. Phys.*, 2018, **20**, 8423–8431.

6 T. Takayama, K. Tanabe, K. Saito, A. Iwase and A. Kudo, *Phys. Chem. Chem. Phys.*, 2014, **16**, 24417–24422.

7 K. Teramura, Z. Wang, S. Hosokawa, Y. Sakata and T. Tanaka, *Chem. Eur. J.*, 2014, **20**, 9906–9009.

8 K. Teramura, H. Tatsumi, Z. Wang, S. Hosokawa and T. Tanaka, *Bull. Chem. Soc. Jpn*, 2015, **88**, 431–437.

9 Z. Wang, K. Teramura, S. Hosokawa and T. Tanaka, *Appl. Catal. B: Environ.*, 2015, **163**, 241–247.

10 Z. Huang, K. Teramura, S. Hosokawa and T. Tanaka, *Appl. Catal. B: Environ.*, 2016, **199**, 272–281.

11 S. Iguchi, S. Kikkawa, K. Teramura, S. Hosokawa and T. Tanaka, *Phys. Chem. Chem. Phys.*, 2016, **18**, 13811–13819.

12 S. Iguchi, K. Teramura, S. Hosokawa and T. Tanaka, *Catal. Sci. Technol.*, 2016, **6**, 4978–4985.

13 Z. Wang, K. Teramura, Z. Huang, S. Hosokawa, Y. Sakata and T. Tanaka, *Catal. Sci. Technol.*, 2016, **6**, 1025–1032.

14 S. Iguchi, Y. Hasegawa, K. Teramura, S. Kidera, S. Kikkawa, S. Hosokawa, H. Asakura and T. Tanaka, *Sustain. Energ. Fuels*, 2017, **1**, 1740–1747.

15 H. Nakanishi, K. Iizuka, T. Takayama, A. Iwase and A. Kudo, *ChemSusChem*, 2017, **10**, 112–118.

16 R. Pang, K. Teramura, H. Asakura, S. Hosokawa and T. Tanaka, *Appl. Catal. B: Environ.*, 2017, **218**, 770–778.

17 R. Pang, K. Teramura, H. Tatsumi, H. Asakura, S. Hosokawa and T. Tanaka, *Chem. Commun.*, 2018, **54**, 1053–1056.

18 A. J. Bard, R. Parsons and J. Jordan, *Standard Potentials in Aqueous Solutions*, Marcel Dekker, New York, 1985.

19 Z. Huang, K. Teramura, H. Asakura, S. Hosokawa and T. Tanaka, *J. Mater. Chem. A*, 2017, **5**, 19351–19357.

20 H. Tatsumi, K. Teramura, Z. Huang, Z. Wang, H. Asakura, S. Hosokawa and T. Tanaka, *Langmuir*, 2017, **33**, 13929–13935.

21 K. Teramura, K. Hori, Y. Terao, Z. Huang, S. Iguchi, Z. Wang, H. Asakura, S. Hosokawa and T. Tanaka, *J. Phys. Chem. C*, 2017, **121**, 8711–8721.

22 M. W. Kanan and D. G. Nocera, *Science*, 2008, **321**, 1072–1075.

23 Y. Park, K. J. McDonald and K. S. Choi, *Chem. Soc. Rev.*, 2013, **42**, 2321–2337.

24 B. Ohtani, *Phys. Chem. Chem. Phys.*, 2014, **16**, 1788–1797.

25 K. Gelderman, L. Lee and S. W. Donne, *J. Chem. Educ.*, 2007, **84**, 685–688.

26 L. M. Peter, *J. Solid State Electrochem.*, 2013, **17**, 315–326.

27 F. F. Abdi, L. Han, A. H. M. Smets, M. Zeman, B. Dam and R. van de Krol, *Nat. Commun.*, 2013, **4**, 2195–2021.

28 K. S. Joya, K. Takanabe and H. J. M. de Groot, *Adv. Energy Mater.*, 2014, **4**, 1400252–1400257.

29 Y. Ma, S. R. Pendlebury, A. Reynal, F. Le Formal and J. R. Durrant, *Chem. Sci.*, 2014, **5**, 2964–2973.

30 A. Yamakata, M. Kawaguchi, N. Nishimura, T. Minegishi, J. Kubota and K. Domen, *J. Phys. Chem. C*, 2014, **118**, 23897–23906.

31 Y. Ma, F. Le Formal, A. Kafizas, S. R. Pendlebury and J. R. Durrant, *J. Mater. Chem. A*, 2015, **3**, 20649–20657.

32 C. Zachaus, F. F. Abdi, L. M. Peter and R. van de Krol, *Chem. Sci.*, 2017, **8**, 3712–3719.

33 A. Kudo and Y. Miseki, *Chem. Soc. Rev.*, 2009, **38**, 253–278.

34 F. F. Abdi and R. van de Krol, *J. Phys. Chem. C*, 2012, **116**, 9398–9404.

35 J. L. Shumaker, C. Crofcheck, S. A. Tackett, E. Santillan-Jimenez, T. Morgan, Y. Ji, M. Crocker and T. J. Toops, *Appl. Catal. B: Environ.*, 2008, **82**, 120–130.

36 A. Grimaud, O. Diaz-Morales, B. Han, W. T. Hong, Y. L. Lee, L. Giordano, K. A. Stoerzinger, M. T. M. Koper and Y. Shao-Horn, *Nat. Chem.*, 2017, **9**, 457–465.

37 W. T. Hong, K. A. Stoerzinger, Y.-L. Lee, L. Giordano, A. Grimaud, A. M. Johnson, J. Hwang, E. J. Crumlin, W. Yang and Y. Shao-Horn, *Energy Environ. Sci.*, 2017, **10**, 2190–2200.

38 K. Sayama and H. Arakawa, *J. Phys. Chem.*, 1993, **97**, 531–533.

39 K. Sayama and H. Arakawa, *J. Photochem. Photobiol. A: Chem.*, 1996, **94**, 67–76.

40 K. Sayama and H. Arakawa, *J. Chem. Soc., Faraday Trans.*, 1997, **93**, 1647–1654.

41 N. Koura, T. Tsukamoto, H. Shoji and T. Hotta, *Jpn. J. Appl. Phys.*, 1995, **34**, 1643–1647.

42 Y. Takayama, H. Negishi, S. Nakamura, N. Koura, Y. Idemoto and F. Yamaguchi, *J. Ceram. Soc. Jpn.*, 1999, **107**, 119–122.

Chapter 7

Effect of Surface Reforming by O_3 Treatment on the Activity of Ag Cathode for Electrochemical Reduction of CO_2

Abstract

We investigated the effect of an oxidation treatment by O_3 on the activity for the electrochemical reduction of CO_2 over Ag cathode and revealed that the reconstructed Ag-electrode surface from AgO precursor was effective for the selective reduction of CO_2 with a high current density: the Ag electrode treated by O_3 (Ag_O_3 electrode) exhibited the current density of 4.0 mA cm^{-2} and the faradaic efficiency toward CO of 96% at an applied voltage of −1.6 V *vs.* Ag/AgCl, whereas those over Ag foil were 1.3 mA cm^{-2} and 62%, respectively. Although the electrochemical surface area of active Ag species was enlarged through the treatment, the turnover frequency of CO evolution over Ag_O_3 electrode was two times higher than that over the pristine Ag foil electrode. Grazing incidence X-ray diffraction revealed that the Ag particles anisotropically grew along the [111] direction over the electrode surface during reduction of AgO species, which were formed through the treatment by O_3, indicating that the obtained Ag surface was effective for the reduction of CO_2 with suppressing H_2 production. Our findings provide a simple surface-reforming technique of Ag electrode for improving the activity for electrochemical reduction of CO_2 toward CO, leading to the electrode-design technology for recycling CO_2 into useful feedstocks.

Introduction

The conversion of CO_2 into useful feedstocks is an urgent topic because it is a solution to prevent the global warming and to create the carbon neutral energy cycle.[1] Especially, the electrochemical reduction of CO_2 is a potential strategy for simultaneously suppressing the increase in global CO_2 concentration and storing the renewable energies such as solar and wind.[2] Among the CO_2-derived value-added products, such as CO, CH_4, HCOOH, and CH_3OH, the production of CO is promising technology for supplying a feedstock for a Fischer-Tropsch process.[3] Hori *et al.*[4] investigated the electrochemical reduction of CO_2 over various metal electrodes: Au, Ag, Zn, Ga, and Pd foil cathodes exhibited the activity for CO evolution. Especially, Ag-based cathodes have attracted the interest because of their relatively higher activity for CO evolution than the other metal cathodes. However, a high applied overpotential was required to achieve a high selective CO_2 reduction over Ag-based cathodes: the faradaic efficiency toward CO (FE_{CO}) over Ag foil was low at a low overpotential owing to the competitive H_2 production.[5-8] To improve the product selectivity and the efficiency at a low overpotential, nanostructured,[5, 6, 9-11] size-controlled,[12, 13] alloying,[14, 15] dealloying,[16] and oxide-derived[7, 8, 17] Ag cathodes have been studied in recent years; thus, it has been gradually unveiled the effect of the surface structure of Ag-based cathodes, including the valence, coordination number, residual oxygen species, or face-orientation, on the activity for the electrochemical reduction of CO_2.

Among the above-mentioned electrode-reforming techniques, the oxidative treatments are promising technologies for improving the selectivity toward CO or the activity for reduction of CO_2 during the electrochemical reduction of CO_2 over various metal cathodes.[7, 8, 17-24] Kanan and co-workers[18, 22] reported that the electrochemically oxidized Au electrode and the annealed Cu (Cu_2O-derived Cu) electrode exhibited the high selectivity toward CO evolution and HCOOH evolution at a low overpotential, respectively: the grain boundary structure formed on the surface of those oxide-derived electrodes were considered to induce the selective CO_2 reduction.[22, 25, 26] Smith and co-workers[7, 17] reported that the Ag_2O-derived electrode, which was fabricated by the anodization of Ag cathode in sodium hydroxide aqueous solution, showed the high FE_{CO} at a low overpotential because the competitive H_2 evolution was suppressed at a high local pH at near the

surface of the electrode and/or COOH intermediates were easily formed in the presence of the residual oxygen species on the electrode surface. Zhou *et al.*[8] mentioned that the Ag electrode, which was anodized in sodium nitrate aqueous solution, also exhibited the high FE_{CO} owing to the face-orientation of Ag species at the electrode surface. With those in mind, it is essential to control the surface structure of the Ag electrode, such as the grain boundary, residual oxygen, and face-orientation, although it is not clear which factor is the dominant in the effective reduction of CO_2. Moreover, the fundamental understanding is required that the effect of the oxidized Ag precursors on the structure of electrochemically formed Ag particles and their activity for electrochemical reduction of CO_2.

Ag(I) oxide (Ag_2O) is recognized to be the only Ag oxide that is stable in the atmosphere.[27] Thus, strong oxidizing agents are required to oxidize Ag species to more than Ag(I) oxide. AgO nanoparticles were obtained through the precipitation of $AgNO_3$ by using potassium persulfate ($K_2S_2O_8$) as an oxidizing reagent.[28] In addition, ozone (O_3), which has a strong oxidation capacity, is also used for the oxidative formation of AgO.[27, 29] Waterhouse *et al.*[29] studied the oxidation mechanism of a polycrystalline Ag foil under O_3 atmosphere and revealed that the obtained Ag_2O film over Ag foil surface was subsequently oxidized to AgO with a prolonged exposure to O_3. The electrochemical reduction of the AgO films is considered to result in the enlarged Ag metal surface as compared to the pristine Ag foil. Moreover, the unique crystal growth of the Ag metal particles is expected during the electrochemical reduction of the AgO films, owing to the different crystal structure of AgO ($P2_1/c$) from that of Ag_2O (cuprous oxide structure, $Pn-3m$).[30, 31] In this study, we therefore fabricated the Ag cathode through the oxidative treatment by O_3 and the following electrochemical reduction and applied it for the electrochemical reduction of CO_2. The relationships between the structure of O_3-treatment-derived Ag particles and the turnover frequency for CO production were investigated.

Experimental

Prior to use, Ag foil (Nilaco Corporation, 99.98%, 6 cm^2) electrodes were sonicated in hexane, ethanol, and Milli-Q water (Milli-Q Integral MT5S, Merck Millipore), in turn. For the treatment with

an O_3 generator (ASM401N, Asumi Giken Limited), the front and back sides of the Ag foil were exposed to O_3 atmosphere for a fixed time (*X* h), respectively,（referred to as Ag_O_3_*X*h electrode, hereinafter）. To reduce the black film on the Ag-electrode surface which was formed by the treatment with O_3 (hereinafter, O_3-treatment-derived powders), Ag_O_3_*X*h electrode was electrochemically reduced in the three electrode system equipped with a Pt wire and a standard Ag/AgCl electrode as a counter electrode and a reference electrode, respectively: the Ag_O_3_*X*h electrode was immersed in 0.1 M $KHCO_3$ aqueous solution and then was applied with a voltage of 0 V *vs*. Ag/AgCl for 5 min. For a control experiment, the O_3-treatment-derived powders were physically removed from the surface of Ag_O_3_20h electrode: after the sonication for 15 min in Mili-Q water, the powders on the surface of Ag_O_3_20h electrode were totally removed (hereinafter, w/o film electrode). For comparison, other Ag precursors, such as AgO, Ag_2O, and $AgNO_3$ (23μmol each, FUJIFILM Wako Pure Chemical Corp.), were deposited on the pristine Ag foil through the electrochemical reduction at an applied voltage of 0 V *vs*. Ag/AgCl for 5 min, which the molar amount of Ag precursors was almost equivalent to the O_3-treatment-derived powders formed on the Ag_O_3_20h electrode.

The electrochemical reduction of CO_2 over Ag electrodes was conducted in a H-type cell, of which two chambers were separated by a cation exchange membrane (Nafion®117, DuPont), equipped with a Pt wire and a standard Ag/AgCl electrode as a counter electrode and a reference electrode, respectively. Each chamber was filled with 100 mL 0.1 M $KHCO_3$ aqueous solution as an electrolyte. CO_2 gas (99.999 %) was bubbled into the solution at a flow rate of 20 mL min^{-1}. An external voltage was applied by using a potentiostat (HZ-5000, Hokuto Denko Corporation). Reduction products, such as CO and H_2, were analyzed every hour by a thermal conductive detector (TCD-GC) using a GC-8A chromatograph (Shimadzu Corporation) equipped with a Molecular Sieve 5A column with Ar as the carrier gas and by a flame ionization detector (FID-GC, Shimadzu Corporation) with a methanizer using a Shincarbon ST column with N_2 as the carrier gas. The cathodic current density (I_d), formation rates of CO (R_{CO}) and H_2 (R_{H2}), faradaic efficiency toward CO (FE_{CO}) and H_2 (FE_{H2}), and turnover frequency of CO (TOF_{CO}) and H_2 (TOF_{H2}) during 1 h of reaction were described as follows:

$$I_d\ (\mathrm{A\ cm^{-2}}) = I_A / S_g \qquad (1)$$

$$R_{CO} \text{ or } R_{H2} \text{ (mol h}^{-1} \text{ cm}^{-2}) = TF \times P_i / S_g \quad (2)$$

$$FE_{CO} \text{ or } FE_{H2} \text{ (\%)} = 100 \times (2 \times R_i \times F / I_d) \quad (3)$$

$$TOF_{CO} \text{ or } TOF_{H2} \text{ (s}^{-1}) = R_i \times S_g / S_{UPD} \quad (4)$$

where, I_A (A), TF (mol h^{-1}), P_i (%), and F (C mol^{-1}) represent the total current, total flow of reaction gas, molar ratio of component of product, i, in the outlet gas, and faraday constant, respectively. The S_g (cm^2) is the geometrical surface area of Ag electrodes which were immersed in the electrolyte (6 cm^2). The S_{UPD} (mol) is the electrochemical surface area (ECSA) of Ag electrodes estimated by using underpotential deposition of Pb.[32, 33]

Underpotential deposition of Pb (UPD Pb)[32-36] was conducted in an aqueous solution containing 0.1 M $HClO_4$, 0.1 M $NaClO_4$, and 1 mM $Pb(ClO_4)_2$. The cyclic voltammogram (CV) was recorded with a potential scan between −0.60 and −0.20 V *vs*. Ag/AgCl at a scan rate of 40 mV min^{-1} by using the three-electrode system as mentioned above. The ECSA of Ag electrodes (S_{UPD}), which were applied for the reaction at an applied voltage of −1.6 V *vs*. Ag/AgCl for 4 h, was determined from the electricity of cathodic current derived from the underpotential deposition of Pb at around −0.28 V *vs*. Ag/AgCl:

$$S_{UPD} \text{ (mol)} = C / F \quad (5)$$

where, C (C) is the electricity of cathodic current derived from the underpotential deposition of Pb. The background voltammogram was recorded in an aqueous solution containing 0.1 M $HClO_4$ and 0.1 M $NaClO_4$ (namely, w/o $Pb(ClO_4)_2$).

Grazing incidence X-ray diffraction (GI-XRD) patterns of Ag electrodes were collected by using an X-ray diffractometer (Multiflex, Rigaku Corporation) with Cu K_α radiation at an acceleration voltage of 40 kV. From the diffraction patterns obtained at various incident angles, the incidence angle was fixed at 1 degree for the surface sensitive analysis (**Figure 1**). The XRD pattern of the O_3-treatment-derived powders was collected by using an X-ray diffractometer (Ultima IV, Rigaku Corporation) using Cu K_α radiation at an acceleration voltage of 40 kV. Scanning Electron Microscope (SEM) images of Ag electrodes were captured by using a Field Emission Scanning Electron Microscope (FE-SEM, SU-8220, Hitachi High-Technologies) at an acceleration voltage of 3.0 kV. The valence of Ag species at the electrode surface was analyzed by X-ray photoelectron spectra (XPS) by using an X-ray photoelectron spectrometer (ESCA3400, Shimadzu Corporation)

with Mg K_α radiation at an acceleration voltage of 10 kV.

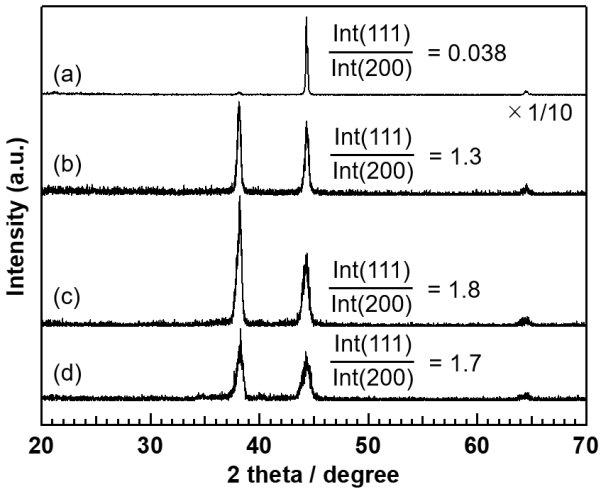

Figure 1. (a) XRD pattern of Ag_O_3_20h electrode after 4 h of reaction. GI-XRD patterns acquired at the incident angle at (b) 5, (c) 2, and (d) 1 degrees. The ratios of peak intensity of (111) facet to that of (200) facet were maintained in the patterns at the incident angle below 2 degrees, indicating that the obtained pattern at the incident angle at 1 degree was attributed to the surface structure of the electrodes.

Results and discussion

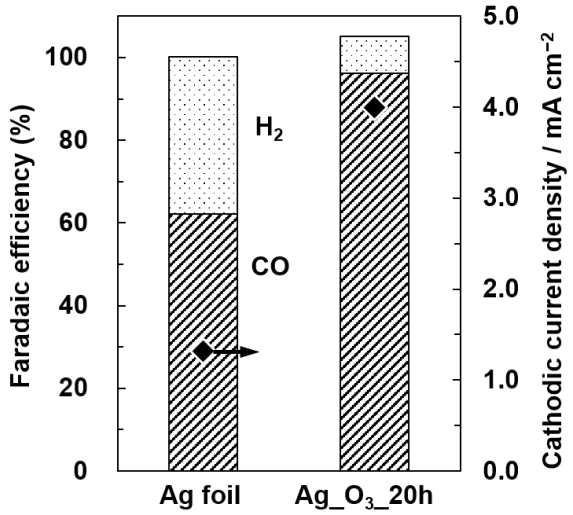

Figure 2. Reaction results for the electrochemical reduction of CO_2 over Ag foil and Ag_O_3_20h electrodes at −1.6 V *vs*. Ag/AgCl for 1 h. FE_{CO}; hatched bar graph, FE_{H2}; dotted bar graph, I_d; diamonds.

Figure 2 shows the activities for the electrochemical reduction of CO_2 over Ag foil and O_3-treated Ag electrodes at an applied voltage of −1.6 V *vs*. Ag/AgCl for 1 h. The current density over Ag foil electrode, (hereinafter, I_d) was 1.3 mA cm^{-2}, which was normalized by the geometrical surface area of the Ag electrode immersed in $KHCO_3$ electrolyte. The faradaic efficiency toward CO (FE_{CO}) and H_2 (FE_{H2}) were 62% and 38%, respectively. It should be note that other reduction products, e. g. HCOOH and CH_4, were not detected. By the treatment under O_3 atmosphere for 20 h, the Ag electrode (Ag_O_3_20h electrode) exhibited three times as high I_d (4.0 mA cm^{-2}) as that over Ag foil. In addition, the FE_{CO} over Ag_O_3_20h electrode dramatically increased to 96%. Since the faradaic efficiency toward reduction products was ~100%, all the electrons were used for the production of CO and H_2, suggesting that the surface of Ag_O_3_20h electrode had reduced even after 1 h of reaction. Those improvements in the I_d and FE_{CO} indicated that the treatment by O_3 was effective for the electrochemical reduction of CO_2 over Ag electrode. The electrochemical surface area (ECSA) of Ag electrodes was evaluated by underpotential monolayer deposition of Pb (UPD Pb) (**Figure 3**).[32-34] During the negative scanning from −0.20 V to −0.60 V, two cathodic current peaks were observed at −0.28 V (C_{up}) and −0.48 V (C_{op}), whereas two anodic peaks appeared at −0.38 V (A_{op}) and −0.25 V (A_{up}) during the positive scanning. The C_{up} and A_{up} were attributed to the underpotential deposition and desorption of Pb, respectively. In contrast, the C_{op} and A_{op} were attributed to the bulk electrolysis, namely, the overpotential deposition and desorption of Pb, respectively. The amount of UPD Pb (S_{UPD}) of Ag_O_3_20h electrode (13 nmol), which was evaluated by the electricity of the C_{up} peak, was more than two times higher than that of Ag foil (6.2 nmol). The turnover frequencies of CO (TOF_{CO}) of Ag_O_3_20h was 9.3 s^{-1}. Since the TOF_{CO} of Ag foil was only 4.1 s^{-1}, the unique surface of the Ag electrode derived from the treatment by O_3 was considered to induce the improvement in the activity for electrochemical reduction of CO_2.

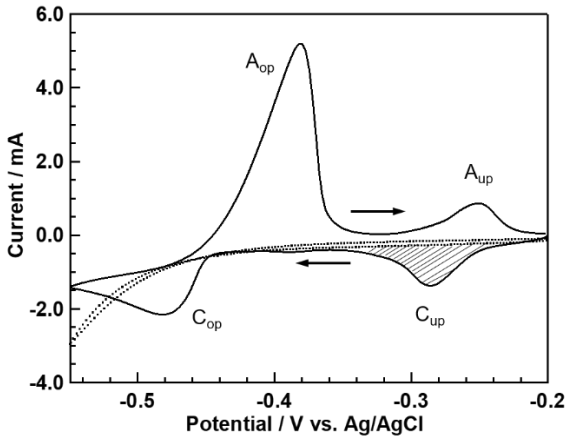

Figure 3. Cyclic voltammograms over Ag foil electrode in the presence of Pb (solid line) and w/o Pb (dashed line). C_{up} and A_{up} are the current peaks derived from the underpotential deposition and desorption of Pb, respectively. C_{op} and A_{op} are the current peaks derived from the overpotential deposition and desorption of Pb, respectively.

Figure 4 shows FE_{CO} over Ag foil and Ag_O_3_20h electrodes at various applied voltages. Overall, Ag_O_3_20h electrode exhibited higher FE_{CO} than Ag foil electrode. For instance, Ag_O_3_20h electrode exhibited much higher FE_{CO} (13%) than that over Ag foil electrode (1.9%) at applied voltage of −1.2 V *vs*. Ag/AgCl. As high voltage was applied, FE_{CO} over Ag foil and Ag_O_3_20h electrodes increased. At −1.4 V, the FE_{CO} over Ag_O_3_20h electrode (73%) was more than three times higher than that over Ag foil electrode. At −1.6 V, FE_{CO} over Ag_O_3_20h reached to 94%, whereas that over Ag foil electrode reached to 95% at applied voltage of −1.8 V. Those clearly indicated that the treatment by O_3 lowered the onset potential for electrochemical reduction of CO_2. In Tafel plots over Ag foil and Ag_O_3_20h electrode (**Figure 5**), both of the logarithm of I_d over them linearly increased between −1.2 and −1.6 V *vs*. Ag/AgCl, indicating that the reduction proceeded without the diffusion limitation at these applied voltages.

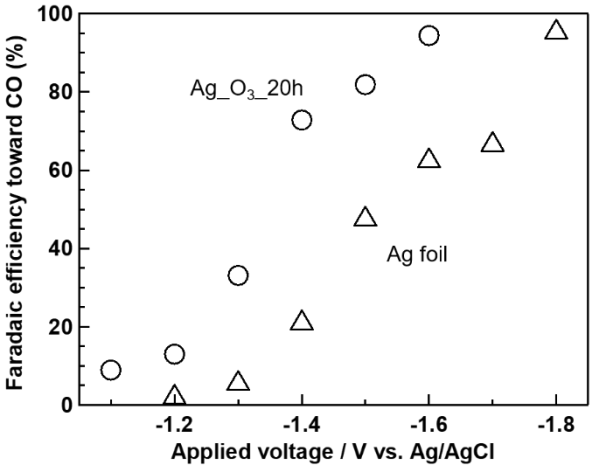

Figure 4. Faradaic efficiencies toward CO over Ag foil electrode (triangles) and Ag_O_3_20h electrode (circles) at various applied voltages.

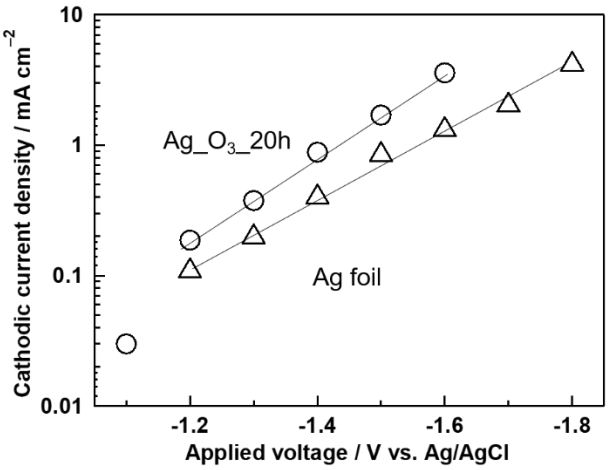

Figure 5. Tafel plots over Ag foil electrode (triangles) and Ag_O_3_20h electrode (circles). The corresponding results for the product selectivity are shown in **Figure 4**.

Figure 6 shows the time courses of the electrochemical reduction of CO_2 over Ag_O_3_20h and Ag foil electrodes at −1.6 V *vs.* Ag/AgCl for 7 h. The FE_{CO} over Ag_O_3_20h electrode (96%, after 1 h of reaction) was maintained above 90% during the 7 h of reaction. Ag foil electrode also exhibited a stable FE_{CO} above 60% throughout the 7 h of reaction. Whereas the I_d of Ag foil electrode was relatively stable between 1.2 and 1.3 mA cm^{-2}, the I_d of Ag_O_3_20h electrode increased from 3.9 to 5.5 mA cm^{-2} as time passed. After 4 h of reaction, the ECSA of Ag_O_3_20h electrode, S_{UPD}, was 13 nmol. The S_{UPD} increased to 16 nmol after 7 h of reaction. We consider that the enlarged ECSA of Ag_O_3_20h electrode resulted in the increase in the I_d.

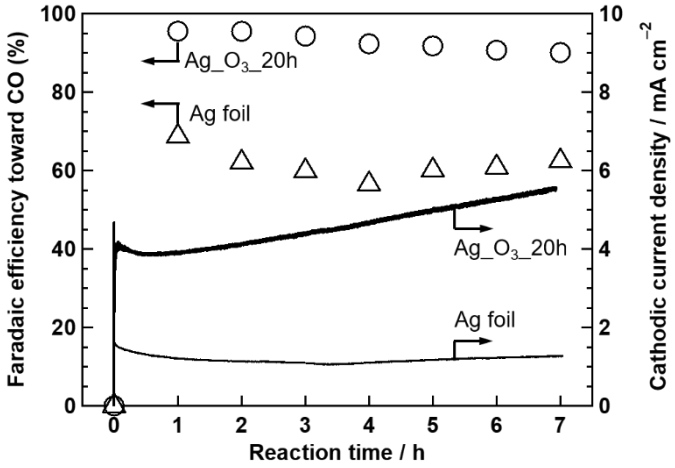

Figure 6. Time courses of the electrochemical reduction of CO_2 over Ag_O_3_20h and Ag foil electrodes at an applied voltage of −1.6 V *vs.* Ag/AgCl for 7 h. Circles; FE_{CO} of Ag_O_3_20h electrode, triangles; FE_{CO} of Ag foil electrode, Thick line; I_d of Ag_O_3_20h electrode, Thin line; I_d of Ag foil electrode.

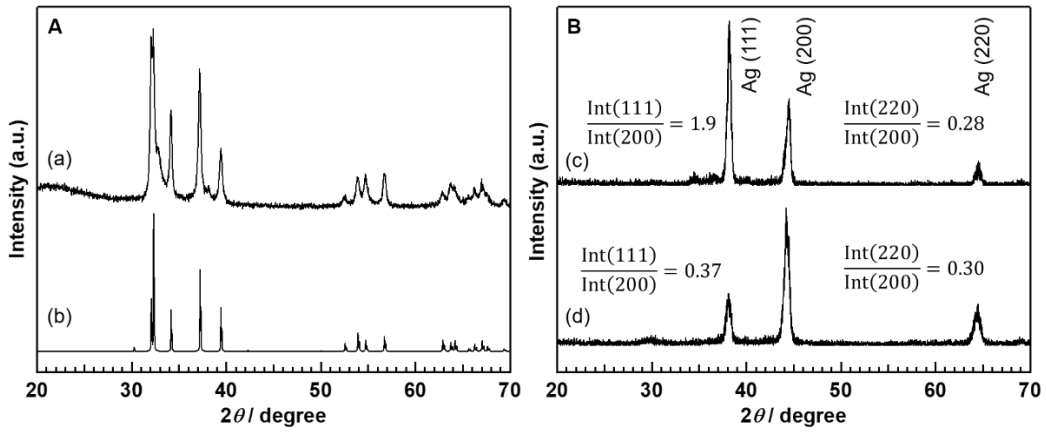

Figure 7. (A) XRD patterns of (a) O_3-treatment-derived powder and (b) the reference AgO (ICSD27659). **(B)** GI-XRD patterns of (c) Ag_O_3_20h and (d) Ag foil electrodes after 4 h of reaction.

The XRD pattern of O_3-treatment-derived powder was assigned to AgO, suggesting that the oxidation treatment by O_3 formed AgO particles on the surface of the Ag electrode (**Figure 7(A)**). **Figure 7(B)** shows the surface-sensitive grazing incidence X-ray diffraction (GI-XRD) patterns of Ag electrodes after 4 h of reaction. The diffraction peak derived from AgO was not observed over Ag_O_3_20h electrode after 4 h of reaction (Ag_O_3_20h_AR electrode), whereas the patterns derived from fcc Ag species were observed. This suggested that AgO species, which were formed *via* the treatment by O_3, were reduced to metallic Ag species during the reaction. In addition, the diffraction peak derived from the Ag(111) facet of Ag_O_3_20h_AR electrode was relatively higher than the

others. In contrast, the highest peak in the pattern of the pristine Ag foil was the diffraction peak derived from the Ag(200) facet. The difference in the intensities of the diffraction peaks were owing to the structural change through the oxidative treatment and the following reduction. Here, the ratio of peak intensity of (111) and (220) to that of (200) facets (Int(111) / Int(200) and Int(220) / Int(200), respectively) were summarized in the inset of **Figure 7(B)**. The Int(220) / Int(200) of Ag foil and Ag_O_3_20h_AR electrodes were the almost same (0.30 and 0.28, respectively). In contrast, the Int(111) / Int(200) of Ag_O_3_20h_AR electrode (1.9) was significantly higher than that of Ag foil (0.37). The relatively high Int(111) / Int(200) of Ag_O_3_20h_AR electrode was likely owing to the anisotropically growth of Ag particles along the [111] direction as compared to the Ag species on the surface of Ag foil electrode.[8, 37-39] Since the (211) and (110) facets are orthogonal to the (111) facet, we consider that the (211) or (110) facets were likely to be exposed on the surface of the Ag particles which anisotropically grew along the [111] direction (**Figure 8**). Hoshi *et al.*[40] investigated the activities for electrochemical reduction of CO_2 over various Ag single-crystal electrodes, revealing that the order of partial current densities of CO evolution over them was Ag(100) < Ag(111) < Ag(110). Rosen *et al.*[9] theoretically estimated that the rate of CO production over Ag(211) facet was higher than Ag(110) facet: their density functional theory (DFT) calculations revealed that the Ag(211) facet stabilized COOH species as intermediates. On these in mind, we consider that the increase in the FE_{CO} and TOF_{CO} by the treatment by O_3 was owing to the active Ag facets, such as (211) and (110) facets, on the surface of Ag particles, which were exposed *via* the anisotropic crystal growth along [111] direction upon the reduction of AgO species.

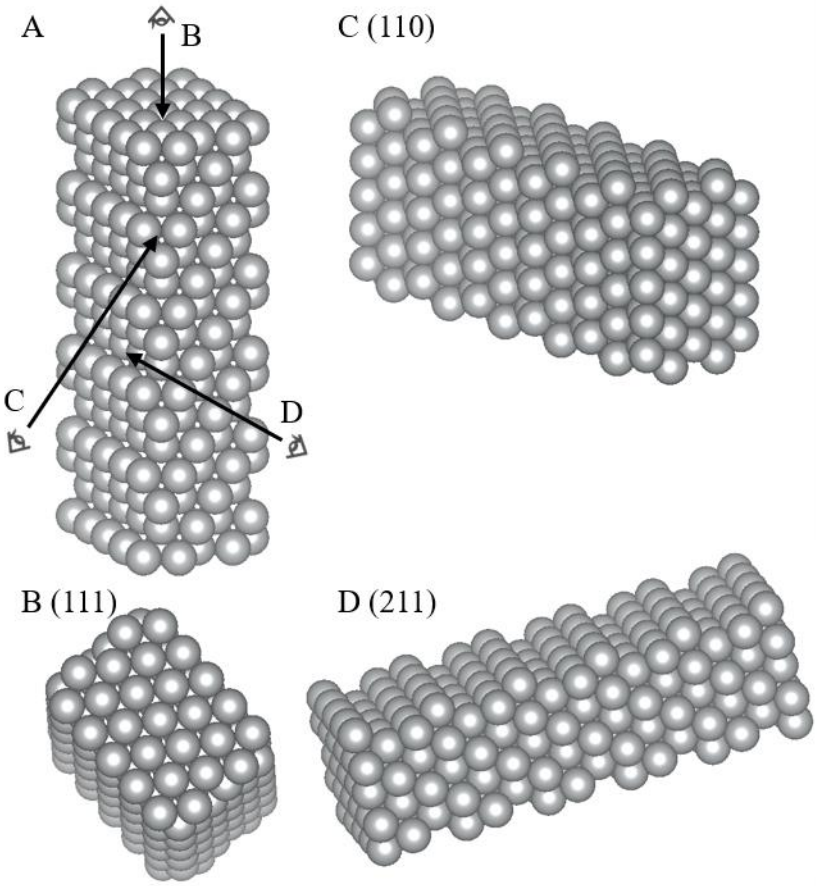

Figure 8. (A) Structure models of Ag particle with an anisotropic growth along [111] direction and their surface structure of **(B)** (111), **(C)** (110), and **(D)** (211) facets viewed from the direction of the arrow in **(A)**.

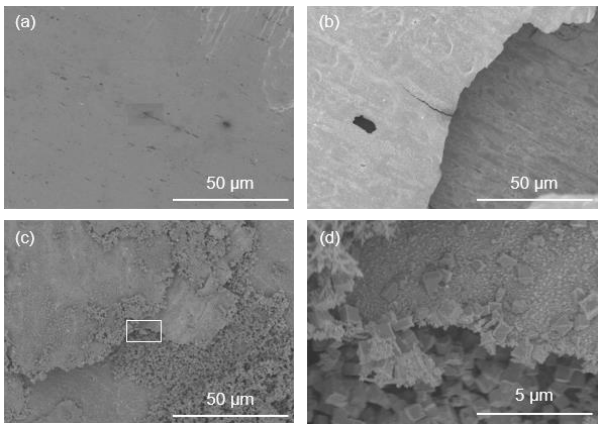

Figure 9. SEM images of the upper view of (a) Ag foil, (b) Ag_O_3_20h, and (c) Ag_O_3_20h_AR electrodes, and (d) the enlarged view of the inset square in (c).

To monitor the morphology of Ag species, the surface structure of the Ag electrodes was observed by using scanning electron microscope (SEM). **Figure 9** shows SEM images of Ag foil, Ag_O_3_20h, and Ag_O_3_20h_AR electrodes. As shown in **Figure 9**(a), the surface of the pristine Ag foil was relatively smooth, although some cracks were observed. Through the treatment by O_3, the sheet-like structure was observed on the surface of Ag foil (**Figure 9**(b)). After the reaction, the sheet-like structure was partially observed over Ag_O_3_20h_AR electrode (**Figure 9**(c) and (d)). In addition, the aggregates of the cubic nanoparticles were included in the sheet-like structure. These images evidenced that the increase in ECSA of Ag_O_3_20h_AR was owing to the formation of the nanostructured Ag particles though the reduction of AgO.

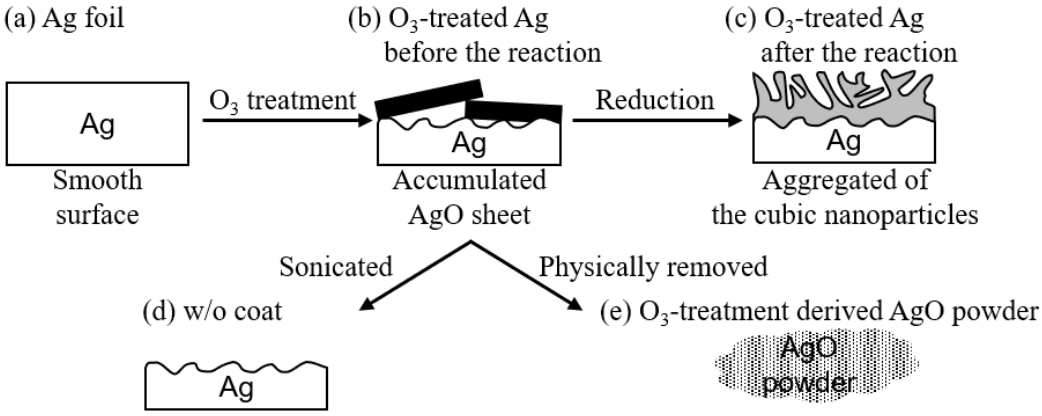

Figure 10. Model scheme of the treatment by O_3 and the following reduction of the Ag foil electrode. (a) Ag foil, (b) O_3-treated Ag electrode, (c) O_3-treated Ag electrode after the reaction, (d) w/o film, and (e) O_3-treatment-derived AgO powder.

From the XRD patterns and SEM images as mentioned above, **Figure 10** shows the schematic view of the morphology change in the surface structure of the Ag electrode through the treatment by O_3 and the following reduction. Upon the exposing by O_3, the sheet-like AgO species were formed on the surface of Ag foil accompanied by the roughened surface structure (**Figure 10**(b)). After the reaction, the AgO species were reduced to Ag metals, which formed the aggregates of cubic particles with high ECSA. (**Figure 10**(c)). Moreover, those Ag particles anisotropically grew along [111] direction. To ensure the importance of the AgO species as precursors, the O_3-treatment-derived powders were physically removed by the sonication from the surface of Ag_O_3_20h electrode (**Figure 10**(d) and (e)).

Table 1. Reaction results for the electrochemical reduction of CO_2 over a series of Ag electrodes as control experiments. The corresponding S_{UPD} and the intensity ratio of (111) to (200) facets of those electrodes after 4 h of reaction.

Entry	Electrode	FE_{CO} (%)	FE_{H2} (%)	I_d / mA cm^{-2}	S_{UPD} / nmol	TOF_{CO} / s^{-1}	TOF_{H2} / s^{-1}	Int(111) / Int(200)
1	Ag foil	62	38	1.3	6.2	4.1	2.5	0.37
2	Ag_O_3_20h	96	9	4.0	13	9.3	0.86	1.9
3	O_3–film-derived	96	6	4.5	9.8	14	0.83	2.3
4	w/o film	56	42	2.1	7.3	5.0	3.7	0.39

Table 1 compiles the results for the control experiments which were performed by using Ag foil electrode (entry 1), Ag_O_3_20h electrode (entry 2), Ag foil electrode with O_3-treatment-derived powder as precursor (O_3-film-derived electrode, entry 3), and Ag_O_3_20h electrode of which the O_3-treatment-derived powders on the surface were removed (w/o film electrode, entry 4). As mentioned above, the FE_{CO} over Ag foil and Ag_O_3_20h electrodes were 62 and 96%, respectively. The S_{UPD} increased upon the treatment by O_3 because the surface of Ag_O_3_20h electrode was reconstructed through the reduction of AgO species. When the O_3-film-derived powders were introduced to Ag foil as a precursor (entry 3), the FE_{CO} and I_d increased as compared to those of the pristine Ag foil electrode. For the surface area of the electrodes, the S_{UPD} of O_3-film-derived electrode was smaller than that of Ag_O_3_20h electrode (entry 2, 9.8 nmol). Since the S_{UPD} of w/o film electrode (entry 4, 7.3 nmol) was larger than that of Ag foil (entry 1), we considered the high S_{UPD} of Ag_O_3_20h electrode as compared to that of O_3-film-derived electrode to be owing to the roughened Ag surface through the oxidation treatment. Although the S_{UPD} of w/o film electrode was larger than that of Ag foil electrode, the FE_{CO} and the Int(111) / Int(200) of w/o film electrode were as low as that of Ag foil electrode even after the electrode surface was roughened. Those suggested that the addition of O_3-treatment-derived powder was essential to form the active Ag surface and improve the FE_{CO}. Moreover, the TOF_{H2} of Ag_O_3_20h and O_3-film-derived electrodes dramatically decreased as compared to that of Ag foil electrode, suggesting that the Ag surface derived from the reduction of O_3-treatment-derived powder effectively suppressed the unfavorable H_2 evolution.

Table 2. Reaction results for the electrochemical reduction of CO_2 over Ag electrodes with various Ag precursors. The corresponding S_{UPD} and the intensity ratio of (111) to (200) facets of those electrodes after 4 h of reaction.

Entry	Precursor (23 μmol)	FE_{CO} (%)	FE_{H2} (%)	I_d / mA cm^{-2}	S_{UPD} / nmol	TOF_{CO} / s^{-1}	TOF_{H2} / s^{-1}	Int(111) / Int(200)
1	-	62	38	1.3	6.2	4.1	2.5	0.37
2	Ag_2O	90	11	2.8	7.8	10	1.2	0.86
3	$AgNO_3$	95	3	3.8	22	5.1	0.14	1.9
4	AgO	95	12	4.2	7.8	16	2.0	3.2

Table 2 shows the reaction results over Ag electrodes with addition of various Ag precursors, such as Ag_2O (entry 2), $AgNO_3$ (entry 3), and AgO (entry 4), compared with that of the pristine Ag foil w/o Ag precursors (entry 1). Those Ag electrodes with addition of Ag precursors showed higher FE_{CO} and I_d than Ag foil, although the properties, such as the S_{UPD} and Int(111) / Int(200) were totally different among the three electrodes. The Ag electrode with using AgO precursor exhibited the highest I_d among the electrodes. The I_d over the Ag electrode with using $AgNO_3$ precursor was higher than that with using Ag_2O precursor. However, the largest S_{UPD} was obtained when the $AgNO_3$ was added as a precursor likely owing to the dendrite-like structure (SEM image, **Figure 11**(c)). The Ag electrodes with using Ag_2O and AgO precursors resulted in the almost same S_{UPD}. As a result, the Ag electrode with using AgO precursor exhibited the highest TOF_{CO} among the Ag electrodes. The Ag electrode with using AgO precursor exhibited the highest Int(111) / Int(200). XPS of the Ag electrodes suggested that the added Ag_2O, $AgNO_3$, and AgO precursors were completely reduced to Ag(0) metal after the reaction (**Figure 12**). We therefore concluded that the AgO precursor favor to grow along [111] direction during the reduction toward Ag(0) metal, leading to form the active Ag surface, resulting the high TOF_{CO} and FE_{CO}.

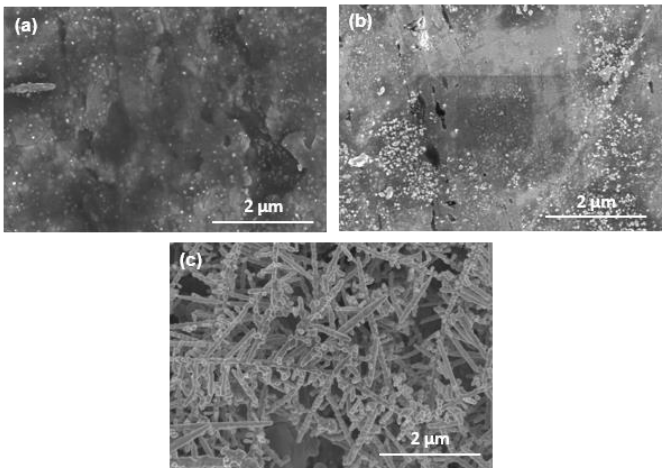

Figure 11. SEM images of Ag electrodes after 4 h of reaction in the presence of Ag precursors: (a) AgO, (b) Ag_2O, and (c) $AgNO_3$.

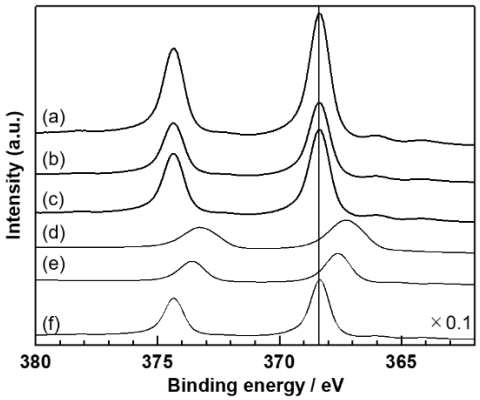

Figure 12. Ag 3*d* XPS of Ag electrodes after 4 h of reaction in the presence of Ag precursors: (a) AgO, (b) Ag_2O, and (c) $AgNO_3$. The reference spectra of (d) AgO, (e) Ag_2O, and (f) Ag.

Our findings provided a simple treatment method by O_3 for the efficient electrochemical reduction of CO_2. The AgO-precursor-derived Ag particles which grew along [111] direction exhibited high FE_{CO} of 96% with suppressing H_2 production. Of course, further investigation on the mechanism over the oxide-derived Ag surface is required to unveil why the Ag particle which grew along [111] direction was effective for the electrochemical reduction of CO_2. Moreover, clear understanding on the growth mechanism of Ag particles from AgO precursor affords us the further effective electrode-design technology: Cheng *et al.*[41] investigated the electrochemical reduction behavior of AgO and Ag_2O by a sweeping voltammogram with different scanning rates, revealing that AgO exhibited two reduction paths to form Ag(0) metal: one was direct reduction to Ag and the

other was indirect path through Ag_2O.

Recent studies on the oxide-derived Ag electrodes for the electrochemical reduction of CO_2 mentioned the importance of the residual oxygen species on the surface of Ag electrodes: Jiang *et al.*[20] reported the surface bonded $O–Ag^{\delta+}$ species by using an angle resolved X-ray photoelectron spectroscopy (XPS). Firet *et al.*[17] also observed the oxygen residue at the surface of the oxide-derived Ag electrode by using an *operando* grazing incidence X-ray absorption spectroscopy (GI-XAS). Those surface-sensitive observations indicated that the residual oxygen species were included in the working state of electrochemical reduction of CO_2 over Ag cathodes. Moreover, in situ attenuated total reflection infrared spectroscopy (ATR-IR) study evidenced that CO_2 species which attached onto the Ag electrode surface existed as intermediate species when an external voltage was applied, although the valence of the surface Ag species was ambiguous in those studies.[42, 43] Firet *et al.*[17] proposed the reduction mechanism including the oxygen residue on the step structure of Ag(110) surface by using a density functional theory with a structure-optimized model: the adsorbed CO_2 species attached on the Ag surface interacted with the proton species attached onto the neighboring oxygen residue sites, leading to the efficient formation of COOH intermediates. Indeed, Katayama *et al.*[44] investigated the reaction mechanism during the electrocatalytic reduction of CO_2: CO was produced *via* C-bound COOH species adsorbed on the electrode surface, not *via* O-bound CO_3 species. On these adsorption models of CO_2 and surface states of the Ag electrode in mind, the presence of the oxygen residue is expected to induce the formation of C-bound COOH species at a low overpotential, leading to a high selectivity toward CO. The combination of spectroscopy, such as ATR-IR spectroscopy and XAS under working state, leads to clarify the mechanism of the electrochemical reduction of CO_2 and to develop the design of further effective Ag cathodes.

Conclusions

The effect of an oxidative treatment for Ag foil cathode on the activity for the electrochemical reduction of CO_2 was investigated by exposing Ag foil to O_3 atmosphere and the following electrochemical reduction under reaction condition. The Ag foil electrode which was

exposed to O_3 atmosphere for 20 h (Ag_O_3_20h electrode) exhibited the excellent faradaic efficiency toward CO (FE_{CO}, 96%) at an applied voltage of −1.6 V *vs*. Ag/AgCl, whereas the FE_{CO} over the pristine Ag foil electrode was 62%. The electrochemical surface area of Ag_O_3_20h electrode (S_{UPD}), which was estimated by underpotential deposition of Pb, increased through the treatment by O_3. However, the turnover frequencies toward CO (TOF_{CO}) over Ag_O_3_20h electrode (9.3 s^{-1}) was more than two times higher than that over Ag foil (4.1 s^{-1}), clearly indicating that the obtained Ag surface through the treatment was effective for the electrochemical reduction of CO_2. Grazing incidence X-ray diffraction patterns revealed that AgO species, which were derived from the treatment by O_3, were reduced to Ag metal particles over the electrode during the electrochemical reduction of CO_2. Moreover, the ratio of the diffraction-peak intensity of (111) facet to that of (200) facet of the fcc-Ag particles which were formed on Ag_O_3 electrode was much higher than that of the surface layer of Ag foil, indicating that the Ag particles were formed with an anisotropic growth along the [111] direction through the reduction of AgO. Furthermore, Ag foil electrode with addition of AgO precursor exhibited the highest TOF_{CO} among a series of Ag precursors, AgO, Ag_2O, and $AgNO_3$, indicating that AgO precursor was essential to form the active Ag surface for the efficient reduction of CO_2 with suppressing H_2 production. In this work, we presented the simple reforming treatment of Ag cathode by O_3, which formed the active Ag species by the reduction of AgO species, resulting in the efficient CO production during the electrochemical reduction of CO_2.

Reference

1 M. Mikkelsen, M. Jørgensen and F. C. Krebs, *Energy Environ. Sci.*, 2010, **3**, 43–81.

2 B. Kumar, J. P. Brian, V. Atla, S. Kumari, K. A. Bertram, R. T. White and J. M. Spurgeon, *Catal. Today*, 2016, **270**, 19–30.

3 D. T. Whipple and P. J. A. Kenis, *J. Phys. Chem. Lett.*, 2010, **1**, 3451–3458.

4 Y. Hori, H. Wakebe, T. Tsukamoto and O. Koga, *Electrochim. Acta*, 1994, **39**, 1833–1839.

5 Y.-C. Hsieh, S. D. Senanayake, Y. Zhang, W. Xu and D. E. Polyansky, *ACS Catal.*, 2015, **5**, 5349–5356.

6 M. Ma, K. Liu, J. Shen, R. Kas and W. A. Smith, *ACS Energy Letters*, 2018, **3**, 1301–1306.

7 M. Ma, B. J. Trzesniewski, J. Xie and W. A. Smith, *Angew. Chem. Int. Ed. Engl.*, 2016, **55**, 9748–9752.

8 L. Q. Zhou, C. Ling, M. Jones and H. Jia, *Chem. Commun.*, 2015, **51**, 17704–17707.

9 J. Rosen, G. S. Hutchings, Q. Lu, S. Rivera, Y. Zhou, D. G. Vlachos and F. Jiao, *ACS Catal.*, 2015, **5**, 4293–4299.

10 K. Sun, L. Wu, W. Qin, J. Zhou, Y. Hu, Z. Jiang, B. Shen and Z. Wang, *J. Mater. Chem. A*, 2016, **4**, 12616–12623.

11 H. Wang, Z. Han, L. Zhang, C. Cui, X. Zhu, X. Liu, J. Han and Q. Ge, *J. CO2 Util.*, 2016, **15**, 41–49.

12 M. S. Jee, H. S. Jeon, C. Kim, H. Lee, J. H. Koh, J. Cho, B. K. Min and Y. J. Hwang, *Appl. Catal. B: Environ.*, 2016, **180**, 372–378.

13 A. Salehi Khojin, H. R. M. Jhong, B. A. Rosen, W. Zhu, S. Ma, P. J. A. Kenis and R. I. Masel, *J. Phys. Chem. C*, 2013, **117**, 1627–1632.

14 H. Park, J. Choi, H. Kim, E. Hwang, D. H. Ha, S. H. Ahn and S. K. Kim, *Appl. Catal. B: Environ.*, 2017, **219**, 123–131.

15 Q. Yu, X. Meng, L. Shi, H. Liu and J. Ye, *Chem. Commun.*, 2016, **52**, 14105–14108.

16 Q. Lu, J. Rosen, Y. Zhou, G. S. Hutchings, Y. C. Kimmel, J. G. Chen and F. Jiao, *Nat. Commun.*, 2014, **5**, 3242–3247.

17 N. J. Firet, M. A. Blommaert, T. Burdyny, A. Venugopal, D. Bohra, A. Longo and W. A. Smith, *J. Mater. Chem. A*, 2019, **7**, 2597–2607.

18 Y. Chen, C. W. Li and M. W. Kanan, *J. Am. Chem. Soc.*, 2012, **134**, 19969–19972.

19 Z. M. Detweiler, J. L. White, S. L. Bernasek and A. B. Bocarsly, *Langmuir*, 2014, **30**, 7593–7600.

20 K. Jiang, P. Kharel, Y. Peng, M. K. Gangishetty, H. Y. G. Lin, E. Stavitski, K. Attenkofer and H. Wang, *ACS Sustain. Chem. Eng.*, 2017, **5**, 8529–8534.

21 S. Y. Lee, H. Jung, N. K. Kim, H. S. Oh, B. K. Min and Y. J. Hwang, *J. Am. Chem. Soc.*, 2018, **140**, 8681–8689.

22 C. W. Li and M. W. Kanan, *J. Am. Chem. Soc.*, 2012, **134**, 7231–7234.

23 M. Ma, K. Djanashvili and W. A. Smith, *Phys. Chem. Chem. Phys.*, 2015, **17**, 20861–20867.

24 D. H. Won, C. H. Choi, J. Chung, M. W. Chung, E. H. Kim and S. I. Woo, *ChemSusChem*, 2015, **8**, 3092–3098.

25 X. Feng, K. Jiang, S. Fan and M. W. Kanan, *J. Am. Chem. Soc.*, 2015, **137**, 4606–4609.

26 R. G. Mariano, K. McKelvey, H. S. White and M. W. Kanan, *Science*, 2017, **358**, 1187–1192.

27 R. O. Suzuki, T. Ogawa and K. Ono, *J. Am. Ceram. Soc.*, 1999, **82**, 2033–2038.

28 A. Sobhani Nasab and M. Behpour, *J. Mater. Sci.: Mater. Electron.*, 2015, **27**, 1191–1196.

29 G. I. N. Waterhouse, G. A. Bowmaker and J. B. Metson, *Appl. Surf. Sci*, 2001, **183**, 191–204.

30 J. A. McMillan, *J. Inorg. Nucl. Chem.*, 1960, **13**, 28–31.

31 R. W. G. Wyckoff, *Am. J. Sci.*, 1922, **3**, 184–188.

32 U. Schmidt, S. Vinzelberg and G. Staikov, *Surf. Sci.*, 1996, **348**, 261–279.

33 M. F. Toney, J. G. Gordon, M. G. Samant, G. L. Borges, O. R. Melroy, D. Yee and L. B. Sorensen, *J. Phys. Chem.*, 1995, **99**, 4733–4744.

34 M. Fayette, Y. Liu, D. Bertrand, J. Nutariya, N. Vasiljevic and N. Dimitrov, *Langmuir*, 2011, **27**, 5650–5658.

35 D. Kolb, M. Przasnyski and H. Gerischer, *J. Electroanal. Chem. Interf. Electrochem.*, 1974, **54**, 25–38.

36 S. Trasatti and O. A. Petrii, *J. Electroanal. Chem.*, 1992, **327**, 353–376.

37 X. Guo, P. Li, S. Yin and W. Qin, *J. Fluor. Chem.*, 2017, **200**, 91–95.

38 J. Y. Kim, S. B. Choi, D. W. Kim, S. Lee, H. S. Jung, J. K. Lee and K. S. Hong, *Langmuir*, 2008, **24**, 4316–4319.

39 B. J. Kwon, K. M. Lee, H. Y. Shin, J. Kim, J. Liu, S. Yoon, S. Lee, Y. H. Ahn and J.-Y. Park, *Mater. Sci. Eng. B*, 2012, **177**, 132–139.

40 N. Hoshi, M. Kato and Y. Hori, *J. Electroanal. Chem.*, 1997, **440**, 283–286.

41 Y. Cheng, M. Yan and Z. Jiang, *Electrochem. Solid-State Lett.*, 2007, **10**, 5–8.

42 W. Deng, L. Zhang, H. Dong, X. Chang, T. Wang and J. Gong, *Chem. Sci.*, 2018, **9**, 6599–6604.

43 N. J. Firet and W. A. Smith, *ACS Catal.*, 2017, **7**, 606–612.

44 Y. Katayama, F. Nattino, L. Giordano, J. Hwang, R. R. Rao, O. Andreussi, N. Marzari and Y. Shao Horn, *J. Phys. Chem. C*, 2018, **123**, 5951–5963.

Summary

This thesis investigated the design of active sites for the selective reduction of CO_2. Parts I and II focused on controlling the selectivity of catalytic hydrogenation of CO_2 over supported metal catalysts. Part III demonstrated improvements in the activity and selectivity of Ga_2O_3-based photocatalysts loaded with an Ag co-catalyst for the photocatalytic conversion of CO_2 in water. The key results are summarized as follows:

Part I described the preparation and use of a Ni-based isolated Pt alloy catalyst for the selective hydrogenation of CO_2 to CH_4. The role of the isolated Pt atoms and their surrounding Ni atoms in the selective hydrogenation of CO intermediates to CH_4 was investigated using *in situ* and transient infrared spectroscopy and kinetic studies.

Chapter 1 demonstrated that the addition of minute quantities of Pt species into a Ni/Al_2O_3 catalyst dramatically improved catalytic activity during the methanation of CO_2 while maintaining excellent selectivity for CH_4 evolution as compared to bulk Ni atoms. This is in contrast to bulk Pt atoms, which favor the production of CO rather than CH_4. X-ray absorption spectroscopy (XAS) and infrared spectroscopy in the presence of CO revealed that isolated Pt atoms formed on the surface of the Ni–Pt solid-solution-alloy with electronic interactions occurring between $Pt^{\delta-}$ atoms and surrounding $Ni^{\delta+}$ atoms. These findings indicated that the unique electronic and geometric characteristics of the isolated Pt atoms alloyed with the Ni matrix promoted efficient and selective hydrogenation of CO_2 to CH_4, despite the tendency of unalloyed Pt catalysts to favor CO production.

Chapter 2 elucidated the cooperative role of Pt and Ni atoms in active sites in promoting the efficient and selective hydrogenation of CO_2 to CH_4. *In situ* observations and transient changes in infrared spectra during the hydrogenation of CO_2 revealed the unique stepwise methanation mechanism involving CO species bridging isolated Pt atoms and neighboring Ni atoms. Kinetic studies revealed that the high H_2 dissociation ability of the Pt species accelerated hydrogenation of the carbon species over the Pt–Ni alloy surface, thereby curtailing the rate limitations of CH_4 formation associated with Ni catalysts. The bifunctional role of isolated Pt atoms therefore allowed for efficient formation of CH_4 while maintaining selective CH_4 formation of the Ni catalyst.

Part II described the effect of interactions between the supported Pt particles and the γ-Al_2O_3 surface on product selectivity during catalytic hydrogenation of CO_2. The mechanism of formation of Pt particles on the γ-Al_2O_3 surface governed by metal-support interactions and the origin of the activity for producing the typically disfavored CH_4 during CO_2 hydrogenation were investigated using *in situ* XAS and infrared spectroscopy, respectively.

In Chapter 3, *in situ* time-resolved XAS was used to describe the dynamics of the reduction of PtO_x particles by H_2 to form two-dimensional, low-coordinated Pt particles mediated by metal-support interactions with γ-Al_2O_3. The temperature-programmed reduction profile of PtO_x on γ-Al_2O_3 under H_2 flow and *in situ* Pt L_3-edge XAS observations clearly indicated that PtO_x particles were stabilized by interaction with the γ-Al_2O_3 surface as compared to a PtO_2 powder reference. The relatively stable PtO_x species were reduced below 423 K, and the interfacial PtO_x species at the Al_2O_3 surface were reduced above 423 K. From time-resolved Pt L_3-edge XAS during the *in situ* reduction of PtO_x on γ-Al_2O_3 by H_2, the morphology change mechanism was proposed that the three-dimensional PtO_x particles were converted to two-dimensional, low-coordinated Pt particles upon the reduction of interfacial PtO_x species.

Chapter 4 elucidated the active sites of the γ-Al_2O_3-supported Pt catalyst involved in the disfavored formation of CH_4 during hydrogenation of CO_2 at ambient pressure using a combination of XAS and diffuse reflectance infrared Fourier transform spectroscopy (DRIFTS) with product analysis. Coordination environment analysis revealed the unique structure of Pt nanoparticles derived from the interaction between Pt and γ-Al_2O_3. Pt L_3- and L_2-edge X-ray absorption near-edge structure spectroscopy was used to quantify the unoccupied density states, including the antibonding orbitals, formed with the intermediates attached to the Pt surface. XAS and DRIFTS spectra revealed that the formation of co-adsorbed H and CO species onto the Pt sites at the interface between Pt particles and the γ-Al_2O_3 surface further supported hydrogenation of CO species to CH_4.

Part III demonstrated three approaches to improve the photocatalytic activity and control the selectivity of Ga_2O_3 photocatalysts loaded with Ag co-catalyst for the conversion of CO_2. First, band engineering was performed by doping Ga_2O_3 with Rh to improve the photoabsorption ability when irradiating with light >300 nm. Second, the effect of modifying the Ga_2O_3 surface with Yb species on the activity of electron donor oxidation was investigated using photoelectrochemical approaches. Finally, the surface characteristics of the Ag cathode were tuned to control the selectivity of the electrochemical CO_2 reduction on Ag species.

Chapter 5 reported that Rh-doped Ga_2O_3 (Ga_2O_3:Rh) exhibited photocatalytic activity for the conversion of CO_2 by H_2O using photoirradiation with light >300 nm. Although Ga_2O_3 is a wide bandgap photocatalyst that is active only under photoirradiation with <300 nm light, the absorption edge shifted to >300 nm as a result of Rh doping. Ag–Cr-loaded Ga_2O_3:Rh (0.7 mol%) generated CO (3.9 μmol h^{-1}) as a reduction product of CO_2. Rh and Ga K-edge XAS revealed that, after doping in Ga_2O_3, the trivalent Rh species did not substitute for the tetrahedral Ga site but for the octahedral Ga site of β-Ga_2O_3. Based on density functional theory calculations, the new energy level from Rh^{3+} was within the Ga_2O_3 bandgap, suggesting that the new absorption arising from the contribution of the Rh *d* t_{2g} orbital to the conduction band contributed to the activity of the photocatalytic conversion of CO_2 by H_2O using light >300 nm.

In Chapter 6, photoelectrochemical techniques revealed the role of modifying Ga_2O_3 photocatalysts with Yb species, which are known to enhance the activity and selectivity of CO formation during the photocatalytic conversion of CO_2 using H_2O as an electron donor. Photocurrent measurements indicated that modification with Yb species *via* hydrothermal treatment enhanced the anodic photocurrent of the Ga_2O_3 photoelectrode in a CO_2-saturated $NaHCO_3$ aqueous solution while maintaining the onset potential of the anodic photocurrent. The positive correlation between the anodic photocurrent value and the concentration of HCO_3^- species, as measured in two-component $NaHCO_3$ and Na_3PO_4 electrolytes, indicated that the concentration of HCO_3^- species near the surface strongly influenced the anodic O_2-formation activity of the Yb-modified Ga_2O_3 photoelectrode. It was therefore concluded that Yb modification improved H_2O oxidation activity on the surface of Ga_2O_3 by enhancing its affinity for intermediate HCO_3^- species, resulting in a high activity during the photocatalytic conversion of CO_2 by H_2O.

Chapter 7 investigated the effect of an oxidation pretreatment with O_3 on the electrochemical reduction of CO_2 using an Ag cathode and revealed that the reconstructed Ag-electrode surface from the AgO precursor was effective for the selective reduction of CO_2. The O_3-pretreated Ag electrode exhibited high faradaic efficiency towards CO (96%) production while suppressing the competitive formation of H_2 as compared to the untreated Ag foil electrode (62%) at an applied voltage of −1.6 V *vs*. Ag/AgCl. Grazing incidence X-ray diffraction revealed that the Ag particles anisotropically grew along the [111] direction over the electrode surface during the reduction of AgO species, which were formed during the O_3 pretreatment, indicating that the Ag surface obtained by oxidation pretreatment with O_3 was effective for the reduction of CO_2 and suppressed H_2 production.

In summary, catalytic systems for the selective conversion of CO_2 over heterogeneous catalysts were constructed through the design of active sites. This work proposes reasonable working mechanisms for the conversion of CO_2 in the active sites. These findings are expected to contribute to the development of technologies for recycling CO_2 into useful feedstocks.

List of Publications

Part I: **Selective Hydrogenation of CO_2 Toward CH_4 over Isolated Pt Atom in Ni–Pt Alloy**

Chapter 1

1. Soichi Kikkawa, Kentaro Teramura, Hiroyuki Asakura, Saburo Hosokawa, and Tsunehiro Tanaka
   Isolated Platinum Atoms in Ni/γ-Al_2O_3 for Selective Hydrogenation of CO_2 Toward CH_4.
   Journal of Physical Chemistry C, 2019, **123**, 23446–23454.

Chapter 2

2. Soichi Kikkawa, Kentaro Teramura, Hiroyuki Asakura, Saburo Hosokawa, and Tsunehiro Tanaka
   Cooperative Alloy Catalyst Composed of the Pt Atoms Isolated by Ni Atoms and Their Neighboring Ni Atoms: In Situ and Transient FT-IR Studies on Selective Hydrogenation of CO_2 Toward CH_4 Evolution.
   ACS Catalysis, in revision.

Part II: **Tuning the Selectivity During Hydrogenation of CO_2 over Supported Pt Catalysts**

Chapter 3

3. Soichi Kikkawa, Kentaro Teramura, Hiroyuki Asakura, Saburo Hosokawa, and Tsunehiro Tanaka
   In situ Time-Resolved XAS Study on Metal-Support-Interaction-Induced Morphology Change of PtO_2 Nanoparticles Supported on Al_2O_3 Under Reduction by H_2.
   Physical Chemistry Chemical Physics, in revision.

Chapter 4

4. Soichi Kikkawa, Kentaro Teramura, Kazuo Kato, Hiroyuki Asakura, Saburo Hosokawa, and Tsunehiro Tanaka

   A Combined *Operando* XAS-DRIFTS Study Elucidating the Active Sites for Undesirable CH_4 Formation at Pt–Al_2O_3 Interface During Hydrogenation of CO_2**.**

   Journal of the American Chemical Society, submitted.

Part III: **Photocatalytic and Electrocatalytic Reduction of CO_2 Toward CO over Ag Species**

Chapter 5

5. Soichi Kikkawa, Kentaro Teramura, Hiroyuki Asakura, Saburo Hosokawa, and Tsunehiro Tanaka

   Development of Rh-Doped Ga_2O_3 Photocatalysts for Reduction of CO_2 by H_2O as an Electron Donor at a More than 300 nm Wavelength.

   Journal of Physical Chemistry C, 2018, **122**, 21132–21139.

Chapter 6

6. Soichi Kikkawa, Yuto Nakatani, Kentaro Teramura, Hiroyuki Asakura, Saburo Hosokawa, and Tsunehiro Tanaka

   Photoelectrochemical Investigation of the Role of Surface-Modified Yb Species in the Photocatalytic Conversion of CO_2 by H_2O over Ga_2O_3 Photocatalysts.

   Catalysis Today, in revision.

Chapter 7

7. Masaatsu Ishida, Soichi Kikkawa, Kazutaka Hori, Kentaro Teramura, Hiroyuki Asakura, Saburo Hosokawa, and Tsunehiro Tanaka

   Effect of O_3 Pretreatment on the Activity of Ag Cathode for the Electrochemical Reduction of CO_2.

   ACS Applied Materials & Interfaces, to be submitted.

The following papers are not included in this thesis

8. Shoji Iguchi, Soichi Kikkawa, Kentaro Teramura, Hiroyuki Asakura, Saburo Hosokawa, and Tsunehiro Tanaka
   Investigation of the Electrochemical and Photoelectrochemical Properties of Ni–Al LDH Photocatalysts.
   Physical Chemistry Chemical Physics, 2016, **18**, 13811–13819.

9. Shoji Iguchi, Soichi Kikkawa, Kentaro Teramura, Hiroyuki Asakura, Saburo Hosokawa, and Tsunehiro Tanaka
   Drastic Improvement in the Photocatalytic Activity of Ga_2O_3 Modified with Mg–Al Layered Double Hydroxide for the Conversion of CO_2 in Water.
   Sustainable Energy & Fuels, 2017, **1**, 1740–1747.

10. Junko N. Kondo, Hiroshi Yamazaki, Asako Ishikawa, Ryota Osuga, Sho Takao, Toshiyuki Yokoi, Soichi Kikkawa, Kentaro Teramura, and Tsunehiro Tanaka
    Monolayer Tantalum Oxide on Mesoporous Silica Substrate.
    Chemistry Select, 2016, **1**, 3124–3131.

11. Masanori Takemoto, Yasuaki Tokudome, Soichi Kikkawa, Kentaro Teramura, Tsunehiro Tanaka, Kenji Okada, Hidenobu Murata, Atsushi Nakahira, and Masahide Takahashi
    Imparting CO_2 Reduction Selectivity to $ZnGa_2O_4$ Photocatalysts by Controlled Crystallization from Hetero Nano Assembly of Amorphous-like Metal Hydroxides.
    RSC advances, in press.